The Dissertation Committee for Yichen Fang Certifies that this is the approved version of the following dissertation:

High Performance Nonwoven Fiber Production via UV-Reactive and Melt State Centrifugal Spinning

Committee:

Christopher J. Ellison, Supervisor

Carlton Grant Willson

Donald R. Paul

Benny D. Freeman

Mourad Krifa

High Performance Nonwoven Fiber Production via UV-Reactive and Melt State Centrifugal Spinning

by

Yichen Fang, B.S.CHEM. & BIO. ENG.

Dissertation

Presented to the Faculty of the Graduate School of

The University of Texas at Austin

in Partial Fulfillment

of the Requirements

for the Degree of

Doctor of Philosophy

The University of Texas at Austin

May, 2016

Dedication

To Mom, Dad, and Zhenpeng, for their endless love and support. And to Grandma, for inspiring me to always strive for better.

Acknowledgements

I would like to express my sincere gratitude to my advisor, Prof. Christopher Ellison, for the guidance, support, encouragement, and motivation that he offered throughout my graduate studies. I would also like to thank the rest of my committee: Prof. Donald R. Paul, Prof. C. Grant Willson, Prof. Benny D. Freeman, and Prof. Mourad Krifa, for providing many valuable suggestions and advice on my research from various perspectives.

I thank my talented fellow labmates for all their help and support along the way and wish them the best of luck in their graduate studies and careers. Special thanks to Dr. Zhenpeng Li, Dr. Kadhir Shanmuganathan, Dr. Dustin W. Janes, Dr. Amanda R. Jones for all the stimulating discussions, interesting ideas, and insightful suggestions on my research and professional career. I am grateful for Heonjoo Ha, who promptly assisted me in a number of experiments, and my undergrads, Austin R. Dulaney and Evan Wong, who patiently performed the tedious (and seemingly endless) fiber spinning runs.

My research cannot be done without the collaborative efforts from other research groups. Special thanks to Matthew Herbert from Prof. David Schiraldi's group for synthesizing tin fluophosphate glass, Jesse Gadley from Prof. João Maia's group for training me to use CaBER, Andrew Worthen from Prof. Keith Johnston's group for measuring the surface tension measurements, Jia Wang from Prof. Eric Baer's group for sharing with me her expertise on the mechanical studies of fiber mats.

I would like to thank the wonderful tech staff from our department, Shallaco McDonald and Butch Cunningham, for helping me design and build many parts and fixing the instruments time that are critical for my research and time again.

I would like to acknowledge FibeRio, DuPont Young Professor Award, and 3M Nontenured Faculty Award for funding my research, and NSF CliPs program for funding research facilities and our interactions with Prof. Schiraldi and Prof. Maia at Case Western Reserve University.

High Performance Nonwoven Fiber Production via UV-Reactive and Melt State Centrifugal Spinning

Yichen Fang, Ph.D.

The University of Texas at Austin, 2016

Supervisor: Christopher J. Ellison

Nonwoven fibers have practical uses in diverse fields ranging from commodity products such as apparel, filtration, and hygiene products to advanced functional materials such as biomimetic scaffold materials, regenerative medicine, and optoelectronics. However, a need still exists to develop techniques to produce fibrous materials with high performance capabilities both economically and sustainably. Current synthetic fiber manufacturing technologies typically use either solvent or heat to transform a solid preformed polymer into a liquid before applying a force to draw the liquid into fiber. While the use of solvent poses concerns regarding process safety, environmental impact, and solvent recovery, the use of heat often leads to polymer degradation and excessive energy consumption.

This dissertation attempts to address the challenging issue of producing high performance microfibers and nanofibers by using centrifugal spinning, an emerging technology and a promising manufacturing alternative to melt blowing and electrospinning. The intrinsically large centrifugal force leads to high throughput and low cost processing, while the capability to process both polymer melts and solutions demonstrates flexibility. The overall objective is to develop and optimize the centrifugal

spinning process to generate novel multifunctional fibrous materials and to establish process-structure-property relationships.

In this dissertation, a new fiber fabrication method combining centrifugal spinning and light initiated polymerization will be introduced. In contrast to traditional methods that utilize preformed polymers, the technique developed in this work produces fibers on demand from liquid monomer mixtures using only light to initiate polymerization. This method presents a potential route for green manufacturing of high performance fibers by reducing and even eliminating the use of both solvent and heat. The underlying physics and the principle parameters governing fiber formation, fiber morphology and fiber diameter are discussed. This knowledge is leveraged to develop new reactive monomer formulations containing high amounts of inorganic content in order to diversify the accessible material profile and enhance fiber properties. In addition, melt state centrifugal spinning of high performance materials with distinct properties is also discussed. Overall, the methods developed in this dissertation will provide key guidance for greener nonwoven fiber manufacturing while greatly expanding the ability to directly tailor fiber properties.

Table of Contents

List of Tables

List of Figures

Chapter 1: Introduction to Nonwoven Fiber Manufacturing Technologies

1.1 NONWOVEN FIBERS

A nonwoven is a sheet of randomly oriented fibers bonded together by physical entanglements **(Figure 1.1 b)**, as opposed to woven **(Figure 1.1 a)** or knitted fabrics. To increase the mechanical integrity, the loose nonwoven mat can subsequently be subjected to spunlace, thermal, or chemical bonding processes to introduce fused junctions between individual fibers (**Figure 1.1 c**). The global nonwoven fiber industry was worth over 14 billion US dollars in 2004 and has been growing at a rate of 7-8% annually.[1] Natural and polymeric nonwoven fibers find practical uses in a wide range of industries, such as consumer hygiene products, apparel, automotive, filtration and geotextiles, among many others.

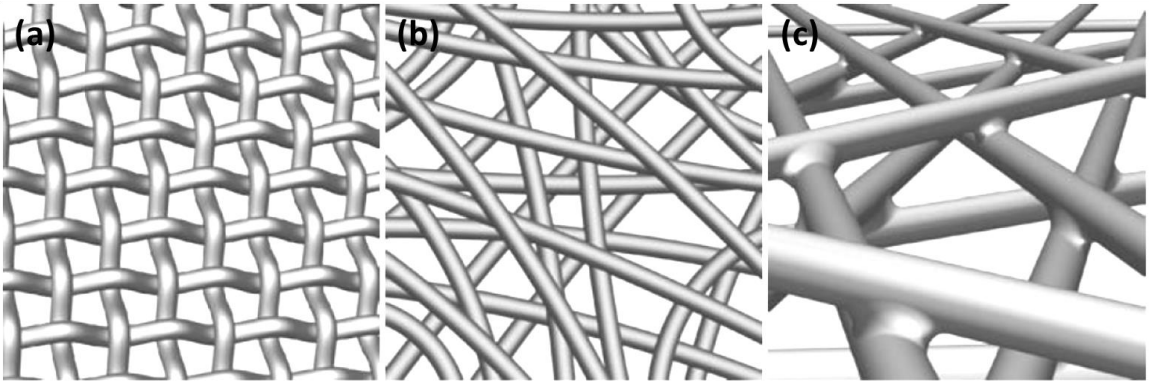

Figure 1.1: Schematic illustrations of (a) woven fabrics, (b) nonwoven fabrics, and (c) thermally or chemically bonded nonwoven fabrics. Images reprinted with permission from [2]. Copyright © 2006 Annual Reviews.

An important feature of nonwoven fibers is the high surface area to volume ratio. For instance, a one gram fiber mat containing single micron sized fibers can have a surface area over 1 m^2. Because the specific surface area of a fiber is inversely proportional to its

diameter, fibers with smaller diameters possess higher specific surface area. Nonwoven fibers with average diameters in the single micron and several hundred nanometer range have been the subject of much research effort and are desired for a number of high performance applications where specific surface area is crucial, such as catalysis, battery components, and water and oil filtration.[3-5]

Combined with their high surface area, there exists a number of versatile surface modification techniques that offer nearly limitless options to develop functional fibrous materials suitable for a wide range of specialty applications. For example, Jiang and others coated nanofibers with polydopamine to control the loading and release of anticancer drugs in a pH responsive manner for oral cancer treatments.[6-7] Starting with commercial cellulose filter paper, Jin and coworkers developed titanium coating strategies coupled with silane treatments to produce amphiphobic filter paper with inhibited bacterial adhesion.[8] In the realm of tissue engineering, numerous studies have shown that introducing functional coatings onto inert polymeric nonwoven fibers can improve cell adhesion and proliferation and lead to viable biomimetic scaffold materials.[9-11]

Despite these advancements, a need still exists to develop techniques to produce fibrous materials with high performance capabilities both economically and sustainably. Additionally, fiber processing significantly impacts the ultimate mat properties, such as average fiber length and diameter, mat porosity, fiber entanglement density, fiber strength, etc., which in turn determine potential end use applications. The following section offers an overview of the existing technologies used to fabricate nonwoven fibers and discusses the advantages and drawbacks of each method.

1.2 Fiber Spinning Technologies and Challenges

1.2.1 Conventional methods

Most commercial fibers are made by wet spinning, dry spinning, and melt spinning. In wet spinning (schematic diagram of this process is presented in **Figure 1.2 a**), a spinning dope is first prepared by dissolving a polymer in a good solvent. The spinning dope is extruded through a multi-orifice spinneret submerged in a coagulation bath containing a liquid that is miscible with the spinning dope solvent but is a non-solvent for the polymer. The spinning dope undergoes elongation and phase separation induced precipitation as it passes through the coagulation bath, solidifying into polymeric fibers.

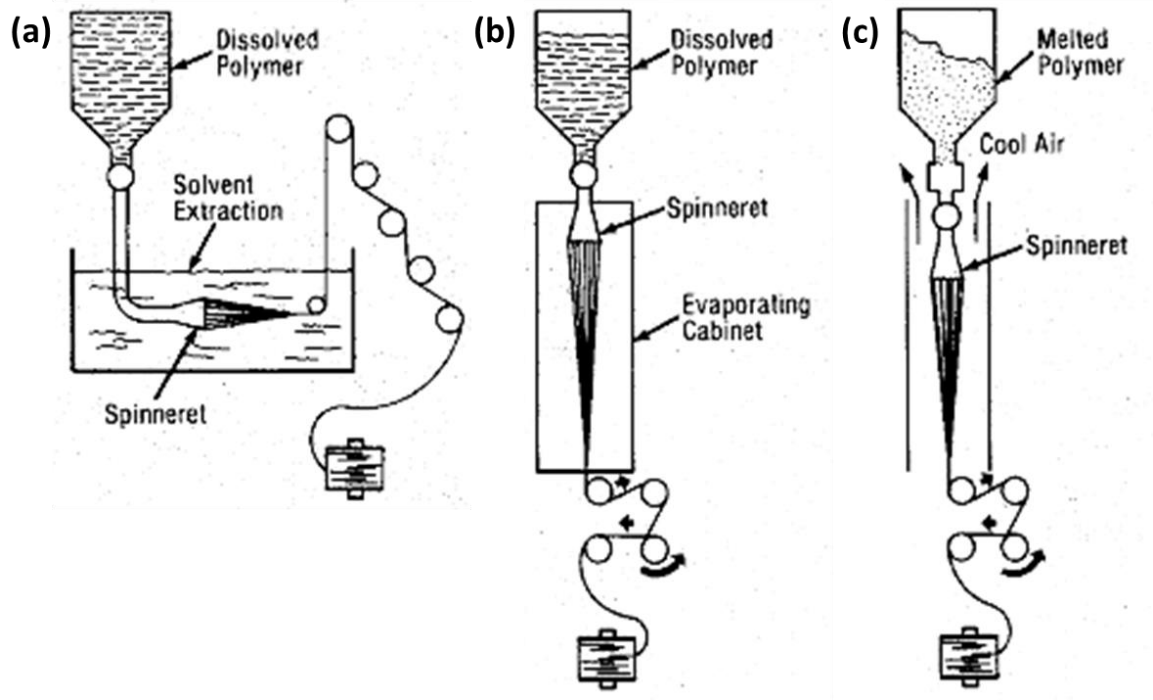

Figure 1.2: Schematic representations of (a) wet spinning, (b) dry spinning, and (c) melt spinning. Image adapted from public domain [12].

Similar to wet spinning, dry spinning (**Figure 1.2 b**) also involves extruding a polymer-solvent spinning dope through a spinneret. However, instead of precipitating the

polymer in a liquid coagulation bath, solid filaments are formed by evaporation of solvent which can be assisted by air jets. On the other hand, melt spinning (**Figure 1.2 c**) involves molten polymer that is extruded through an orifice, drawn by take-up wheels, and eventually solidified by cooling. Melt spinning is the most cost effective of the three methods because it is high speed and requires no solvent. Solvents can be hazardous and expensive to implement in high volume manufacturing and typically must be recovered or recycled.

Following fiber formation, additional steps such as washing, fiber finishing, dyeing, uni-axial stretching may be performed as required. To process fibers into nonwovens, fibers are sometimes cut into fragments typically shorter than a few inches, called staple fibers, and dispersed by air (air-laid) or water (wet-laid) to form a nonwoven web on a substrate for collection.

These conventional fiber spinning methods have also been used to produce advanced functional fibrous materials. For instance, wet spinning was employed to fabricate multifunctional carbon fibers from well-aligned carbon nanotubes[13-14] and graphene oxide,[15] as well as biomimetic fibers from recombinant spider silk proteins.[16-18] These studies elicit the profound impact of processing on development of microscopic structure (crystal phase, orientation and alignment, etc.) and its effect on the enhancement of final fiber properties. However, these common methods typically generate fibers with fairly large diameters in the range of tens to hundreds of microns.

1.2.2 Melt blowing

Melt blowing is the most widely used process to produce commercial nonwoven fibers with average diameters around one micron and it has been implemented by a number of companies such as 3M, Hollingsworth & Vose, Kimberly Clark, and Fleetguard/Cummins. Most commonly, melt blowing generates fibers with average

diameters exceeding 1-2 μm,[19-20] although melt blown nanofibers have also been reported previously.[20-21] **Figure 1.3** is a schematic illustration of the melt blowing process.[22] As shown, a molten polymer is first extruded through a die and attenuated into thin continuous fibers by hot air jets with high velocity. The liquid fiber jet solidifies as the temperature drops below the glass transition or crystallization temperature of the polymer. The governing process parameters in melt blowing include flow rates and temperatures of the polymer melt and hot air,[21] die design, [23-24] die to collector distance,[25] and other intrinsic material properties.[21, 26-27]

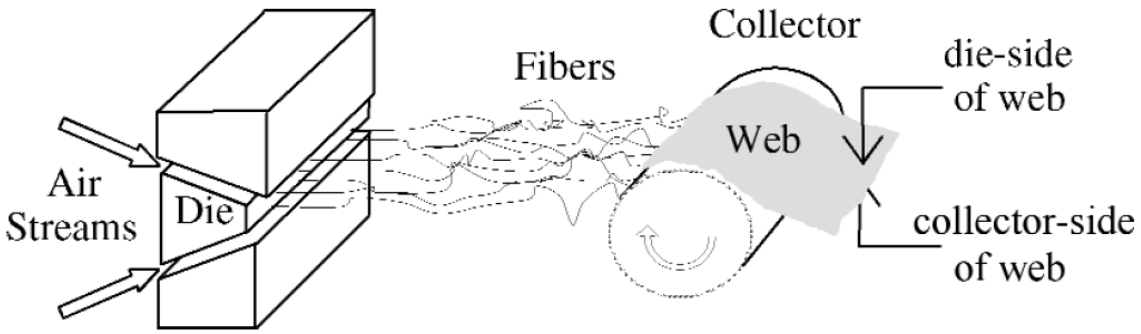

Figure 1.3: Schematic of a melt blowing apparatus. Image is from public domain [22].

Melt blowing offers high throughput because all the material that passes through the spinneret orifice ends up in the final product, but it uses significant thermal energy both for melting the polymer and sustaining the continuous hot air jets. In fact, heating air is one of the largest costs in melt blown nonwoven products.[28] This energy cost, which directly translates to processing and manufacturing costs, can fluctuate wildly in the short term and is likely to continue to rise with the cost of energy in the long term. Another challenge for melt blowing is related to the fact that the ideal melt blowing temperature is typically 30 to 50 ^{o}C higher than the melting temperature of the polymer being processed. Although melt blowing is capable of processing a wide range of polymers including polypropylene,[25,

[29] polystyrene,[21, 24] poly(butylene terephthalate),[21, 30] and polyamides,[31] the upper processing limit is predetermined by the degradation temperature of the polymer. This presents significant challenges in processing polymers with high melting temperatures (particularly ones with melting temperature close to the degradation temperature) leading to a narrow processing window and potential for fibrous products with degraded properties.

1.2.3 Electrospinning

Electrospinning is a versatile and flexible fiber spinning technology that has been widely studied since it was first developed by Rayleigh, Zeleny, and Formhals in the early 1900s.[32-33] As illustrated in **Figure 1.4**, electrospinning uses a strong electric field to draw a polymer-solvent solution into a thin jet; the polymer solution jet thins and solidifies due to rapid solvent evaporation to form polymer fibers. Electrospinning has attracted much attention, particularly in the research community, due to its capability to yield fibers ranging from tens of nanometers to several micrometers in diameter. This technique can process a versatile range of polymers, as long as a solvent exists with suitable volatility. The polymer must also be used at the right concentration for its given molecular weight, forming a polymer solution with so called 'good spinnability'. The importance of individual parameters that contribute to spinnability and in turn the formation, morphology, diameter, and final properties of electrospun fibers are still debated. These parameters are complex and often interrelated; they include process parameters (applied voltage, flow rate, spinneret and electrode configuration[34-35]) and material parameters (polymer concentration, molecular weight and its distribution,[36-38] solution viscoelasticity,[38-40] surface tension,[41] conductivity,[42] and solvent quality[43]).

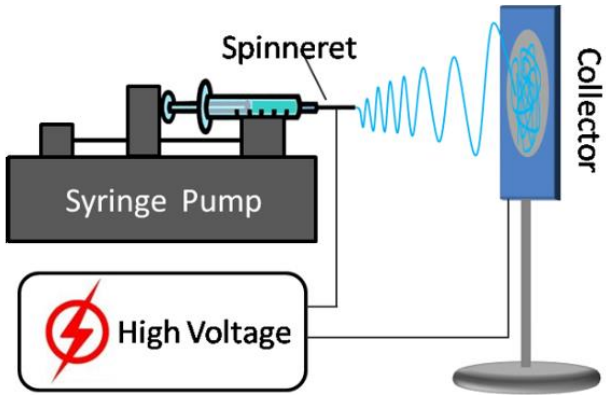

Figure 1.4: Schematic of an electrospinning apparatus. Image is reprinted with permission from [44]. Copyright © 2013 InTech.

Although electrospinning has been a popular fiber spinning method for academic research owing to its versatility and simple instrumental set up, issues like low process throughput, solvent recovery, and process safety makes it inherently challenging to commercialize. Modifications and variations of the electrospinning process, for instance, replacing single orifice electrospinning with multiple-jet electrospinning,[45-46] free surface/needleless electrospinning,[47-48] and rotary cone electrospinning[49] have successfully increased process throughput. However, these modifications do not address the biggest challenge in that the process uses polymer solutions containing large amounts (typically 85-90 wt%) of solvent. Furthermore, many polymers with desirable properties such as polyethylene, polypropylene, poly(butylene terephthalate), etc. cannot be dissolved in common organic solvents, making them difficult to be electrospun. The environmental, safety, and economic concerns posed by the heavy use of solvent and the need for solvent recovery still need to be addressed for the widespread application of electrospinning in the nonwoven industry.

1.2.3 Centrifugal spinning

Centrifugal spinning or rotary spinning, has been used in industry for mass production of glass fiber for over half a century. However, it was not until the 1990s that centrifugal spinning was employed to produce polymer fibers by companies such as BASF Aktiengesellschaft, Owens Corning, and AkzoNobel.[50-52] Recently, a centrifugal spinning design for polymer nanofiber mass production has been developed and patented by Lozano and Sarkar[53-54] and commercialized by FibeRio Technology Corporation under the tradename Forcespinning™. A photograph of a bench scale Forcespinning instrument, the Cyclone, and the schematic representation of the spinneret is shown in **Figure 1.5**. This commercial instrument is equipped with a high speed motor, enabling rotational speeds up to 20,000 revolutions per minute (rpm) and hence large centrifugal forces. A polymer melt or solution is delivered through the orifices of the fast rotating spinneret. When the rotational speed reaches a threshold value, the centrifugal force overcomes the surface tension of the drop formed at the orifice exit and the droplet is stretched into a fluid jet and attenuated into submicron fibers.

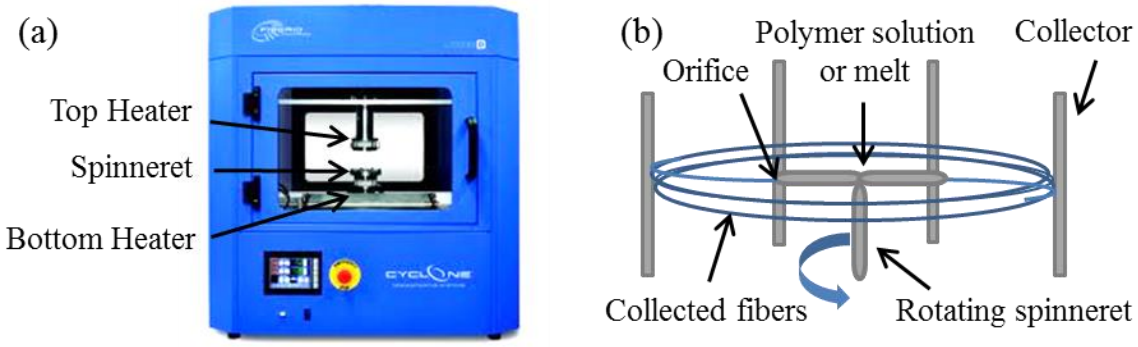

Figure 1.5: (a) A photograph of a lab-scale centrifugal Forcespinning™ apparatus. (b) A schematic diagram of fiber delivered through the rotating spinnerets and being deposited on the circumferential collector.

To further understand fiber formation in centrifugal spinning, several groups independently captured the initial stages of fiber formation utilizing high-speed photography.[55-56] **Figure 1.6** presents the digital images and schematic diagrams that describe the process of jet initiation and formation in centrifugal spinning as reported by Xu and coworkers[56]. When the spinneret rotates, the centrifugal force acts against the viscous force of the solution and the friction force between the solution and the orifice wall, pushing the solution in the outward/radial direction, forming a pendant droplet at the orifice outlet (**Figure 1.6** Stage 1). Once the angular velocity reaches a threshold value, the centrifugal force overcomes the surface tension of the pendant drop, causing the droplet to travel outward and further deform (**Figure 1.6** Stage 2). As the spinneret continues to rotate, the jet undergoes necking and elongation with a droplet on the end (**Figure 1.6** Stage 3). Note that the droplet lags behind while the necked segment travels at almost the same speed as the orifice. This is because as rotation continues, the end droplet, which has larger weight, travels faster than the thinned necked segment under the effect of inertia, forming a signature 'anti-S' jet trajectory (**Figure 1.6** Stage 4). Eventually, a steady curved jet is sustained (**Figure 1.6** Stage 5).

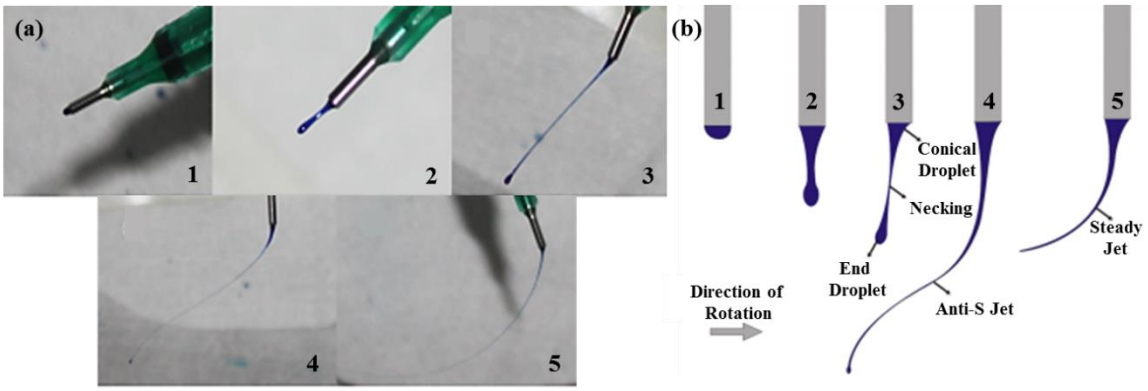

Figure 1.6: (a) Digital images and (b) schematic representations of the initiation of jet formation in centrifugal spinning. Image reprinted with permission from [56]. Copyright © 2014 Wiley Periodicals, Inc.

Compared to melt blowing, melt state centrifugal spinning requires significantly less thermal energy input since only the spinneret and the polymer feed needs to be heated (i.e., there are no hot air jets). On the other hand, solution state centrifugal spinning allows for one to two orders of magnitude higher throughput compared to electrospinning owing to the large centrifugal drawing force, which enables the use of much more concentrated polymeric solutions.[57-59]

Centrifugal spinning enables low cost and high throughput production of micro- and nanofibers from a wide range of polymeric,[54, 60-62] ceramic,[63-64] and metallic[65-66] materials. Several studies aimed to understand the physics and governing parameters for fiber formation in centrifugal spinning. Mellado and coworkers described a scaling framework that relates fiber diameter to the spinning parameters such as viscosity, angular speed, distance to the collector, and orifice radius, supported by experimental observations and simulations.[67] Taghavi and Larson used a regularized string model to quantitatively determine fiber velocity and diameter by balancing centrifugal, inertial, and viscous forces. They concluded the results can be described by the Rossby number (the ratio of inertial to centrifugal forces) and Reynolds number (the ratio of inertial to viscous forces).[68] More recently, Ren et al. analyzed fiber morphology in terms of solution viscoelasticity, centrifugal forces, and solvent mass transfer. It was found that fiber formation and morphology can be predicted by the Weissenberg number (the ratio of centrifugal time to fluid relaxation time) and Capillary number (the ratio of viscous time to centrifugal time), while fiber diameter is largely determined by spinning solution elasticity and solvent evaporation.[62]

However, most studies have focused on solution state centrifugal spinning to date. Melt state centrifugal spinning has been limited to processing of commodity polymers such as polypropylene.[69] With intrinsically large centrifugal force and heating capability,

centrifugal spinning has great potential to produce microfibers and nanofibers on a large scale, even using materials that could not be spun using melt blowing and electrospinning.

1.3 Objective and Overview

As discussed above, all of the methods require large quantities of solvent or thermal energy input to transform a solid pre-formed polymer into a liquid prior to application of a drawing force. However, high performance polymers such as poly(p-phenylene sulfide), poly(butylene terephthalate), polyoxymethylene, etc., can be particularly problematic because they usually possess high solid-to-liquid transition temperatures and limited solubility in common organic solvents. This often requires the polymers to be melt processed within a narrow processing window close to their degradation temperature with the associated risk of polymer degrading within processing equipment and diminished thermal stability or mechanical properties of the final fiber product. On the other hand, solution processing such materials usually requires harsh solvents, which is not attractive for large scale manufacturing and can limit end-use applications due to residual solvent concerns.

This dissertation attempts to address the challenging issue of producing high performance microfibers and nanofibers. As previously discussed, centrifugal spinning is an emerging technology and a promising manufacturing alternative to melt blowing and electrospinning. Its intrinsically large centrifugal force leads to high throughput and low cost processing, while its capability to process both polymer melts and solutions demonstrates flexibility; all of which are important aspects to consider for industrial scale-up. Therefore, the overall objective of this thesis was to further develop and optimize the centrifugal spinning process to generate novel multifunctional fibrous materials ultimately establishing process-structure-property relationships.

In addition to conventional melt state and solution state processing, a new fiber fabrication method involving simultaneous centrifugal spinning and light initiated polymerization will be introduced. The concept of simultaneous fiber spinning and photo-polymerization of reactive liquid monomers not only is novel, but also presents a potential route for green manufacturing of high performance fibers by reducing and even eliminating the use of both solvent and heat. Chapter 2 describes this reactive centrifugal spinning method in detail and offers fundamental understanding of the underlying physics that govern fiber formation and fiber morphology, while Chapter 3 presents crucial parameters that determine the fiber diameter in this process. These findings not only offer qualitative understanding, but also serve as predictive guidance for reactive mixture formulation and process optimization. Leveraging this knowledge, we develop new reactive monomer mixtures containing high amounts of inorganic content in Chapter 4, in hopes to diversify the accessible material profile and enhance the thermal and mechanical properties of the final fibers.

The second part of the dissertation focuses on optimizing melt state processing of high performance materials that are not easily processed into fibers. In Chapter 5 to 7, we describe the melt state centrifugal spinning of three high performance materials with distinct properties, poly(butylene terephthalate), tin fluorophosphate glass, and a commercial liquid crystalline polymer known as Vectra A950. In addition to optimizing the processing conditions, the properties of the resultant fibers are characterized to establish the process-structure-property relationships. Lastly, Chapter 8 provides a brief outlook on the future of centrifugal spinning and several future research directions suggested by the research in this thesis.

1.4 REFERENCES

1. Luitel, K.; Hudson, D.; Ethridge, D. In *Evaluating Potential for Cotton Utilization in Alternative Nonwoven Textile Technologies*, 2013 Annual Meeting, February 2-5, 2013, Orlando, Florida, Southern Agricultural Economics Association: **2013**.
2. Burger, C.; Hsiao, B. S.; Chu, B., *Annual Review of Materials Research* **2006,** *36*, 333-368.
3. Lu, P.; Xia, Y., *ACS Applied Materials & Interfaces* **2013,** *5* (13), 6391-6399.
4. Wang, N.; Wang, X.; Ding, B.; Yu, J.; Sun, G., *Journal of Materials Chemistry* **2012,** *22* (4), 1445-1452.
5. Zhang, J.; Liu, Z.; Kong, Q.; Zhang, C.; Pang, S.; Yue, L.; Wang, X.; Yao, J.; Cui, G., *ACS Applied Materials & Interfaces* **2012,** *5* (1), 128-134.
6. Jiang, J.; Xie, J.; Ma, B.; Bartlett, D. E.; Xu, A.; Wang, C.-H., *Acta Biomaterialia* **2014,** *10* (3), 1324-1332.
7. Jassal, M.; Sengupta, S.; Bhowmick, S., *Journal of Biomaterials Science, Polymer Edition* **2015**, 1-14.
8. Jin, C.; Jiang, Y.; Niu, T.; Huang, J., *Journal of Materials Chemistry* **2012,** *22* (25), 12562-12567.
9. Chen, J.-P.; Su, C.-H., *Acta Biomaterialia* **2011,** *7* (1), 234-243.
10. Gustafsson, Y.; Haag, J.; Jungebluth, P.; Lundin, V.; Lim, M. L.; Baiguera, S.; Ajalloueian, F.; Del Gaudio, C.; Bianco, A.; Moll, G., *Biomaterials* **2012,** *33* (32), 8094-8103.
11. Ma, Z.; Kotaki, M.; Yong, T.; He, W.; Ramakrishna, S., *Biomaterials* **2005,** *26* (15), 2527-2536.
12. LLC, C. A. Textile Glossary. http://textileengineerr.blogspot.com/p/textile-glossary_06.html.
13. Behabtu, N.; Young, C. C.; Tsentalovich, D. E.; Kleinerman, O.; Wang, X.; Ma, A. W.; Bengio, E. A.; ter Waarbeek, R. F.; de Jong, J. J.; Hoogerwerf, R. E., *Science* **2013,** *339* (6116), 182-186.
14. Alemán, B.; Reguero, V.; Mas, B.; Vilatela, J. J., *ACS Nano* **2015,** *9* (7), 7392-7398.
15. Cong, H.-P.; Ren, X.-C.; Wang, P.; Yu, S.-H., *Scientific Reports* **2012,** *2*.
16. Liivak, O.; Blye, A.; Shah, N.; Jelinski, L. W., *Macromolecules* **1998,** *31* (9), 2947-2951.
17. Lazaris, A.; Arcidiacono, S.; Huang, Y.; Zhou, J.-F.; Duguay, F.; Chretien, N.; Welsh, E. A.; Soares, J. W.; Karatzas, C. N., *Science* **2002,** *295* (5554), 472-476.

18. Heidebrecht, A.; Eisoldt, L.; Diehl, J.; Schmidt, A.; Geffers, M.; Lang, G.; Scheibel, T., *Advanced Materials* **2015,** *27* (13), 2189-2194.

19. Lee, Y. E.; Wadsworth, L. C., *Journal of Applied Polymer Science* **2007,** *105* (6), 3724-3727.

20. Grafe, T.; Graham, K., *Nonwoven Technol Rev* **2003,** *12*, 51-55.

21. Ellison, C. J.; Phatak, A.; Giles, D. W.; Macosko, C. W.; Bates, F. S., *Polymer* **2007,** *48* (11), 3306-3316.

22. Bresee, R. R.; Ko, W.-c., *International Nonwovens Journal* **2003,** *12* (2), 21-28.

23. Xie, S.; Zheng, Y.; Zeng, Y., *Industrial & Engineering Chemistry Research* **2014,** *53* (32), 12866-12871.

24. Tan, D. H.; Herman, P. K.; Janakiraman, A.; Bates, F. S.; Kumar, S.; Macosko, C. W., *Chemical Engineering Science* **2012,** *80*, 342-348.

25. Lee, Y.; Wadsworth, L. C., *Polymer* **1992,** *33* (6), 1200-1209.

26. Tan, D. H.; Zhou, C.; Ellison, C. J.; Kumar, S.; Macosko, C. W.; Bates, F. S., *Journal of Non-Newtonian Fluid Mechanics* **2010,** *165* (15), 892-900.

27. Zhou, C.; Tan, D. H.; Janakiraman, A. P.; Kumar, S., *Chemical Engineering Science* **2011,** *66* (18), 4172-4183.

28. Tate, B. D.; Shambaugh, R. L., *Industrial & engineering chemistry research* **2004,** *43* (17), 5405-5410.

29. Zhao, R.; Wadsworth, L. C., *Polymer Engineering and Science* **2003,** *43* (2), 463.

30. Chen, T.; Li, L.; Huang, X., *Journal of Applied Polymer Science* **2005,** *97* (4), 1750-1752.

31. Wang, X.; Ke, Q., *Polymer Engineering and Science* **2006,** *46* (1), 1.

32. Anton, F., Process and Apparatus for Preparing Artificial Threads. Google Patents: **1934**.

33. Zeleny, J., *Physical Review* **1917,** *10* (1), 1.

34. Tan, S.; Inai, R.; Kotaki, M.; Ramakrishna, S., *Polymer* **2005,** *46* (16), 6128-6134.

35. Deitzel, J.; Kleinmeyer, J.; Harris, D.; Tan, N. B., *Polymer* **2001,** *42* (1), 261-272.

36. Tirtaatmadja, V.; McKinley, G. H.; Cooper-White, J. J., *Physics of Fluids (1994-present)* **2006,** *18* (4), 043101.

37. Palangetic, L.; Reddy, N. K.; Srinivasan, S.; Cohen, R. E.; McKinley, G. H.; Clasen, C., *Polymer* **2014,** *55* (19), 4920-4931.

38. Gupta, P.; Elkins, C.; Long, T. E.; Wilkes, G. L., *Polymer* **2005,** *46* (13), 4799-4810.

39. Yu, J. H.; Fridrikh, S. V.; Rutledge, G. C., *Polymer* **2006,** *47* (13), 4789-4797.

40. McKee, M. G.; Wilkes, G. L.; Colby, R. H.; Long, T. E., *Macromolecules* **2004,** *37* (5), 1760-1767.

41. Regev, O.; Vandebril, S.; Zussman, E.; Clasen, C., *Polymer* **2010,** *51* (12), 2611-2620.

42. Uyar, T.; Besenbacher, F., *Polymer* **2008,** *49* (24), 5336-5343.

43. Shenoy, S. L.; Bates, W. D.; Frisch, H. L.; Wnek, G. E., *Polymer* **2005,** *46* (10), 3372-3384.

44. Huang, J.; You, T., *by R. Maguire,(InTech, 2013)* **2013**, 35-83.

45. Kim, G.; Cho, Y.-S.; Kim, W. D., *European Polymer Journal* **2006,** *42* (9), 2031-2038.

46. Theron, S.; Yarin, A.; Zussman, E.; Kroll, E., *Polymer* **2005,** *46* (9), 2889-2899.

47. Lukas, D.; Sarkar, A.; Pokorny, P., *Journal of Applied Physics* **2008,** *103* (8), 084309.

48. Forward, K. M.; Rutledge, G. C., *Chemical Engineering Journal* **2012,** *183*, 492-503.

49. Lu, B.; Wang, Y.; Liu, Y.; Duan, H.; Zhou, J.; Zhang, Z.; Wang, Y.; Li, X.; Wang, W.; Lan, W., *Small* **2010,** *6* (15), 1612-1616.

50. Meerman, J. J.; Jelijs, R., Centrifugal Spinning Process for Spinnable Solutions. Google Patents: **2000**.

51. Voelker, H.; Zettler, H. D.; Fath, W.; Berbner, H., Production of Fibers by Centrifugal Spinning. Google Patents: **1996**.

52. Watton, W. A.; Snyder, J. G., Fiber Manufacturing Spinner and Fiberizer. Google Patents: **1996**.

53. Lozano, K.; Sarkar, K., Superfine Fiber Creating Spinneret and Uses Thereof. Google Patents: **2012**.

54. Sarkar, K.; Gomez, C.; Zambrano, S.; Ramirez, M.; de Hoyos, E.; Vasquez, H.; Lozano, K., *Materials Today* **2010,** *13* (11), 12-14.

55. Padron, S.; Fuentes, A.; Caruntu, D.; Lozano, K., *Journal of Applied Physics* **2013,** *113* (2), 024318.

56. Xu, H.; Chen, H.; Li, X.; Liu, C.; Yang, B., *Journal of Polymer Science Part B: Polymer Physics* **2014,** *52* (23), 1547-1559.

57. Padron, S.; Patlan, R.; Gutierrez, J.; Santos, N.; Eubanks, T.; Lozano, K., *Journal of Applied Polymer Science* **2012,** *125* (5), 3610-3616.

58. McEachin, Z.; Lozano, K., *Journal of Applied Polymer Science* **2012,** *126* (2), 473-479.

59. Vazquez, B.; Vasquez, H.; Lozano, K., *Polymer Engineering & Science* **2012,** *52* (10), 2260-2265.

60. Lu, Y.; Li, Y.; Zhang, S.; Xu, G.; Fu, K.; Lee, H.; Zhang, X., *European Polymer Journal* **2013,** *49* (12), 3834-3845.

61. Hammami, M. A.; Krifa, M.; Harzallah, O., *The Journal of The Textile Institute* **2014,** *105* (6), 637-647.

62. Ren, L.; Ozisik, R.; Kotha, S. P.; Underhill, P. T., *Macromolecules* **2015**.

63. Liu, H.-Y.; Chen, Y.; Liu, G.-S.; Pei, S.-G.; Liu, J.-Q.; Ji, H.; Wang, R.-D., *Materials and Manufacturing Processes* **2013,** *28* (2), 133-138.

64. Ren, L.; Kotha, S. P., *Materials letters* **2014,** *117*, 153-157.

65. Altecor, A.; Mao, Y.; Lozano, K., *Functional Materials Letters* **2012,** *5* (03), 1250020.

66. Bao, N.; Wei, Z.; Ma, Z.; Liu, F.; Yin, G., *Journal of hazardous materials* **2010,** *174* (1), 129-136.

67. Mellado, P.; McIlwee, H. A.; Badrossamay, M. R.; Goss, J. A.; Mahadevan, L.; Parker, K. K., *Applied Physics Letters* **2011,** *99* (20), 203107.

68. Taghavi, S.; Larson, R., *Physical Review E* **2014,** *89* (2), 023011.

69. Raghavan, B.; Soto, H.; Lozano, K., *Journal of Engineered Fabrics & Fibers (JEFF)* **2013,** *8* (1).

Chapter 2: Controlling Characteristic Timescales and Fiber Morphology in Simultaneous Centrifugal Spinning and Photopolymerization[1]

2.1 INTRODUCTION

2.1.1 Synthetic and natural fiber spinning methods

As discussed in Chapter 1, despite the significant advancements in fiber spinning technology for many practical applications of fibrous materials, the production of microfibers and nanofibers from high performance materials still remains a challenge and is an active area of research. Currently, all synthetic fiber spinning methods involve transforming a pre-formed polymer into a liquid by either the application of heat or the addition of solvent, followed by applying an extensional drawing force to draw the liquid into fibers. The fibers later solidify by sufficient cooling or solvent evaporation. Melt state processing, although simple and convenient, requires significant thermal energy input and has its upper processing limit constrained by the degradation temperature of the material. On the other hand, solution state processing is versatile, but suffers from issues such as solvent recovery/recycling, safety of volatile/flammable solvents, and low process throughput, all of which present significant challenges for industrial scale up and commercial viability.

Conversely, nature has evolved and engineered benign ways to produce silk fibers with outstanding performance. For example, the dragline silk of certain spiders can be stronger than steel (by weight) and elastic like rubber bands.[1] In addition, spiders can produce up to seven different kinds of silk for their daily functions such as prey capture,

[1]This chapter is adapted from "Manipulating characteristic timescales and fiber morphology in simultaneous centrifugal spinning and photopolymerization" published in *Polymer* (2015). Yichen Fang was responsible for design of experiments, data collection and analysis; Austin R. Dulaney conducted part of fiber spinning experiments and SEM analysis; Jesse Gadley and Prof. Joao Maia collaborated with us on CaBER measurements; Prof. Ellison provided overall guidance for this project.

web construction, and reproduction by varying silk composition and spinning conditions (speed, temperature, humidity, etc.).[2-3] Viewed broadly, nature's approach of producing fibers involves chemically linking small functional building blocks (proteins) into oligomers and then fibrous structures as the silk is extruded from the spinning duct of the spider.[2, 4] This is conceptually different from the synthetic fiber spinning methods discussed above, and does not require heat or organic solvent.

Inspired by nature's approach, our group developed a new fiber spinning approach by extruding small reactive molecules and simultaneously polymerizing them into solid fibers. One of the challenges is to identify a suitable chemistry where the reactions between small molecules match the extrusion speeds of typical fiber spinning methods (tens to hundreds of meters per second). One promising chemistry that we have identified is UV initiated thiol-ene polymerization, for reasons which will be outlined in the following section.

2.1.2 UV initiated thiol-ene chemistry

Thiol-ene chemistry was first reported in the early 1900's,[5-6] and it has gained revitalized interest in the past two decades for the use in conventional applications such as coatings,[7] adhesives.[8] It has also gained traction in emerging applications such as dental restorative materials,[9] extracellular matrices,[10] gas transport membranes,[11] and high resolution lithography.[12] Thiol-ene photopolymerization is a type of "click" chemistry, where a radical polymerization is initiated upon exposure to a suitable light source. It is versatile in that almost any type of "thiol", a monomer that contains sulfur, and "ene", a monomer that contains a double bond, can participate. The general reaction scheme is shown in **Figure 2.1**.[13] The photoinitiator generates one or two radicals when irradiated by UV light and each abstracts a hydrogen atom from thiol, forming a thiyl radical. The thiyl

radical reacts with the ene monomer to generate a carbon centered radical, which then reacts with another thiol, reforming the thiyl radical, and propagation/chain transfer thus proceeds in an ideal step-growth manner. Some ene monomers such as acrylates and methacrylates also undergo homopolymerization, in which the carbon radical can react with either another ene monomer or a thiol. The polymerization in this case is considered a mixed step-growth chain-growth polymerization. Termination occurs via the coupling of any two radical species.[13]

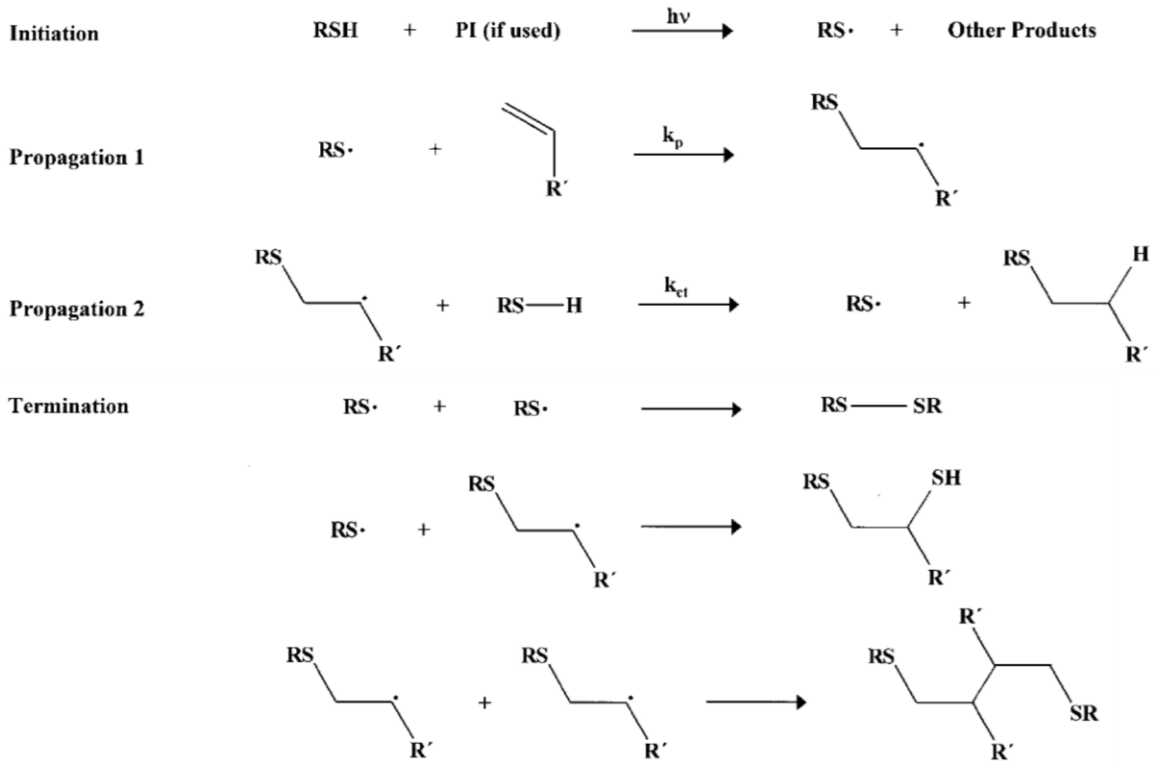

Figure 2.1: General thiol-ene photopolymerization mechanism. Reprinted with permission from Ref. [13]. Copyright © 2004 Wiley Periodicals, Inc.

Thiol-ene chemistry is robust in ambient conditions, because the presence of thiol in the range of 1-10 wt% is sufficient to suppress oxygen inhibition, which is a critical problem in the traditional homopolymerization of acrylates or methacrylates [14-15]. The UV

light mediated reaction offers spatial control so that polymerization occurs only outside the spinneret where light is present to initiate photopolymerization; this feature could be difficult to achieve by thermally initiated polymerizations. In addition, the diversity of thiol and ene monomers (functional groups, functionality, backbone structure, formulation, etc.) that are already commercially available from the coatings and adhesives industries presents substantial opportunities for fabrication of functional fibers with highly tailorable properties.

2.1.3 UV-reactive fiber spinning

The integration of in-situ photo-crosslinking reactions with fiber formation has been previously reported by several research groups. Notably, Boyd and coworkers fabricated thiol-ene and thiol-yne fibers using hydrodynamic shaping in microfluidic channels.[16] In other studies, an extra step of thermal polymerization to convert a fraction of the monomers into prepolymers prior to electrospinning or the incorporation of a high molecular weight (MW) polymer in significant amounts was necessary to produce crosslinked fibers due to the typical slow reaction kinetics.[17-19] Most of these studies only reported the chemical formulations and processing conditions that generated fibers, but did not address the many other factors that impact fiber formation and fiber morphology. In addition, the reported conditions usually do not reflect the entire operating space or the extent of tunability of the methods.

Recently, our group demonstrated a new method for fabricating nonwoven fibers directly from non-volatile liquid monomer mixtures instead of from polymer solutions or polymer melts,[20] thereby foregoing the use of solvent and heat altogether. In this method, a mixture containing monomers and a photoinitiator was simultaneously electrospun and photopolymerized via UV initiated thiol-ene chemistry to produce solid fibers in ambient

conditions. A schematic diagram of the electrospinning apparatus with a UV light source is shown in **Figure 2.2**.[20] The method was also made even greener by replacing more than 50 wt% of petroleum based monomer with a bio-renewable soybean oil derived monomer without sacrificing the final fiber quality.[21] Despite the very limited curing time during the fiber spinning process, the fibers made by this method contained a highly crosslinked network, which imparted high thermal stability, chemical resistance, and mechanical strength to the resulting fibers.[20] Owing to the versatility of thiol-ene chemistry, fibers with drastically different mechanical, thermal, and network structural properties can also be fabricated by incorporating monomers with different chemical structures.[22]

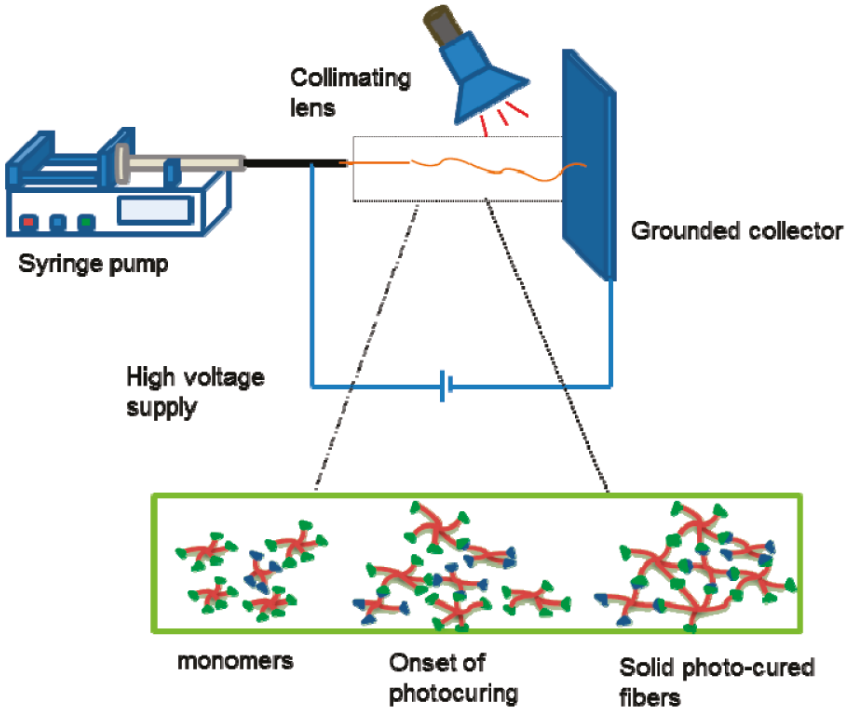

Figure 2.2: Schematic representation of electrospinning equipped with UV light source for in-situ photopolymerization during fiber spinning. Reprinted with permission from Ref. [20]. Copyright © 2011 American Chemical Society.

2.1.4 Objective

Although thiol-ene chemistry has been successfully implemented into solventless electrospinning and fibers with various properties were fabricated,[20-21, 23] one major challenge that we must address in order to achieve widespread acceptance is the low process throughput due to the limited drawing force provided by the high voltage electric field in electrospinning. Therefore, the first objective in this study is to integrate thiol-ene photopolymerization with a bench-scale centrifugal spinning apparatus, because the intrinsically larger fiber drawing force and higher throughput of centrifugal spinning constitute significant advantages over electrospinning. The successful integration of thiol-ene chemistry and centrifugal spinning will demonstrate not only the scale-up potential but also the universality of this bio-inspired fiber spinning concept.

Second, controlling fiber formation and morphology has long been the subject of research for the more commonly studied fiber spinning techniques, since fiber diameter, quality and morphology ultimately determine fiber mat properties[24-26] and in turn the end use of the fibers. The incorporation of in-situ photopolymerization is a unique feature in this fiber spinning method, and therefore the role of reaction kinetics on fiber formation and morphology represents a new research area for fundamental study. However, to date, a systematic and fundamental examination of the important parameters and underlying physics that govern fiber formation and fiber morphology in simultaneous photopolymerization and fiber spinning is still lacking. Therefore, this will be the second objective of the present chapter.

In this photopolymerization process, the principle parameters that govern fiber formation and morphology include: reaction parameters through the stoichiometric ratio of thiol to ene groups, monomer functionality and reactivity, light intensity, and photoinitiator content; viscoelastic parameters such as viscosity and elasticity; and process parameters

including spin speed, orifice diameter, and the location and width of the UV illuminated region. These three categories of parameters form a convoluted and in some cases interactive set of variables, making it challenging to study the effect of each variable in isolation. For example, a penta-functional acrylate monomer is different from a tetra-functional acrylate in terms of both monomer functionality and viscosity.

To overcome this complication, we examined the characteristic timescales related to these categories: namely those of the reaction kinetics, viscoelastic response, and the orifice-to-collector processing time. By carefully selecting variables that are associated with only one of the aforementioned timescales, the morphology of the photopolymerized fibers could be finely tuned while keeping all other parameters constant. In this study, the light intensity, the concentration of an elasticity modifier, and the spin speed of the spinneret were varied systematically to change the reaction kinetics, the viscoelastic response, and the processing time, respectively. The morphological appearances of the resulting fibers, ranging from beads, beads-on-string, uniform fibers, fused fibers, to well cured fibers, were characterized using scanning electron microscopy (SEM), while the timescales were measured experimentally by a variety of characterization methods as described in detail in later sections. The morphological appearance and associated timescales for each condition were superimposed to construct an operating diagram.

These experiments and the resulting operating diagram elucidated the role of each timescale as well as the intricate interplay between the timescales and their effects on the formation and morphological evolution of the fibers. Leveraging this fundamental knowledge, we hope the process could be readily adapted to include many different monomer chemistries to produce a diverse profile of fibers, and implemented within other industrial fiber production technologies for widespread use in manufacturing.

2.2 EXPERIMENTAL

2.2.1 Materials and monomer mixture preparation

Dipentaerythritol pentaacrylate (5A) was provided by Sartomer USA. Pentaerythritol tetrakis (3-mercaptopropionate) (4T) was purchased from Sigma Aldrich. A commercially available photoinitiator, Irgacure 2100, was kindly provided by BASF Switzerland. Polyethylene oxide (PEO) with viscosity average molecular weight (MW) of 10^6 g/mol and anhydrous ethyl acetate were obtained from Sigma Aldrich. **Figure 2.3** presents the ideal chemical structures of 5A, 4T, and Irgacure 2100. All chemicals were used as received.

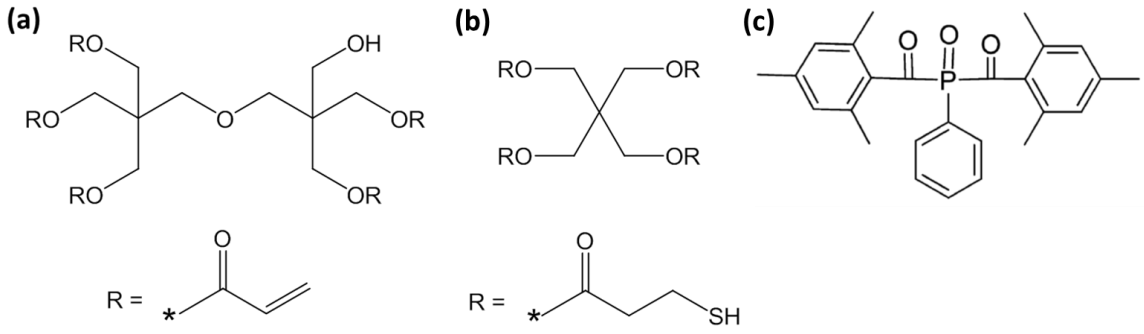

Figure 2.3: Chemical structures of (a) 5A, (b) 4T, and (c) Irgacure 2100.

To impart elasticity to the monomer mixtures and prevent fiber jet breakup, trace amounts of PEO were included in the monomer mixture formulation. Because PEO did not readily dissolve in the monomer mixture at room temperature, an appropriate amount of PEO was first added to 4T at elevated temperature. PEO containing 4T was heated at 70 ^oC for 18 hours to ensure complete dissolution. It is worth noting that prolonged heating of PEO/4T solution should be avoided, since oxidative degradation of PEO becomes significant at temperatures above the melting point of PEO, which results in reduced PEO MW[27] and reduced elasticity of the PEO containing 4T.

The monomer mixture was prepared by mixing together 66 wt% 5A, 19 wt% 4T with appropriate amounts of PEO, 3 wt% Irgacure 2100, and 12 wt% ethyl acetate using a vortex mixer (Thermolyne 37600) in a room with no stray UV light to prevent pre-exposure that could initiate the polymerization prior to fiber spinning. This monomer mixture composition yielded an ene to thiol functional group molar ratio of 4:1. This stoichiometric ratio has been shown suitable for fiber spinning processes by providing both sufficient polymerization kinetics and reducing the oxygen inhibition effect due to the presence of thiol.[20-22] It should be noted that under optimized centrifugal spinning conditions, defect-free fibers have been spun from monomer mixtures with ene to thiol functional group molar ratios ranging from 3:1 to 8:1.

In addition, ethyl acetate was added as a diluent to reduce the viscosity of the monomer mixture which ensures sufficient monomer mix delivery through the spinneret orifices. Ethyl acetate can also be substituted by reactive monomers with low viscosity such as 1,6-hexanediol diacrylate and tri(ethylene glycol) divinyl ether, which can participate in the photopolymerization and thus incorporated into the fiber network. However, ethyl acetate was a preferred diluent in this study as it reduces the monomer mix viscosity without affecting the polymerization kinetics.

2.2.2 Light design and centrifugal spinning

A bench scale centrifugal Forcespinning™ apparatus (FibeRio Cyclone L-1000) was equipped with a custom made UV light source as shown in **Figure 2.4**. The light source arrangement included a power supply (Photon Technology International LPS-220), a lamp housing (Photon Technology International A1010) for a mercury short-arc lamp (Ushio USH-103D), and a UV transparent mirror (Edmund Optics) mounted at a 45 degree angle to reflect the light vertically onto the collector, casting an illumination spot 10 cm in

diameter. In this process, the monomer jets undergo simultaneous filament thinning and solidification through thiol-ene polymerization as they pass through this illuminated spot and deposit onto the stainless steel collector bars.

The placement of the mirror and the illumination spot is important for fiber formation. In general, the edge of the illumination spot should be very close to the needle tips (spinneret orifices). If the illumination spot is too far away from the needle tips, the monomer jets dissipate completely into droplets by surface tension driven instabilities before reaching the light; conversely, if the illumination spot is too close, some UV light can be scattered inside the needle tip, curing the monomer mixture at the tip and clogging the spinneret orifices. When working with highly reactive (fast curing) or very viscous (slow delivery rate) monomer mixtures, one should consider moving the illumination spot slightly further away from the tip of the spinneret to prevent clogging of the spinneret.

For fiber spinning, 2 mL of monomer mixture was loaded into the spinneret attached to two needle tips (210 mm inner diameter, 1.5 inch length) masked by tape, and spun at specified light and spin speed conditions. Finally, scanning electron microscopy (SEM, Hitachi S-5500) was used to characterize the fiber morphology.

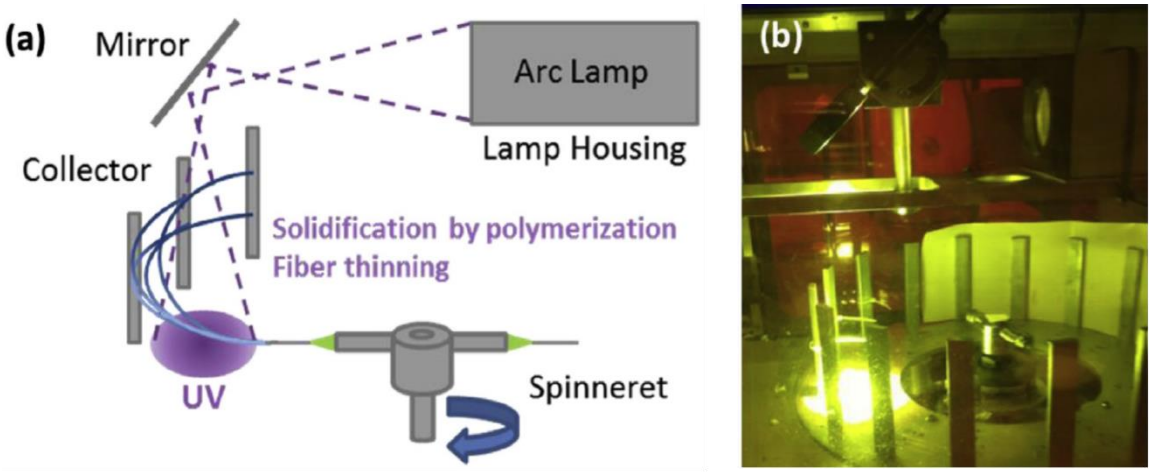

Figure 2.4: (a) A schematic diagram and (b) a photograph of a UV light design adopted in centrifugal Forcespinning™. Reprinted with permission from Ref. [28]. Copyright © 2015 Elsevier Ltd.

2.2.3 Real time Fourier transform infra-red spectroscopy (RT-FTIR)

RT-FTIR (Nicolet Magna-IR 550) was employed to determine the curing kinetics of the monomer mixture exposed at different light intensities. 15 µL of freshly prepared monomer mixture was dispensed by a micropipette and sandwiched between two NaCl windows to form a continuous film. This sample preparation protocol ensured the sample was thin enough for both UV (for initiating polymerization) and IR (for tracking polymerization kinetics) light to transmit through the film under conditions where ethyl acetate could not evaporate. A spot cure xenon lamp (Optical Building Blocks, OBB Scopelite 200) with a collimating lens was fixed at a distance of 10 cm from the sample. UV grade neutral density (ND) filters with optical densities (OD) of 0.3, 0.6, and 1.0 (Thor Lab) were used to adjust the light intensity output of the spot cure xenon lamp. The UV transmittance spectra of the ND filters used to adjust the light intensity output of the OBB xenon lamp are shown in **Figure 2.5**.

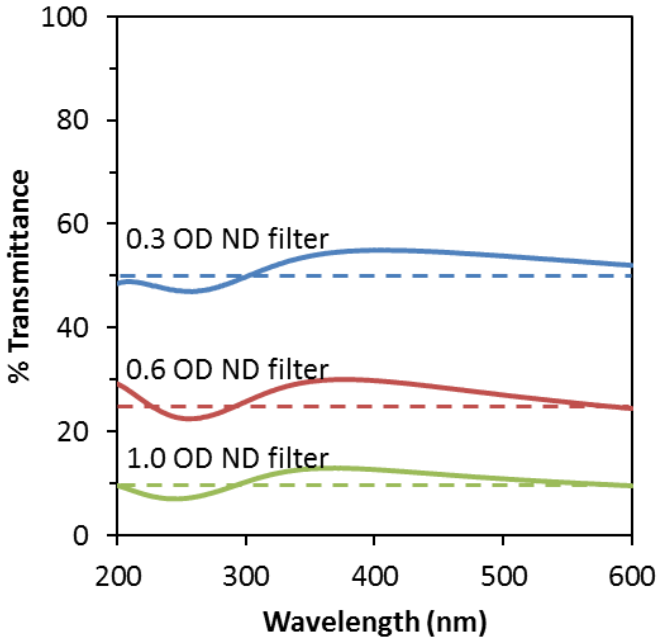

Figure 2.5: UV-Vis spectra of UV neutral density filters with optical densities of 0.3 (blue solid line), 0.6 (red solid line), and 1.0 (green solid line). The blue, red, and green dash lines represent 50%, 25%, and 10% UV transmittance, respectively, and are drawn to guide the eyes. Reprinted with permission from Ref. [28]. Copyright © 2015 Elsevier Ltd.

However, the xenon lamp used in the RT-FTIR studies and the mercury arc lamp used in the fiber spinning runs have different spectral outputs and intrinsic light intensities. In order to accurately track the polymerization kinetics in the fiber spinning process, we define the effective light intensity, I_{eff}, to be the light intensity at wavelengths lower than 435 nm, which is the absorbance range of the photoinitiator used in this study. Here we assume that only the light with such wavelengths can effectively excite the photoinitiator to generate radicals and that the light excitation efficiency in this wavelength range is 100%.

The following protocol was used to determine I_{eff} of the two light sources. A 435 nm band pass filter (Thor lab) was used to measure the light intensity at wavelengths of

435 nm and above. The UV transmittance spectrum of the 435 nm band pass filter was measured by UV-Vis spectrophotometer and is presented in **Figure 2.6**. The absolute light intensity (I_{abs}) from the broadband light sources was measured by a radiometer (Coherent Field Max II) without any band pass filter, while the intensity of the light with wavelength above 435 nm ($I_{\lambda>435\ measured}$) was measured by covering the radiometer sensor completely with the 435 nm band pass filter. However, because the 435 nm band pass filter absorbs 10% of the light at wavelengths greater than 435 nm, $I_{\lambda>435\ measured}$ was then divided by 0.9 to correct for this 10% absorption ($I_{\lambda>435\ corrected}$). I_{eff} was then calculated by subtracting $I_{\lambda>435\ corrected}$ from I_{abs}. The measured and calculated values of light intensities of the OBB xenon lamp and the mercury arc lamp are summarized in **Table 2.1**. It should be noted that the light intensity of the mercury arc lamp was adjusted by simply varying the voltage supplied to the arc lamp.

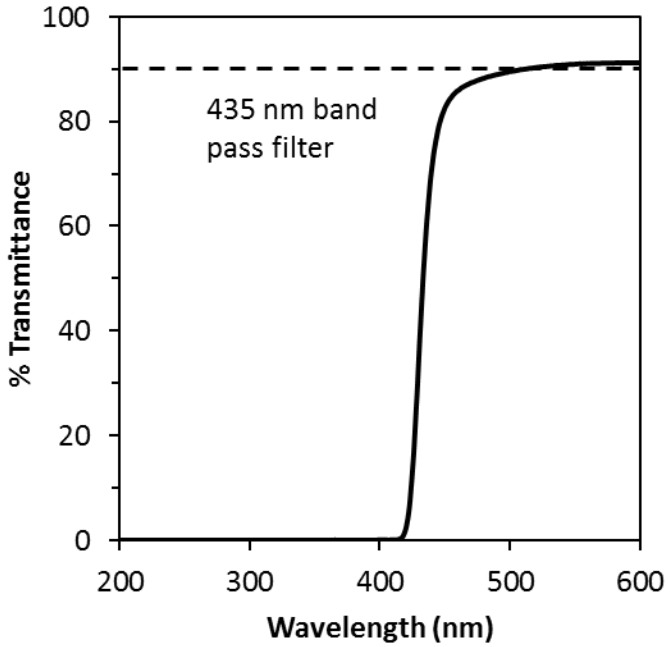

Figure 2.6: UV-visible transmission spectrum of a 435 nm band pass filter. The dashed line represents 90% UV transmittance and is drawn to guide the eyes. Reprinted with permission from Ref. [28]. Copyright © 2015 Elsevier Ltd.

I_{abs} (mW/cm^2)	$I_{\lambda>435\ measured}$ (mW/cm^2)	$I_{\lambda>435\ corrected}$ (mW/cm^2)	I_{eff} (mW/cm^2)
OBB Xenon Lamp			
23.43	12.51	13.90	9.53
Mercury Arc Lamp			
1319	621	690.0	629.0
1167	536.5	596.1	570.9
903	450	500.0	403.0
719	372.5	413.9	305.1
566	276	306.7	259.3
392	177	196.7	195.3
244.7	117	130.0	114.7
82	38	42.2	39.8
47.7	21.08	23.4	24.3

Table 2.1: Light intensity values of the OBB xenon lamp used in RT-FTIR studies and the mercury arc lamp used in fiber spinning experiments. Reprinted with permission from Ref. [28]. Copyright © 2015 Elsevier Ltd.

The light intensity of the xenon lamp was adjusted with ND filters. The absolute light intensity output (I_{abs}) with different ND filters was measured by placing a ND filter on top of the radiometer sensor; results of these experiments are shown in **Table 2.2**. Note that for the condition of OD 1.3 ND filter with OBB xenon lamp Aperture 4, I_{abs} was measured by placing both the OD 0.3 and OD 1.0 ND filters on top of the radiometer sensor. From **Table 2.1**, I_{eff} of the OBB xenon lamp is calculated to be 40.7% of I_{abs}. This value was used to then calculate the I_{eff} for each ND filter adjusted light intensity as shown in **Table 2.2**.

ND Filter	Aperture	I_{abs} (mW/cm^2)	I_{eff} (mW/cm^2)	$(I_{eff})^{-1/2}$ ($cm/mW^{1/2}$)
--	3	97	39.46	0.16
OD 0.3	4	12.95	5.27	0.44
OD 0.6	4	7.25	2.95	0.58
OD 1.0	4	2.78	1.13	0.94
OD 1.3	4	1.05	0.43	1.52

Table 2.2: Adjusted light intensity values of the OBB xenon lamp with ND filters. For this light source, I_{eff} is calculated to be 40.7% of I_{abs}. Reprinted with permission from Ref. [28]. Copyright © 2015 Elsevier Ltd.

2.2.4 Capillary breakup extensional rheometer (CaBER) measurements

The extensional properties of the monomer mixtures containing various amounts of PEO, ranging from 0 to 600 ppm, were measured by CaBER (Thermo Haake CaBER 1) equipped with 4 mm diameter plates. The filament diameter evolution with time was recorded by a laser micrometer at 1000 Hz. Five measurements were collected for each monomer mixture.

The density of the monomer mixture was determined to be 1.15 g/cm^3 by measuring the weight of a known volume of the monomer mix. The surface tension was determined using an axisymmetric pendant droplet of the monomer mix with methods described previously.[29] The droplet was held for 2 minutes to equilibrate before measurements were made. The droplet shape profile was fit according to the Young/Laplace equation with a software package (CAM200, KSV Ltd., Finland). The surface tension of the monomer mixture was measured to be 40.93 mN/m.

The shear rheology of monomer mixtures containing the least and most amounts of PEO (0 ppm and 600 ppm, respectively) were measured by a shear rheometer (TA

instruments AR-2000 EX). Frequency sweeps were performed from 0.628 to 62.8 rad/s with 5% strain in the linear viscoelastic regime. The complex viscosities of the monomer mixtures are shown in **Figure 2.7.** The complex viscosities of the neat monomers, 5A and 4T, are also plotted in the same figure for comparison.

It should be noted that the monomer mixtures used in the CaBER analysis, viscosity measurement, as well as the density and surface tension characterizations contained no photoinitiator to simplify the measurements. It was assumed that such low loadings of photoinitiator in our studies did not alter the viscoelastic and physical properties of the monomer mix significantly.

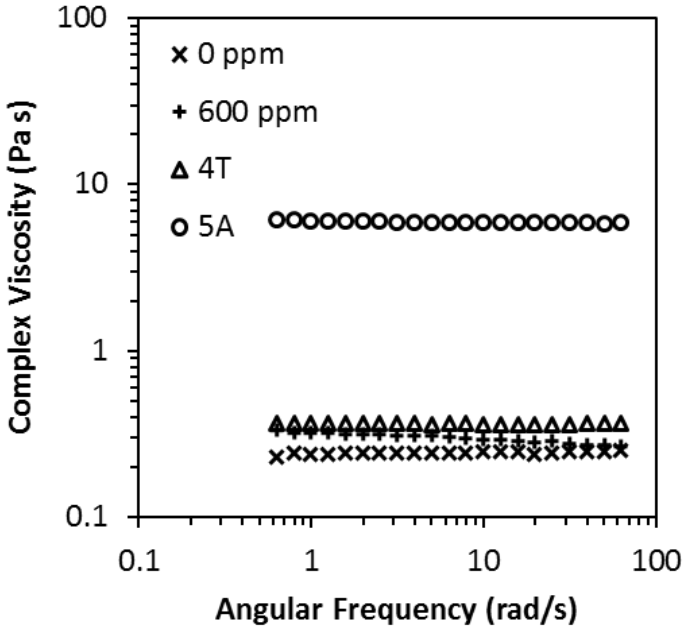

Figure 2.7: Complex viscosities of neat monomers (5A, 4T), and monomer mixtures containing 0 ppm and 600 ppm high MW PEO. Reprinted with permission from Ref. [28]. Copyright © 2015 Elsevier Ltd.

2.3 Results and Discussion

2.3.1 Fiber morphology evolved with light intensity and characterization of gel time

In thiol-ene chemistry, the reaction kinetics can be manipulated in a number of ways. For instance, one can change the functionality of monomers, stoichiometric ratio of ene to thiol functional groups, or employ other ene functional groups with different reactivity. However, varying these parameters can also lead to changes in the viscoelasticity of the monomer mix and polymerization type (chain growth, step growth, mixed, etc.) that occur. In order to isolate a single independent variable, we chose instead to vary I_{eff}, which allowed tuning of the reaction kinetics while keeping monomer mix properties and other processing parameters constant.

A series of 5A-4T monomer mixtures with containing 0.02 wt% PEO, 3 wt% Irgacure 2100, and 12 wt% ethyl acetate were processed at 2500 rpm and at various I_{eff} values ranging from 629 to 24 mW/cm^2 by changing the voltage supplied to the mercury arc lamp light source. The resulting fibers are shown in **Figure 2.8**.

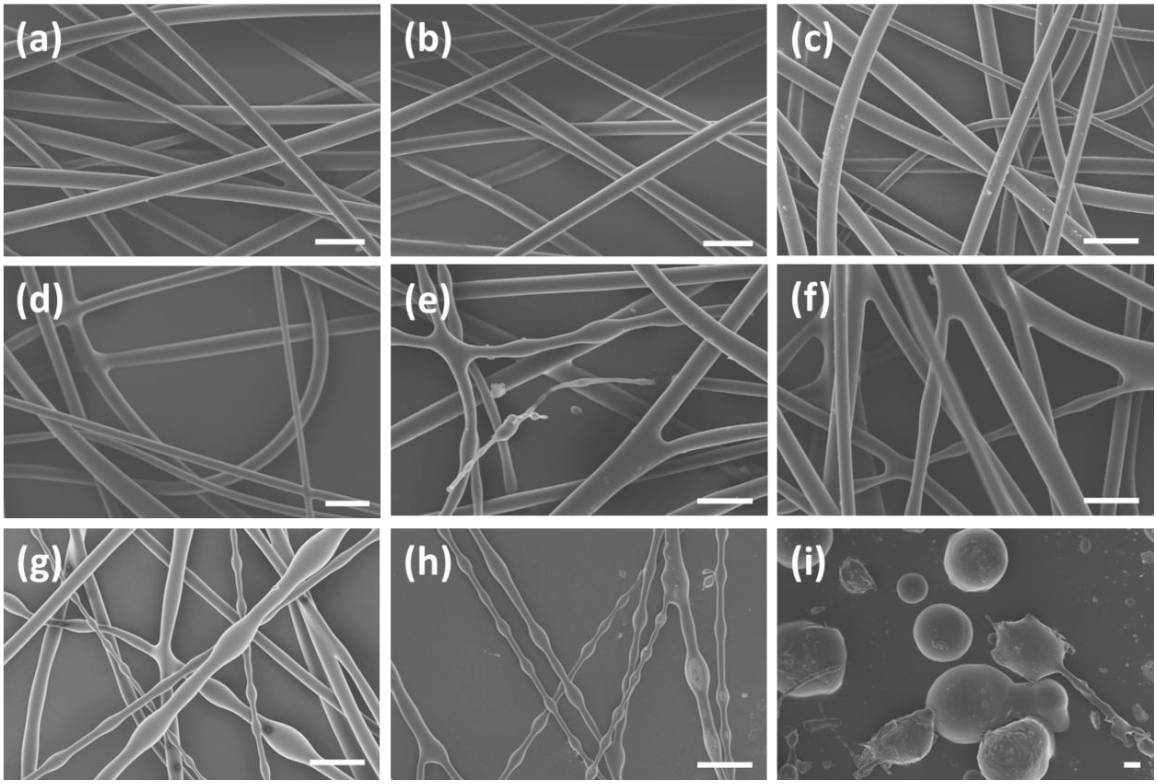

Figure 2.8: SEM images of fibers from monomer mixtures containing 200 ppm PEO, at spin speeds of 2500 rpm, and I_{eff} of (a) 629, (b) 571, (c) 403, (d) 305, (e) 259, (f) 195, (g) 115, (h) 38, and (i) 21 mW/cm^2, respectively. All scale bars in this figure correspond to 25 μm. Reprinted with permission from Ref. [28]. Copyright © 2015 Elsevier Ltd.

At high I_{eff} (**Figure 2.8 a-c**), the fibers are uniform in diameter and well cured. As I_{eff} incrementally decreases to 305 mW/cm^2 (**Figure 2.8 d**), the fibers developed fused junctions, indicating that they are not fully cured when deposited onto the collector. As I_{eff} continues to decrease (**Figure 2.8 e-h**), the fibers also become increasingly less uniform in diameter. In this range of I_{eff}, the onset of surface tension driven Rayleigh instabilities occurs prior to solidification. Rayleigh instabilities result in necking along the fibers axis and cassociated periodic variations in fiber diameter. When I_{eff} drops below 21 mW/cm^2 (**Figure 2.8 i**), the solidification via photopolymerization occurs so slowly that the

instability has caused complete breakup of filaments, depositing only droplets on the collector.

To quantitatively investigate how the photopolymerization kinetics evolve with light intensity and how the kinetics timescale relates to the instability growth timescale and the fiber spinning timescale, RT-FTIR studies were performed using the same spinning mixture at various light intensities. A useful way to describe the curing kinetics of a cross-linked network is by its gel point, the point at which a continuous, cross-linked network is formed and the gel time (T_{gel}), the time for a monomer mixture to reach the gel point. According to the gelation theory developed by Bowman and coworkers, the gel point of a mixed chain growth and step growth cross-linked network such as the one under investigation in this report can be calculated using the equation below:[21, 30]

$$\frac{2}{r}(f_{ene}-1)\frac{k_{CC}}{k_{CS}}p_{\alpha}+(f_{ene}-1)(f_{SH}-1)\left(1+\frac{2}{r}\frac{k_{CC}}{k_{CS}}\right){p_{\alpha}}^{2}=1 \qquad \text{(Eq. 1)}$$

where r is the stoichiometric ratio of thiol to ene, f_{ene} and f_{SH} are the functionality of ene and thiol monomer, respectively, p_{α} is the gel point in terms of degree of acrylate conversion, and k_{CC}/k_{CS} is the ratio of the propagation constant for acrylate-acrylate reactions to the chain transfer constant of acrylate-thiol reactions, which has been previously reported to be around 1.5.[21, 30-31] The gel point was calculated to be 2.2% for the acrylate double bond conversion. The double bond conversion over time was tracked by the reduction of the peak area of the acrylate group at 1636 cm^{-1}.[20-21, 32]

Figure 2.9 is a typical RT-FTIR kinetics curve of the monomer mixture, with time zero being the onset of the UV exposure. The inset shows the double bond conversion at longer times. Because the gel time of the monomer mixture occurs so fast that it nearly approaches the resolution of the instrument, directly interpolating gel time using a few data points does not yield very accurate or consistent results. Instead, the conversion-time data was fit up to 20% conversion to a least squares fit linear equation as indicated by the solid

line in **Figure 2.9**, where polymerization rate is zeroth order with respect to acrylate double bonds[33]. The gel time was then calculated by using this linear fit equation. The polymerization kinetics at five different light intensities were measured and data were processed as described. The gel times were calculated according to Eq. 1 as values averaged between four independent RT-FTIR measurements at each I_{eff}. The results are presented in **Figure 2.10**.

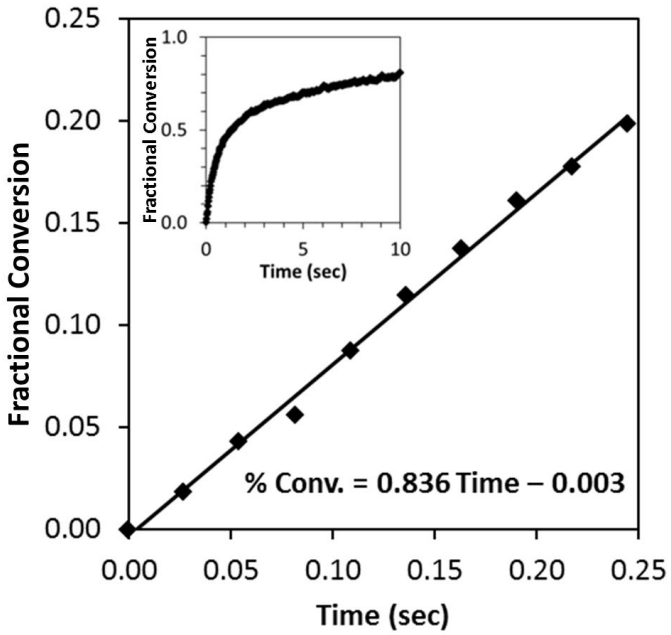

Figure 2.9: A representative polymerization kinetic curve of the monomer mix employed in this study. The inset shows the double bond conversion at longer times. I_{eff} for this particular run was 5.27 mW/cm^2 and the gel time was calculated to be 29.0 ms. Reprinted with permission from Ref. [28]. Copyright © 2015 Elsevier Ltd.

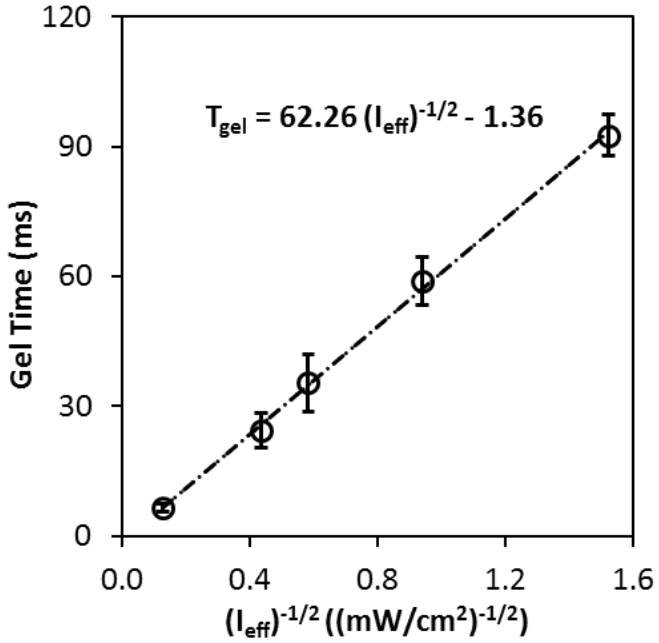

Figure 2.10: Gel time of the monomer mix as a function of I_{eff} as obtained from polymerization kinetics. The dashed line represents the best fit line through all data points. The error bars indicate the standard deviation between four independent measurements at each I_{eff}. Reprinted with permission from Ref. [28]. Copyright © 2015 Elsevier Ltd.

The gel times were plotted against $(I_{eff})^{-1/2}$ because for a conventional free radical polymerization, the polymerization proceeds at a rate proportional to the -1/2 power of the initiation constant,[34] while for a light initiated polymerization such as thiol-ene chemistry, the initiation constant is in turn linearly dependent on the light intensity.[35] The correlation between the gel time and I_{eff} can thereby be obtained from the RT-FTIR studies as shown by the dashed line in **Figure 2.10**.

Using this correlation, the gel times of monomer mixtures, exposed to various light intensities in the fiber spinning process, were calculated and presented in **Figure 2.11** along with the corresponding fiber morphology. As I_{eff} decreases from 629 to 24 mW/cm^2, the gel time increases substantially. It was found that in this process, the reaction kinetics need

to be sufficiently fast with a gel time less than 2 ms for defect free fibers to form, as highlighted in the grey shaded region in **Figure 2.11**.

It should be noted that the I_{eff} in the RT-FTIR studies ranged from 62 to 0.5 mW/cm^2, while the I_{eff} in fiber spinning experiments were an order of magnitude higher, ranging from 629 to 21 mW/cm^2. As a result, some of the gel time calculations for fiber spinning needed to be extrapolated using data presented in **Figure 2.10**. The I_{eff} in the RT-FTIR studies was intentionally kept low because the polymerization kinetics timescale was approaching the instrument resolution limit. Further increasing the light intensity used in RT-FTIR studies leads to a large noise to signal ratio and inconsistent measurements of gel time. In addition, the excellent fit to the linear model with a residual value very close to 1 suggests the validity of data extrapolated to higher light intensity.

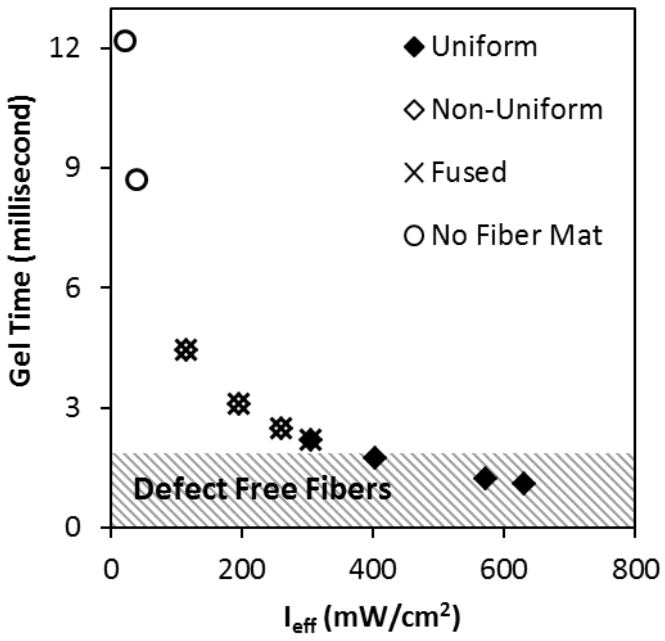

Figure 2.11: The gel times of the monomer mix processed at various light intensities. The corresponding fiber morphologies are superimposed on each data point. The shaded region represents the range of gel times of the monomer mix where defect free fiber mats can be produced. Reprinted with permission from Ref. [28]. Copyright © 2015 Elsevier Ltd.

2.3.2 Fiber morphology varied by elasticity and characterization of relaxation times

Next, we discuss the role of elasticity imparted by the high MW PEO on fiber morphology. A series of six monomer mixtures containing 600, 200, 100, 50, 20, and 0 ppm PEO were prepared and processed at a spin speed of 2500 rpm and I_{eff} of 571 mW/cm^2. Such a high I_{eff} ensures the rapid curing and solidification of the monomer jets and negates the kinetics contribution to morphological evolution in this section. **Figure 2.12** shows the morphology of the fibers made from these monomer mixtures.

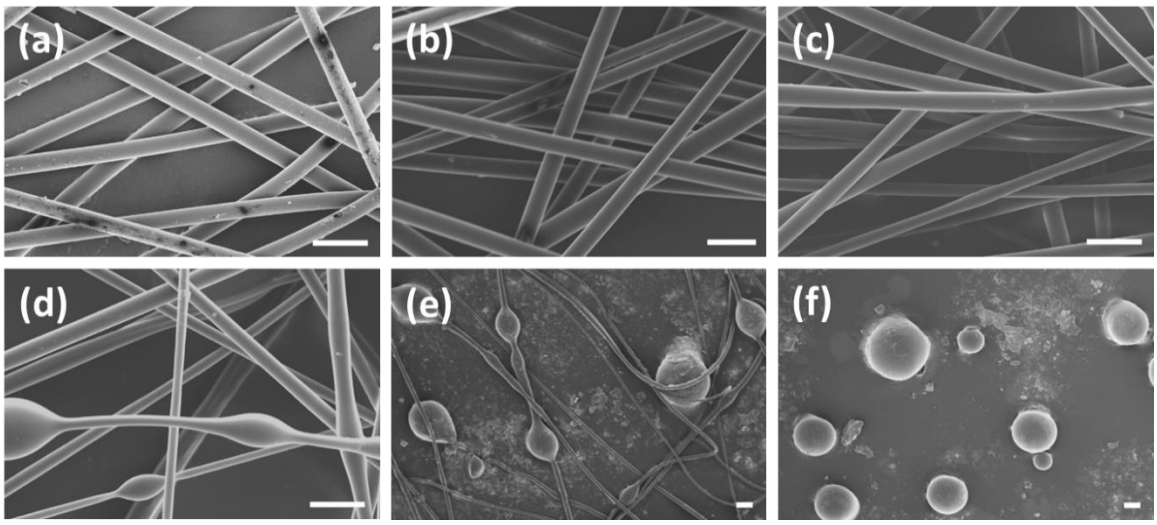

Figure 2.12: SEM images of fibers made from monomer mixes containing (a) 600, (b) 200, (c) 100, (d) 50, (e) 20, and (f) 0 ppm PEO, respectively, at a spin speed of 2500 rpm, and an I_{eff} of 571mW/cm^2. The scale bars in this figure correspond to 25 μm. Reprinted with permission from Ref. [28]. Copyright © 2015 Elsevier Ltd.

The fibers transitioned from smooth fiber, to non-uniform fiber, to beads-on-string, and finally to droplets, with decreasing PEO loading. These morphological transitions are similar to the ones caused by reducing I_{eff} as described in the previous section, but occur due to the decrease in monomer mix elasticity of the fluids. As shown in **Figure 2.12 d-f**, reducing PEO concentration to a point where the surface tension driven instabilities can no

longer be suppressed by elastic forces leads to many defects. It is worth noting that all fiber samples in this section contained no fibers with fused junctions, confirming that the polymerization kinetics are sufficiently fast.

The extensional properties of the monomer mixtures containing various amounts of PEO can be quantified by their characteristic relaxation times. This timescale can be captured by the time evolution of filament diameter measured by CaBER. As shown in **Figure 2.13**, the decay of the filament diameter of five monomer mixtures containing PEO were numerically fit to the elastic fluid model using the following equation:[36]

$$D(t) = D_0 \left(\frac{D_0 G}{4\sigma}\right)^{\frac{1}{3}} e^{-\frac{t}{\lambda_c}} \qquad \text{(Eq. 2)}$$

where $D(t)$ is the time dependent filament diameter measured at the midpoint of the filament by the CaBER micrometer, D_0 is the initial diameter of the filament, G is the elastic modulus, σ the surface tension, and λ_c is the characteristic relaxation time of the monomer mixture. The characteristic relaxation times of the monomer mixtures were extracted by fitting the data to this model and are reported in **Figure 2.14**. The error bars in **Figure 2.14** represent the standard deviations from five CaBER measurements for each monomer mixture.

On the other hand, the decay of the filament diameter of the monomer mixture containing no PEO was best described by the Newtonian fluid model using the following equation:[37-38]

$$D(t) = 0.1418 \frac{\sigma}{\eta_s}(t_c - t) \qquad \text{(Eq. 3)}$$

where t_c is the critical time to break up, and η_s is the viscosity of the solvent, which is the viscosity of the entire monomer mix containing no PEO, measured to be 0.24

Pa-s by shear rheometry (TA instruments AR-2000 EX). The excellent fit to the Newtonian fluid model is expected since the monomer mix was inelastic without PEO.

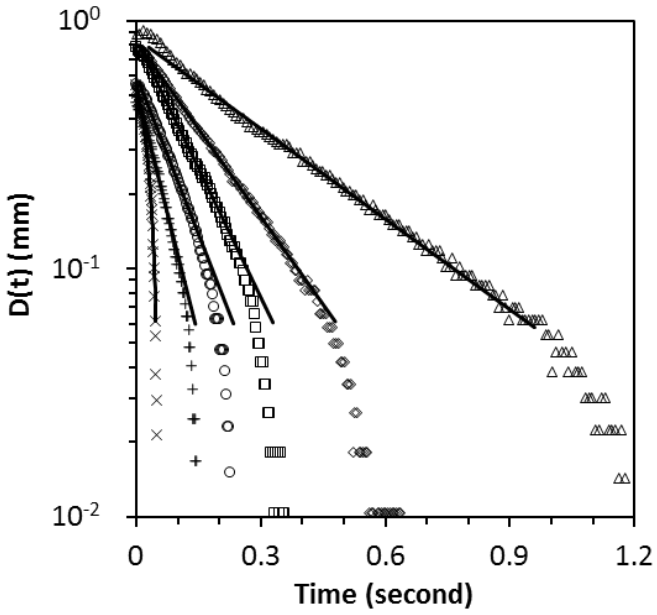

Figure 2.13: Evolution of the midpoint filament diameter D(t) during filament thinning of monomer mixtures containing 600 ppm (△), 200 ppm (◊), 100 ppm (□), 50 ppm (○), 20 ppm (+), and 0 ppm (×) PEO, respectively. Solid lines are best fit lines to either the elastic fluid model (600 to 20 ppm PEO) or the Newtonian fluid model (0 ppm PEO). Reprinted with permission from Ref. [28]. Copyright © 2015 Elsevier Ltd.

In **Figure 2.14**, the characteristic fluid relaxation times of the PEO containing monomer mixtures are plotted as a function of the PEO concentrations by weight. The dashed line represents the least squares power law fit to the data with an exponent of 0.486. Previously, the concentration dependence of relaxation times of unentangled semi-dilute polymer solutions has been established and empirically determined to follow a power law dependence. In this regime, the power law scaling exponent, equal to $(2-3\nu)/(3\nu-1)$, is equal to 1 for a θ-solvent and around 0.31 for a good solvent. The symbol ν represents the excluded volume scaling parameter, which indicates the solvent quality for a polymer and

spans from 0.5 for a θ-solvent to 0.588 for a good solvent.[39] This scaling law has been verified by several experiments with different semi-dilute polymer-solvent systems.[40-42] The good fit of our data to the power law equation with an exponent between 0.31 and 1 confirms that the series of monomer mixtures with various PEO concentrations falls in the dilute unentangled polymer solution regime. In addition, the scaling exponent of 0.486 from the fit in this study corresponds to $\nu = 0.558$, which indicates that the monomer mixture is a fair solvent for PEO, but not as good as that of water, a commonly used solvent for PEO.[43-45] Furthermore, the good fit in **Figure 2.14** demonstrates that, although the monomer molecules used here are relatively large in size, they essentially behave like other conventional small molecule organic solvents for the dissolution of PEO.

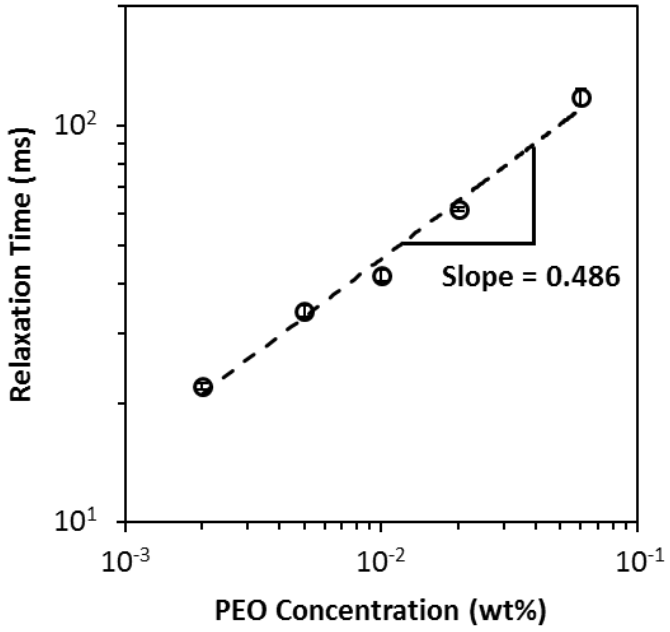

Figure 2.14: Relaxation time of monomer mixtures as a function of the concentration of PEO. The dashed line represents a least squares power law fit to the data. The error bars are standard deviations of five independent CaBER measurements. Reprinted with permission from Ref. [28]. Copyright © 2015 Elsevier Ltd.

In addition to fluid relaxation times, the apparent extensional viscosity (η_{app}), of the monomer mixture as a function of Hencky strain (ε), can be calculated using the following equations:[36]

$$\varepsilon = ln\left(\frac{D(t)}{D_0}\right) \qquad \text{(Eq. 4)}$$

$$\eta_{app}(\varepsilon) = -\frac{\sigma}{dD(t)/dt} \qquad \text{(Eq. 5)}$$

In CaBER experiments, filament thinning is solely driven by surface tension, while in centrifugal spinning, it is driven by both inertia and surface tension. Despite the differences, this analysis still captures the viscoelastic response for an exponentially thinning filament. The results are presented in **Figure 2.15**. Expectedly, the monomer mixture containing no PEO behaves like a Newtonian fluid, and the apparent extensional viscosity is independent of Hencky strain, whereas the monomer mixtures containing PEO show a strain hardening effect, which becomes more prominent with increasing PEO concentration.

η_{app} of the monomer mixture containing 200 ppm PEO (the typical PEO loading for the monomer mix) increases by almost two orders of magnitude over the range of Hencky strains accessible in CaBER studies, showing that adding a trace amount of high MW PEO can significantly enhance the extensional behavior of the monomer mixture. In contrast, the shear viscosities of the monomer mixtures containing 0 ppm and 600 ppm PEO were measured by a parallel plate rheometer to be 0.24 and 0.33 Pa-s, respectively (see **Figure 2.7**). The dramatic change in η_{app} combined with the narrow range of the shear viscosity indicates that these monomer mixtures are typical Boger fluids, whose extensional properties can be tuned independently of their shear properties.[46] A Boger fluid is commonly a dilute polymer solution with a viscous solvent,[46] which in this study is a dilute PEO solution with a viscous thiol-ene monomer mixture.

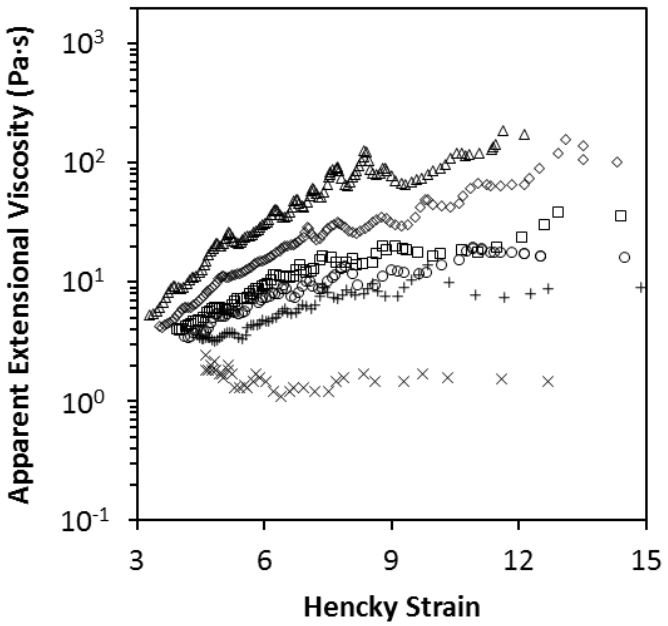

Figure 2.15: Apparent extensional viscosities of the monomer mixtures containing 600 ppm (△), 200 ppm (◊), 100 ppm (□), 50 ppm (○), 20 ppm (+), and 0 ppm (×) of PEO. Reprinted with permission from Ref. [28]. Copyright © 2015 Elsevier Ltd.

The evolution of fiber morphology from uniform fiber, non-uniform fiber, beads-on-string, and finally droplets depends on the balance between the viscous, elastic, inertial stresses, thinning due to centrifugal force and the capillary pressure inside the jet. In order to evaluate quantitatively the relative importance of each force, we introduce three dimensionless parameters: the Deborah number (De), Weissenberg number (Wi), and Ohnesorge number (Oh). De measures the ratio of the characteristic timescale of fluid relaxation to the timescale of Rayleigh inertio-capillary breakup, and is defined as $De = \lambda_c/\sqrt{\rho R^3/\sigma}$,[37, 45] where R is the radius of the initial fluid jet (0.105 mm). Using the relaxation times obtained from the CaBER experiments, the calculated De numbers for monomer mixtures containing 20, 50, 100, 200, 600 ppm PEO are 3.8, 6.0, 7.3, 10.8, and 20.6, respectively. For our system and process, uniform fiber formation requires the De to

be well above unity (De > 7.3), where fluid relaxation time is much greater than the Rayleigh instability timescale, and the onset of capillary breakup is completely suppressed by the elastic stresses. When Rayleigh instabilities are not completely suppressed (De < 7.3), significant beading in monomer jets is observed, leading to a beads-on-string morphology. If the elastic response is absent altogether, as in the case of the monomer mix containing no elasticity modifier, Rayleigh instabilities develop and the monomer jets readily dissipate into droplets upon exiting the spinneret. The fiber morphology developed with reducing De number is very similar to a study reported by Yu and coworkers on electrospinning PEO in water/PEG solutions.[43]

On the other hand, Wi is defined as the ratio of the characteristic timescales of fluid relaxation to fiber thinning due to centrifugal force, and can be expressed as $\mathrm{Wi} = \lambda_c \Omega / \sqrt{R/a}$, where Ω is the spin speed and a is the distance between the orifice and the spinning axis.[47] Wi numbers for monomer mixtures containing 20, 50, 100, 200, 600 ppm PEO are 30.3, 46.9, 57.7, 84.8, and 162.4, respectively. The transition from uniform fibers to beads-on-string or to bead formation occurs when Wi number falls below 46.9, again demonstrating the significance of elastic stresses for fiber formation. This correlation agrees well with a recent mechanistic study on solution state centrifugal spinning by Ren et al., where it was found for a variety of polymer-solvent systems and various processing conditions that fibers were formed when Wi numbers exceeded 28, while beads-on-string and beads were formed if Wi numbers fell below 28.[47] These interesting similarities of fiber morphology development as a function of De and Wi suggest that, despite the drastic differences in fiber formation mechanisms, the conditions required to form a stable fluid jet and uniform fibers in this reactive fiber spinning method are comparable to that of a non-reactive fiber spinning method, provided sufficiently rapid curing kinetics.

In contrast, the Ohnesorge number relates viscous forces to inertial and surface tension forces, and is defined as $Oh = \eta/\sqrt{\rho\sigma R}$,[37, 45] where η is the viscosity of the monomer mixture. The Ohnesorge number is around 4 for all monomer mixtures, because the addition of PEO does not significantly influence the viscosity, density, and surface tension of the monomer mixtures. An Oh number greater than unity also implies that viscous stress is enough to stabilize the filament, again confirming that the morphological changes mainly arise as a result of changes in monomer mix elastic properties.

2.3.3 Fiber morphology evolved with spin speed and estimation of flight time

In addition to gel time and fluid relaxation time, the fiber jet flight time is another important time scale in this process because it dictates the available time for light exposure and photopolymerization of the monomer jet before it hits the collector. The monomer mix that makes good fibers at 2500 rpm (as shown in **Figure 2.8 b**) was also processed at 3500 rpm and 4500 rpm using the same illumination condition, as shown in **Figure 2.16**. Fibers processed at 3500 rpm were well cured (**Figure 2.16 a**) while fibers spun at 4500 rpm were fused at their junctions (**Figure 2.16 b**). At 4500 rpm, the fibers did not have enough time to cure completely before depositing onto other fibers on the collector.

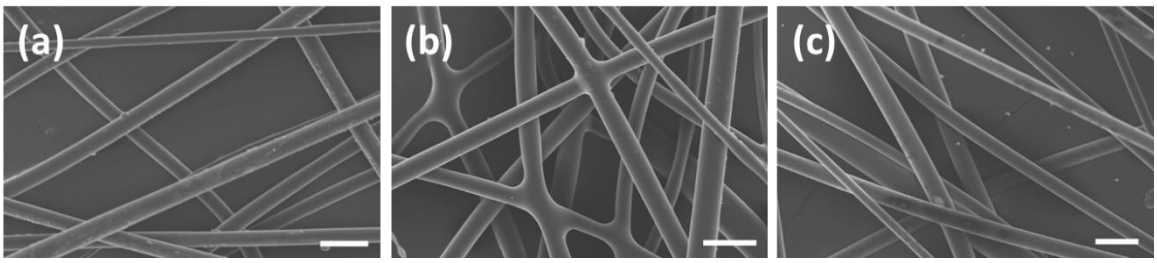

Figure 2.16: SEM images of fibers at a spin speed of (a) 3500 rpm and (b, c) 4500 rpm. The monomer mix contains 3 wt% Irgacure 2100 in (a, b) and 5 wt% Irgacure 2100 in (c). The PEO loading is 200 ppm and the I_{eff} is 571mW/cm^2 for all three runs. The scale bars in this figure correspond to 25 μm. Reprinted with permission from Ref. [28]. Copyright © 2015 Elsevier Ltd.

The flight time can be defined as the fiber flight distance divided by the fiber velocity. In centrifugal spinning, the fluid jet follows a spiral trajectory outward from the spinneret tip to the vertical collector bars, which depends on spin speed, solution viscosity and elasticity, ratio of length to diameter of the orifice and other process variables.[48-50] In addition, the fiber velocity is not constant as the fluid jet attenuates in diameter.[48] Both parameters are difficult to assess accurately by either empirical measurement or theoretical calculation. In this study, the flight time is estimated by using the diameter of the illuminated beam spot on the circular collector (10 cm) as the flight distance and the linear velocity of the tip of the spinneret as the fiber velocity. Although the fiber does not travel in a linear fashion through the center of the illuminated region, this is the most straightforward estimate for this reactive fiber spinning process. The linear velocity of the spinneret tip can also be viewed as the initial velocity of the fiber as it exits the spinneret. The respective flight times of fiber jets processed at 2500, 3500, and 4500 rpm are 3.4, 2.4, and 1.9 ms. With all other conditions and material properties being the same, a minimum of 2.4 ms flight time was required to produce defect free fibers.

However, flight time is meaningful only when it is placed in context with other timescales. For example, avoiding the formation of fused fibers can be achieved in several ways, such as increasing flight time by spinning at lower spin speeds as shown in **Figure 2.16 a** and decreasing gel time by increasing reaction kinetics. **Figure 2.16 c** is an SEM image of fibers made at the exact same spinning and lighting condition as **Figure 2.16 b**, but with a monomer mix that contained 5 wt% of photoinitiator instead of 3 wt%. The higher loading of photoinitiator increases the curing speed, allowing the fiber jet to cure completely before deposition. This again exemplifies the complexity and the intertwined variables of this simultaneous fiber spinning and photopolymerization process.

2.3.4 Operating diagram describing the interactions of the three timescales

The process conditions, the corresponding timescales, and fiber morphologies of the three fiber spinning tests conducted in this study are summarized in **Table 2.3**. Also presented are the ratio of fluid relaxation time (T_{relax}) to gel time (T_{gel}), and the ratio of flight time (T_{flight}) to T_{gel}. An operating diagram is constructed by plotting the ratios of timescales along with the fiber morphologies as shown in **Figure 2.17**.

Variable	I_{eff} (mW/cm^2)	C_{PEO} (ppm)	Spin Speed (rpm)	T_{gel} (ms)	$T_{relaxation}$ (ms)	T_{flight} (ms)	$T_{relaxation}/T_{gel}$	T_{flight}/T_{gel}	Fiber Morphology
I_{eff}		200	2500		61.7	3.4			
	629			1.1			54.9	3.0	Uniform, cured
	571			1.2			49.5	2.7	Uniform, cured
	403			1.7			35.4	2.0	Uniform, cured
	305			2.2			28.0	1.5	Uniform, fused
	259			2.5			24.6	1.4	Wavy, fused
	195			3.1			19.9	1.1	Wavy, fused
	115			4.4			13.9	0.8	Wavy, fused
	38			8.7			7.1	0.4	Beads-on-string, fused
	21			12.2			5.1	0.3	Droplet
C_{PEO}	571		2500	1.2		3.4			
		600			118.1		94.8	2.7	Uniform, cured
		200			61.7		49.5	2.7	Uniform, cured
		100			41.9		33.7	2.7	Uniform, cured
		50			34.1		27.4	2.7	Wavy, cured
		20			22.0		17.7	2.7	Beads-on-string, cured
		0			NA		NA	2.7	Droplet
Spin Speed	571	200		1.2	61.7				
			2500			3.4	49.5	2.7	Uniform, cured
			3500			2.4	49.5	1.9	Uniform, cured
			4500			1.9	49.5	1.5	Uniform, fused

Table 2.3: A summary of fiber spinning conditions, related time scales, and fiber morphology. The first row in each data set indicates the variable of interest and the other parameter values that were held constant in the experimental runs below the first row. Reprinted with permission from Ref. [28]. Copyright © 2015 Elsevier Ltd.

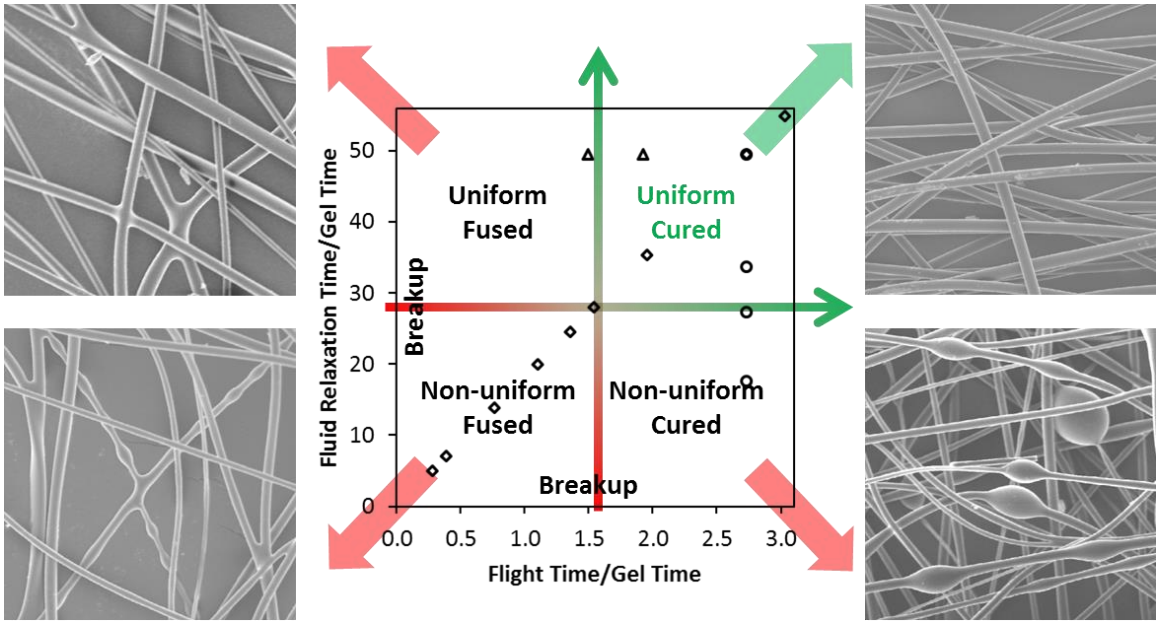

Figure 2.17: Operating diagram relating fluid relaxation time, gel time, and flight time in the reactive centrifugal fiber spinning process. ◊, ○, △ represent the fiber sample series made by varying I_{eff}, C_{PEO}, and spin speed, respectively. Reprinted with permission from Ref. [28]. Copyright © 2015 Elsevier Ltd.

Despite the complexity of this multivariable process, the fiber morphology evolves as a result of the competition between three phenomena: the solidification by thiol-ene photopolymerization, the surface tension driven instability growth which can be suppressed by monomer mix elasticity, and the orifice-to-collector flight time, characterized by T_{gel}, T_{relax}, and T_{flight}, respectively. In **Figure 2.17**, the horizontal arrow indicates the threshold value for the formation of uniform fiber, whereas the vertical arrow indicates the threshold value for the formation of well cured fiber. Defect free fibers are formed when gel time is sufficiently small compared to both the fluid relaxation time and the flight time. When a mismatch of timescales occurs such that either one or both ratios fall below the threshold value, fiber defects such as uncured fibers, non-uniform fibers, or

a combination of the two develop. When timescales become significantly mismatched, fiber jets readily dissipate into droplets.

2.4 CONCLUSION

In this chapter, we have demonstrated the fabrication of fibers by simultaneous thiol-ene photopolymerization and centrifugal spinning an optimized formulation containing multifunctional thiol and ene monomers, photoinitiator, high MW PEO as a elasticity modifier, and ethyl acetate as a diluent. Fundamental understanding of conditions that lead to a variety of fiber morphologies, including droplets, beads-on-string, uniform fibers, fused fibers, and well cured fibers was developed by systematically varying three carefully chosen parameters: light intensity, PEO concentration, and spin speed, which independently affect the reaction kinetics, monomer mix viscoelasticity, and orifice-to-collector flight time, respectively. To quantify these transitions further, the relevant timescales, namely the gel time, the characteristic relaxation time, and the fiber flight time, at each fiber spinning condition were measured, calculated and compared.

An operating diagram was constructed by comparing ratios of the three timescale measurements at each fiber spinning condition, which explicitly illustrates that the fiber morphology is determined not only by the individual parameters of the process, but also by the interplay between them. Although there are numerous combinations of these parameters, the ultimate fiber morphology will always be governed by the relative speeds of solidification by photopolymerization, surface tension driven instability growth, and fiber deposition. Our qualitative understanding of the fundamental physics and quantitative operating diagram for controlling fiber formation and morphology can serve as a predictive guideline for the implementation of photopolymerization into other fiber spinning

processes and the fabrication of fibers with designed morphology and properties, which we will continue to discuss in the following chapters.

2.5 REFERENCES

1. Termonia, Y., *Macromolecules* **1994,** *27* (25), 7378-7381.
2. Vollrath, F.; Knight, D. P., *Nature* **2001,** *410* (6828), 541-548.
3. Liu, Y.; Shao, Z.; Vollrath, F., *Nature Materials* **2005,** *4* (12), 901-905.
4. Jin, H.-J.; Kaplan, D. L., *Nature* **2003,** *424* (6952), 1057-1061.
5. Marvel, C.; Caesar, P., *Journal of the American Chemical Society* **1951,** *73* (3), 1097-1099.
6. Marvel, C.; Chambers, R., *Journal of the American Chemical Society* **1948,** *70* (3), 993-998.
7. Lundberg, P.; Bruin, A.; Klijnstra, J. W.; Nyström, A. M.; Johansson, M.; Malkoch, M.; Hult, A., *ACS Applied Materials & Interfaces* **2010,** *2* (3), 903-912.
8. Sparks, B. J.; Hoff, E. F.; Hayes, L. P.; Patton, D. L., *Chemistry of Materials* **2012,** *24* (18), 3633-3642.
9. Lu, H.; Carioscia, J. A.; Stansbury, J. W.; Bowman, C. N., *Dental Materials* **2005,** *21* (12), 1129-1136.
10. Fairbanks, B. D.; Schwartz, M. P.; Halevi, A. E.; Nuttelman, C. R.; Bowman, C. N.; Anseth, K. S., *Advanced Materials* **2009,** *21* (48), 5005-5010.
11. Kwisnek, L.; Nazarenko, S.; Hoyle, C. E., *Macromolecules* **2009,** *42* (18), 7031-7041.
12. Campos, L. M.; Meinel, I.; Guino, R. G.; Schierhorn, M.; Gupta, N.; Stucky, G. D.; Hawker, C. J., *Advanced Materials* **2008,** *20* (19), 3728-3733.
13. Hoyle, C. E.; Lee, T. Y.; Roper, T., *Journal of Polymer Science Part A: Polymer Chemistry* **2004,** *42* (21), 5301-5338.
14. O'Brien, A. K.; Cramer, N. B.; Bowman, C. N., *Journal of Polymer Science Part A: Polymer Chemistry* **2006,** *44* (6), 2007-2014.
15. Nason, C.; Roper, T.; Hoyle, C.; Pojman, J. A., *Macromolecules* **2005,** *38* (13), 5506-5512.
16. Boyd, D. A.; Shields, A. R.; Naciri, J.; Ligler, F. S., *ACS Applied Materials & Interfaces* **2012,** *5* (1), 114-119.
17. Yang, H.; Zhang, Q.; Lin, B.; Fu, G.; Zhang, X.; Guo, L., *Journal of Polymer Science Part A: Polymer Chemistry* **2012,** *50* (20), 4182-4190.

18. Kim, S. H.; Kim, S.-H.; Nair, S.; Moore, E., *Macromolecules* **2005,** *38* (9), 3719-3723.

19. Ji, Y.; Ghosh, K.; Li, B.; Sokolov, J. C.; Clark, R. A.; Rafailovich, M. H., *Macromolecular Bioscience* **2006,** *6* (10), 811-817.

20. Shanmuganathan, K.; Sankhagowit, R. K.; Iyer, P.; Ellison, C. J., *Chemistry of Materials* **2011,** *23* (21), 4726-4732.

21. Janes, D. W.; Shanmuganathan, K.; Chou, D. Y.; Ellison, C. J., *ACS Macro Letters* **2012,** *1* (9), 1138-1142.

22. Shanmuganathan, K.; Elliot, S. M.; Lane, A. P.; Ellison, C. J., *ACS Applied Materials & Interfaces* **2014,** *6* (16), 14259-14265.

23. Shanmuganathan, K.; Fang, Y.; Chou, D. Y.; Sparks, S.; Hibbert, J.; Ellison, C. J., *ACS Macro Letters* **2012,** *1* (8), 960-964.

24. Ma, M.; Gupta, M.; Li, Z.; Zhai, L.; Gleason, K. K.; Cohen, R. E.; Rubner, M. F.; Rutledge, G. C., *Advanced Materials* **2007,** *19* (2), 255-259.

25. Ma, M.; Mao, Y.; Gupta, M.; Gleason, K. K.; Rutledge, G. C., *Macromolecules* **2005,** *38* (23), 9742-9748.

26. Wang, N.; Wang, X.; Ding, B.; Yu, J.; Sun, G., *Journal of Materials Chemistry* **2012,** *22* (4), 1445-1452.

27. Crowley, M. M.; Zhang, F.; Koleng, J. J.; McGinity, J. W., *Biomaterials* **2002,** *23* (21), 4241-4248.

28. Fang, Y.; Dulaney, A. D.; Gadley, J.; Maia, J. M.; Ellison, C. J., *Polymer* **2015,** *73*, 42-51.

29. Adkins, S. S.; Chen, X.; Nguyen, Q. P.; Sanders, A. W.; Johnston, K. P., *Journal of Colloid and Interface Science* **2010,** *346* (2), 455-463.

30. Reddy, S. K.; Okay, O.; Bowman, C. N., *Macromolecules* **2006,** *39* (25), 8832-8843.

31. Cramer, N. B.; Bowman, C. N., *Journal of Polymer Science Part A: Polymer Chemistry* **2001,** *39* (19), 3311-3319.

32. Reddy, S. K.; Cramer, N. B.; Bowman, C. N., *Macromolecules* **2006,** *39* (10), 3681-3687.

33. Cramer, N. B.; Davies, T.; O'Brien, A. K.; Bowman, C. N., *Macromolecules* **2003,** *36* (12), 4631-4636.

34. Rodriguez, F.; Cohen, C.; Ober, C.; Archer, L. A., *Principles of Polymer Systems*. Taylor & Francis Washington, DC: **1996**; Vol. 4.

35. Anseth, K. S.; Bowman, C. N.; Peppas, N. A., *Journal of Polymer Science Part A: Polymer Chemistry* **1994,** *32* (1), 139-147.

36. Regev, O.; Vandebril, S.; Zussman, E.; Clasen, C., *Polymer* **2010,** *51* (12), 2611-2620.

37. Campo-Deano, L.; Clasen, C., *Journal of Non-Newtonian Fluid Mechanics* **2010,** *165* (23), 1688-1699.

38. McKinley, G. H.; Tripathi, A., *Journal of Rheology (1978-present)* **2000,** *44* (3), 653-670.

39. Rubinstein, M.; Colby, R., *Polymers Physics*. Oxford: **2003**.

40. Patel, S. S.; Takahashi, K. M., *Macromolecules* **1992,** *25* (17), 4382-4391.

41. Liu, Y.; Jun, Y.; Steinberg, V., *Journal of Rheology (1978-present)* **2009,** *53* (5), 1069-1085.

42. Hur, J. S.; Shaqfeh, E. S.; Babcock, H. P.; Smith, D. E.; Chu, S., *Journal of Rheology (1978-present)* **2001,** *45* (2), 421-450.

43. Yu, J. H.; Fridrikh, S. V.; Rutledge, G. C., *Polymer* **2006,** *47* (13), 4789-4797.

44. Tirtaatmadja, V.; McKinley, G. H.; Cooper-White, J. J., *Physics of Fluids (1994-present)* **2006,** *18* (4), 043101.

45. Oliveira, M. S.; Yeh, R.; McKinley, G. H., *Journal of Non-Newtonian Fluid Mechanics* **2006,** *137* (1), 137-148.

46. James, D. F., *Annual Review of Fluid Mechanics* **2009,** *41*, 129-142.

47. Ren, L.; Ozisik, R.; Kotha, S. P.; Underhill, P. T., *Macromolecules* **2015**.

48. Taghavi, S.; Larson, R., *Physical Review E* **2014,** *89* (2), 023011.

49. Xu, H.; Chen, H.; Li, X.; Liu, C.; Yang, B., *Journal of Polymer Science Part B: Polymer Physics* **2014**.

50. Padron, S.; Fuentes, A.; Caruntu, D.; Lozano, K., *Journal of Applied Physics* **2013,** *113* (2), 024318.

Chapter 3: A Comparative Study: Controlling Fiber Diameter and Diameter Distribution in Centrifugal Spinning of Photocurable Monomers and Polymeric Solutions[2]

3.1 INTRODUCTION

In Chapter 2, the integration of thiol-ene photopolymerization with centrifugal Forcespinning to fabricate crosslinked thermoset fibers was described. It focused on identifying process conditions for fabricating defect free fibers or developing fundamental understanding of the physics and mechanics of the reactive fiber formation process. In summary, a variety of fiber morphologies, such as droplets, beads-on-string, uniform fibers, fused fibers, and well cured fibers developed due to the interplay between reaction kinetics, monomer mixture viscoelasticity, and orifice-to-collector flight time. The morphological transitions of fibers were quantified by measuring the characteristic process timescales, namely gel time, fluid relaxation time, and fiber flight time.

In addition to fiber morphology, the average fiber diameter and diameter distribution are important parameters for nonwovens because the size of the fiber primarily determines the specific surface area and pore size of the final nonwoven mat, properties that ultimately dictate suitability for end use applications. For example, numerous studies have found that fiber diameter has profound impact on cell proliferation and controlled drug release in scaffolds,[1-3] and filtration properties of nonwoven membranes.[4]

As surveyed in Chapter 1, there is a wealth of literature on controlling average fiber diameter by varying process parameters, material properties, fiber spinning instrumentation, etc., in conventional fiber spinning methods such as electrospinning, melt

[2]This chapter is adapted from "A comparative parameter study: controlling fiber diameter and diameter distribution in centrifugal spinning of photocurable monomers" published in *Polymer* (2016). Yichen Fang was responsible for design of experiments, data collection and analysis; Austin R. Dulaney conducted part of fiber spinning experiments and SEM analysis; Jesse Gadley and Prof. Joao Maia collaborated with us on CaBER measurements; Prof. Ellison provided overall guidance for this project.

spinning and melt blowing. Some of the general design and processing principles can be generalized to centrifugal spinning. For instance, the 'spinnability' of a polymer solution is a common topic in solution state fiber processing regardless of spinning method.[5-8] However, a special attribute of centrifugal spinning is that the centrifugal force determines both the feed material delivery rate through the orifices and the amount of drawing force to which the fiber jets are subjected. This is contrary to other fiber spinning methods, where the material delivery rate, often controlled by a syringe/piston pump or an extruder, and the fiber drawing force, governed by either the hot air flow rate in melt blowing or the applied voltage field in electrospinning, can be independently manipulated.

Several studies have focused on the physics governing fiber initiation and attenuation in centrifugal spinning. Notably, Mellado et al. established a semi-empirical scaling framework for fiber radius as a function of viscosity, angular speed, distance to the collector, and radius of the orifice.[9] Ren et al identified and analyzed key dimensionless groups such as Weissenberg number, Capillary number, and Ohnesorge number, that determine fiber morphology and diameter using a variety of polymer-solvent solutions.[10] Taghavi and Larson proposed a theoretical model that allows for determination of fiber velocity and diameter by balancing centrifugal, inertial, and viscous forces.[11] Others have provided insight on the jet initiation stage and fiber flight trajectory using high speed photography.[12-13]

There have been a number of studies on tuning the diameter distributions of fibers made by polymer-solvent solution[9, 14-15] and melt state[16] centrifugal spinning. Most of these studies concluded that the dominant parameters for controlling fiber diameter include polymer-solvent solution concentration, orifice diameter, spin speed, and processing temperature (melt state). It is expected that there will be intrinsic differences between reactive fiber processing and polymer-solvent solution or polymer melt centrifugal

spinning processes. First, the photopolymerizable feedstock used in the present reactive processing study contains mostly monomers with trace amounts of polymer to tailor the rheology; the total polymer concentration is too low to be in the semi-dilute entangled regime typically required for forming defect free fibers by solution spinning.[17-19] As a result, the viscoelastic properties and the delivery and drawing of the monomer mixtures are very different from those of typical polymer-solvent solutions and melts. Second, the solidification mechanism in reactive centrifugal spinning is through photopolymerization, whereas in solution state spinning solidification it is driven by solvent evaporation and in melt state spinning it is crystallization or vitrification induced by sufficient cooling. It is apparent that the parameters influencing these mechanisms are different. For these reasons, it is difficult to predict how the fiber diameter distribution can be manipulated in reactive centrifugal spinning simply based on previous solution or melt studies.

Therefore, the primary objective of this paper is to investigate how the average fiber diameter and diameter distribution can be controlled by varying process and material parameters such as monomer feed viscoelasticity, orifice size and spin speed. This will not only demonstrate the tunability of the process, but will also shed light on the underlying physics of fiber thinning in reactive centrifugal spinning. Another area of focus will be to establish the lower limit in average fiber diameter that is attainable using this method. Smaller fibers close to and below one micron provide large surface area to volume ratios, and are light weight. The ability to produce small fibers is particularly attractive for a number of applications and this capability could further establish simultaneous centrifugal spinning and photopolymerization technology as a competitive alternative to existing approaches.

3.2 EXPERIMENTAL

3.2.1 Materials

Dipentaerythritol pentaacrylate (5A), pentaerythritol tetrakis (3-mercaptopropionate) (4T), polyethylene oxide (PEO) with a viscosity average molecular weight (MW) of 10^6 g/mol, anhydrous ethyl acetate (EA), and formic acid (>88 wt%, reagent grade) were purchased from Sigma Aldrich. A commercial photoinitiator, Irgacure 2100, was kindly provided by BASF. Polyamide 6 (PA6, Aegis H95ZI) was purchased from Honeywell Co. All chemicals were used as received.

3.2.2 Photocurable monomer mix preparation

The photocurable monomer feed consists of ene functional monomer, thiol functional monomer with a trace amount of PEO, photoinitiator and EA. Previously, it had been demonstrated that the elasticity of the monomer mixture, imparted by the addition of high MW PEO, plays an important role in controlling fiber formation and morphology in the in-situ centrifugal spinning and photopolymerization process. It was determined that a minimum of 100 ppm high MW PEO was necessary to suppress surface tension driven instabilities to form uniform fibers, provided that photocuring kinetics and fiber solidification were sufficiently fast.[20] In this study, dilute mixtures of high MW PEO in thiol monomer were prepared by dissolving appropriate amounts of PEO in 4T monomer at 70 ^{o}C for 18 hours. Unless otherwise specified, the stock concentration of PEO is 0.1 wt% in 4T, which is equivalent to 180 – 210 ppm in the final photocurable monomer feed depending on the final proprotion of all components.

The final monomer ene to thiol functional group molar ratio was kept constant at 4 to 1 for all monomer mixes to provide sufficient curing kinetics and reduce the oxygen inhibition effect of acrylate polymerizations.[21-22] The photoinitiator loading was kept

constant at 5 wt% of the overall monomer feed. In addition, various amounts of EA ranging from 0 - 18 wt% were added to adjust the final viscosities of the monomer feed. Although other reactive monomers with low viscosties such as 1, 6-hexanediol diacrylate can also be used, EA was preferred in this study because it could adjust viscosity without significantly affecting the photopolymerization kinetics or gel point.

The components were mixed in a scintillation vial using a vortex mixer (Thermolyne 37600) to make a homogeneous monomer feed mixture. The solution was then loaded into a syringe masked from room light, which was used to transfer the monomer mixture into the spinneret. The monomer mixture was prepared in a room that minimized stray UV light to prevent pre-exposure that could initiate photopolyerization prior to fiber spinning.

3.2.3 Nylon-formic acid solution preparation

As a comparison to reactive centrifugal spinning, various amounts of PA6 were added to formic acid to form solutions containing 71 to 83 wt% formic acid. Although polymer-solvent solutions are typically described in terms of the concentration of polymer, in this study these solutions were labeled by the wt% of the solvent in order to allow easier comparison with the photocurable monomer feed mixtures. The solution was gently stirred at room temperature overnight to ensure complete dissolution. The solution was loaded into a syringe, which was used to transfer the solution into the spinneret.

3.2.4 Centrifugal spinning

The in-situ centrifugal spinning and photopolymerization of the monomer feed mixture was performed using a lab scale Forcespinning apparatus (FibeRio Cyclone L1000) equipped with a custom UV light source comprised of a power supply, an igniter, a lamp housing (Photon Technology International LPS-220, LPS-221, LPS-A1010), a

Mercury short arc lamp (Osram HBO 103W/2), and a UV transparent reflective mirror (Edmund optics). A detailed description and schematic representation (**Figure 2.3)** of the light source design was presented previously in Chapter 2. The pre-mixed monomer feed was transferred to the spinneret by a masked syringe to prevent exposure to stray UV light. The spinneret holds about 2 mL of liquid and is cylindrical with two opposing orifices. Two Luer-lock blunt-tip needles 3.81 cm in length with different diameters (337 µm, 260 µm, 210 µm) were connected to both sides of the spinneret, leading to a rotational radius of 11.6 cm. It should also be mentioned that in Section 3.3.4, Luer-lock blunt-tip needles of 2.54 cm in length and 159 µm in diameter were employed to fabricate fibers with smaller diameters, because a needle length of 3.81 cm was not available for this diameter. All photopolymerized fibers were formed at a constant light intensity of 1160 mW/cm^2, measured by a radiometer (Coherent Field Max II) in the same plane as the orifice outlet, and a spin speed of 2500 rpm (unless otherwise specified in Section 3.3.2). For PA6-formic acid solution state centrifugal spinning, the spinning procedure was essentially identical to the aforementioned method, except no light source was used. The spin speed was held constant at 4500 rpm (unless otherwise specified in Section 3.3.2).

3.2.5 Flow rate measurement

The single orifice flow rates were measured by precisely weighing the spinneret containing the desired feed before and after the spinning process. The spin times ranged between 30 and 180 seconds to ensure accurate measurements of the flow rates. The spin time was determined to be long enough to minimize the effects of cycle initiation and termination, but short enough to prevent the spinneret from being starved of feed during the spinning cycle. This is important because in centrifugal spinning, the hydrostatic pressure of fluid inside the spinneret can influence the feed delivery rate through the

orifice.[15] Therefore, to determine the change in flow rate as a function of spinning time, we conducted five consecutive fiber spinning runs of the same monomer mixture, each lasted one minute under identical conditions. The raw data are presented in **Table 3.1**. The total weight refers to the weight of the entire spinneret assembly, which includes the spinneret, the pair of Luer-lock blunt tip needles, and the monomer mixture inside the spinneret. In between each run, the total weight was measured and recorded. Note that the total weight after spinning is always slightly higher than the total weight before spinning on the subsequent run, because a new pair of Luer-lock blunt tip needles was used for each run, and there was monomer mixture left inside the discarded needles.

The weight of a clean spinneret with two new Luer-lock blunt tip needles was measured to be 312.201 g. The monomer mixture flow rate was calculated by subtracting the total weight after spinning from the total weight before spinning. The weight of monomer mixture left inside the spinneret was calculated subtracting the weight of needles and spinneret from the total weight before spinning to extract the total flow rate through both orifices. After dividing by two orifices per spinneret, the per orifice flow rate is obtained.

The average of the monomer mixture delivery rate between five consecutive runs is 0.113 ± 0.007 g/min, and there was no significant change in the monomer delivery rate as the fluid level inside spinneret and hydrostatic pressure decreases. Even when the spinneret is filled to 25% of its capacity, the solution delivery rate remains mostly constant. In addition, Mellado et al. also established a simple model to describe the fiber formation process of centrifugal spinning, and determined that the hydrostatic pressure is three orders of magnitude smaller than the centrifugal force at the orifice, and thus has negligible impact on jet initiation.[9] Therefore, the duration of spinning is very unlikely to have an impact on the monomer mixture or polymer solution delivery rate, as long as effects of cycle initiation

and termination are minimized, and the spinneret is not starved of feed during the spinning cycle.

Run	Total Weight Before Spinning (g)	Total Weight After Spinning (g)	Flow Rate (g/min)	Weight of Monomer Left in Spinneret (g)
1	314.343	314.117	0.113	2.142
2	313.991	313.787	0.102	1.812
3	313.592	313.368	0.112	1.393
4	313.175	312.936	0.120	0.961
5	312.775	312.538	0.118	0.563

Table 3.1: Monomer mixture delivery rate as a function of remaining fluid level inside the spinneret. Reprinted with permission from Ref. [23]. Copyright © 2016 Elsevier Ltd.

3.2.6 Material characterization

Viscosities of feed materials were measured by a shear rheometer (TA instruments AR-2000 EX). Frequency sweeps were performed from 0.1 to 10 rad/s with 5% strain in the linear viscoelastic regime. Elasticities of the monomer mixtures were measured by a capillary breakup extensional rheometer (CaBER, Thermo Haake CaBER 1) equipped with parallel plates 4 mm in diameter. The laser micrometer of CaBER recorded the filament diameter evolution over time at 1000 Hz. Five measurements were taken for each monomer mixture. The time evolution of filament diameter was fit to an elastic fluid model to obtain the fluid relaxation time.[24]

The density of the monomer mix was determined to be 1.15 g/cm^3 by measuring the weight of a known volume of the solution. The surface tension was determined to be

40.93 mN/m using an axisymmetric pendant droplet of the monomer mix with methods described previously.[25] To avoid curing of monomers in ambient light during measurement, photoinitiator was not added in the mixtures used for these characterizations.

3.2.7 Fiber diameter characterization

Fiber morphologies were examined by scanning electron microscopy (SEM, Hitachi S-5500). ImageJ (National Institutes of Health) was used to measure the diameters of the fibers. For every fiber sample, 15 to 20 SEM images were taken and more than 150 counts of fibers were measured to provide a representative statistical analysis of fiber diameter. Fiber diameters were fit to log-normal distributions as previously described [26-27].

3.2.8 Thermal characterization

Thermogravimetric analysis (TGA, Mettler Toledo TGA/DSC 1) was used to determine the residual EA content in the fiber. TGA measurements were conducted immediately after fibers were fabricated. The fibers were heated to 1000 ^{o}C at 10 ^{o}C/minute in a Nitrogen atmosphere.

3.3 Results and Discussion

3.3.1 Effect of viscosity and orifice diameter on average fiber diameter

In this section, a spin speed of 2500 rpm was employed because it provided both a sufficient centrifugal force for fiber formation and adequate fiber flight time for solidification by photopolymerization. This allows access to a relatively wide processing window for testing a range of monomer feed viscosities and orifice diameters.

Figure 3.1 displays the photographs of the entire fiber mats, while **Figure 3.2** displays collages of SEM images, in which fibers were formed using different orifices (337 μm, 260 μm, or 210 μm) and monomer feed viscosities controlled by varying non-reactive

EA diluent between 0 and 18 wt%. Fiber mats containing large filaments (i.e., roughly equal to or greater than 10 μm in diameter), uniform and well cured fibers, and fibers with fused junctions were obtained. This matrix of conditions demonstrates that the fiber morphology can be manipulated by controlling either the viscosity or the orifice size independently, or tailoring them in concert. In the upcoming section, the effects of the two individual parameters and the interactions between them in defining the final fiber morphology and diameter distribution will be the focus.

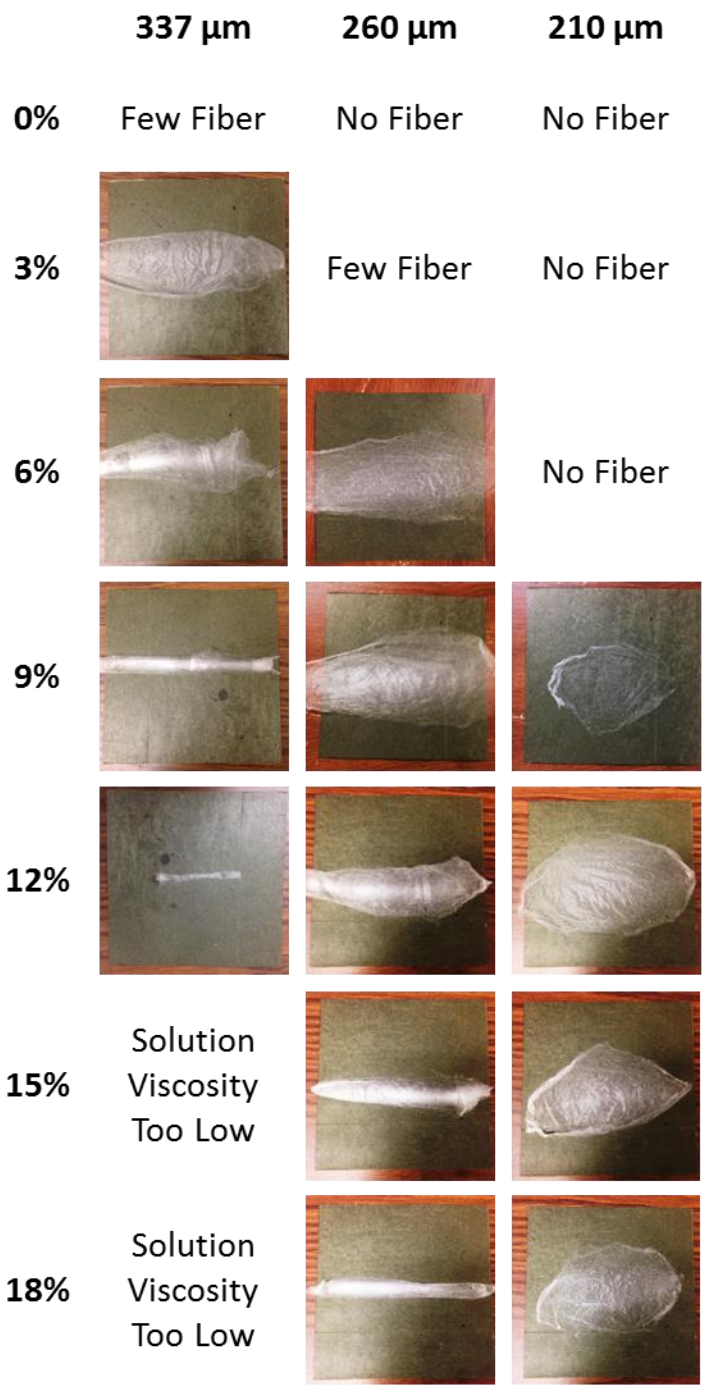

Figure 3.1: SEM images of fibers made from monomer feeds containing various amounts of EA (ranging from 3 wt% to 18 wt%) and different orifice diameters (337 µm, 260 µm, and 210 µm). The dark green background is 15 cm x 15 cm. Reprinted with permission from Ref. [23]. Copyright © 2016 Elsevier Ltd.

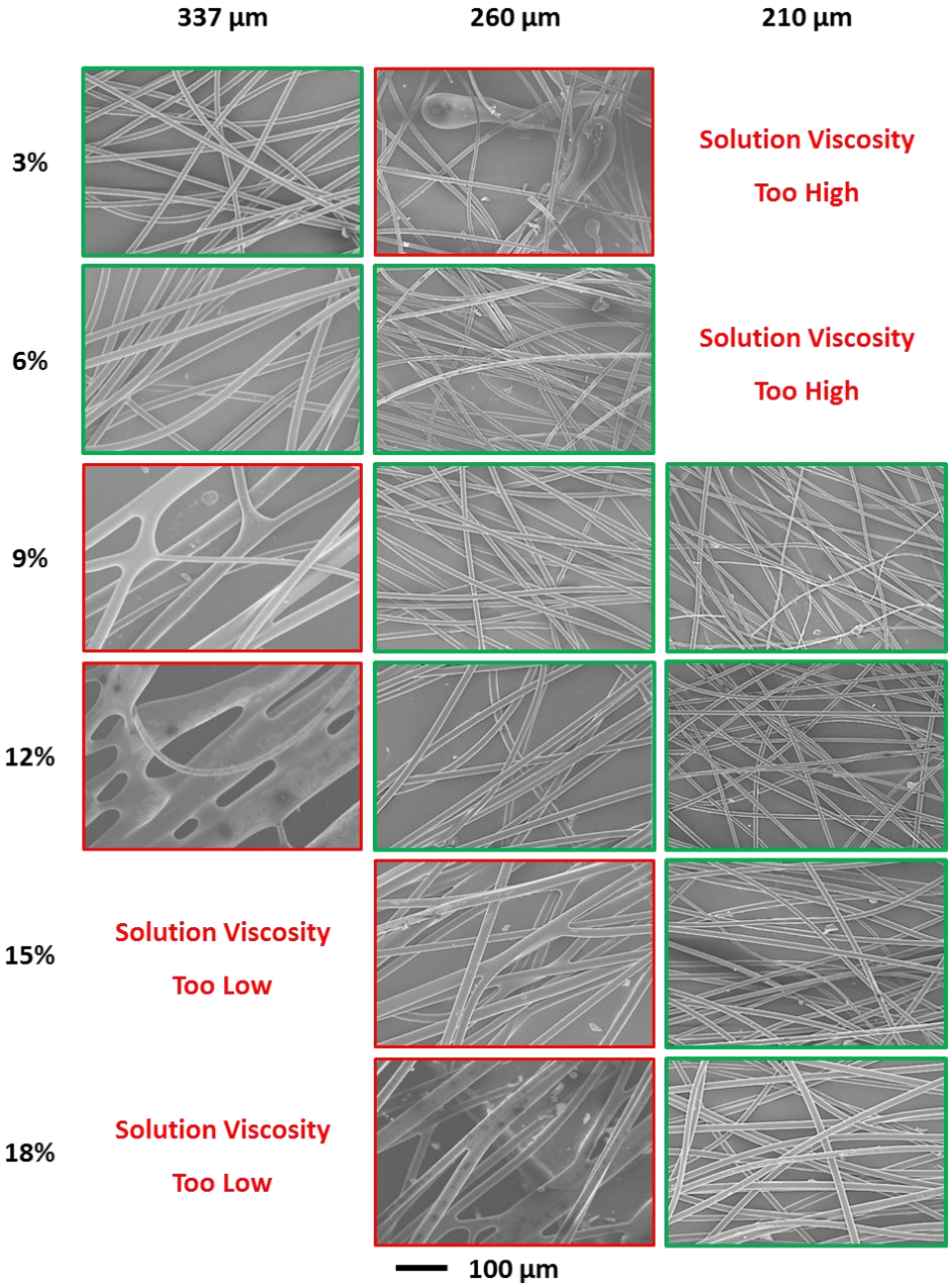

Figure 3.2: Representative SEM images of fibers made from monomer feeds containing various amounts of EA (ranging from 3 wt% to 18 wt%) and different orifice diameters (337 µm, 260 µm, and 210 µm). Images with green frames indicate conditions that formed defect free fibers, while images with red frames indicate conditions that formed fused fibers or unstretched fibers. The 100 µm scale bar applies to all images. Reprinted with permission from Ref. [23]. Copyright © 2016 Elsevier Ltd.

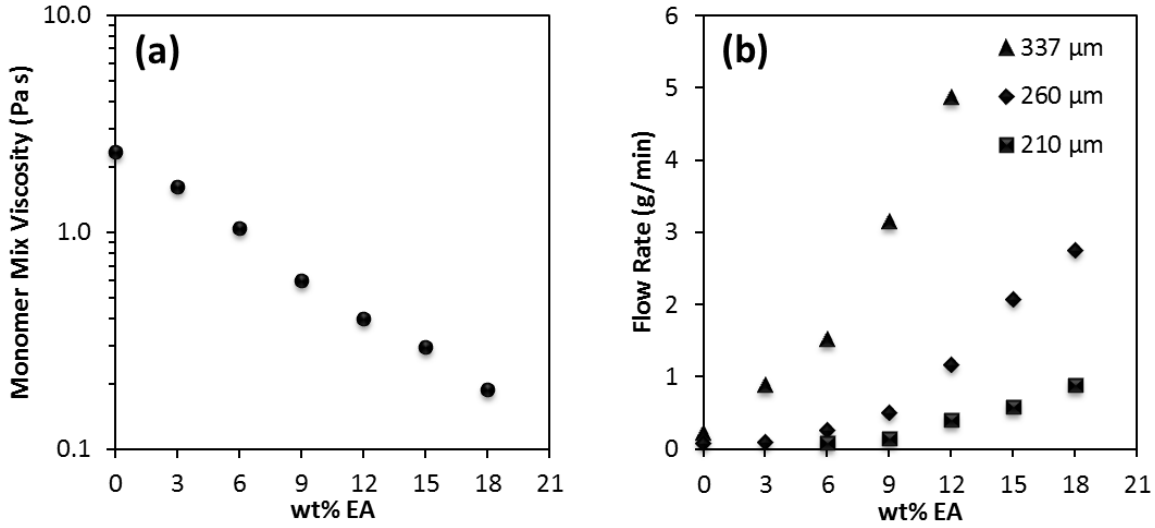

Figure 3.3: (a) Viscosities and (b) single orifice delivery rates of monomer feed mixtures containing various amounts of EA. Reprinted with permission from Ref. [23]. Copyright © 2016 Elsevier Ltd.

The viscosities of the monomer feed mixtures containing different amounts of EA are shown in **Figure 3.3 a**, while the flow rates through the orifices at various spinning conditions (varying wt% EA and orifice diameter) are shown in **Figure 3.3 b**. It is expected that for any given monomer mixture, the flow rate is higher with increasing orifice diameter. It is also expected that the flow rate increases with increasing wt% EA (i.e., decreasing mixture viscosity) for any given orifice diameter. This can be rationalized by considering the viscous resistance to flow, which acts against the outwardly directed capillary force and centrifugal force as the monomer mixture travels along the narrow and long needle/capillary toward the orifice opening, is reduced for lower viscosities and larger orifices. It should also be noted that the effect of viscosity on flow rate is more profound for larger orifices, indicated by the steeper slope of the flow rate curve as orifice diameter increases from 210 µm to 337 µm.

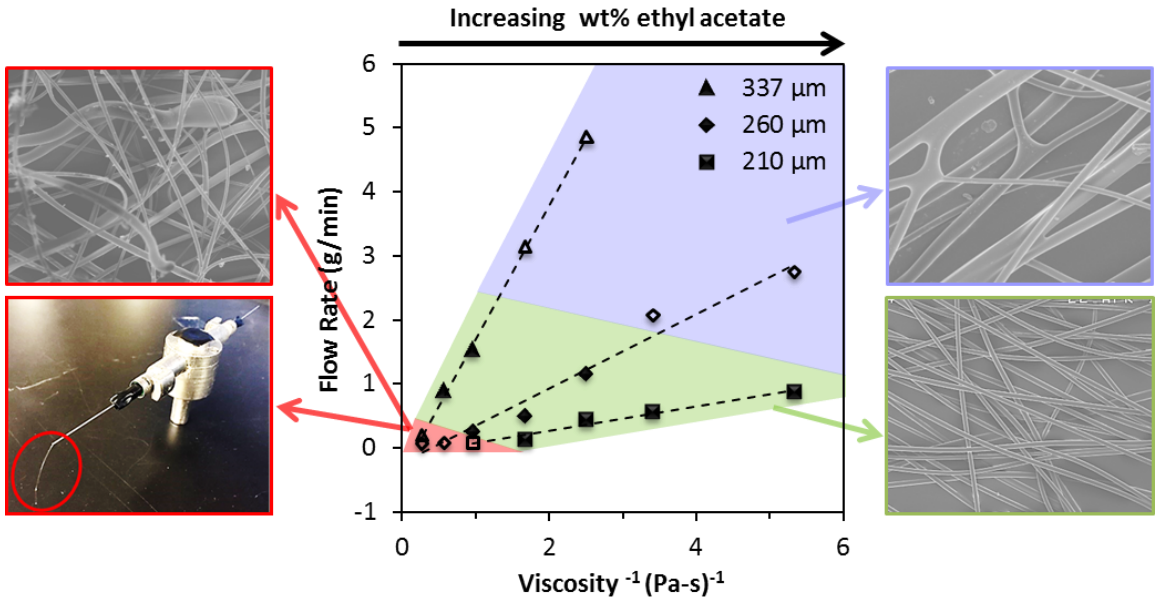

Figure 3.4: Data of Figure 3.3 plotted as monomer mix flow rate versus inverse of its viscosity. The red, green, and purple areas correspond to a flow rate that is too low, close to optimal, and too high, respectively, to form continuous and defect-free fibers at this particular spin speed. The solid symbols represent conditions where defect free fibers were made, and open symbols represent conditions where the resultant fibers contained defects or no fiber could be made. The SEM images and photograph shows typical fiber morphologies in each regime. Reprinted with permission from Ref. [23]. Copyright © 2016 Elsevier Ltd.

In **Figure 3.4**, data from **Figure 3.3** are replotted as flow rate versus the inverse of viscosity. The flow rates are clearly linearly proportional to the inverse of viscosity. This behavior (i.e., liquid flow through a long and narrow tube) is analogous to pressure driven capillary flow, where a liquid is forced through a capillary of known diameter under a fixed pressure drop and its flow rate is measured. The viscosity of the fluid can be described and measured by the following:

$$\eta = \frac{\Delta P R^4}{8QL}$$

where η is the viscosity of the fluid, ΔP is the applied pressure drop, R and L are the radius and length of the capillary, and Q is the fluid flow rate through the capillary. In centrifugal spinning, the fluid flow through the needle capillary during the jet initiation stage is similar to that in pressure driven capillary flow, where the centrifugal force and the hydrodynamic pressure can be combined and considered as an effective pressure drop, ΔP. Although the above equation is appropriate for a Newtonian fluid in a capillary, the monomer mixtures in this case contain such low concentrations of polymer that they can essentially be considered near-Newtonian fluids for this analysis. Using this relationship, it is therefore expected that at the same spin speed and orifice diameter, the flow rate and the viscosity are inversely proportional to each other and this was the motivation for plotting **Figure 3.4** in this manner.

The final fiber morphologies corresponding to the data in **Figure 3.4** can be categorized into three regimes. In the first regime shaded red in **Figure 3.4** (also corresponds to the upper right corner in **Figure 3.1** and **3.2**), either no fiber was formed or the fiber mat contained significant amounts of large filaments around 10 μm in diameter or larger. Both scenarios are results of the monomer mixture being too viscous. In the first case, the centrifugal force was insufficient to overcome the capillary force and surface tension of the monomer mixture, and therefore very little monomer was delivered through the orifice. This can be confirmed by flow rates that were close to zero. In the latter scenario, the centrifugal force exceeded the surface tension and stretched the exiting monomer into filament jets, but failed to overcome the viscous and elastic stresses, which act to stabilize the filament and resist further jet thinning. As a result, the initial thick filament jet either remained attached to the spinneret orifice, indicated by the red circle in the lower left photograph of the spinneret in **Figure 3.4**, or was disengaged from the spinneret (possibly facilitated by the action of centrifugal forces) and deposited in the fiber

mat as shown in the upper left SEM micrograph in the same figure. These phenomena have been reported in other spinning methods previously, and such spinning mixtures have been commonly referred to in the literature as 'having poor spinnabilty' due to an excessively high viscosity.[28-29]

In the shaded green region in **Figure 3.4** (also corresponds to the center images in **Figure 3.1** and **3.2**), the fibers were relatively uniform and well cured. The monomer mixture viscosity was well-matched with the selected orifice size to provide moderate material delivery rate through the orifice. The randomness of the fiber orientations in the mat shown in the SEM image also suggests that fibers may have undergone a sufficient amount of whipping during processing and lay down on the collector. It is also worth noting that the optimal flow rates for this photocurable system are up to 100 g/hour per orifice, which is one to two orders of magnitude higher than most solution state bench-scale electrospinning conditions reported in the literature.[19, 25, 29-30]

In the shaded blue region in **Figure 3.4** (also corresponds to the left bottom corner images in **Figure 3.1** and **3.2**), the process becomes limited by the reaction kinetics; because fibers did not completely cure before being deposited onto the collector they form fused fibers. It is anticipated that the low viscosity and high flow rates in this regime also produce high fiber flight velocities leading to insufficient total flight time for the fibers to cure. In addition, the fibers that were produced in this regime appeared to be much more aligned along the spinning direction. This is an indication that the monomer jets exit the orifice with a high linear velocity along the orifice axis and are directly deposited onto the collector without whipping, unlike the more randomly oriented fibers in the green regime of **Figure 3.4**.

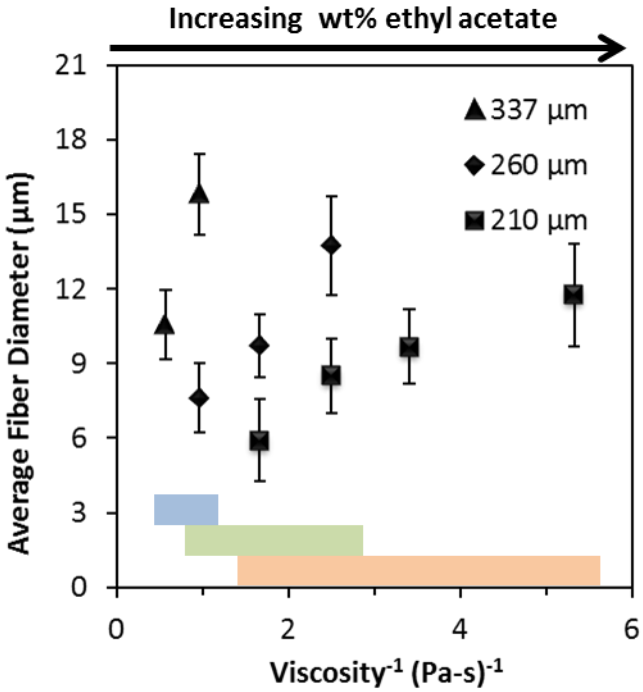

Figure 3.5: Average diameters of fibers made from monomer mixtures containing various amounts of EA and different orifice sizes as a function of inverse monomer mix viscosity. The blue, green, and orange tiles indicate the optimal viscosity range for orifice diameters of 337 µm, 260 µm, and 210 µm, respectively. The error bars represent the standard deviations of the fiber diameter distributions. Reprinted with permission from Ref. [23]. Copyright © 2016 Elsevier Ltd.

Figure 3.5 shows the average diameters and standard deviations of fiber diameters produced from monomer mixtures with different viscosities and from three different orifice sizes. Average fiber diameter clearly increases with increasing orifice diameter. This is expected because more monomer can be delivered through a larger orifice while holding centrifugal force (i.e., correlated to spin speed) constant. Under conditions where there is a similar extent of drawing, the fibers with larger initial fiber diameters would also have larger final fiber diameters.

There is an optimal viscosity window for each orifice size, labeled by the blue, green, and orange bars for orifices with 337 µm, 260 µm, and 210 µm diameters,

respectively. Further, the suitable monomer viscosity range is narrower for larger orifices, because the flow rates of liquids through larger orifices have a stronger dependence on viscosity, as demonstrated previously in **Figure 3.4**.

In addition, **Figure 3.5** shows that holding orifice size constant but increasing the amount of EA diluent increases fiber diameter. This is contrary to the common knowledge of polymer-solvent solution state spinning, regardless of whether the process is electrospinning, centrifugal spinning, or blow spinning, where increasing the amount of solvent or decreasing polymer concentration typically generates fibers with smaller diameters.[14, 28, 31-33] As will be discussed shortly, this is most likely because a significant portion of fiber thinning during processing of a polymer-solvent solution (e.g., 70-95 wt% solvent) is due to solvent evaporation.

Even more interestingly, the average fiber diameters of the three spinning series with different orifice diameters in **Figure 3.5** collapse into a single master curve when plotted against flow rate as shown in **Figure 3.6**. This shows that when the spin speed was kept constant, fiber diameter can be practically determined by the flow rate, regardless of solution viscosity or orifice size.

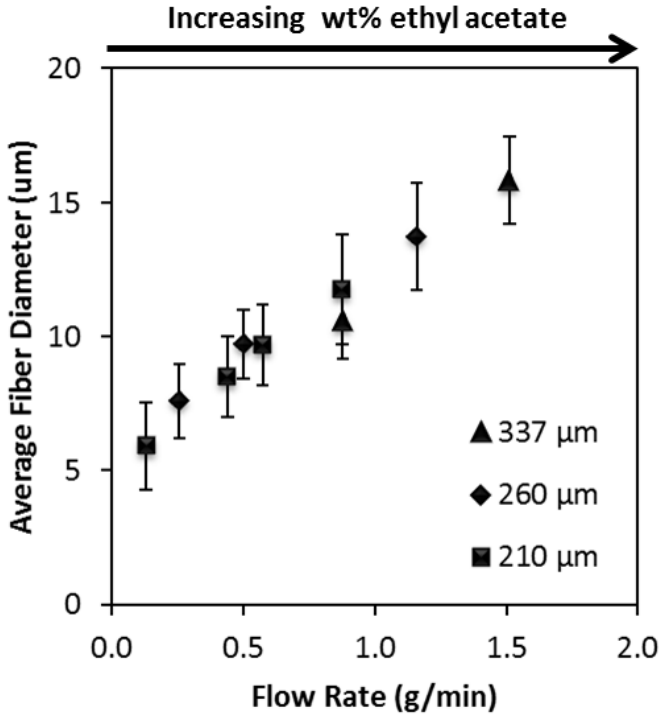

Figure 3.6: Master curve of average fiber diameter plotted against flow rate made from monomer mixtures containing various amounts of EA and using different orifices. All runs were conducted at 2500 rpm. The error bars represent the standard deviations of the fiber diameter distributions. Reprinted with permission from Ref. [23]. Copyright © 2016 Elsevier Ltd.

PA6-formic acid solutions with viscosities similar to the photocurable monomer mixtures were processed using centrifugal spinning to compare the factors affecting fiber diameter in the photocurable system to a conventional polymer-solvent solution system. The spin speed was kept at 4500 rpm to provide sufficient centrifugal force for drawing the PA6-formic acid solutions while maintaining a reasonably wide processing window that resulted in defect free fibers. The SEM images of fiber samples obtained from various spinning conditions are presented in **Figure 3.7**. The viscosity and flow rates measurements are shown in **Figure 3.8 a** and **b**, respectively.

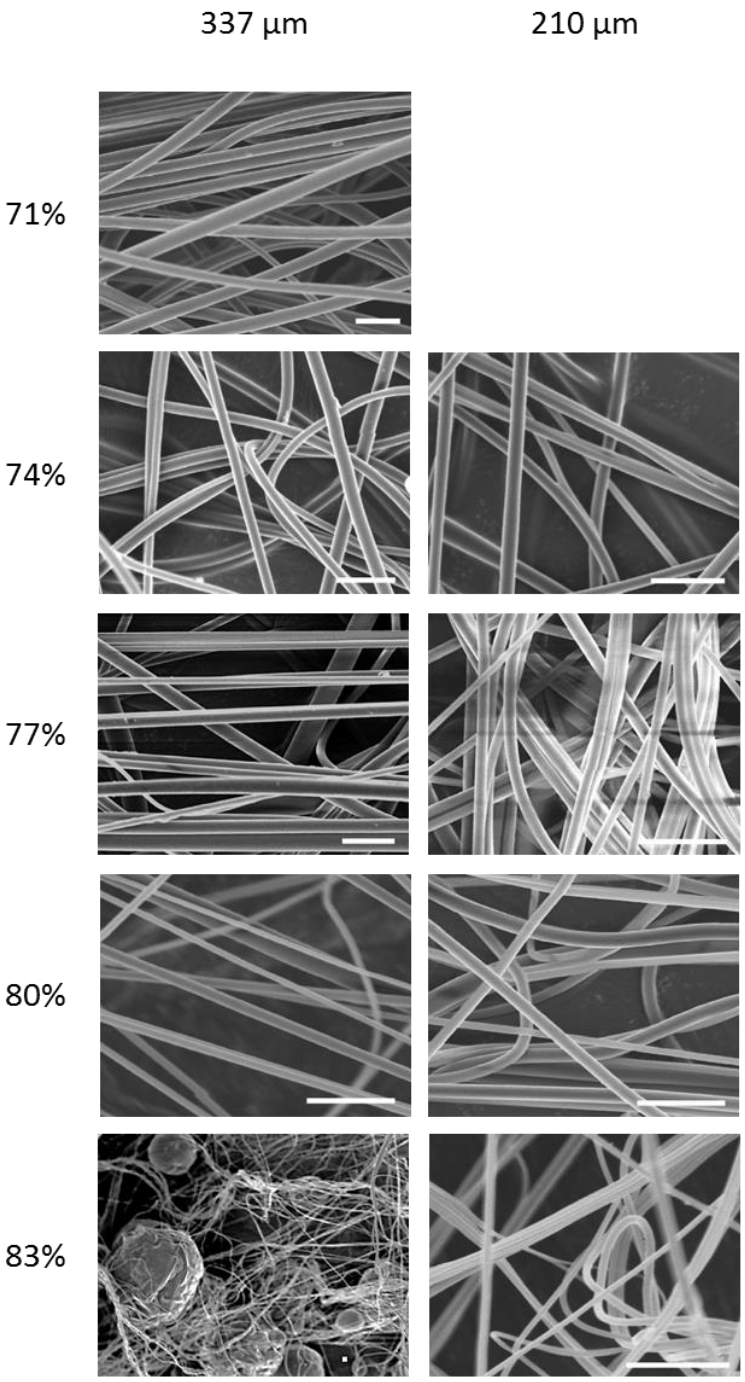

Figure 3.7: SEM images of PA6 fibers made from various concentrations of PA6-formic acid solutions and orifices with two different diameters. The scale bars in this figure represent 5 µm. Reprinted with permission from Ref. [23]. Copyright © 2016 Elsevier Ltd.

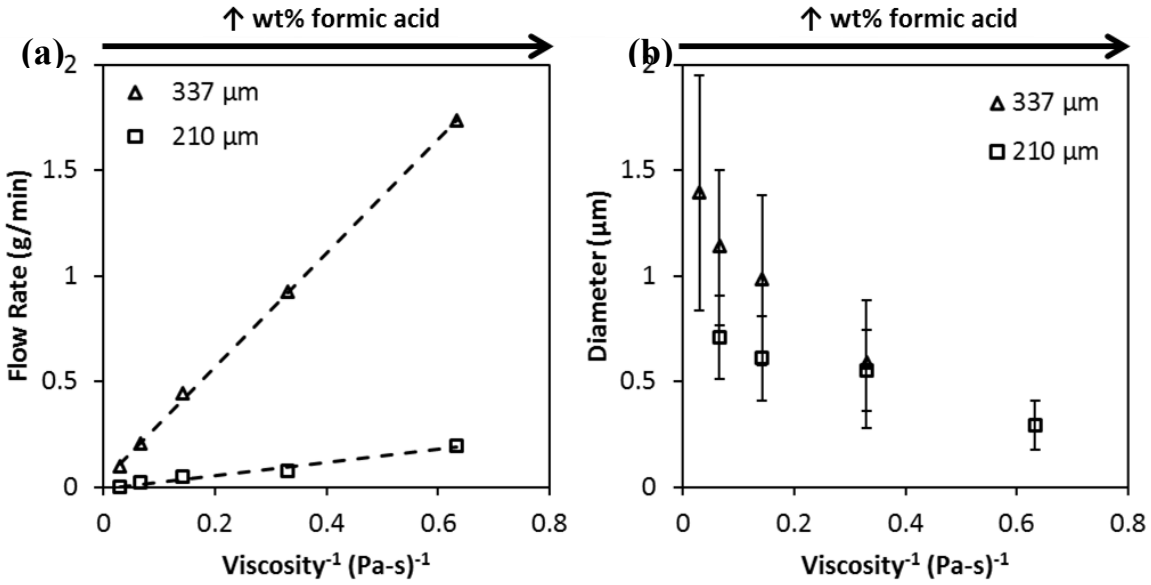

Figure 3.8: (a) Delivery rates of and (b) average diameters of fibers made from PA6-formic acid solutions containing various amounts of formic acid and different orifice sizes as a function of inverse monomer mix viscosity. The error bars in (b) represent the standard deviation of the fiber diameter distribution. Reprinted with permission from Ref. [23]. Copyright © 2016 Elsevier Ltd.

Figure 3.8 a shows that the delivery rates of PA6-formic acid solutions are linearly proportional to the inverse of solution viscosity. This behavior is analogous to pressure driven flow through a capillary. Further, as shown in **Figure 3.8 b**, average fiber diameter decreases with increasing formic acid content (or decreasing PA6 concentration) and decreasing viscosity. This trend is expected and has been previously reported in numerous conventional polymer-solvent solution spinning papers regardless of fiber spinning technique (electrospinning, free surface electrospinning, centrifugal spinning, etc.).[17, 28, 32-33]

Figure 3.9 shows the fiber diameter distributions of PA6 fibers processed from solutions with different viscosities using two different orifice diameters as a function of the flow rate. Comparing **Figure 3.6** and **3.9**, two contrasting trends can be observed for

photocurable and solution state centrifugal spinning. First, as flow rate increases, the average fiber diameter increases for the photocurable system, but decreases for the PA6-formic acid system. Second, the fiber diameters of the photocured fibers depend solely on the flow rate through the orifices, whereas the average fiber diameters of fibers processed from 210 um diameter orifices were three to four times smaller than those from 337 um diameter orifices at the same flow rate.

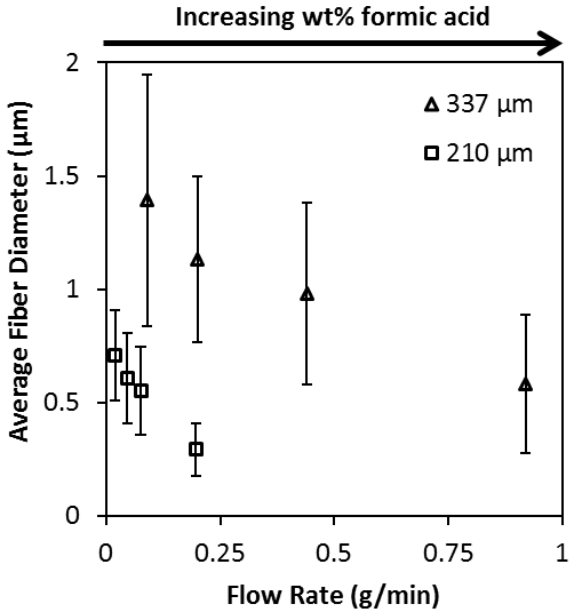

Figure 3.9: Average fiber diameter produced from PA6-formic acid solutions (71-83 wt% formic acid, at increments of 3 wt%) plotted against flow rate. The error bars represent the standard deviations of the fiber diameter distributions. Reprinted with permission from Ref. [23]. Copyright © 2016 Elsevier Ltd.

These trends can be mainly attributed to the fundamentally different fiber solidification mechanisms of the two systems. In the photocurable system, the solidification is mainly driven by photopolymerization. Although the monomer mixtures contain some solvent, the amount is small enough (<18 wt% as compared to 70-95 wt% used in typical solution state fiber processing) that the effect of solvent evaporation on fiber

diameter reduction is minimal. This is evidenced by the residual amounts of EA in the final fiber product, measured by TGA as shown in **Figure 3.10**.

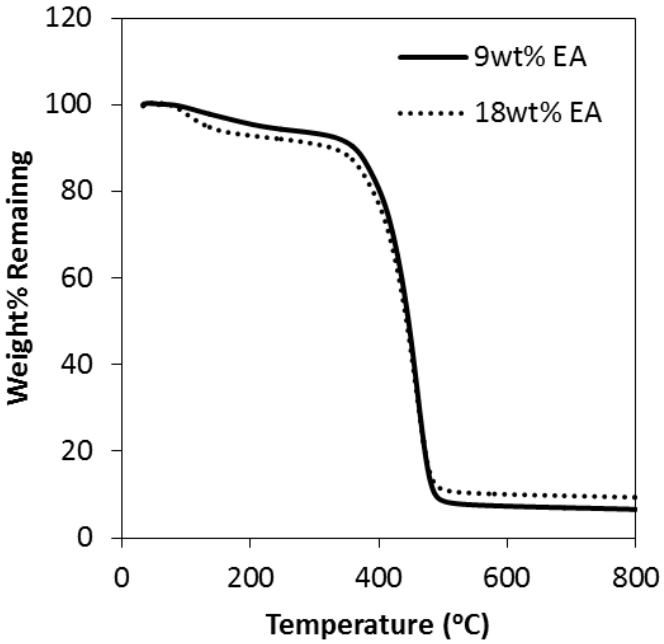

Figure 3.10: TGA traces of fiber mats made from monomer mixtures containing 9 wt% and 18 wt% EA. Reprinted with permission from Ref. [23]. Copyright © 2016 Elsevier Ltd.

TGA thermograms of fiber mats made from monomer mixtures with 9 wt% and 18 wt% EA indicate that they had 5% and 9% weight loss below 200 ^{o}C, respectively. Such weight loss can be largely attributed to residual EA in the fibers, which can be removed by holding samples under vacuum overnight. This experiment also shows only approximately half of the diluent in the monomer mixture was evaporated during fiber spinning. Such a small amount of EA evaporation was clearly insufficient to account for any significant reductions in fiber diameter as observed here. Therefore, as EA content increases, the increase in monomer mix flow rate strongly dominates any filament thinning due to solvent evaporation, leading to an overall increase in final fiber diameter. For this reason, the

photocurable fiber process more closely resembles a melt state fiber process, where fiber diameters are strongly dependent on melt delivery rate and the ratio between material delivered through the orifice and fiber drawing force applied.[16, 26, 34-35]

Alternatively, in polymer-solvent solution state fiber spinning, fiber solidifies following sufficient solvent evaporation. Solutions containing more solvent take longer to evaporate to a point that results in solidification, thereby rendering more time for the fluid jets to be drawn. In addition, solutions containing more solvent may undergo additional thinning due to reduced viscous stresses even before solvent evaporation takes place.[14] In total, as solvent content increases, the enhanced thinning of fibers due to solvent evaporation and lower viscosity overwhelms the incremental increase of solution delivery rate as shown in **Figure 3.8**, generating smaller fibers. Numerous reports concerning centrifugal spinning or electrospinning of a variety of polymer-solvent systems have commented on polymer concentration as the most important process parameter on impacting fiber formation and fiber diameter distribution.[17, 28, 36-38]

3.3.2 Effect of spin speed

To investigate the impact of spin speed on fiber diameter and distribution, spin speed was varied from 1500 to 6500 rpm for photocurable monomer mixtures and from 2500 to 10500 rpm for PA6-formic acid solutions. The diluent content was 12 wt% EA and 80 wt% formic acid for the photocurable monomer mixture and the polymer-solvent solution, respectively. The orifice diameter was kept constant at 210 μm.

Figure 3.11 shows SEM images of photocured fibers processed at various spin speeds from the same monomer mixture. Below 1500 rpm, no fiber was formed, because the centrifugal force did not sufficiently exceed the surface tension and capillary force of the exiting liquid at the orifice outlet, and no monomer was delivered through the orifices

as a result. From 1500 to 5500 rpm, fibers were produced without defects, indicating the centrifugal force at this spin speed is strong enough to consistently deliver solution through the orifices. This range of spin speeds also provides sufficient flight time for the fibers to cure completely.[20] At 6500 rpm and above, the fibers passed through the UV exposed region too rapidly and did not completely solidify before being deposited onto the collector, forming fused fiber junctions.

For comparison, PA6 solution containing 80 wt% formic acid was processed at spin speeds ranging from 2500 to 10500 rpm at increments of 2000 rpm. SEM images of the resulting samples revealed that fibers were free of defects in this operating window, and the images are presented in **Figure 3.12**.

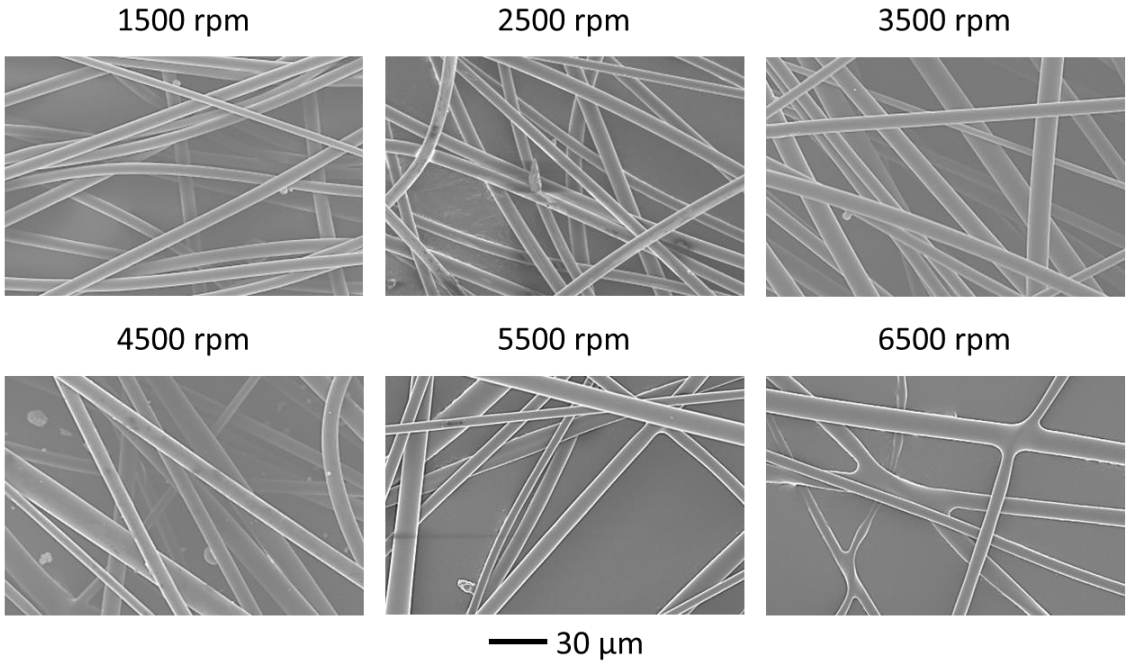

Figure 3.11: SEM images of photocured fibers made at various spin speeds ranging from 1500 to 6500 rpm. The monomer mixture contained 64 wt% 5A, 19 wt% 4T, 12 wt% EA, 5 wt% Irgacure 2100 and 190 ppm high MW PEO, and was processed from 210 µm diameter orifices. The 30 µm scale bar applies to all images in this figure. Reprinted with permission from Ref. [23]. Copyright © 2016 Elsevier Ltd.

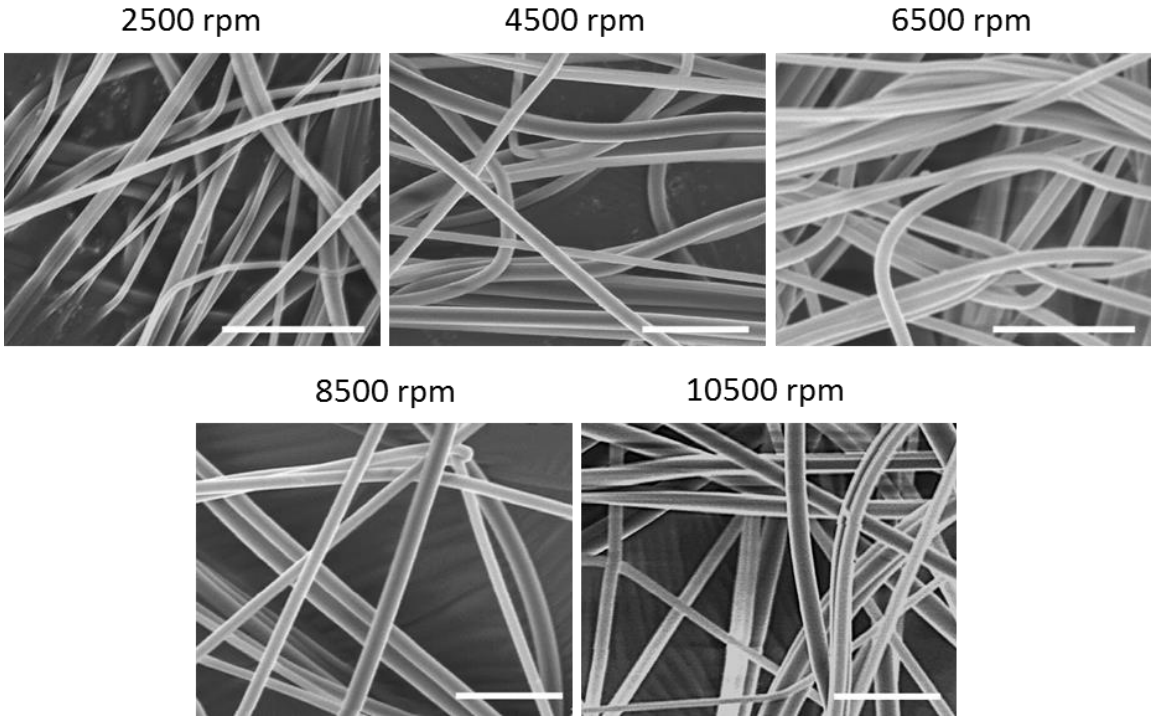

Figure 3.12: SEM images of PA6 nanofibers made at various spin speeds ranging from 4500 to 10500 rpm. The polymer solution contained 20 wt% PA6 and 80 wt% formic acid. All scale bars in this figure represent 5 μm. Reprinted with permission from Ref. [23]. Copyright © 2016 Elsevier Ltd.

Fiber diameter analysis was performed on all defect free fiber samples and the distributions were fit to a log normal function as previously described.[26] Sample log normal fits to photocured fiber diameter distributions are also provided in **Figure 3.13**. For all fiber samples, the average and median of fiber diameters are nearly equal, indicating that the distribution of fibers produced by centrifugal spinning approximately follows a log-normal distribution. This is in good agreement with previous studies on solution or melt state centrifugal spinning.[16, 26, 39] In this chapter, all fiber diameter distributions were fit to log-normal functions in this manner. Flow rate measurements and parameters of log normal distribution fitting are summarized in **Table 3.2** (photocurable) and **Table 3.3** (PA6-formic acid).

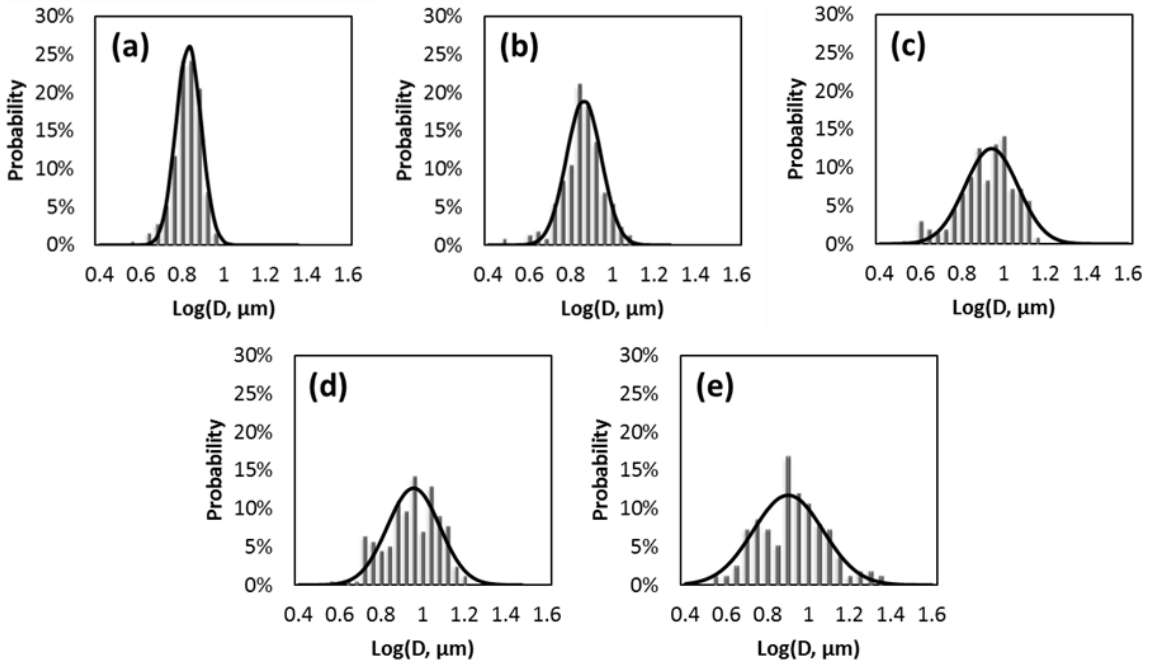

Figure 3.13: Fiber diameter distributions of photocured fibers processed at spin speeds of (a) 1500, (b) 2500, (c) 3500, (d) 4500, and (e) 5500 rpm presented on logarithmic scales. The black lines show the respective best fit normal distribution to log(D). Reprinted with permission from Ref. [23]. Copyright © 2016 Elsevier Ltd.

Spin Speed (rpm)	Flow Rate (g/min)	d_{av} (µm)	µ	σ	Med[log(D)]	X_c	δ	R^2
1000	0	No fiber formed.						
1500	0.13	6.38 ± 0.92	0.80	0.07	0.80	0.83	0.06	0.99
2500	0.39	7.00 ± 1.55	0.83	0.10	0.84	0.86	0.08	0.96
3500	0.65	8.21 ± 2.32	0.90	0.13	0.91	0.94	0.13	0.91
4500	1.26	8.79 ± 2.54	0.92	0.13	0.94	0.96	0.14	0.85
5500	1.80	8.56 ± 3.44	0.90	0.17	0.90	0.90	0.17	0.84
6500	2.13	Fibers were fused.						

Table 3.2: Flow rates and fiber diameter distribution of photocured fibers made at various spin speeds. Reprinted with permission from Ref. [23]. Copyright © 2016 Elsevier Ltd.

Spin Speed (rpm)	Flow Rate (g/min)	d_{av} (μm)	μ	σ	Med[log(D)]	X_c	δ	R^2
2500	0.03	0.42 ± 0.19	-0.41	0.19	-0.40	-0.38	0.21	0.85
4500	0.09	0.51 ± 0.20	-0.32	0.15	-0.32	-0.32	0.17	0.93
6500	0.20	0.55 ± 0.23	-0.29	0.17	-0.32	-0.29	0.17	0.85
8500	0.46	0.68 ± 0.25	-0.19	0.15	-0.19	-0.17	0.13	0.91
10500	0.73	0.71 ± 0.26	-0.17	0.15	-0.18	-0.16	0.15	0.94

Table 3.3: Flow rates and fiber diameter distribution of PA6 fibers made at various spin speeds. Reprinted with permission from Ref. [23]. Copyright © 2016 Elsevier Ltd.

Figure 3.14 and **Figure 3.15** show the fit log-normal diameter distribution functions for photocurable and PA6-formic acid fibers, respectively, processed at various spin speeds. For both systems, although the material flow rate increases by over an order of magnitude over the range of spin speeds, the average fiber diameter increases consistently but still remains within one standard deviation. This can be understood as the result of two concurrent phenomena unique to centrifugal spinning. As spin speed increases, the centrifugal force delivers more material through the orifice, forming liquid jets with larger initial diameter which translates to a larger final diameter. On the other hand, the larger centrifugal force also enhances fiber thinning, leading to a smaller final fiber diameter. The coupled but opposite effects of material delivery and fiber drawing by centrifugal force eventually lead to only subtle changes in average fiber diameter. Similar trends in diameter progression as a function of spin speed have been previously observed by other researchers in both solution state and melt state centrifugal spinning.[14-16, 28, 40]

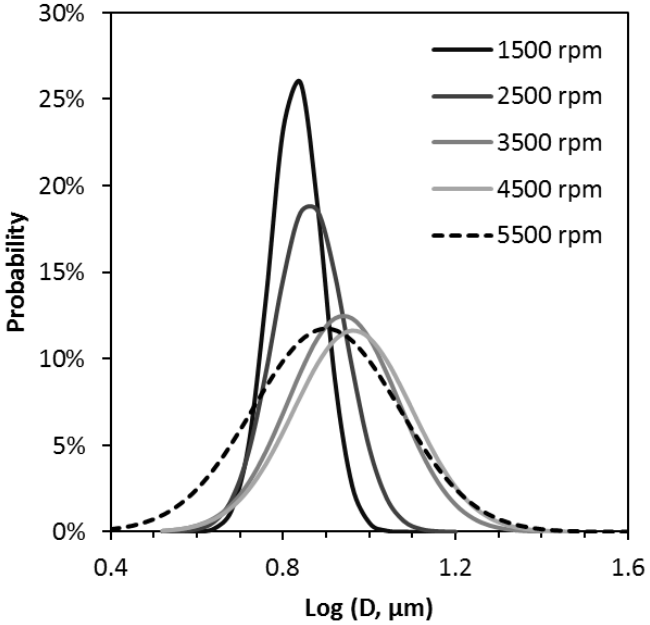

Figure 3.14: Fit log-normal distribution functions for photocured fibers processed at different spin speeds. Reprinted with permission from Ref. [23]. Copyright © 2016 Elsevier Ltd.

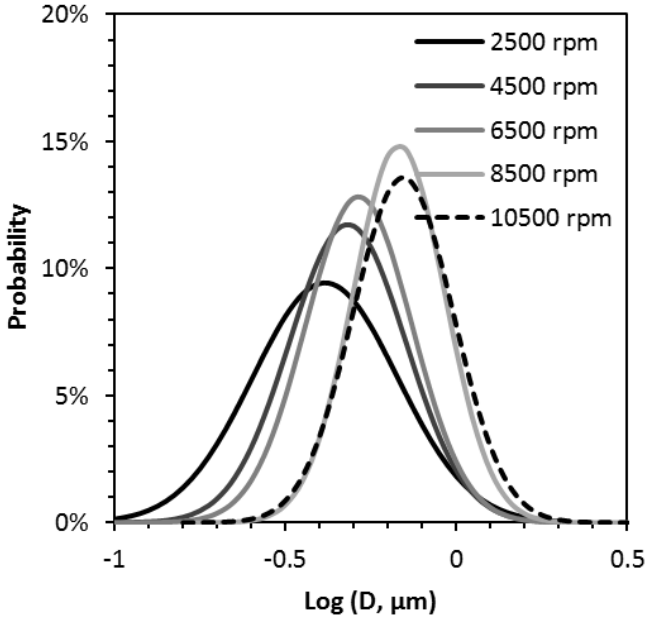

Figure 3.15: Fit log-normal distribution functions for PA6-formic acid based fibers processed at different spin speeds. Reprinted with permission from Ref. [23]. Copyright © 2016 Elsevier Ltd.

It is also worth noting that as spin speed increases, the width of fiber diameter distribution increases for photocured fibers, but decreases for PA6-formic acid based fibers consistent with other polymeric fibers produced by solution state centrifugal spinning.[14, 28] SEM images in **Figure 3.11** clearly show that thick fibers appear more frequently at higher spin speeds for the photocurable system. One possible conjecture is that at higher spin speeds, the monomer jets are first exposed to UV light earlier in their flight path and have less time to undergo thinning before photoreactions begin. However, it is presently difficult to definitively conclude the exact cause of this contrasting trend in the breadth of the fiber diameter distribution for these two systems. Unfortunately, there are not many existing studies to compare to because the majority report only the fiber morphology and average fiber diameter.

3.3.3 Effect of elasticity

In our previous report, it was shown that monomer mixture elasticity is crucial for fiber formation. Monomer mix elasticity, imparted by the addition of high MW PEO, helps stabilize liquid jets against surface tension driven Rayleigh instabilities and prevents formation of undesired morphologies such as fibers with non-uniform diameters, beads-on-string and droplets.[20] Others have also shown similar effects of elasticity in the formation of electrospun or melt blown fibers.[39, 41]

Despite its crucial role in fiber formation, we found that monomer elasticity has minimal influence on fiber diameter distribution. Four monomer mixtures with the exact same monomer, photoinitiator and diluent content, but containing 100, 200, 400, and 600 ppm of high MW PEO, were processed under the same conditions (spin speed = 2500 rpm, orifice diameter = 260 μm, light intensity = 1160 mW/cm^2) by centrifugal spinning to form defect free fibers. **Figure 3.16 a** shows that average diameters of fibers processed from the

four solutions are statistically the same. This result is unexpected, because the monomer jets with higher elasticity should possess higher resistance against self-thinning forming larger final fibers, all other parameters equal.

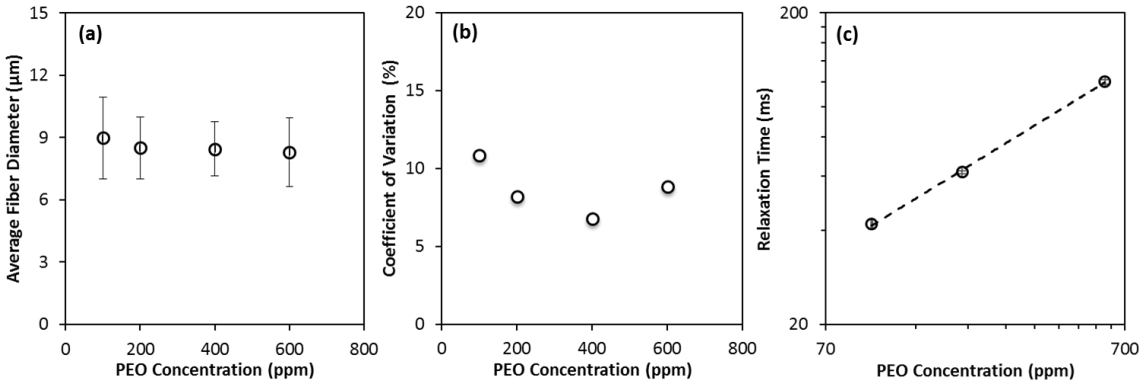

Figure 3.16: (a) Average diameter and (b) coefficient of variation of photocured fibers made from monomer mixtures containing 100, 200, 400, and 600 ppm high MW PEO. (c) Relaxation times of the monomer mixtures containing 100, 200, and 600 ppm high MW PEO. Reprinted with permission from Ref. [23]. Copyright © 2016 Elsevier Ltd.

This trend can be explained by the relative timescales of polymerization kinetics and self-thinning of monomer jets. As previously reported, gel time, the time it takes for the monomers to form an infinite network, is the relevant characteristic timescale of the polymerization kinetics. For the 5A-4T system, the gel time is around 1 millisecond at the specified light intensity in this study.[20] On the other hand, the fluid relaxation time is a timescale related to elasticity and it ranged between 30 and 100 milliseconds as shown in **Figure 3.16 c**. The dashed line indicates a power law fitting to the fluid relaxation times. The original CaBER data are presented in **Figure 2.11**. The polymerization timescale is one to two orders of magnitude smaller than the elasticity timescale, suggesting that monomer jets have very limited time to undergo thinning before solidification. Therefore,

the thinning behavior of monomer jets with different elasticities may not be drastically different during such a short timeframe.

The coefficient of variance presented in **Figure 3.16 b**, which describes the normalized width of the log normal distribution, was calculated as previously reported.[39] There is only a 6% maximum difference in the coefficient of variation (CV) across the entire range of PEO content, with the minimum CV occurring at 400 ppm PEO. Such a small change in the CV may be simply attributed to the relatively small range of solution relaxation times in this study. For example, Tan et al. reported a decrease in the CV of melt blown fibers from 60% to 10% when the fluid relaxation times of a polymer melt increased over five orders of magnitude.[39] Such a large range of elasticity is difficult to achieve in this system due to the limited solubility of PEO in 4T. Nonetheless, this analysis suggests that the optimal loading of PEO to achieve a narrow fiber distribution is around 400 ppm.

3.3.4 Smallest and largest fibers achieved

To demonstrate the tunability of this process, four representative samples with distinctive average fiber diameters and diameter distributions were fabricated by leveraging the results obtained from the previous sections and varying processing parameters such as the solution viscosity, orifice size, and spin speed. **Figure 3.17** compares the diameter distribution fit functions of the largest and smallest fibers. The process conditions and the fitting parameters are reported in **Table 3.4**, where μ and X_c are the measured and fit average of logarithmic diameter, σ and δ are the measured and fit standard deviation of logarithmic diameter, Med[log(d)] is the median of the fiber diameter distribution, and R^2 is the coefficient of determination. The SEM images of the corresponding fiber samples from **Figure 3.17** are presented in **Figure 3.18**.

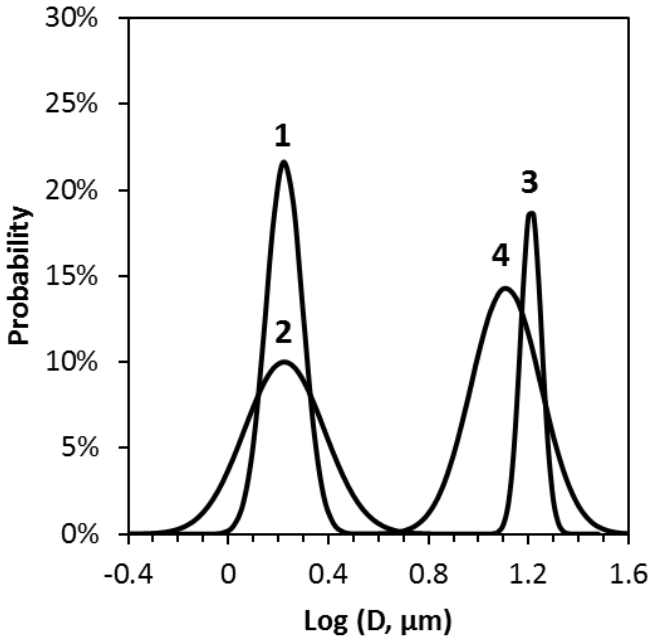

Figure 3.17: Smallest and largest fibers made by simultaneous photopolymerization and centrifugal spinning. The four different samples clearly indicate the tunability of the process with regards to both average diameter and width of the diameter distribution. Reprinted with permission from Ref. [23]. Copyright © 2016 Elsevier Ltd.

Run	wt% EA	Spin Speed (rpm)	Orifice Diameter (µm)	Orifice Length (inch)	d_{av} (µm)	µ	σ	Med [log(D)]	x_c	δ	R^2
1	12	1500	159	1	1.55 ± 0.37	0.18	0.11	0.19	0.22	0.07	0.97
2	12	3500	159	1	1.71 ± 0.61	0.21	0.15	0.20	0.22	0.16	0.97
3	6	2500	337	1.5	15.81 ± 1.63	1.20	0.05	1.20	1.21	0.04	0.96
4	6	4000	337	1.5	12.22 ± 4.01	1.06	0.15	1.07	1.11	0.14	0.96

Table 3.4: Process conditions and statistical analysis of the fiber diameter distributions for the smallest and largest thiol-ene fibers achieved in simultaneous photopolymerization and centrifugal spinning. Run numbers are correlated with **Figure 3.17**. Reprinted with permission from Ref. [23]. Copyright © 2016 Elsevier Ltd.

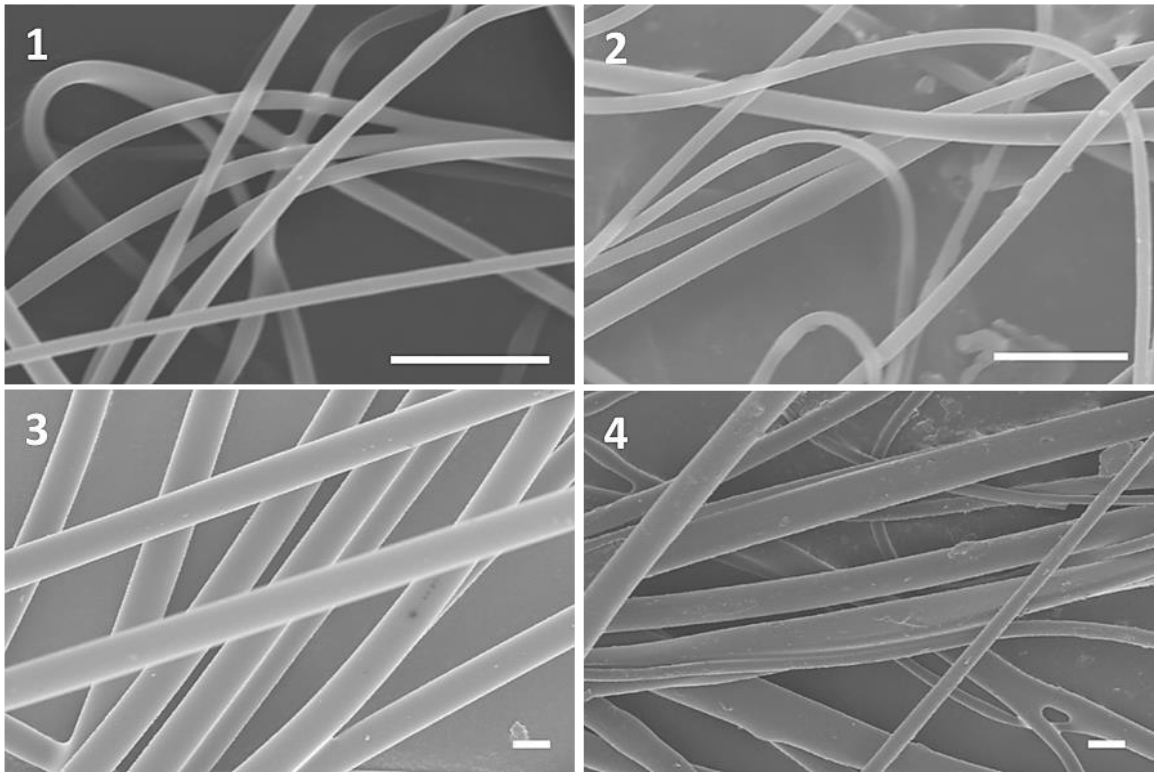

Figure 3.18: SEM images of finest and largest thiol-ene fibers achieved in centrifugal spinning. All scale bars in this figure represent 15 μm. Reprinted with permission from Ref. [23]. Copyright © 2016 Elsevier Ltd.

As shown in **Figure 3.17** and **Table 3.4**, the average fiber diameter and the width of the diameter distribution can be manipulated essentially independently. The average fiber diameters in this demonstration span across an order of magnitude, highlighting the processability and tunability of this fabrication method. By optimizing process variables, we were able to obtain fibers with average diameters just above one micron, comparable with the smallest nonwoven fibers made commercially by melt blowing methods.[26, 39, 42] In addition, it is worth noting that the smallest orifices used in this study are 0.15 mm in diameter, which are much larger than the orifices used in some studies that produce electrospun and melt blown submicron fibers.[43-44] The use of exceedingly small orifices

is often considered difficult in industrial settings because of orifice clogging by foreign materials such as dust particles (typically tens of microns in diameter).

3.4 CONCLUSIONS

In this chapter, we have investigated parameters affecting fiber quality and final fiber diameters in the simultaneous centrifugal spinning and thiol-ene photopolymerization process. It was found that monomer mix viscosity and orifice diameter have significant impact on monomer delivery rate through the orifice which ultimately affects the final fiber diameter. Spin speed influences the width of diameter distribution but not the average fiber diameter, which can be attributed to the coupled but opposite effects of centrifugal force on solution delivery and fiber drawing. Monomer mixture elasticity has minimal effect on fiber diameter and distribution despite its crucial role in fiber formation. In addition, we observed that the dominating factors in determining final fiber diameter are solution delivery rate for centrifugal spinning of photocurable monomer mixtures, but concentration of polymer for centrifugal spinning of polymer-solvent solutions. We believe such differences originate from the different mechanisms of fiber solidification in the two fiber fabrication methods.

Using parameters from this study, the average fiber diameter and the width of the distribution can be widely and independently tuned. The smallest photocured fibers fabricated in this study were approximately 1.5 μm in diameter, which is comparable to typical melt blown fibers. We believe the ability to precisely control fiber diameter distribution and fabricate fibers in the single-micron range demonstrates the potential of this technology as a scalable and tunable method for novel high performance fiber fabrication.

3.5 REFERENCES

1. Badami, A. S.; Kreke, M. R.; Thompson, M. S.; Riffle, J. S.; Goldstein, A. S., *Biomaterials* **2006,** *27* (4), 596-606.
2. Christopherson, G. T.; Song, H.; Mao, H.-Q., *Biomaterials* **2009,** *30* (4), 556-564.
3. Moroni, L.; Licht, R.; de Boer, J.; de Wijn, J. R.; van Blitterswijk, C. A., *Biomaterials* **2006,** *27* (28), 4911-4922.
4. Hassan, M. A.; Yeom, B. Y.; Wilkie, A.; Pourdeyhimi, B.; Khan, S. A., *Journal of Membrane Science* **2013,** *427*, 336-344.
5. Paul, D., *Journal of Applied Polymer Science* **1968,** *12* (10), 2273-2298.
6. Bhattarai, N.; Edmondson, D.; Veiseh, O.; Matsen, F. A.; Zhang, M., *Biomaterials* **2005,** *26* (31), 6176-6184.
7. Mahalingam, S.; Raimi-Abraham, B. T.; Craig, D. Q.; Edirisinghe, M., *Chemical Engineering Journal* **2015,** *280*, 344-353.
8. Li, X.; Chen, H.; Yang, B., *Carbohydrate Polymers* **2016,** *137*, 459-465.
9. Mellado, P.; McIlwee, H. A.; Badrossamay, M. R.; Goss, J. A.; Mahadevan, L.; Parker, K. K., *Applied Physics Letters* **2011,** *99* (20), 203107.
10. Ren, L.; Ozisik, R.; Kotha, S. P.; Underhill, P. T., *Macromolecules* **2015**.
11. Taghavi, S.; Larson, R., *Physical Review E* **2014,** *89* (2), 023011.
12. Padron, S.; Fuentes, A.; Caruntu, D.; Lozano, K., *Journal of Applied Physics* **2013,** *113* (2), 024318.
13. Xu, H.; Chen, H.; Li, X.; Liu, C.; Yang, B., *Journal of Polymer Science Part B: Polymer Physics* **2014,** *52* (23), 1547-1559.
14. Weng, B.; Xu, F.; Salinas, A.; Lozano, K., *Carbon* **2014,** *75*, 217-226.
15. McEachin, Z.; Lozano, K., *Journal of Applied Polymer Science* **2012,** *126* (2), 473-479.
16. Shanmuganathan, K.; Fang, Y.; Chou, D. Y.; Sparks, S.; Hibbert, J.; Ellison, C. J., *ACS Macro Letters* **2012,** *1* (8), 960-964.
17. Gupta, P.; Elkins, C.; Long, T. E.; Wilkes, G. L., *Polymer* **2005,** *46* (13), 4799-4810.
18. McKee, M. G.; Wilkes, G. L.; Colby, R. H.; Long, T. E., *Macromolecules* **2004,** *37* (5), 1760-1767.
19. Shenoy, S. L.; Bates, W. D.; Frisch, H. L.; Wnek, G. E., *Polymer* **2005,** *46* (10), 3372-3384.

20. Fang, Y.; Dulaney, A. D.; Gadley, J.; Maia, J. M.; Ellison, C. J., *Polymer* **2015,** *73*, 42-51.

21. Janes, D. W.; Shanmuganathan, K.; Chou, D. Y.; Ellison, C. J., *ACS Macro Letters* **2012,** *1* (9), 1138-1142.

22. Shanmuganathan, K.; Sankhagowit, R. K.; Iyer, P.; Ellison, C. J., *Chemistry of Materials* **2011,** *23* (21), 4726-4732.

23. Fang, Y.; Dulaney, A. R.; Gadley, J.; Maia, J.; Ellison, C. J., *Polymer doi:10.1016/j.polymer.2016.02.029*.

24. Regev, O.; Vandebril, S.; Zussman, E.; Clasen, C., *Polymer* **2010,** *51* (12), 2611-2620.

25. Adkins, S. S.; Chen, X.; Nguyen, Q. P.; Sanders, A. W.; Johnston, K. P., *Journal of Colloid and Interface Science* **2010,** *346* (2), 455-463.

26. Ellison, C. J.; Phatak, A.; Giles, D. W.; Macosko, C. W.; Bates, F. S., *Polymer* **2007,** *48* (11), 3306-3316.

27. Tan, A. R.; Ifkovits, J. L.; Baker, B. M.; Brey, D. M.; Mauck, R. L.; Burdick, J. A., *Journal of Biomedical Materials Research Part A* **2008,** *87* (4), 1034-1043.

28. Hammami, M. A.; Krifa, M.; Harzallah, O., *The Journal of The Textile Institute* **2014,** *105* (6), 637-647.

29. Ahn, Y.; Hu, D.-H.; Hong, J. H.; Lee, S. H.; Kim, H. J.; Kim, H., *Carbohydrate Polymers* **2012,** *89* (2), 340-345.

30. Zhang, S.; Shim, W. S.; Kim, J., *Materials & Design* **2009,** *30* (9), 3659-3666.

31. Deitzel, J.; Kleinmeyer, J.; Harris, D.; Tan, N. B., *Polymer* **2001,** *42* (1), 261-272.

32. Fridrikh, S. V.; Jian, H. Y.; Brenner, M. P.; Rutledge, G. C., *Physical Review Letters* **2003,** *90* (14), 144502.

33. Medeiros, E. S.; Glenn, G. M.; Klamczynski, A. P.; Orts, W. J.; Mattoso, L. H., *Journal of Applied Polymer Science* **2009,** *113* (4), 2322-2330.

34. Milligan, M.; Haynes, B., *Journal of Applied Polymer Science* **1995,** *58* (1), 159-163.

35. Shambaugh, R. L., *Industrial & Engineering Chemistry Research* **1988,** *27* (12), 2363-2372.

36. Palangetic, L.; Reddy, N. K.; Srinivasan, S.; Cohen, R. E.; McKinley, G. H.; Clasen, C., *Polymer* **2014,** *55* (19), 4920-4931.

37. Wang, C.; Fang, C.-Y.; Wang, C.-Y., *Polymer* **2015**.

38. Zong, X.; Kim, K.; Fang, D.; Ran, S.; Hsiao, B. S.; Chu, B., *Polymer* **2002,** *43* (16), 4403-4412.

39. Tan, D. H.; Zhou, C.; Ellison, C. J.; Kumar, S.; Macosko, C. W.; Bates, F. S., *Journal of Non-Newtonian Fluid Mechanics* **2010,** *165* (15), 892-900.

40. Vazquez, B.; Vasquez, H.; Lozano, K., *Polymer Engineering & Science* **2012,** *52* (10), 2260-2265.

41. Yu, J. H.; Fridrikh, S. V.; Rutledge, G. C., *Polymer* **2006,** *47* (13), 4789-4797.

42. Chen, T.; Wang, X.; Huang, X., *Textile Research Journal* **2005,** *75* (1), 76-80.

43. Macossay, J.; Marruffo, A.; Rincon, R.; Eubanks, T.; Kuang, A., *Polymers for Advanced Technologies* **2007,** *18* (3), 180-183.

44. Ward, G., *Filtration & Separation* **2001,** *38* (9), 42-43.

Chapter 4: Polyhedral Oligomeric Silsequioxane-Containing Thiol-Ene Fibers with Tunable Thermal and Mechanical Properties

4.1 Introduction

In the previous chapters, we demonstrated a robust and environmentally friendly fiber manufacturing approach combining UV initiated thiol-ene polymerization and centrifugal spinning. The mechanics and major parameters that govern fiber formation, fiber morphology, and fiber diameter distribution were investigated. These findings not only offered qualitative understanding but also served as quantitative predictive guidance for reactive mixture formulation and process optimization.

Apart from significantly reducing and even eliminating the use of heat energy and organic solvent, one of the major advantages of this fiber spinning method is that the photopolymerization of multifunctional reactive thiol and ene moieties lead to highly crosslinked thermoset fibers. As a result, the fibers are typically thermally stable up to 350-400 ^{o}C (i.e., dictated by degradation temperature) and are capable of maintaining their shape at even higher temperatures and in most organic solvents.[1] This is difficult to achieve by other conventional fiber spinning technologies that produce thermoplastic fiber whose service temperature is limited by the glass transition temperature or melting temperature of the polymer.

The rapid kinetics of thiol-ene photopolymerizations that can produce thermally stable crosslinked networks using a versatile profile of commercially available monomers from the coatings and adhesives industries has greatly facilitated its integration into other additive and continuous manufacturing approaches. In some cases, this strategy has enabled fabrication of polymer-derived ceramic functional materials. For instance, Reddy et al. used photolithographic processes and thiol-ene polymerization of siloxane containing monomers to fabricate polymer-derived ceramic microstructures,[2] while Cramer et al.

investigated the polymerization kinetics of a similar thiol-ene mixture containing a ceramic precursor monomer.[3] However, a detailed study of the thermomechanical properties of the resulting polymer-derived ceramic materials was not reported. Very recently, Eckel et al. utilized photopolymerization based 3D additive manufacturing techniques to fabricate geometrically complex polymer-derived ceramic structures. These materials are of interest for a wide range of applications that require materials fashioned into complex shapes coupled with thermal/environmental tolerance including thermal protection systems, porous burners, propulsion components, and microelectromechanical systems.[4]

Inspired by these studies, we seek to further expand the profile of fibrous materials that can be formed by thiol-ene photopolymerizations to polymer-derived ceramic fibers by incorporating high performance reactive precursor monomers. One of the ideal candidates is polyhedral oligomeric silsesquioxanes (POSS), a class of inorganic-organic hybrid building blocks which consist of an inorganic core with one or more pendant organic groups. The rigid siloxane cage structure provides thermal stability and mechanical strength, while the versatile and tailorable pendant group functionalization can promote compatibilization with a palette of polymers.

POSS materials have attracted much attention in recent years due to potential applications as reinforcement nanofillers, thermal stabilizers, and rheological modifiers that can improve thermomechanical properties of polymer matrices.[5-7] However, several studies have also reported decreased mechanical performance due to a high degree of POSS aggregation and potential for reduced crystallization of the polymer matrix.[8-10] To address the issue of POSS aggregation in host polymers, Milliman and others developed a framework based on Hansen solubility parameters to predict POSS-polymer matrix interactions which is a crucial aspect in controlling POSS dispersion.[11-12]

Besides polymer nanocomposites, POSS has also been demonstrated as an immobilization agent for metal and metal oxide nanoparticle catalysts in solution and solid states. For example, Naka and coworkers used amine-functionalized POSS as a linker to assemble spherical Palladium (Pd) nanoparticles in methanol,[13] while Letant et al. demonstrated the catalytic activity of POSS stabilized Pd nanoparticles.[14] Jefferson and coworkers successfully developed photocatalytic and self-cleaning coatings using POSS to disperse photocatalytic titania particles.[15] Notably, Gardella et al. anchored Pd and Ti-based catalysts on electrospun polymeric-POSS fibers and demonstrated the catalytic performance of these materials.[16-17] However, the reported electrospun fibers contained only 5 wt% POSS, potentially to avoid POSS aggregation which can compromise fiber spinning when aggregates block spinneret orifices.

Although many previous studies have focused on the use of POSS in bulk nanocomposite materials[5, 9-10] or in coatings,[15, 18-19] fibers have distinct advantages of being free-standing and possessing high surface area to mass ratios. POSS contained within elongated fibrillar structures could be very attractive given the ease of separation and recovery of fibrous materials from reagents and their higher catalytic activity by weight compared to spherical analogs. These features suggest the potential use of POSS fibers for catalysis applications. However, manufacturing fibers with high POSS content remains a challenge.

Utilizing the robust photopolymerization-based fiber spinning platform as described in the previous chapters, here we report the simple and rapid fabrication of unique organic-inorganic hybrid crosslinked POSS fibers. Mixing POSS and thiol-ene molecules as monomeric liquids allows the incorporation of a large amount of POSS (up to 80 wt%), yet the mixture still maintains good miscibility. Further, a POSS molecule with appropriate reactive moieties allows chemical integration of the inorganic content into the

thiol-ene network. Fibers were later thermally treated at different temperatures and subsequently characterized to investigate the connection between POSS content and processing protocols on network structure and thermomechanical properties. By optimizing the fiber processing conditions and the monomer mixture formulations, thiol-ene fibers with 80 wt% POSS exhibited significantly enhanced thermal stability and mechanical properties compared to all organic thiol-ene analogs suggesting applications in harsh or high temperature environments.

4.2 EXPERIMENTAL

4.2.1 Materials

Dipentaerythritol pentaacrylate (5A) and pentaerythritol tetrakis (3-mercaptopropionate) (4T) were purchased from Sigma-Aldrich. Acrylo POSS cage mixture (P8A), an inorganic-organic hybrid POSS monomer with eight pendant acrylate functional groups, was purchased from Hybrid Plastics. **Figure 4.1** shows the ideal chemical structures of the monomers used in this work. Irgacure 2100, a commercially available phosphine oxide based photoinitiator, was kindly donated by BASF Switzerland. High molecular weight (MW) polyethylene oxide (PEO) with a viscosity average MW of 10^6 g/mol, and anhydrous ethyl acetate were purchased from Sigma Aldrich. All chemicals were used as received without further purification.

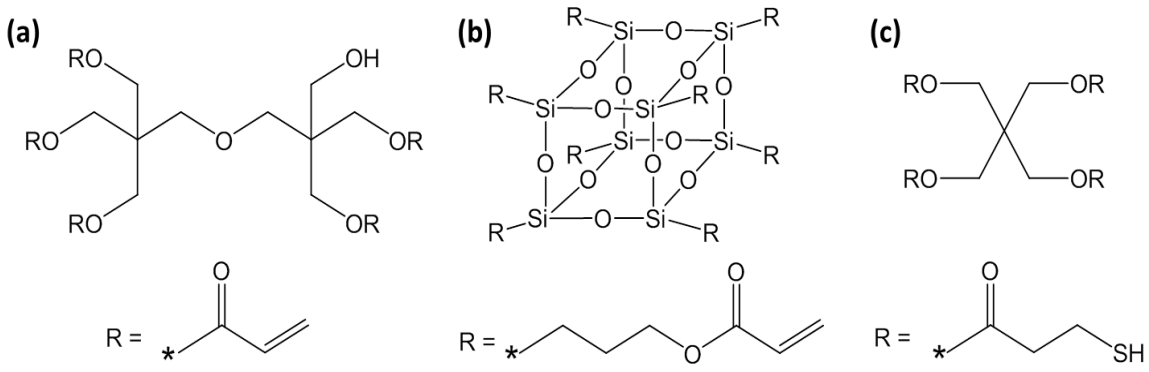

Figure 4.1: Chemical structures of (a) 5A, (b) P8A, and (c) 4T.

4.2.2 Monomer mixture preparation

Monomer mixtures used in this study contained various amounts of 5A, P8A, 4T, Irgacure 2100, PEO and ethyl acetate. The exact formulations of the monomer mixtures are presented in the results and discussion section. All components were added to a scintillation vial and mixed for 2 minutes using a vortex mixer (Thermolyne 37600). It was observed that the resulting monomer mixtures appeared clear and without phase separation, indicating homogeneity of the monomer mixture. The monomer mixture was then transferred into a masked syringe, which was used to load the monomer mix into the spinneret. The monomer mixtures were prepared in a room with no stray UV light to prevent polymerization prior to fiber spinning.

As shown in the previous chapters and recent publications from our group,[20] the elasticity of the monomer mixture plays a major role in suppressing surface tension driven instabilities or fiber jet breakup and is therefore essential for defect free fiber formation. In this study, 4T solution containing 0.1 wt% PEO (equivalent to 160 – 190 ppm PEO by weight of the entire monomer mixture) was used to impart elasticity to the monomer mixtures. This 4T stock solution was prepared by gently stirring PEO in 4T at 70 ^{o}C for 18 hours.

4.2.3 Centrifugal fiber spinning

A bench scale Forcespinning apparatus (FibeRio Cyclone L-1000) was equipped with an in-house UV light source. The light source arrangement included an arc lamp power supply and igniter (Photon Technology International, PTI LPS-220 and LPS-221), a lamp housing with reflector (PTI LPS-A1010), a 100 W Mercury arc lamp (Ushio), and a UV transparent mirror (Edmund Optics) to reflect the light onto the collector. This light arrangement was described in detail previously[20] and in Chapter 2.2.2.

For all fiber spinning studies, each orifice of the 2-orifice rotating spinneret was attached to a blunt end Luer lock needle with a diameter of 260 μm and length of 1.5 inches. The spin speed was set to 1500 rpm to allow for sufficient flight time; the broadband light intensity was set to 1,100 mW/cm^2 (determined using a Coherent Fieldmax TO radiometer) to provide rapid photopolymerization kinetics. Using this optimized processing condition, all monomer mixture formulations resulted in uniform and well-cured fibers.

4.2.4 Rheology

Complex viscosities of various monomer mixture formulations were measured by a rheometer (TA instruments, AR 2000) equipped with 40 mm Peltier plate fixture. Dynamic frequency sweep measurements were conducted at frequencies from 0.628 to 62.8 rad/s with 5% strain. To avoid problems of curing due to exposure to ambient room light during these measurements, photoinitiator was not added to the monomer mixtures used in this rheology study.

4.2.5 Thermal treatment

Thermal treatments of fibers were performed in a tube furnace (Thermo Scientific Lindberg/Blue tube furnace) under Argon atmosphere. A fiber mat sample was scrolled and placed in a quartz boat inside the tube furnace. The tube furnace was first purged with

Argon for one hour. The furnace temperature was ramped from room temperature to the desired thermal treatment temperature (500 ^{o}C, 750 ^{o}C, or 1000 ^{o}C) at 1 ^{o}C/minute and held constant for 60 minutes. The furnace was then allowed to cool to room temperature. The weight and size of the fiber mats before and after thermal treatments were measured.

4.2.6 Thermal characterization

The thermal transitions of fibers were characterized by differential scanning calorimetry (DSC, Mettler Toledo DSC1). All heating and cooling cycles were conducted at a rate of 10 ^{o}C/minute under a Nitrogen atmosphere. A first heating cycle from 30 ^{o}C to 70 ^{o}C was employed to remove any volatile compounds in the fiber network. The glass transition temperatures were obtained during the second heating cycle from 30 ^{o}C to 180 ^{o}C. The thermal stability of the fibers was characterized by thermogravimetric analysis (TGA, Mettler Toledo TGA/DSC 1). The fibers were heated to 1000 ^{o}C at 10 ^{o}C/minute in a Nitrogen atmosphere.

4.2.7 Acrylate conversion measurement

Fourier transform infra-red spectroscopy (FTIR, Thermo Scientific Nicolet 6700) with a KBr beam splitter and a MCT-A detector was employed to determine the acrylate conversion of each monomer mixture after being processed into fibers. The acrylate content of the initial monomer mixture was measured in transmission mode. A droplet of monomer mixture was sandwiched between two NaCl windows to form a thin continuous film. To obtain accurate measurements, monomer mixtures were freshly prepared and analyzed within 15 minutes. The acrylate content of the as spun fiber was measured using attenuated total reflection-FTIR (ATR-FTIR) with a diamond ATR crystal accessory (PIKE MIRacle™).

The acrylate double bond content was calculated by the area of the acrylate absorption peak at 1630 cm^{-1} normalized by the area of the carbonyl absorption peak at 1730 cm^{-1}. The conversion of the acrylate groups was calculated as follows:

$$\% \text{ Conversion} = \frac{A_0 - A_{final}}{A_0} \times 100$$

where A_0 is the normalized area of the acrylate absorption peak of the monomer mixture measured by transmission FTIR, and A_{final} is the normalized area of the acrylate absorption peak of as-processed fibers measured by ATR-FTIR.

4.2.8 Fiber imaging and diameter analysis

Scanning electron microscopy (SEM, Hitachi S-5500) was used to characterize the morphology of the fibers. For every fiber sample, the fiber diameter, orientation and their respective distributions were determined by measuring the diameters of approximately 100 fibers on 10 to 15 different SEM images using ImageJ (National Institutes of Health) software.

4.2.9 Composition characterization

The composition of fibers before and after different thermal treatments was analyzed by SEM (Hitachi S-5500) equipped with an energy dispersive spectrometer (EDS) detector (Bruker EDS Quantax 4010). SEM-EDS data were analyzed by Esprit software (Bruker). The instrumental errors of SEM-EDS analysis in terms of atomic % for Carbon (C), Oxygen (O), Silicon (Si), and Sulfur (S) were within 4.5%, 3.4%, 1.0%, and 0.9%, respectively. For each condition, six SEM-EDS spectra and measurements were taken at different areas of the SEM sample to accurately characterize the elemental composition of the fibers.

4.2.10 Tensile testing

The mechanical properties of the fiber mat were measured by a dynamic mechanical analyzer (DMA, TA instruments Q800). Because the mechanical performance of fiber mats were normalized based on the total cross-sectional area occupied by fiber excluding void space, the thickness and porosity of fiber mats must be obtained. The thickness of fiber mats with known widths and lengths were measured according to ASTM D5729. The volume of a fiber mat was calculated from the measured dimensions, while the mass of the fiber mat sample was measured by an analytical balance. The density of the fiber mats can be thereby determined.

To determine the density of the bulk material, film samples were made from the same monomer mixtures used for fiber spinning. The density of the bulk samples were measured by an analytical balance (Mettler Toledo, Excellence Plus XP/XS) equipped with a density determination kit. The densities of the three formulations were measured to be 1.309 ± 0.003, 1.311 ± 0.005, 1.324 ± 0.004 g/cm^3 for 100/0, 60/40, 20/80 5A/P8A samples, respectively. The porosity of the fiber mats can then be calculated using the following equation:

$$\%\ \text{Porosity} = \left(1 - \frac{density\ of\ mat}{density\ of\ bulk}\right) \times 100\%$$

The porosity of fiber mats in this study ranged from 87.3% to 90.4%. To prepare samples for tensile testing, fiber mats of known porosity and thickness were cut into rectangles 15 mm in length x 2 mm in width along their machine directions. Then, a mounting window was prepared by cutting a 10 mm x 10 mm square in the center of a cardboard template. The fiber sample was then secured across the window using two part epoxy glue. The mounting window with the fiber sample was placed in the tensile film grips of the DMA. The two sides of the mounting window were cut, leaving only the fiber

mat sample between the grips. This mounting technique successfully reduced the probability of breaking the sample at the grip due to stress concentration as well as slipping of the fiber sample from the grip. Stress-strain tests on fiber mats were conducted at ambient conditions with a displacement of 10 mm/minute and a 0.01 N preload force.

To measure the mechanical properties of as-processed single fibers, the single fibers were first carefully pulled out from as-processed fiber mats. The sample preparation and DMA measurement of single fibers was similar to that of fiber mats, except that a 0.005 N preload force was used in the case of the single fiber DMA measurement.

4.3 RESULTS AND DISCUSSION

4.3.1 Monomer mixture formulations

To investigate the influence of inorganic-organic hybrid POSS molecules incorporated into an organic thiol-ene network, three monomer mixtures containing different amounts of P8A were made as shown in **Table 4.1**. The numbers in the abbreviations indicate the wt% of 5A and P8A out of all ene monomers. For example, 20/80 5A/P8A indicates that 20 wt% ene monomers are 5A and 80 wt% ene monomers are P8A, and the two ene monomers combined to constitute 69.8 wt% of the entire monomer mixture.

Component	Weight %		
	100/0 5A/P8A	60/40 5A/P8A	20/80 5A/P8A
5A	65.3	40.0	14.0
P8A	0	27.0	55.8
4T (with PEO)	18.8	16.9	15.2
Irgacure 2100	6.0	6.0	6.0
Ethyl Acetate	10.0	9.5	9.0

Table 4.1: Chemical compositions of monomer mixtures to produce inorganic-organic hybrid thiol-ene crosslinked fibers.

In these three formulations, the total molar ratio of ene to thiol was kept constant at 4:1 to provide optimal photopolymerization kinetics as demonstrated in several previous studies.[20-21] Incorporating small amounts of thiol in the monomer mixture is sufficient to alleviate issues associated with an oxygen inhibition induction time that commonly plagues conventional (meth)acrylate free radical polymerizations.[22-23] The photoinitiator content was kept constant at 6 wt% to promote a rapid and consistent initiation rate for forming defect free solid fibers.

Ethyl acetate was added as a diluent to reduce the viscosity of the monomer mixture to facilitate sufficient solution delivery through the spinning spinneret orifices. The ethyl acetate content was adjusted for each formulation to produce similar viscosities for all monomer mixtures. Monomer mixture viscosity is a crucial parameter because it is inversely proportional to flow rate though the orifice which in turn predominantly determines the average fiber diameter and diameter distribution.[24] Furthermore, for solution state centrifugal spinning it has been reported that fiber flight paths as well as fiber orientation within the fiber mat are highly dependent on the polymer concentration and viscosity of the solution.[25] In this study, we targeted fiber mats with similar diameter distributions and fiber orientations in order to make fair comparisons in the following mechanical property studies. The complex viscosities of all monomer mixtures were adjusted to around 0.3 Pa-s for all formulations and the rheology data are shown in **Figure 4.2**.

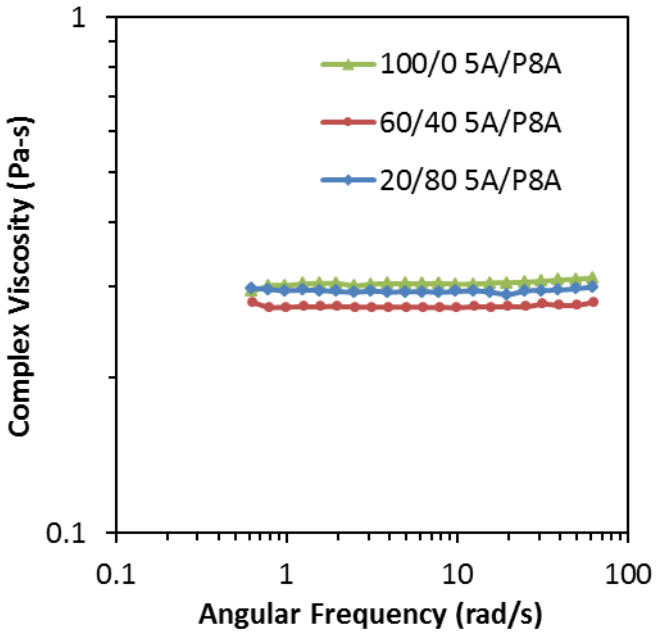

Figure 4.2: Complex viscosities of 100/0, 60/40, and 20/80 5A/P8A monomer mixtures.

As expected, the average fiber diameters of the as-processed fibers were similar, and measured to be 11.3 ± 2.7, 14.3 ± 3.5, and 13.8 ± 3.8 μm for 100/0, 60/40, and 20/80 5A/P8A fibers, respectively. The orientation of fibers within the mat, as shown in **Figure 4.3**, was found to be similar across fiber samples prepared from the different formulations. The maximum frequency in fiber orientation for all fiber mat samples occur at about 0 degrees, indicating the fiber's long axis is biased towards the direction of the spinning orifice as it is deposited on the circumferential collector. The mechanical tests in this study were conducted along this same direction (i.e., the 0 degree direction following the path swept out by the spinning orifice).

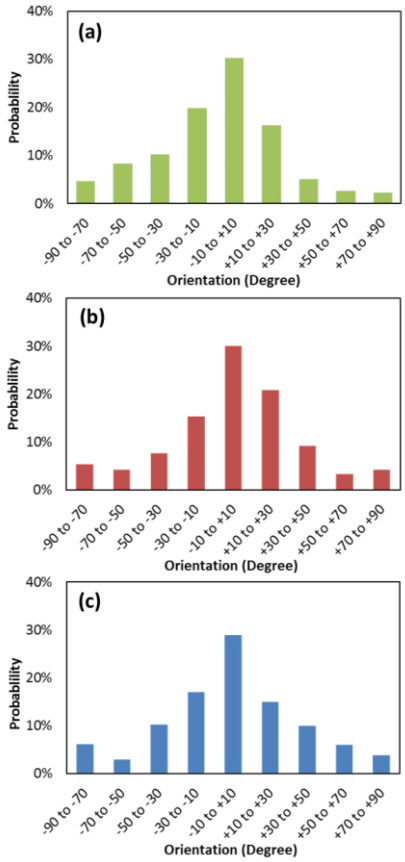

Figure 4.3: Orientation of individual fibers in (a) 100/0, (b) 60/40, and (c) 20/80 5A/POSS mats.

It is important to note that the incorporation of more than 50 wt% POSS into polymeric fibers has not been demonstrated before. This was achieved largely owing to the selection of monomers and the features of the photo-reactive fiber spinning method. First, P8A was selected for its high ene-functionality, physical properties and commercial availability. The multiple acrylate groups participate in rapid photopolymerization and anchor the inorganic POSS structures in the thiol-ene network, thereby facilitating a uniform distribution of POSS. Second, the mixing of organic and inorganic components was performed in the monomeric liquid state prior to fiber spinning and photopolymerization. This is advantageous in producing a homogeneous monomer

mixture, because the entropy of mixing of such a system is much higher compared to mixing of POSS components with high molecular weight preformed polymers.

4.3.2 Thermal characterization

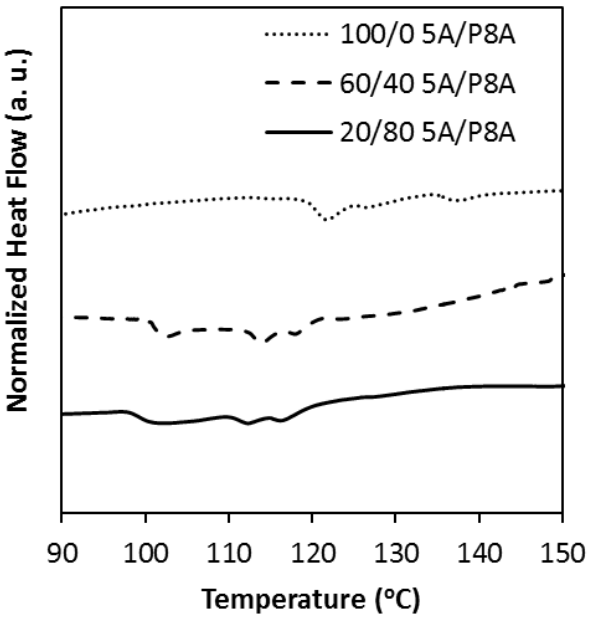

Figure 4.4: DSC thermograms of as-processed fibers made from various formulations. The heat flow (exothermic up) is from the second heat and has been normalized by sample weight and shifted vertically for clarity.

As shown in **Figure 4.4**, DSC thermograms of as-processed fibers revealed that the primary glass transition temperatures (T_g) are 115 °C, 102 °C and 98 °C for 100/0, 60/40, and 20/80 5A/P8A fibers, respectively. The primary T_g shifts towards lower temperature with increasing P8A content. It is expected that P8A monomers could affect the network structure in a number of different ways. First, POSS molecules contain rigid cores whereas 5A molecules have flexible ether linkages near the center; the steric hindrance of the rigid core probably prevents tight packing of POSS molecules, leading to a more expanded network. Second, the alkyl chain length of acrylate branches on P8A monomers is longer

than that on the 5A monomers, which could lead to internal plasticization and the formation of a larger crosslinked network pore size with lower crosslink density.

It was also observed that as P8A content increases in the monomer mixture formulation, the final conversion of acrylate groups in the as-processed fibers decreases from 84% for 100/0 5A/P8A to 71% for 20/80 5A/P8A calculated from the FTIR spectra (**Figure 4.5**) as described in Section 4.2.7. It should be noted that the baseline of the ATR-FTIR spectra of as–processed fibers (**Figure 4.5 d-f**) is tilted upwards with higher wavenumber due to scattering of light from fiber surfaces. On the other hand, the baseline of the transmission mode FTIR spectra of monomer mixtures (**Figure 4.5 a-c**) is flat, indicating the monomer mixtures are homogeneous and free of POSS aggregation.

The lower final conversion of acrylate groups with increasing P8A content in the thiol-ene formulation is also aligned with the decreasing primary T_g. This result also agrees with the aforementioned reports regarding multifunctional siloxane containing thiol-ene polymerizations. For example, Cole and coworkers evaluated the reaction kinetics of thiol- and ene-functionalized polysiloxane and observed that the polymerization rate is sensitive to the chemical environment/composition of siloxane formulations.[26] In another study, Naumov et al. suggested that inflexibilities of the nonreactive segments as possible sources of radical trapping.[27]

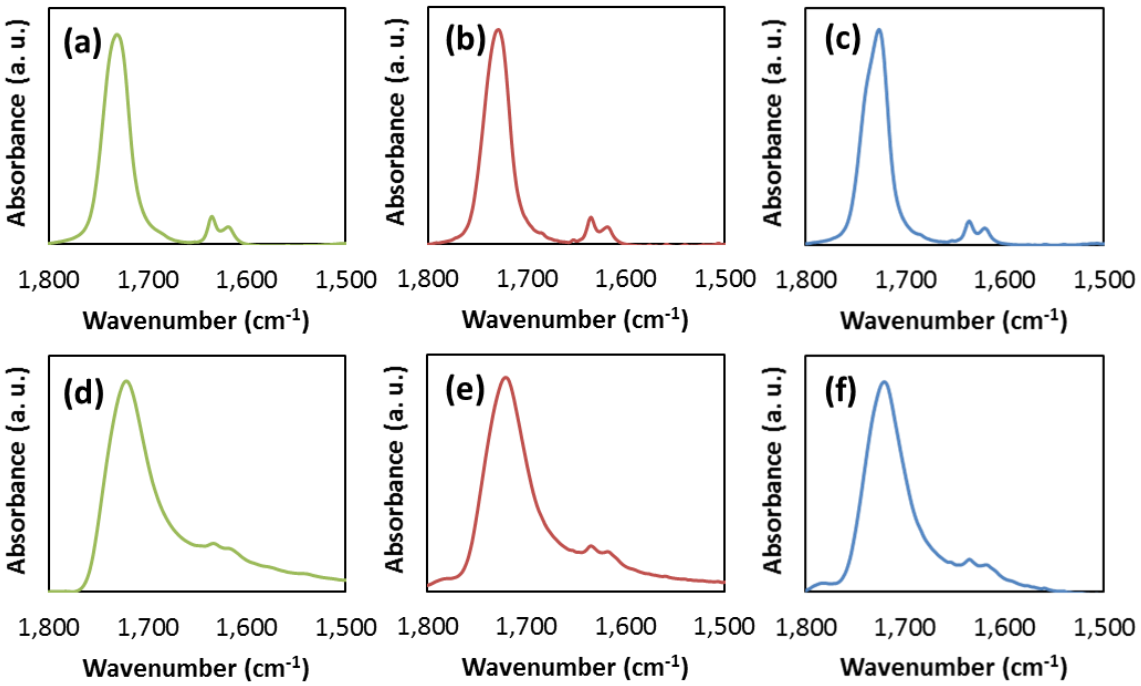

Figure 4.5: FTIR spectra of 100/0, 60/40, and 20/80 5A/P8A monomer mixtures (a, b and c, respectively) and the corresponding as-processed fibers (d, e and f, respectively).

Besides the primary T_g, all as-processed samples possess additional thermal events resembling T_gs typically appearing 20-30 ^oC higher than the primary T_g. Because this phenomena occurs for all fiber samples made both with and without P8A, the presence of multiple T_gs does not reflect aggregation of inorganic POSS in the organic matrix, a common problem in the physical blending of POSS filler in polymeric matrices.[9-11] In this case, the secondary T_g occurring 20-30 ^oC higher than the primary T_g is a hallmark of mixed step growth / chain growth polymerization of acrylate-thiol / acrylate-acrylate monomers, respectively;[28] this is in contrast to the single, narrow T_g that reflects the homogeneity of a pure step-growth thiol-ene network.[29-30] The different reaction mechanisms can result in different extents of polymerization and segmental mobilities in

localized regions that give rise to inhomogeneities in the crosslinked network, reflected as multiple T_g's or a broadened T_g.[1, 31-32]

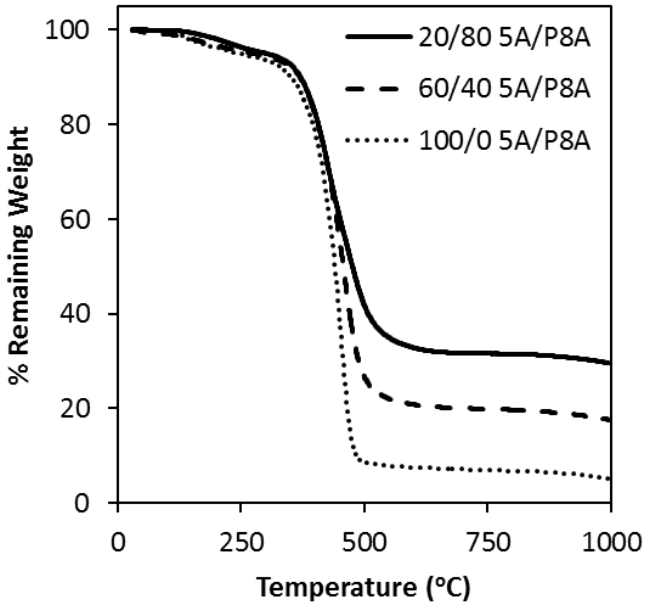

Figure 4.6: TGA thermograms of as-processed fibers containing various amounts of 5A and P8A.

TGA was used to characterize the thermal stability of the as-processed fibers. **Figure 4.6** shows that the onset degradation temperature is around 400 °C for all samples, which is typical for materials containing a highly crosslinked thiol-ene network.[1, 29] The residual weights at 500 °C were 8.6%, 26.7%, and 41.9% for 100/0, 60/40, and 20/80 5A/P8A fibers, respectively. This continuous change in residual weight clearly indicates that the incorporation of inorganic components significantly improves the thermal stability of the thiol-ene fibers. The residual weight remains stable at 500°C and above for all samples, demonstrating their potential for application in high temperature environments.

4.3.3 Thermal treatment and resulting fiber morphology

To investigate the effect of thermal treatments on fiber properties, the fibers were thermally treated at 500 ^{o}C, 750 ^{o}C, and 1000 ^{o}C in an Argon atmosphere inside a tube furnace. **Figure 4.7** displays the morphology of 20/80 5A/P8A fibers before and after thermal treatments. The fibers made from 100/0 5A/P8A and 60/40 5A/P8A formulations also exhibit similar morphological transitions.

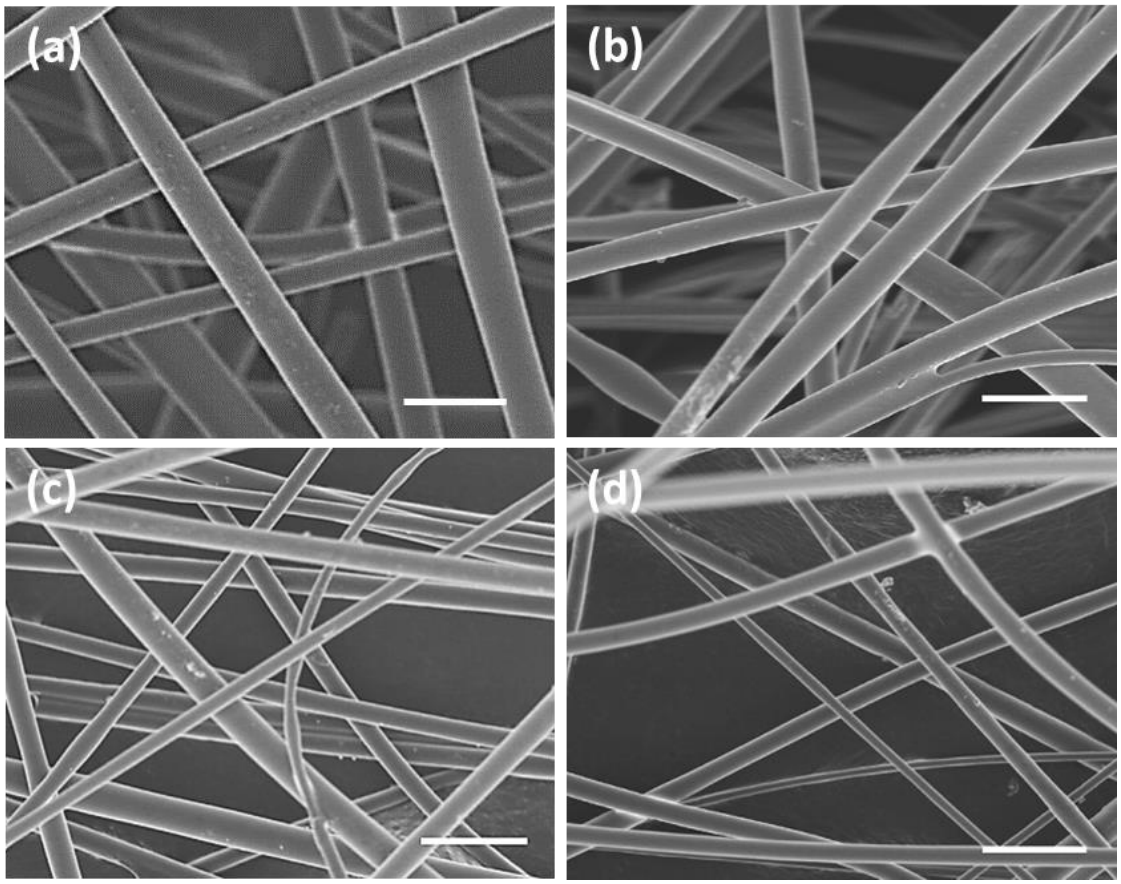

Figure 4.7 SEM micrographs of 20/80 5A/P8A fibers (a) as-processed and thermally treated at (b) 500 ^{o}C, (c) 750 ^{o}C, and (d) 1000 ^{o}C. Scale bars in all images represent 30 μm.

Comparing untreated fibers in **Figure 4.7 a** to thermally treated fibers in **Figure 4.7 b-d** under the same magnification, it is obvious that fibers shrink significantly in

diameter, but the fiber mat itself remains intact and free of defects. It is reasonable to conclude that the chemical crosslinks of the macromolecular network and inorganic POSS content are both critical aspects of their survival at high temperature.

Sample	Treatment Temperature (°C)	Weight Reduction (%)	Mat Area Reduction (%)	Fiber Dia. Reduction (%)
100/0 5A/P8A	500	93.2	89.4	69.8
	750	93.3	91.9	73.1
	1000	95.6	92.9	77.5
60/40 5A/P8A	500	80.7	76.5	64.5
	750	80.8	73.6	58.5
	1000	85.0	83.1	63.0
20/80 5A/P8A	500	64.3	64.8	50.8
	750	67.7	68.8	51.5
	1000	71.6	74.4	60.6

Table 4.2: Residual weight, mat area, and diameter reduction of inorganic-organic hybrid fibers after thermal treatments.

The % change in weight, physical dimension, and average diameter after thermal treatments at different temperatures were measured and tabulated in **Table 4.2**. The weight changes after thermal treatment in the tube furnace are in good agreement with the TGA results of **Figure 4.6.** Fiber mats also undergo reduction in both mat area and fiber diameter, but to a lesser extent than the reduction in weight, indicating that the fibers shrink in three dimensions during the thermal treatment. In addition, fibers containing more inorganic POSS content have a smaller reduction in weight, mat area and fiber diameter. This again shows the superior thermal stability of the inorganic-organic hybrid fibers.

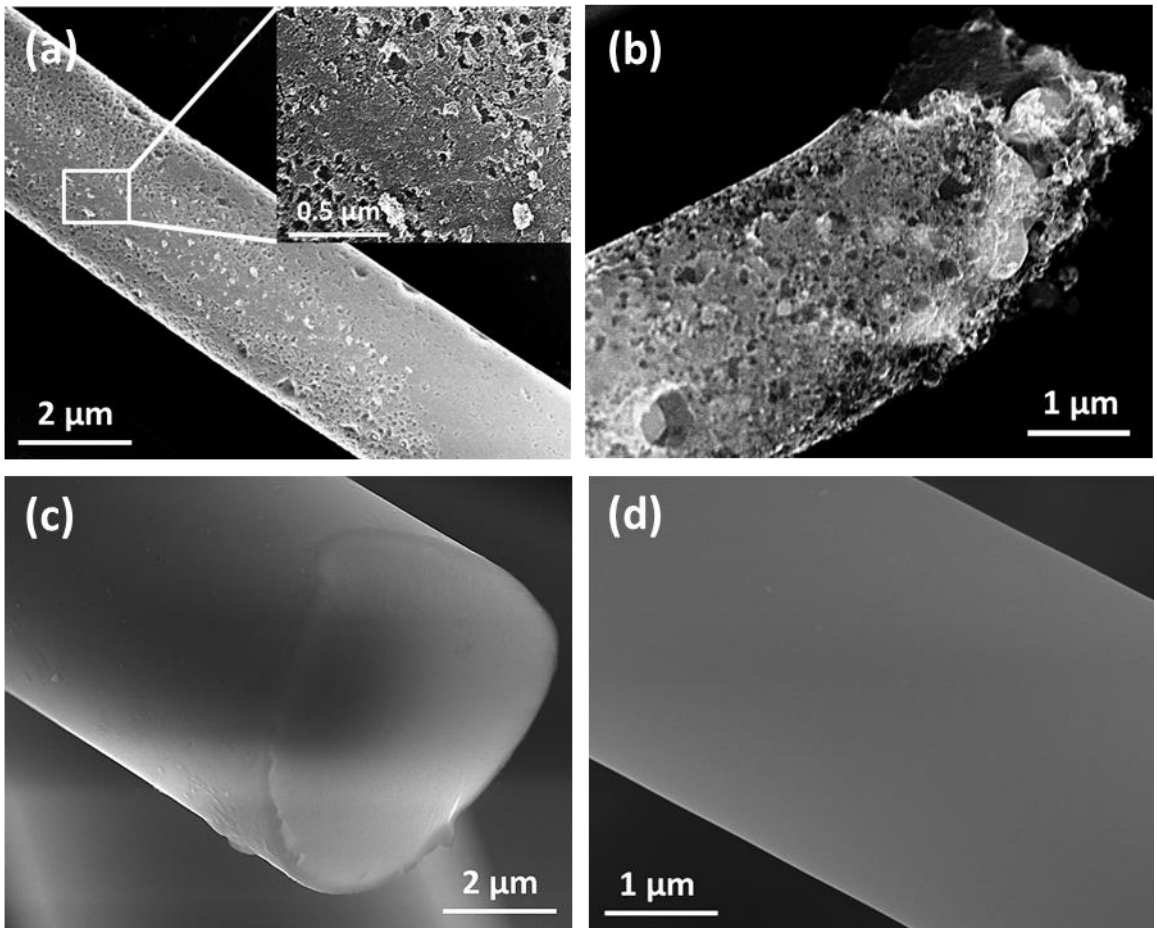

Figure 4.8: SEM micrographs of (a) 100/0 5A/P8A fibers thermally treated at 750 ºC, (b) 100/0 5A/P8A fibers thermally treated at 1000 ºC, (c) 60/40 5A/P8A fibers thermally treated at 1000 ºC and (d) 20/80 5A/P8A fibers thermally treated at 1000 ºC.

Interestingly, high magnification SEM images of 100/0 5A/P8A fibers reveal that thermal treatments at 750 ºC and 1000 ºC (**Figure 4.8 a and b**) produce mesoporous structures. The porous structures appear on both the surface and throughout the core of the fibers. It is likely that they are formed from the deterioration of the organic crosslinked network followed by evaporation of volatile organic species as thermal treatment continues. In contrast, replacing only 40% of the organic ene monomer with inorganic-organic hybrid P8A sufficiently stabilizes the crosslinked network. The SEM image of

60/40 and 80/20 5A/P8A fiber after thermal treatment at 1000 ^{o}C in **Figure 4.8 c and d** reveals a smooth fiber surface and cross section without any mesoporous structure, indicating not only the integrity of the POSS containing crosslinked network at elevated temperature but also the good miscibility of 5A and P8A.

3.4 Composition characterization

SEM-EDS elemental analysis was employed to investigate the compositional evolution of the inorganic-organic hybrid fibers that have been treated at different temperatures. Although SEM-EDS analysis provides a semi-quantitative measure, it offers useful insight about the effect of thermal treatment on the composition and network structure. Further, the elemental compositions of as-processed fiber samples from SEM-EDS analysis are in good agreement with those calculated based on the monomer mixture formulations as shown in **Table 4.3**.

	100/0 5A/P8A		**60/40 5A/P8A**		**20/80 5A/P8A**	
	SEM-EDS	Calc.	SEM-EDS	Calc.	SEM-EDS	Calc.
C	73.3 ± 2.9	69.2	65.6 ± 1.8	63.9	57.0 ± 1.6	59.3
O	21.7 ± 3.6	27.5	26.1 ± 2.8	29.8	33.2 ± 2.7	32.2
Si	-	-	4.4 ± 0.8	3.6	7.2 ± 1.5	6.2
S	4.9 ± 2.0	3.3	3.9 ± 0.8	2.7	2.7 ± 0.5	2.3

Table 4.3: Comparisons of C, O, Si, and S elemental compositions of 100/0, 60/40, and 20/80 5A/P8A monomer mixtures measured by SEM-EDS and calculated based on monomer mixture formulations.

Figure 4.9 displays the elemental compositions of 100/0, 60/40, and 20/80 5A/P8A fibers before and after thermal treatments. All three samples showed significant changes in composition after undergoing thermal treatments at 500, 750, 1000 ^{o}C. Interestingly,

despite the fact that all are produced via the same thiol-ene photopolymerization mechanism by reacting similar chemical moieties, the elemental changes after thermal treatment are very different for the three formulations. This can be contributed to two factors. First, it is well known that ester linkages undergo cleavage at high temperature, forming CO_2, CO, and small volatile organics. As shown in numerous thermoplastics and thermosets containing ester groups, the cleaving of ester linkages is typically initiated at about 400 ^oC,[33-35] which coincides with the onset degradation temperature of crosslinked thiol-ene fiber samples. On the contrary, the O rich inorganic POSS cage is preserved, as Si-O-Si linkages have better thermal stability even at extreme temperatures. For example, the decomposition of silicon oxycarbide, SiO_xC_y, rarely occurs below 1300 ^oC.[36-37]

For 100/0 5A/P8A fibers, O content decreases while C content increases monotonically with thermal treatment at higher temperatures. This can be attributed to the decomposition of ester groups, leaving behind a residue mostly composed of C. On the other hand, the O content of 60/40 and 20/80 5A/P8A samples increases indicating that the retention of O content from the POSS cages is greater than the loss of O content via decomposition of ester bonds. The C content of all thermally treated inorganic-organic hybrid fibers decreases, again due to the presence of the more thermally stable Si-O-Si linkages compared to alkyl and ester linkages. Finally, the S atom% significantly decreases for all fiber samples after thermal treatment, indicating the thermal cleavage of C-S linkages at elevated temperatures.[38]

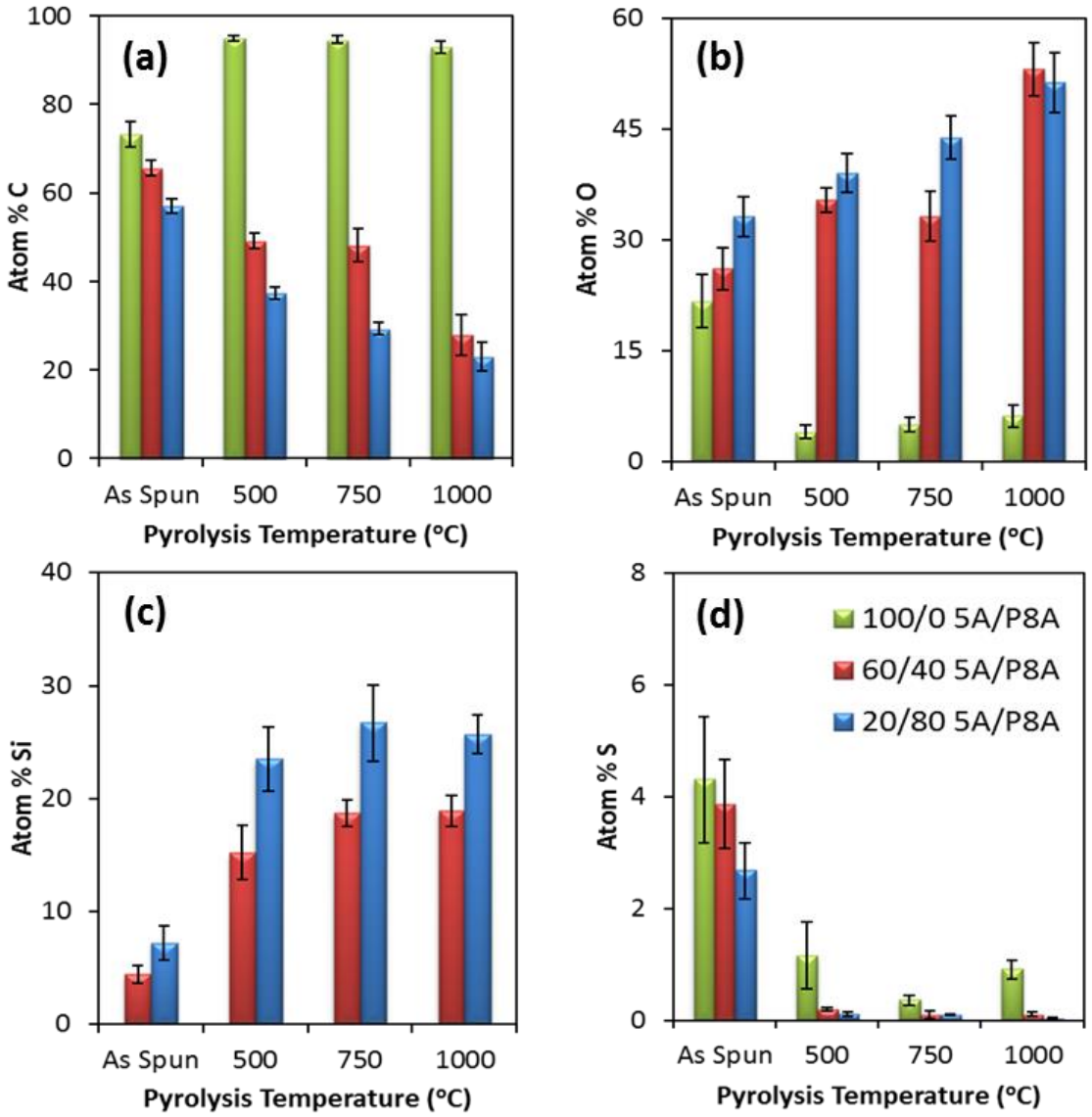

Figure 4.9: Elemental composition of as-processed and thermally treated fibers obtained from EDS: (a) C, (b) O, (c) Si, and (d) S. The legend in (d) applies to all graphs in this figure. The error bars represent the standard deviation of six measurements in different areas of each sample.

Figure 4.10 compares the Si/O ratio for 60/40 and 20/80 5A/P8A fibers as-processed and after thermal treatment at different temperatures. The Si/O ratios of POSS containing fibers that have been thermally treated at 500 and 750 ^{o}C are approximately 0.6,

close to the Si/O ratio for the POSS cage (0.66). This again confirms that the thermally treated fiber network consists of significant amounts of POSS structures, while the organic content, particularly ester and C-S linkages from POSS pendant branches and 5A, decomposes and volatilizes from the network.

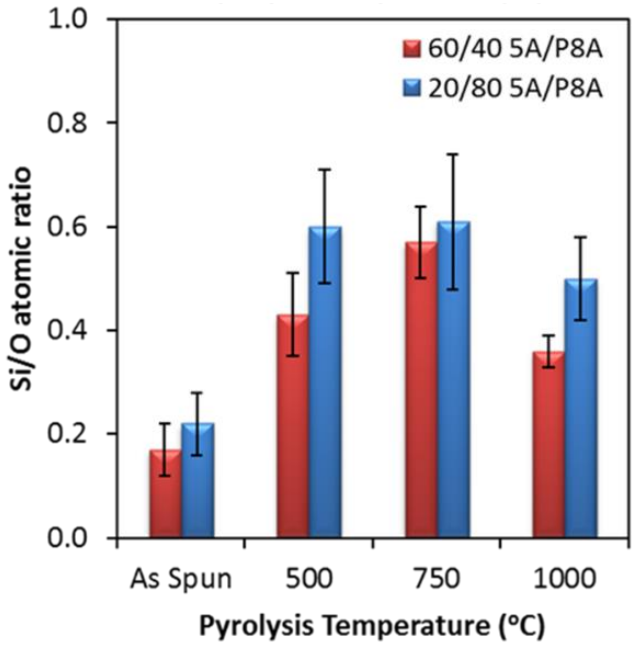

Figure 4.10: Atomic Si/O ratio EDS results from fiber samples undergoing different thermal treatments.

3.5 Mechanical characterization

The tensile properties of as-processed and thermally treated fibers were characterized by stress-strain experiments. All measurements were normalized by the physical dimensions (thickness, width, and porosity) of fiber mats as described in the experimental section. **Figure 4.11** shows representative stress-strain curves of the fiber mats made from three different formulations. Most samples exhibit a maximum in stress followed by sudden rupture without yielding, which is indicative of brittle-hard materials and typical for materials containing a highly crosslinked network.[28, 30, 39] At least four

samples from each fiber mat were prepared and measured. The compiled values of ultimate stress, ultimate strain and modulus are presented in **Figure 4.12**.

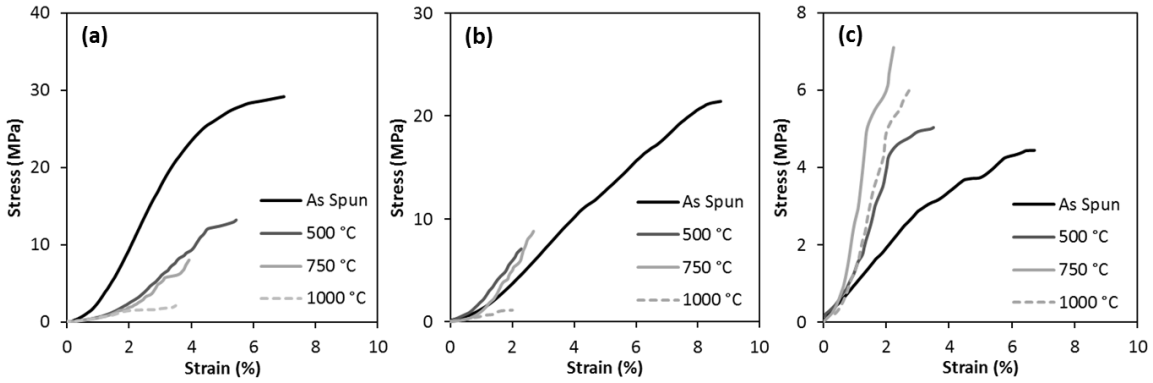

Figure 4.11: Representative stress-strain curves of (a) 100/0 5A/P8A, (b) 60/40 5A/P8A, and (c) 20/80 5A/P8A fibers as-processed and after being thermally treated at 500 °C, 750 °C, and 1000 °C, respectively.

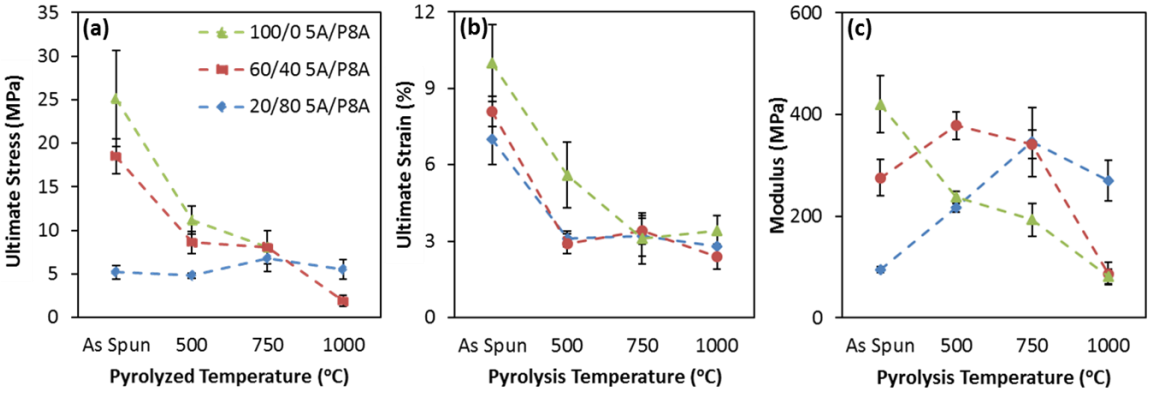

Figure 4.12: (a) Ultimate stress, (b) ultimate strain, and (c) modulus of 100/0, 60/40, 20/80 5A/P8A fibers as-processed and after thermal treatment at 500 °C, 750 °C, and 1000 °C, respectively. The legend in (a) applies to all panels in this figure. The error bars represent one standard deviation of at least four samples.

With increasing thermal treatment temperature, the ultimate stress (**Figure 4.12 a**) of the thermally treated 100/0 and 60/40 5A/P8A fibers reduces dramatically, while the ultimate stress of the thermally treated 20/80 5A/P8A fibers stays constant at 500 °C and

even increases slightly at higher temperature. These differences can be attributed to the extent of degradation and rearrangement of the organic-inorganic hybrid network. During thermal treatment, the organic components degrade, leaving behind the inorganic components which can undergo a number of reactions. For example, cleavage of the Si-C bond occurs above 400 ^{o}C which can lead to an exchange reaction between the Si-C bond and Si-O bond, or formation of Si-C-Si bridges.[40-42] Residual units not functionalized with pendant organic branches, such as Si-OH groups, in the P8A monomer can also undergo condensation reactions to form additional Si-O-Si bridges.[40, 43-44] For 20/80 5A/P8A fibers, it is plausible that the formation of a silicon oxycarbide network compensated for the degradation of the organic thiol-ene network and resulted in a near constant ultimate stress. Conversely, for fibers containing lesser amounts of POSS, the degradation of the thiol-ene network dominated leading to a reduced ultimate stress. The ultimate strain (**Figure 4.12 b**) reduces significantly to similar values for all samples after being thermally treated. This shows the fiber mats become more brittle after undergoing thermal treatments.

Previous research has shown that the modulus of the fiber mat, defined by the slope of the stress-strain curve, can be more than an order of magnitude lower than the single fiber from which the mat is composed, depending on the porosity, radius of curvature, and distance between physical contacts of fibers.[45-46] As a result, it is essential in this study to measure the physical dimensions of the fiber mats rigorously, and to prepare fiber mats with similar fiber orientations. The moduli of fiber mats from different compositions and thermal treatments were calculated from the stress-strain curves, and the values are shown in **Figure 4.12 c**. The modulus for the as-processed 100/0 5A/P8A fiber mat is 420 MPa, which is 6 times lower than the modulus of the single fiber made with a similar composition.[1] It is noteworthy that the stress-strain tests on as-processed 100/0 5A/P8A single fibers (as shown in **Figure 4.13**) yielded similar ultimate stress and strain, and

modulus values compared to the previously reported thiol-ene electrospun fibers with similar compositions.[1, 21]

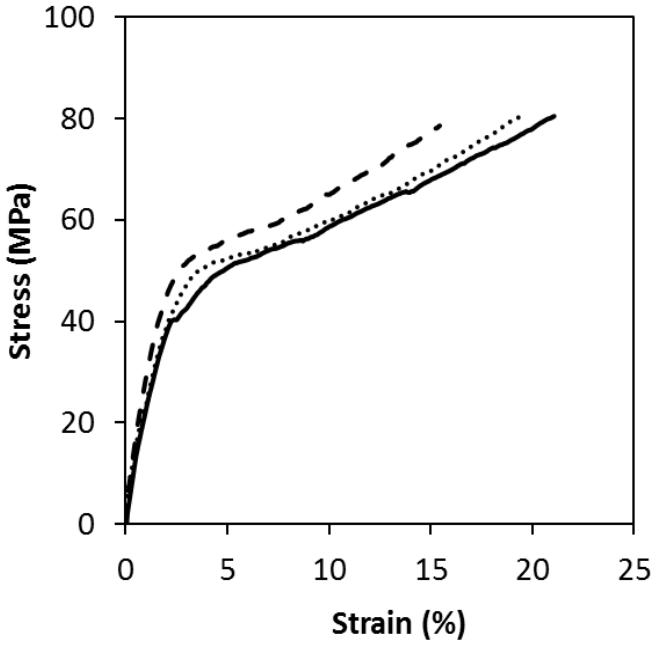

Figure 4.13: Representative stress-strain curves of three separate 100/0 5A/P8A as-processed single fibers.

Interestingly, the moduli of the fiber mats decreased significantly as the POSS content increased. This can be largely attributed to the presence of rigid POSS cores which may not densely pack and the more extensible R groups compared to 5A resulting in a more open network. This is also consistent with a reduced primary T_g as POSS content increased. As thermal treatment temperature increased, the modulus of the 100/0 5A/P8A fiber mat decreased monotonically. The reduction in modulus along with the formation of macroscopic pores after thermal treatments, revealed by the previously detailed SEM images, clearly indicate the degradation of the purely organic crosslinked network. On the contrary, the moduli of organic-inorganic hybrid fibers increased after thermal treatments and showed significant improvement in mechanical properties at elevated temperatures

compared to their purely organic counterpart. The modulus of 60/40 5A/P8A reached a maximum at the 500 ^{o}C thermal treatment and then decreased at 750 ^{o}C and 1000 ^{o}C, while the modulus of 20/80 5A/P8A increased up to 750 ^{o}C and was approximately maintained at 1000 ^{o}C.

One potential explanation of the drop in modulus for the 60/40 5A/P8A sample at higher thermal treatment temperatures (750 ^{o}C and 1000 ^{o}C) is that the fibers still consist of a significant amount of organic material which decomposes at these higher temperatures. This leads to a loosely connected network, although void formation and internal fracture was not observed from the SEM images of these samples. Further, the moduli of the two inorganic-organic fiber mats after thermal treatments follow the trend of Si/O ratio as presented in **Figure 4.10**, suggesting that the mechanical properties are highly dependent on the network composition. After the decomposition and volatilization of organic components in the network, the residual network is composed mainly of rigid POSS molecules and thereby exhibits more brittle material characteristics with higher modulus. Nonetheless, it is clear that varying the organic/inorganic content and the thermal treatment temperature could be attractive for tuning the thermal stability and mechanical properties of the thiol-ene hybrid fibers to targeted values.

4.4 CONCLUSION

In this chapter, inorganic-organic hybrid fibers composed of a thiol-ene crosslinked network that contains POSS molecules have been successfully prepared directly from monomeric liquids by simultaneous centrifugal spinning and UV initiated thiol-ene chemistry. This robust and unique approach allows up to 80 wt% POSS to be chemically integrated into the thiol-ene network, simultaneously achieving both high loading and excellent dispersion of the inorganic material. Thermal treatments were performed on

fibers containing various ratios of organic and POSS thiol-ene monomers. Thermal, compositional, and mechanical studies were subsequently conducted to characterize the properties of fibers at elevated temperature.

It was observed that, owing to the Si-O-Si cage structure and its inorganic nature, POSS is highly effective in modulating the properties of thiol-ene fibers. Incorporating POSS enhanced the thermal stability and mechanical properties after thermal treatments at temperatures of up to 1000 ^{o}C that can be attributed to the preservation of a thermally stable network composed mostly of rigid POSS cage structures. Considering the simple and robust fabrication process and the tunable and enhanced fiber properties, these POSS containing thiol-ene fibers have potential applications as catalysis supports and filtration media, particularly in high temperature and harsh environments.

4.5 REFERENCES

1. Shanmuganathan, K.; Elliot, S. M.; Lane, A. P.; Ellison, C. J., *ACS Applied Materials & Interfaces* **2014,** *6* (16), 14259-14265.
2. Cramer, N. B.; Reddy, S. K.; Lu, H.; Cross, T.; Raj, R.; Bowman, C. N., *Journal of Polymer Science Part A: Polymer Chemistry* **2004,** *42* (7), 1752-1757.
3. Reddy, S. K.; Cramer, N. B.; Cross, T.; Raj, R.; Bowman, C. N., *Chemistry of Materials* **2003,** *15* (22), 4257-4261.
4. Eckel, Z. C.; Zhou, C.; Martin, J. H.; Jacobsen, A. J.; Carter, W. B.; Schaedler, T. A., *Science* **2016,** *351* (6268), 58-62.
5. Joshi, M.; Butola, B.; Simon, G.; Kukaleva, N., *Macromolecules* **2006,** *39* (5), 1839-1849.
6. Zeng, J.; Kumar, S.; Iyer, S.; Schiraldi, D. A.; Gonzalez, R., *High Performance Polymers* **2005,** *17* (3), 403-424.
7. Zhao, Y.; Schiraldi, D. A., *Polymer* **2005,** *46* (25), 11640-11647.
8. Iyer, S.; Schiraldi, D. A., *Macromolecules* **2007,** *40* (14), 4942-4952.
9. Milliman, H. W.; Ishida, H.; Schiraldi, D. A., *Macromolecules* **2012,** *45* (11), 4650-4657.
10. Fina, A.; Tabuani, D.; Frache, A.; Camino, G., *Polymer* **2005,** *46* (19), 7855-7866.

11. Milliman, H. W.; Boris, D.; Schiraldi, D. A., *Macromolecules* **2012,** *45* (4), 1931-1936.

12. Guenthner, A. J.; Lamison, K. R.; Lubin, L. M.; Haddad, T. S.; Mabry, J. M., *Industrial & Engineering Chemistry Research* **2012,** *51* (38), 12282-12293.

13. Naka, K.; Itoh, H.; Chujo, Y., *Nano Letters* **2002,** *2* (11), 1183-1186.

14. Létant, S. E.; Herberg, J.; Dinh, L. N.; Maxwell, R. S.; Simpson, R. L.; Saab, A. P., *Catalysis Communications* **2007,** *8* (12), 2137-2142.

15. Jefferson, L. U.; Netchaev, A. D.; Jefcoat, J. A.; Windham, A. D.; McFarland, F. M.; Guo, S.; Buchanan, R. K.; Buchanan, J. P., *ACS Applied Materials & Interfaces* **2015**.

16. Cozza, E. S.; Bruzzo, V.; Carniato, F.; Marsano, E.; Monticelli, O., *ACS Applied Materials & Interfaces* **2012,** *4* (2), 604-607.

17. Gardella, L.; Basso, A.; Prato, M.; Monticelli, O., *ACS Applied Materials & Interfaces* **2013,** *5* (16), 7688-7692.

18. Koo, S. H.; Lee, S. G.; Bong, H.; Kwark, Y.-J.; Cho, K.; Lim, H. S.; Cho, J. H., *Polymer* **2014,** *55* (11), 2661-2666.

19. Sparks, B. J.; Hoff, E. F.; Xiong, L.; Goetz, J. T.; Patton, D. L., *ACS Applied Materials & Interfaces* **2013,** *5* (5), 1811-1817.

20. Fang, Y.; Dulaney, A. D.; Gadley, J.; Maia, J. M.; Ellison, C. J., *Polymer* **2015,** *73*, 42-51.

21. Shanmuganathan, K.; Sankhagowit, R. K.; Iyer, P.; Ellison, C. J., *Chemistry of Materials* **2011,** *23* (21), 4726-4732.

22. O'Brien, A. K.; Cramer, N. B.; Bowman, C. N., *Journal of Polymer Science Part A: Polymer Chemistry* **2006,** *44* (6), 2007-2014.

23. Cramer, N. B.; Bowman, C. N., *Journal of Polymer Science Part A: Polymer Chemistry* **2001,** *39* (19), 3311-3319.

24. Fang, Y.; Dulaney, A. R.; Gadley, J.; Maia, J. M.; Ellison, C. J., *Polymer doi:10.1016/j.polymer.2016.02.029*.

25. Padron, S.; Fuentes, A.; Caruntu, D.; Lozano, K., *Journal of Applied Physics* **2013,** *113* (2), 024318.

26. Cole, M. A.; Bowman, C. N., *Journal of Polymer Science Part A: Polymer Chemistry* **2013,** *51* (8), 1749-1757.

27. Naumov, S.; Schöneich, C., *The Journal of Physical Chemistry A* **2009,** *113* (15), 3560-3565.

28. McNair, O. D.; Brent, D. P.; Sparks, B. J.; Patton, D. L.; Savin, D. A., *ACS Applied Materials & Interfaces* **2014,** *6* (9), 6088-6097.

29. Yang, G.; Kristufek, S. L.; Link, L. A.; Wooley, K. L.; Robertson, M. L., *Macromolecules* **2015**.

30. Senyurt, A. F.; Hoyle, C. E.; Wei, H.; Piland, S. G.; Gould, T. E., *Macromolecules* **2007,** *40* (9), 3174-3182.

31. Anseth, K. S.; Bowman, C. N.; Peppas, N. A., *Polymer Bulletin* **1993,** *31* (2), 229-233.

32. Beigi, S.; Yeganeh, H.; Atai, M., *Dental Materials* **2013,** *29* (7), 777-787.

33. Tibiletti, L.; Ferry, L.; Longuet, C.; Mas, A.; Robin, J.-J.; Lopez-Cuesta, J.-M., *Polymer Degradation and Stability* **2012,** *97* (12), 2602-2610.

34. Chrissafis, K.; Paraskevopoulos, K.; Bikiaris, D., *Thermochimica Acta* **2005,** *435* (2), 142-150.

35. Guo, W.; Leu, W.-T.; Hsiao, S.-H.; Liou, G.-S., *Polymer Degradation and Stability* **2006,** *91* (1), 21-30.

36. Wang, B.; Wang, Y.; Lei, Y.; Wu, N.; Gou, Y.; Han, C.; Fang, D., *Journal of Materials Chemistry A* **2014,** *2* (48), 20873-20881.

37. Colombo, P.; Mera, G.; Riedel, R.; Sorarù, G. D., *Journal of the American Ceramic Society* **2010,** *93* (7), 1805-1837.

38. Tarbell, D. S.; Harnish, D. P., *Chemical Reviews* **1951,** *49* (1), 1-90.

39. Senyurt, A. F.; Wei, H.; Hoyle, C. E.; Piland, S. G.; Gould, T. E., *Macromolecules* **2007,** *40* (14), 4901-4909.

40. Černý, M.; Chlup, Z.; Strachota, A.; Halasová, M.; Rýglová, Š.; Schweigstillová, J.; Svítilová, J.; Havelcová, M., *Ceramics International* **2015,** *41* (5), 6237-6247.

41. Mantz, R.; Jones, P.; Chaffee, K.; Lichtenhan, J.; Gilman, J.; Ismail, I.; Burmeister, M., *Chemistry of Materials* **1996,** *8* (6), 1250-1259.

42. Mutin, P. H., *Journal of the American Ceramic Society* **2002,** *85* (5), 1185-1189.

43. Liu, Y.; Huang, Y.; Liu, L., *Polymer Degradation and Stability* **2006,** *91* (11), 2731-2738.

44. Campostrini, R.; D'Andrea, G.; Carturan, G.; Ceccato, R.; Sorarù, G. D., *Journal of Materials Chemistry* **1996,** *6* (4), 585-594.

45. Pai, C.-L.; Boyce, M. C.; Rutledge, G. C., *Polymer* **2011,** *52* (26), 6126-6133.

46. Silberstein, M. N.; Pai, C.-L.; Rutledge, G. C.; Boyce, M. C., *Journal of the Mechanics and Physics of Solids* **2012,** *60* (2), 295-318.

Chapter 5: Solventless Manufacturing of Poly(butylene terephthalate) Nanofibers via Centrifugal Spinning[3]

5.1 INTRODUCTION

In the previous chapters, a new fiber fabrication method was described that couples centrifugal spinning and UV initiated thiol-ene polymerization. The underlying mechanics of the process were investigated and major factors that impact fiber formation, morphology, diameter, and properties were identified. Owing to the use of reactive monomers with multiple functional groups, the fibers that were formed are classified as thermosets. They contain a highly crosslinked network which allows them to be chemically inert in most organic solvents and thermally stable in that they can maintain their size and shape at temperatures of up to 400 ^{o}C.

Although it is envisioned that thiol-ene thermoset fibers have great potential in a number of specialty applications such as hot oil and air filtration, immobilization of catalysts for performing reactions, etc., the reality is that the current nonwovens industry primarily relies on thermoplastic polymers. Therefore, in the remainder of this dissertation, the focus will be on the production of thermoplastic fibers via melt state centrifugal spinning. As discussed in Chapter 1, low cost and high throughput production of micro- and nanofibers from commodity thermoplastics is still challenging and remains an active area of research. It is an even greater challenge to make nanofibers from high performance polymers, because these polymers do not dissolve in common organic solvents and typically have high melting temperatures required for demanding applications.

[3]This chapter is adapted from "Solventless high throughput manufacturing of poly(butylene terephthalate) nanofibers" published in *ACS Macro Letters* (2012). Kadhir Shanmuganathan and Yichen Fang contributed equally to design of experiments, data collection and analysis; Daniel Y. Chou, Sarah Sparks, Jarett Hibbert contributed to optimization of fiber spinning protocols; Prof. Christopher J. Ellison provided overall guidance of this project.

One example is poly(butylene terephthalate) (PBT), a semicrystalline engineering thermoplastic polymer that belongs to the class of linear aromatic polyesters. It is well known for its excellent chemical resistance, thermal stability, mechanical behavior, electrical resistance, low moisture absorption, etc.[1] The rapid crystallization kinetics of PBT as compared to poly(ethylene terephthalate) (PET)[2] leads to shorter cycle times in injection molding and hence this polymer has been used for a variety of applications in automobile parts, electrical components and consumer goods.[3, 4] PBT nanofibers with superior chemical resistance are very attractive for the filtration of physiological fluids and hot chemicals. Moreover, these nanofibers are a candidate to replace PET in tissue engineering applications as scaffolds for endothelial cells.[5]

However, PBT suffers from very limited solubility in common organic solvents and hence electrospinning of PBT nanofibers is typically performed with solvents such as trifluoroacetic acid or hexafluoropropanol.[4, 6] Apart from solvent recovery and productivity issues associated with electrospinning, these solvents may not be suitable for certain applications where solvent accumulation or toxicity is a major concern. Recently, Ellison et al.[7] demonstrated that melt blowing could be used to produce PBT nanofibers under special conditions. However, the process requires a very high velocity hot air jet which is also energy intensive. Using melt state centrifugal spinning, it is anticipated that many of the aforementioned challenges can be overcome to reveal a new pathway for high throughput melt processing of PBT micro- and nano-fibers. Our investigations will also show that these nanofibers have high crystallinity and enhanced molecular orientation which is important for realizing desirable physical and chemical properties of many high performance polymer fibers.

5.2 EXPERIMENTAL

5.2.1 Materials

PBT (Celanex 2008) was kindly donated by Ticona USA and used as received. The reported values of melting temperature and density of PBT are 228°C and 1.38-1.55 g/cm^3. PBT pellets were dried in an oven at 80 ^{o}C for at least 24 hours to remove any moisture on the pellet surface before centrifugal spinning.

5.2.2 Centrifugal spinning

PBT nanofibers were made by Forcespinning™ technology using a Cyclone L-1000M (FibeRio Technology Corporation). A 30 gauge stainless steel spinneret (89 mm in diameter) with 24 equally circumferentially spaced orifices (160 µm inner diameter) was used. In this set up, the spinneret assembly is heated from the top and bottom with temperature controlled radiant heater rings. A schematic diagram of the melt state centrifugal spinning apparatus and a digital photograph of the actual spinneret used in this study is shown in **Figure 5.1**.

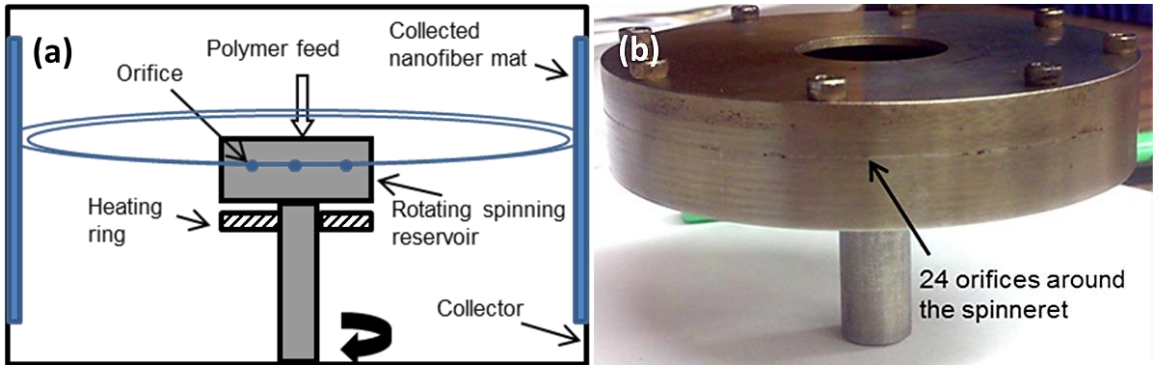

Figure 5.1: (a) A schematic representation of the melt state centrifugal spinning process and (b) an image of the 24-orifices spinneret used to spin PBT fibers in this study. Reprinted with permission from [8]. Copyright © 2012 American Chemical Society.

PBT fibers were spun at different spin speeds (10000, 12000, 15000 rpm) and temperatures (280, 300, 320 ˚C). For each run, the spinneret was heated to the desired temperature monitored by a thermocouple and then approx. 0.25g of PBT pellets were added through the spinneret opening in the top. Loading the polymer pellets after the desired temperature is reached instead of at the beginning of the heating cycle ensures that the polymer pellets were heated quickly (within one minute) in order to minimize sample degradation from oxygen and heat exposure. Additionally, purging the spinneret with an inert gas such as nitrogen or argon gas prior to melting the polymer also helps minimize polymer degradation if necessary. Molten PBT was extruded through the spinneret orifices due to centrifugal force during spinning. Cooled and solidified fibers were collected on the circumferential collector located 15 cm away from the spinneret.

After each experiment, a purge run was conducted to clear residual polymer from the spinneret. However, it should be noted here that the purge run cannot completely remove all residual polymer from the spinneret, and after several runs (typically no more than three), the resulting fiber quality becomes compromised due to residual built up. The best practice is to remove all polymer residuals completely by heating the spinneret at 350 ^{o}C (or above the degradation temperature of the polymer used) overnight after every single run.

5.2.3 Scanning electron microscopy (SEM)

A thin layer of fibers was attached to the SEM sample holder with double sided carbon tape and sputter coated with Au/Pd to minimize charging. The coated samples were imaged by a Hitachi S-4500 SEM at an accelerating voltage of 15 kV. Several low and high magnification images were taken from different areas of the sample. Fiber diameters of 200 to 250 fibers were measured from 15 to 20 randomly sampled SEM images using

an image analysis software (Image J, National Institute of Health). The average diameter and standard deviation of the fibers were reported and a histogram was constructed for each fiber sample.

5.2.4 Differential scanning calorimetry

Melting and crystallization behavior of the fiber samples was investigated by differential scanning calorimetry (DSC, DSC-1, Mettler Toledo). About 2 mg of fiber sample was used for each run and two runs were conducted at each condition to ensure reproducibility. The sample was held at 25 ˚C for two minutes, and then heated to 300˚C at a rate of 10˚C/min. The sample was held at 300 ˚C for two minutes before cooling down to 25˚C at a rate of 10˚C/min. The sample was again held at 25 ˚C for two minutes and heated to 300˚C at a rate of 10˚C/min. The peak values of the heating and cooling scans were taken as the melting and crystallization temperature, respectively. Percentage crystallinity was estimated from the area of melting endotherm using 140 J/g as the heat of fusion for 100% crystalline PBT.[9-11]

5.2.5 Rheometry

An AR2000ex rheometer (TA instruments) was used to study the effect of temperature on the rheological properties of the bulk material. Nitrogen gas was used at all times to avoid sample degradation. After conducting a strain sweep experiment to determine the linear viscoelastic region, oscillatory shear experiments were conducted on PBT resin at 10% strain with frequency ranging from 0.1Hz to 100 Hz. Experiments were conducted at multiple temperatures (260, 280, 300 and 320 ˚C) using 25 mm diameter steel parallel plates.

5.2.6 Optical microscopy

Molecular orientation within fibers was analyzed using an optical microscope (Olympus BX 60) with crossed polarizers. Fibers were sandwiched between a glass slide and a cover slip that was placed on a hot stage and the birefringence behavior imaged at different temperatures with an associated Nikon camera.

5.3 Results and Discussion

5.3.1 Fiber morphology

We report here the first melt extrusion of PBT nanofibers using the centrifugal spinning process. The percentage of nanofibers (based on the ratio of number of submicron diameter fibers to the total number of fibers in the sampling) was as high as 55%, with a range of 300 nanometers to several microns and an average fiber diameter close to one micron in most cases. This is especially interesting given the high mass throughput of this melt process compared to solution electrospinning. **Figure 5.2** and **5.3** show the representative SEM images of PBT nanofibers made under different processing conditions at high and low magnification. The fibers were smooth and defect free.

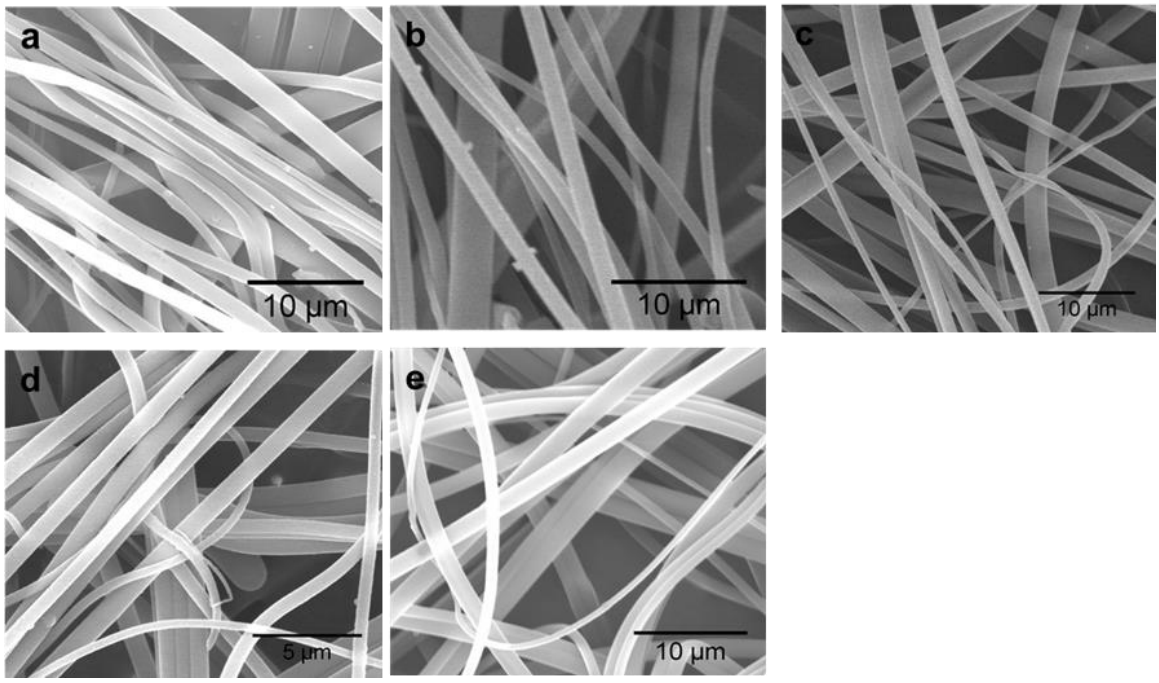

Figure 5.2: Representative SEM images of PBT nanofibers extruded under different conditions at high magnification. (a) 10000 rpm at 300 °C (b) 12000 rpm at 300 °C (c) 15000 rpm at 300 °C (d) 12000 rpm at 320 °C (e) 12000 rpm at 280 °C. Reprinted with permission from [8]. Copyright © 2012 American Chemical Society.

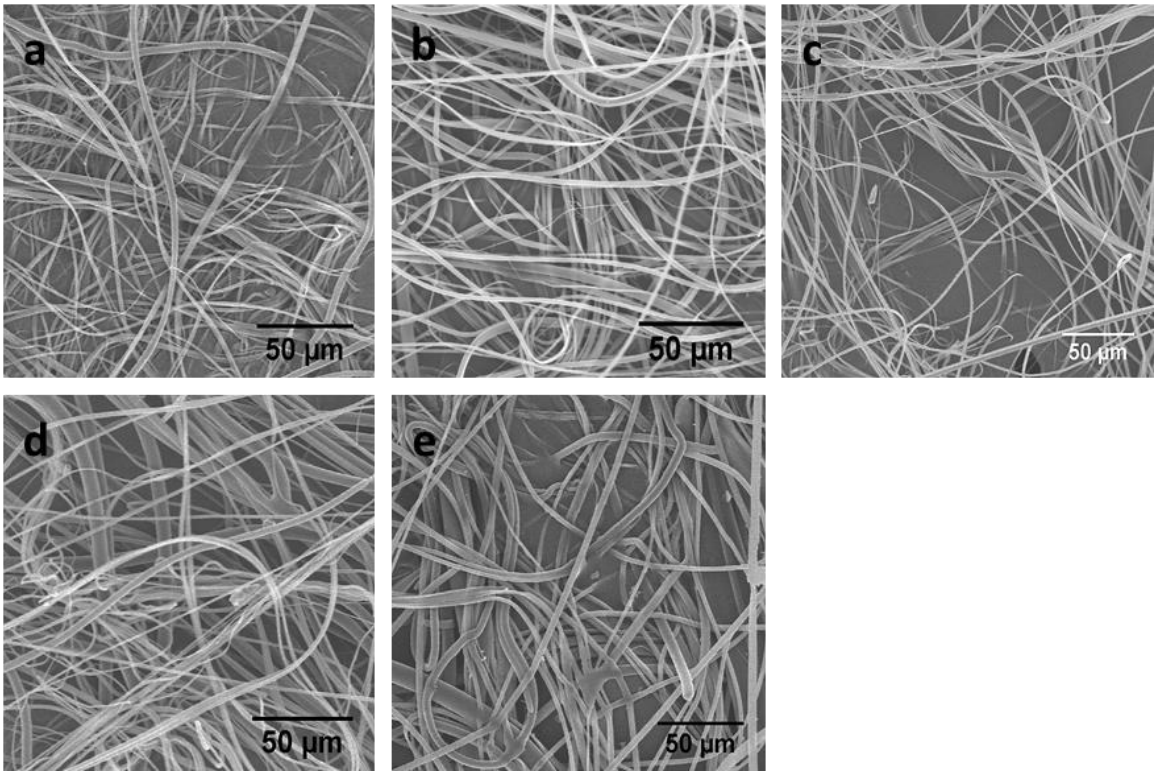

Figure 5.3: Representative SEM images of PBT nanofibers extruded under different conditions at low magnification. (a) 10000 rpm at 300 °C (b) 12000 rpm at 300 °C (c) 15000 rpm at 300 °C (d) 12000 rpm at 320 °C (e) 12000 rpm at 280 °C. Reprinted with permission from [8]. Copyright © 2012 American Chemical Society.

5.3.2 Effects of temperature and spin speed on fiber diameter

The fiber diameter is influenced by several variables including spinneret rotational speed (rpm), polymer melt/spinneret temperature, orifice diameter and collector distance. Our systematic investigations revealed that temperature has a stronger effect on fiber diameter distribution relative to other factors. PBT nanofibers were spun at an intermediate spin speed of 12000 rpm at three different polymer melt temperatures, 280 ^{o}C, 300 ^{o}C, and 320 ^{o}C.

To ensure reproducibility of the results, two batches of fibers were made independently for each condition and all SEM images were analyzed by separate

researchers. The average fiber diameter and other data related to fiber dimensions are based on the average of all measurements that were made (more than a few hundred per sample with random image sampling). Histograms of fiber diameters at different conditions were constructed using 25 bins across the entire fiber diameter distribution. We found this number of bins captures the nature of the distribution and results in a smoothened shape of the distribution. A sample histogram (for PBT fibers extruded at 12000 rpm and 320 ^{o}C) is shown in **Figure 5.4**. We found that fiber diameter distributions appear to follow a log-normal function;[7] this sample exhibits an average log(diameter, microns) of -0.0076 and standard deviation of 0.23. The fiber diameter distribution statistics for PBT fibers made at various conditions were analyzed accordingly and shown in **Table 5.1**.

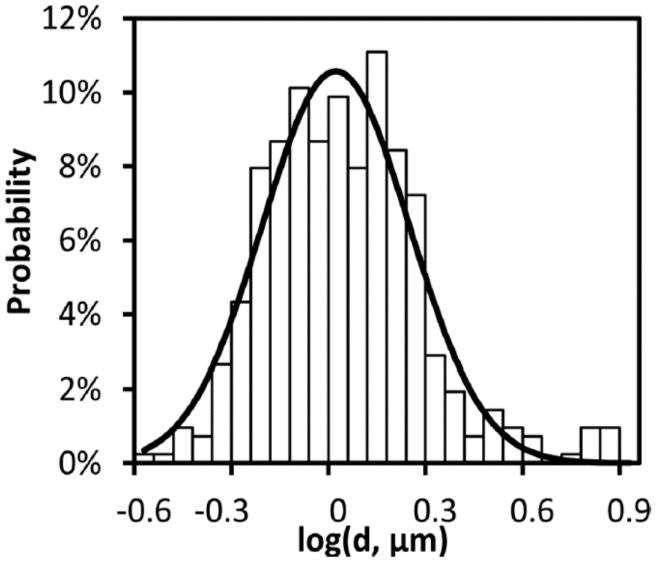

Figure 5.4: A sample fiber diameter histogram of PBT fibers (spun at 12000 rpm, 320 ^{o}C). Fiber diameter distribution was fit to logarithmic normal distributions (solid lines). Reprinted with permission from [8]. Copyright © 2012 American Chemical Society.

Sample	Rotational Speed (rpm)	Temperature (°C)	Average Fiber Diameter (μm)	%Nanofibers	25th percentile (μm)	50th percentile (μm)	75th percentile (μm)
A	10000	300	1.35 ± 0.78	36.3	0.85	1.20	1.67
B	12000	300	1.31 ± 0.68	40.4	0.79	1.19	1.67
C	15000	300	1.38 ± 0.68	27.7	0.96	1.26	1.61
D	12000	280	1.67 ± 1.02	25.8	0.99	1.53	2.05
E	12000	320	1.17 ± 0.92	54.5	0.66	0.94	1.36

Table 5.1: Average fiber diameter and diameter distribution information for PBT fibers made by centrifugal spinning at different processing conditions. Reprinted with permission from [8]. Copyright © 2012 American Chemical Society.

As shown in **Table 5.1**, increasing the spinneret temperature from 280 °C to 320 °C led to a significant increase in percentage of submicron fibers from 26 to 55%. The effect of processing temperature can influence fiber formation in different ways. First, increasing the extrusion temperature allows the polymer jet to remain in a molten state for a longer period of time promoting additional stretching before solidification by crystallization. The fiber cools rapidly due to its exposure to ambient air after it is ejected from the spinneret. Secondly, temperature has a significant effect on polymer melt viscosity. Dynamic shear experiments (**Figure 5.5**) revealed nearly an order of magnitude reduction in shear viscosity of PBT from 14.56 Pa-s at 280 °C to 0.88 Pa-s at 320 °C. Therefore, the thinner fibers obtained at higher extrusion temperatures could be due to lower viscosity and/or additional stretching before sufficient cooling takes place for onset of crystallization. With the fast crystallization kinetics of PBT, it is likely that the difference between the process and crystallization temperature has a more dominant effect than viscosity in controlling the fiber diameter.

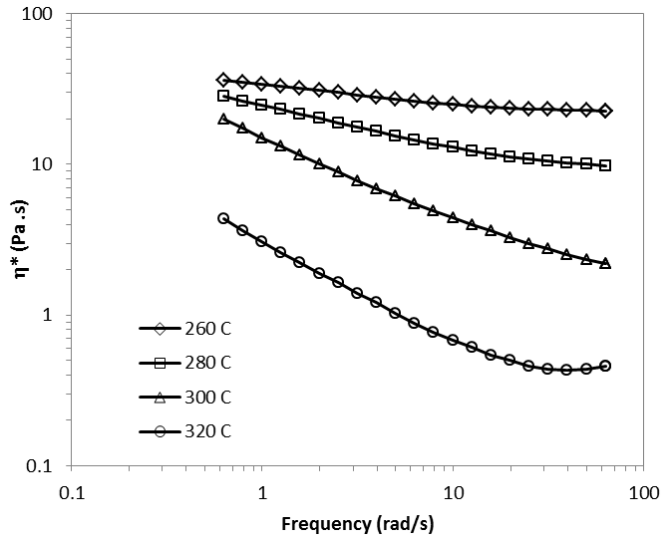

Figure 5.5: Complex viscosity of PBT resin at different temperatures. Reprinted with permission from [8]. Copyright © 2012 American Chemical Society.

On the other hand, spinneret rotational speed has a more subtle effect on PBT fiber formation for the conditions evaluated here. Below a spin speed of 10,000 rpm, a majority of fibers were between 1-3 microns in diameter (data now shown here). Increasing spin speed to 10,000 or 12,000 rpm resulted in a significant increase in the nanofiber population. While average fiber diameter was approximately the same, the percentage of submicron diameter fibers reduced slightly as the speed was increased from 10,000 or 12,000 to 15,000 rpm. At first glance, this appears counterintuitive as one may expect higher spinneret speeds to produce smaller fibers from enhanced stretching of the fiber with higher centrifugal forces. However, an important feature of this process is that it does not require a positive displacement feed system to deliver the melt through the orifice. In fact, the polymer mass flow rate through the spinneret is partially governed by pressure driven flow from the outward centrifugal force acting on the melt at the spinneret entrance. Thus it is possible that higher melt flow rates and associated larger fiber populations can result from

the aforementioned contrasting effects of higher rotational speed under some circumstances.

5.3.3 Structural and thermal properties of PBT fibers

An attractive aspect of these PBT nanofibers is their high crystallinity and enhanced molecular orientation. Polarized optical microscopy (**Figure 5.6**) of PBT fibers revealed birefringence behavior indicative of enhanced molecular orientation from the fiber stretching process. The birefringence diminished as the fibers were heated above 220 °C, near the melting point of the polymer.

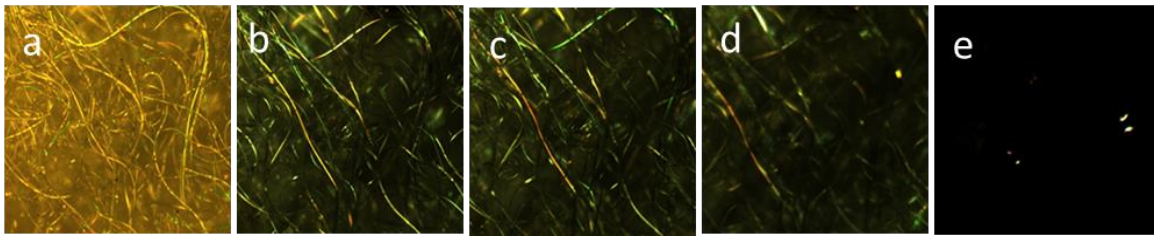

Figure 5.6: Polarized optical microscopy images at 10x magnification, showing birefringence behavior indicative of a high degree of molecular orientation in PBT fibers. From left to right (a) without cross polarizers at room temperature (b) with cross polarizers at room temperature (c) with cross polarizers at 200 °C (d) with cross polarizers at 220 °C (e) with cross polarizers at 240 °C. Reprinted with permission from [8]. Copyright © 2012 American Chemical Society.

The crystallinity can be estimated from the area under the melting peak of DSC thermograms (**Figure 5.7**) and the results are tabulated in **Table 5.2**. Irrespective of spinning speed, all PBT nanofibers displayed a high level of crystallinity (~40%), close to or slightly higher than bulk PBT pellets as measured from the DSC cooling curve. This is significantly different from what is generally observed in electrospun semicrystalline nanofibers, where the crystallinity of as spun fibers is typically low[12-15] and post processing is required to improve crystallinity. Though one could argue that fast crystallization

characteristics of PBT are helping to attain a higher degree of crystallinity, it is important to note that solution electrospun PBT nanofibers typically have lower crystallinity than the bulk resin.[4]

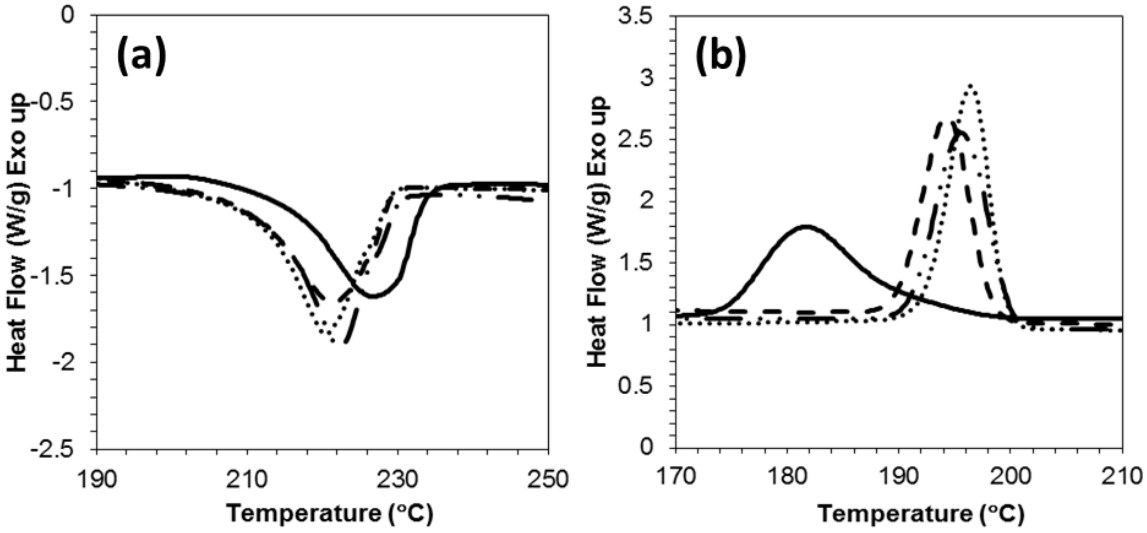

Figure 5.7: DSC thermograms of PBT nanofibers upon (a) first heating and (b) subsequent cooling. PBT pellet (solid line), PBT fibers at 10000 rpm (dotted line), PBT fibers at 12000 rpm (dashed line), PBT fibers at 15000 rpm (dash dot line). Reprinted with permission from [8]. Copyright © 2012 American Chemical Society.

Sample	T_m (°C)	T_{crys} (°C)	% Crystallinity
PBT Pellet	227 ± 1	181 ± 1	39.1 ± 0.8
Fibers 10000 rpm	220 ± 1	196 ± 1	38.4 ± 1.3
Fibers 12000 rpm	221 ± 1	193 ± 1	39.8 ± 0.5
Fibers 15000 rpm	221 ± 1	196 ± 1	42.0 ± 0.4

Table 5.2: Melting and crystallinity data of the PBT resin and PBT nanofibers made at various rotational speeds at 300 ˚C. +/- in temperature is standard instrument error while +/- in crystallinity is standard deviation from three independent measurements. Reprinted with permission from [8]. Copyright © 2012 American Chemical Society.

Although the fibers processed here at different spinning speeds displayed similar melting behavior, the peak melting temperature of the fibers was 6-7 °C lower than that of the bulk PBT resin. This could be due to smaller crystals or the presence of larger amounts of surface in nanofibers as compared to a bulk polymer. PBT is also known to exhibit polymorphic behavior with an α-crystal phase characterized by *gauche-trans-gauche* conformation of the 4 methylene segments and a β-crystal phase characterized by an extended *all-trans* conformation of the 4 methylene segments. Studies also report that the α-crystal phase is typically formed under relaxed crystallization conditions while the β-crystal phase is formed under stress[16]. The high extensional stress conditions present in the centrifugal spinning process and the confined geometry of nanofibers could favor specific crystal morphologies which may result in a shift in the peak melting temperature.

In the subsequent cooling scan (**Figure 5.7 b**), the PBT resin displayed a very broad crystallization exotherm with a peak at 181 °C, while all PBT fibers exhibited very narrow crystallization exotherms with peak crystallization temperatures between 193 and 196 °C. The molecular orientation present in the fibers is probably not completely erased in the first heating scan which could affect later crystallization processes. Completely erasing the memory of the fiber structure could require annealing for long periods of time, longer than were employed in this study. Nonetheless, the intrinsic molecular orientation and confinement effect induced by the fiber structure could enhance the number of nucleation sites increasing the crystallization temperature. An important finding is that the thermo-mechanical history applied to PBT nanofibers during centrifugal spinning seems to help attain enhanced molecular orientation and high crystallinity, two key features that contribute strongly to ultimate mechanical behavior and chemical stability of high performance semicrystalline polymer fibers.

Lastly, the chemical stability of PBT nanofibers were tested by immersing the fiber sample (12000 rpm, 300 ºC) in hot toluene at 60 °C for 24 hours. SEM image (**Figure 5.8**) reveals that the fibers remain intact with smooth surfaces after the hot toluene test. Additionally, there is no statistically significant change in fiber diameter, confirming the chemical stability of the PBT fibers.

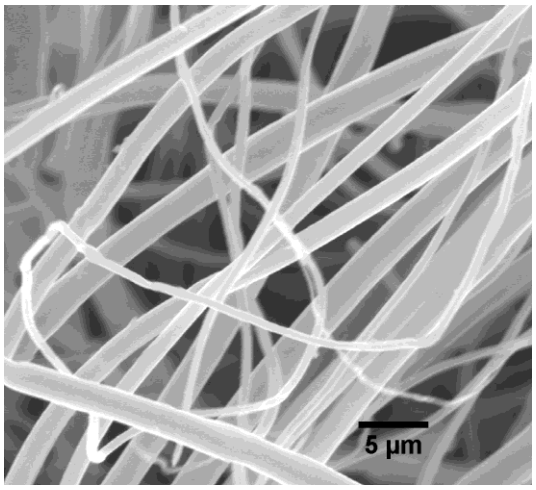

Figure 5.8: SEM image of fibers made at 12000 rpm at 300 °C after immersing in hot toluene at 60 °C for 24 hours. Reprinted with permission from [8]. Copyright © 2012 American Chemical Society.

5.4 CONCLUSION

In this chapter, we demonstrated a facile approach for high throughput manufacturing of micro- and nano-fibers from a high performance PBT polymer that doesn't dissolve in common organic solvents. While the fiber diameters fall within a range of 300 nm to several microns, we have shown that under optimized process conditions the population of submicron fibers can be as high as 55% with an average diameter close to one micron. Our results also show these nanofibers have high crystallinity comparable to the bulk resin and enhanced molecular orientation, which is crucial for realizing desirable physical and chemical properties of the high performance polymer fibers.

5.5 REFERENCES

1. Deshmukh, G. S.; Peshwe, D. R.; Pathak, S. U.; Ekhe, J. D., *Journal of Polymer Research* **2011,** *18* (5), 1081-1090.
2. Chuah, H. H., *Polymer Engineering & Science* **2001,** *41* (2), 308-313.
3. Banik, K.; Mennig, G., *Polymer Engineering & Science* **2008,** *48* (5), 957-965.
4. Catalani, L. H.; Collins, G.; Jaffe, M., *Macromolecules* **2007,** *40* (5), 1693-1697.
5. Ma, Z.; Kotaki, M.; Yong, T.; He, W.; Ramakrishna, S., *Biomaterials* **2005,** *26* (15), 2527-2536.
6. Forouharshad, M.; Saligheh, O.; Arasteh, R.; Farsani, R. E., *Journal of Macromolecular Science Part B-Physics* **2010,** *49* (4), 833-842.
7. Ellison, C. J.; Phatak, A.; Giles, D. W.; Macosko, C. W.; Bates, F. S., *Polymer* **2007,** *48* (11), 3306-3316.
8. Shanmuganathan, K.; Fang, Y.; Chou, D. Y.; Sparks, S.; Hibbert, J.; Ellison, C. J., *ACS Macro Letters* **2012,** *1* (8), 960-964.
9. Nichols, M. E.; Robertson, R. E., *Journal of Polymer Science Part B: Polymer Physics* **1992,** *30* (7), 755-768.
10. Huo, P. P.; Cebe, P., *Macromolecules* **1993,** *26* (12), 3127-3130.
11. Hanrahan, B.; Angeli, S.; Runt, J., *Polymer Bulletin* **1985,** *14* (5), 399-406.
12. Zong, X.; Kim, K.; Fang, D.; Ran, S.; Hsiao, B. S.; Chu, B., *Polymer* **2002,** *43* (16), 4403-4412.
13. Zhou, H. J.; Green, T. B.; Joo, Y. L., *Polymer* **2006,** *47* (21), 7497-7505.
14. Wang, M.; Jin, H.-J.; Kaplan, D. L.; Rutledge, G. C., *Macromolecules* **2004,** *37* (18), 6856-6864.
15. Wang, D.; Sun, G.; Chiou, B.-S.; Hinestroza, J. P., *Polymer Engineering & Science* **2007,** *47* (11), 1865-1872.
16. Carr, P. L.; Jakeways, R.; Klein, J. L.; Ward, I. M., *Journal of Polymer Science Part B: Polymer Physics* **1997,** *35* (15), 2465-2481.

Chapter 6: Tin Fluorophosphate Nonwovens by Melt State Centrifugal Forcespinning[4]

6.1 INTRODUCTION

Phosphate glasses are a collection of diverse inorganic ceramics that possess many unique properties such as optical transparency,[1-2] good chemical durability,[3-5] and high thermal expansion coefficients.[6-7] These properties make phosphate glasses excellent candidates for many applications, ranging from optical components, host matrices for radioactive waste, inorganic-metal sealing materials, and packaging.[1-10] In addition, phosphate glasses are known to behave like polymeric materials in the melt state[8, 11-12] and are regarded as inorganic polymers because they contain chains and crosslinked networks analogous to organic polymers.[13-16]

Phosphate glasses in fiber form have interesting properties that are not present in the bulk material such as a high surface area to volume ratio and a high degree of anisotropy. Ahmed et al. demonstrated the relevance of phosphate glass fibers in the biomedical and tissue engineering field as degradable bone repair materials, antibacterial delivery systems, and scaffolds.[17-20] Other researchers have used phosphate glass fibers for photonic and laser applications.[21-22] However, the production of large quantities of continuous inorganic phosphate glass fibers remains challenging. Due to the high melting temperature of phosphate glasses, excessive heating protocols exceeding 1000 ^{o}C are often required to melt process the glass into fibers.[17-20] In addition, the melt processes reported in the literature so far typically require manual drawing or other special fiber forming

[4]This chapter is adapted from "Tin fluorophosphate nonwovens by melt state centrifugal Forcespinning" published in *Journal of Material Science* (2014). Yichen Fang contributed to design of experiments, data collection and analysis; Matthew Herbert and Prof. David A. Schiraldi synthesized tin fluorophosphate glass used in this study; Prof. Christopher J. Ellison provided overall guidance for this project.

assemblies and the resulting phosphate fibers typically have average diameters in the range of tens or hundreds of microns with low aspect ratios.

A type of phosphate glass of particular interest in our study is tin fluorophosphate (TFP) glass, first prepared by Tick et al,[23] with a proposed idealized network structure[24-26] as shown in **Figure 6.1**. It is worth noting that this idealized structure is not strictly correct and one would expect the actual structure to contain dangling ends, loops, residual functional groups, etc. similar to other highly crosslinked polymeric networks. TFP glass has an unusually low glass transition temperature (T_g) of < 200 ºC, and is a liquid over a large temperature range.[25-28] This feature allows TFP to be mixed in the liquid state with commodity organic polymers using conventional polymer processing methods and conditions.[9-10, 29]

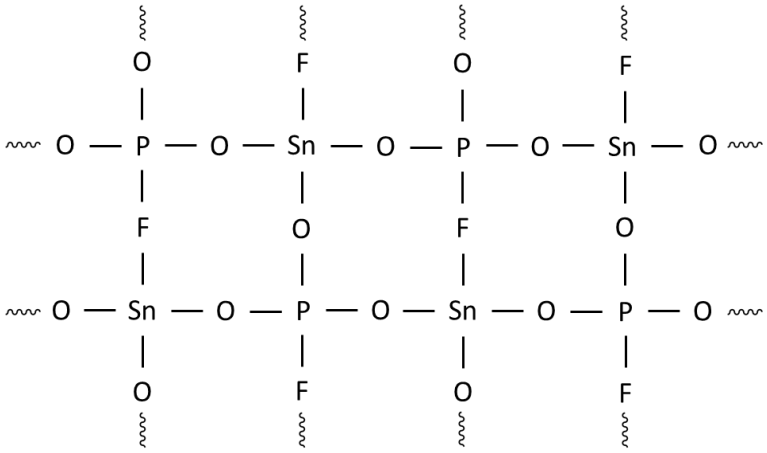

Figure 6.1: Proposed structure for TFP glass. Reprinted with permission from Ref. [30]. Copyright © 2014 Springer Science+Business Media New York.

In this chapter, we report the high throughput melt processing of continuous TFP glass fibers using centrifugal spinning. Previously, researchers have reported the production of inorganic nanofibers via centrifugal spinning of solutions containing inorganic precursors, followed by sintering of the fibers to produce the desired final

form.[31-32] In contrast, the present report describes a simple, one step melt processing of inorganic TFP glass fibers with diameters in the single micron range by taking advantage of the large drawing force of centrifugal spinning and the low T_g and polymeric nature of TFP glass. The thermal and structural properties of the resulting TFP fibers will also be the focus of the present chapter.

6.2 EXPERIMENTAL

6.2.1 TFP glass preparation

TFP glass was prepared as follows by Matthew Herbert from Prof. David Schiraldi's group at Case Western Reserve University. Reagent grade tin fluoride (SnF_2), tin oxide (SnO) and ammonium dihydrogen phosphate ($NH_4H_2PO_4$) were all used as received (Sigma-Aldrich). TFP glass was prepared on a 25 g scale with a molar composition of 50% SnF_2 + 20% SnO + 30% P_2O_5. The ingredients were carefully weighed, added into a closed jar and tumble mixed for 10-15 min to obtain a uniform mixture. This mixture was then transferred to a 50 mL capacity vitreous carbon crucible and was placed, uncovered, into a Thermolyne FA 1635 muffle furnace at 450 °C for 15 min. Fluid melts obtained using this procedure were quenched onto a stainless steel plate and annealed in an oven at approximately 20 °C above the T_g for about 90 min. The annealed glass was subsequently ground into a fine powder using an IKA Werke M20 universal mill. This process resulted in a TFP glass powder with a T_g of 100 ± 5 °C.

6.2.2 TFP glass fiber spinning

TFP glass was melt-processed into fibers by centrifugal spinning using a Fiberio Cyclone L-1000M. Commercially available spinnerets (FibeRio) with 24 orifices of 20 or 30 gauge diameter (inner diameters of 603 μm and 159 μm, respectively) were used in this study. The heater temperature was set to 320 ºC, while the spinneret temperature was

maintained at 270 ^{o}C. The TFP bulk powder was introduced into the spinneret and allowed to melt for 45 seconds prior to Forcespinning at 10,000 rpm. During spinning, the fibers were deposited on the collector ring that surrounds the rotating spinneret.

6.2.3 Thermal treatment of fibers

The neat fibers (NF) were pre-conditioned in ambient air in a Thermo-1000 furnace at 150, 200 and 250 ^{o}C for half an hour each, and thermally annealed at 300 ^{o}C for 1 hour (annealed fiber for 1 hour; AF1H) or 2 hour (AF2H). When the fibers were annealed directly at 300 ^{o}C without the aforementioned step-wise preconditioning, the fibers showed significant softening and developed wrinkles on the surface.

6.2.4 Fiber diameter distribution analysis

TFP glass fibers were imaged using a scanning electron microscope (Hitachi S-4500). Image analysis software (Image J^{TM}, National Institute of Health) was used to measure the fiber diameters of 150 randomly selected fibers from at least 15 high magnification SEM images taken at various areas across each fiber sample. The fiber diameter distributions were fit to logarithmic normal distributions as previously reported.[33]

6.2.5 Characterization of thermal properties

The glass transition behavior of the bulk TFP glass and fiber samples was investigated by differential scanning calorimetry (DSC, Mettler Toledo DSC-1). All DSC experiments were carried out in a dry N_2 atmosphere by first heating from 25 to 120 ^{o}C, cooling back to 25 ^{o}C, and then reheating to 350 ^{o}C in the second scan. All heating and cooling rates were 10 ^{o}C/min unless otherwise specified. The first heating was performed to remove any water condensed on the surface of the glass and to remove previous thermal history. The glass transition was measured using the second heating scan. Around 5 mg of

the bulk powder or fiber sample was used and the heat flow was normalized by the sample weight.

Thermal stability of TFP samples was studied using thermogravimetric analysis (TGA, Mettler Toledo TGA/DSC 1). The samples were conditioned at 25 ^{o}C for two minutes and then heated from room temperature to 500 ^{o}C at 10 ^{o}C/min in a dry N_2 atmosphere. The weight loss of an empty pan was subtracted from the weight loss of each sample to account for the buoyancy effect during heating.

6.2.6 Characterization of composition and structure

The elemental composition of bulk powder and fiber samples was investigated using an SEM (Hitachi S-5500) equipped with an energy-dispersive spectrometry (EDS) detector (Bruker EDS Quantax 4010). EDS data were analyzed by Esprit software (Bruker). The fibers were ground to a fine powder prior to imaging in order to receive sufficient signal for EDS analysis. The systematic errors in terms of atomic % from EDS analysis for fluorine (F), oxygen (O), tin (Sn), and phosphorus (P) were 4.75 %, 5.07%, 1.93%, and 0.47%, respectively.

Fourier Transform Infrared Spectroscopy (FTIR, Nicolet Magna IR 550) was used to study the structural change in TFP glass fibers. Bulk powder and ground fiber samples were dispersed in carbon tetrachloride to make a 1 wt% solution. The solution was deposited onto a 2 mm thick NaCl salt plate and dried to form a continuous film. The FTIR scans were conducted in transmission mode.

Wide angel X-ray diffractometry (WXRD) was used to investigate the structure of the TFP glass samples. The as-made TFP fibers were ground to a fine powder in order to receive good signal from the measurement.

6.3 Results and Discussion

6.3.1 Processing approach to TFP glass fiber

Figure 6.2 displays SEM images of TFP glass fibers at high and low magnification. The fibers were made from two spinnerets with different orifice sizes, 20 gauge and 30 gauge, which correspond to orifice inner diameters of 603 μm and 159 μm, respectively. When the orifice diameter was reduced, the fiber diameter distribution shifted significantly towards fibers with smaller diameters as shown in **Figure 6.2 c** and **f**. This can be expected because the initial fiber diameter is decreased by the smaller orifice and the material delivery rate through the smaller orifice decreases at a given centrifugal drawing force/speed. It is worth noting that other process variables, such as heating temperature and rotational speed, can also influence the average and distribution of fiber diameters.[34] The fiber diameter distribution of TFP glass fibers could be further fine-tuned for target applications by adjusting these process variables but this was beyond the scope of this study.

The fiber diameter distributions of the two fiber samples in **Figure 6.2** fit logarithmic normal (Gaussian) distributions, which is in accord with previously reported melt state centrifugal spinning and melt blowing of polymeric fibers.[33-34] The nominal and log average fiber diameters along with the fit parameters are reported in **Table 6.1**. To the best of our knowledge, these are the smallest phosphate glass fibers with high aspect ratio made directly by melt processing. In addition, the glass fibers in this report are already in a nonwoven form, which is advantageous for some applications. For example, bioresorbable composite materials made from nonwoven fibers can enhance the composite mechanical properties and lower the composite dissolution rate more than unidirectional fibers.[20] Nonwoven glass fibers made directly from this process obviate the need for post-

processing unidirectional glass fibers produced by other methods into a randomly oriented nonwoven mat, which may lead to fiber breakage and reduced aspect ratio.

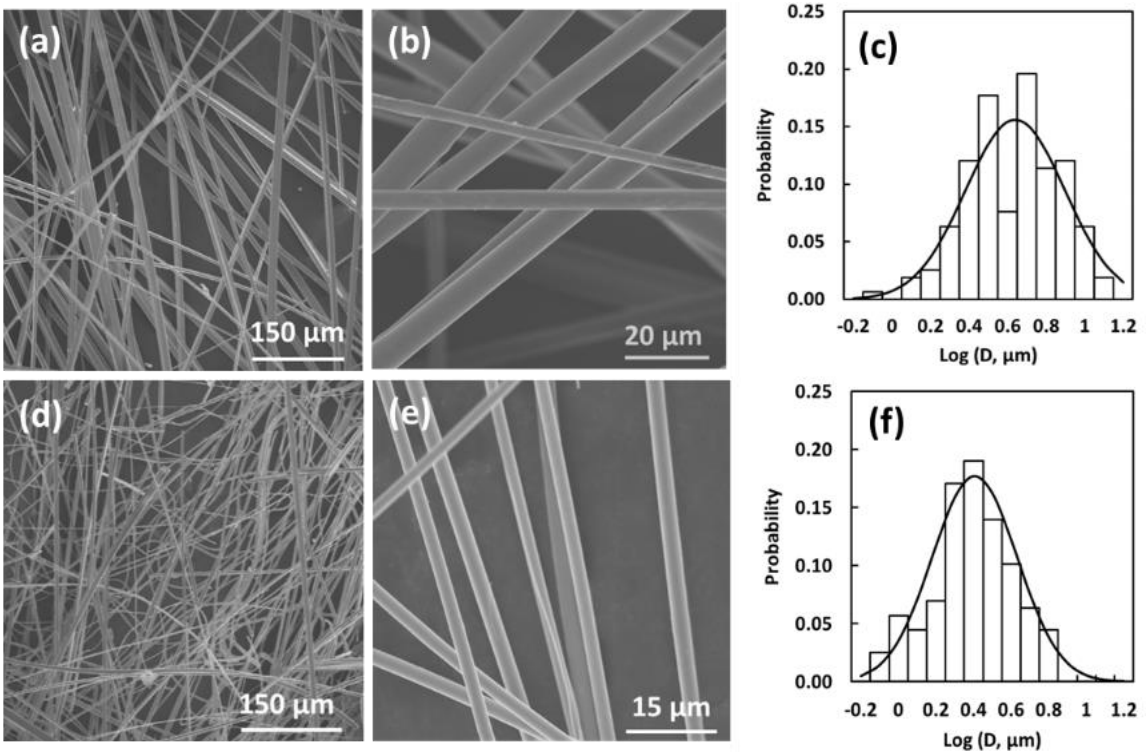

Figutre 6.2: Representative SEM images and fiber diameter distributions of TFP fibers made at 270 ºC, 10000 rpm, with a 20 gauge spinneret (a)-(c) and 30 gauge spinneret (d)-(f), respectively. The fiber diameter distributions were fit to logarithmic normal distributions (solid lines). Reprinted with permission from Ref. [30]. Copyright © 2014 Springer Science+Business Media New York.

Sample	Nominal Min. Dia. (µm)	Nominal Max. Dia. (µm)	Nominal Avg. Dia. (µm)	Log Avg. Dia. Log (µm)	Log Avg. Dia. from Gaussian Fit Log (µm)
20 Gauge	0.77	11.57	4.34 ± 2.24	0.58 ± 0.23	0.64 ± 0.26
30 Gauge	0.50	6.26	2.43 ± 1.16	0.34 ± 0.21	0.41 ± 0.23

Table 6.1: Fiber diameter distribution information for TFP fibers made by Forcespinning at 270 oC, 10000 rpm. Reprinted with permission from Ref. [30]. Copyright © 2014 Springer Science+Business Media New York.

6.3.2 Bulk and fiber thermal properties

In addition to the small and controllable fiber diameters, the as-made TFP fibers also exhibited interesting thermal behavior. As mentioned in the Experimental section, the as-spun fibers subjected to step-wise pre-conditioning prior to being thermally annealed at 300 ^{o}C retained their fiber shape and smooth fiber surface (see SEM images in **Figure 6.3**), while the fibers directly thermally annealed at 300 ^{o}C showed significant softening and developed a wrinkled fiber surface. The step-wise pre-conditioning treatments are therefore essential for developing smooth, nontextured fiber surfaces with desired final fiber properties.

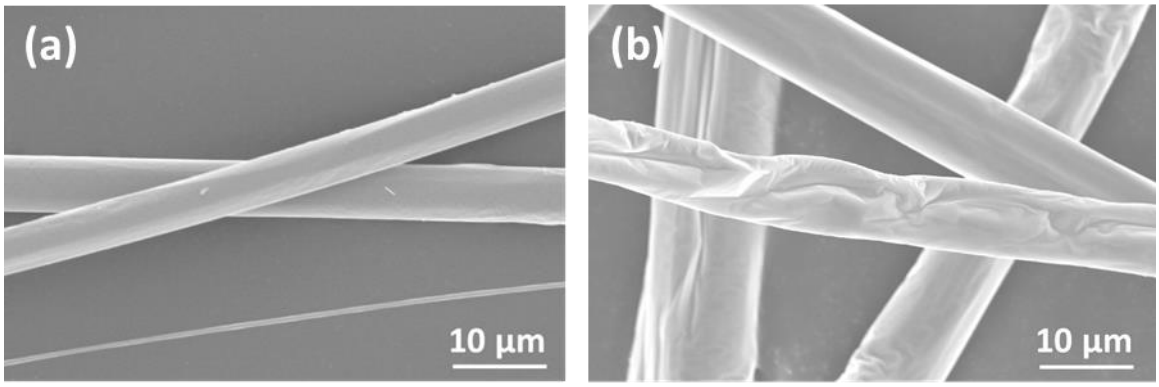

Figure 6.3: Representative SEM images of (a) neat fiber subjected to step-wise preconditioning before thermally annealing at 300 ^{o}C for 2 hours and (b) neat fiber directly thermally annealed at 300 ^{o}C for 2 hours. Reprinted with permission from Ref. [30]. Copyright © 2014 Springer Science+Business Media New York.

DSC thermograms (**Figure 6.4**) revealed that the T_g of NF was 20 ^{o}C higher than that of the bulk powder (BP). The increase in T_g of the NF can be as much as 50 ^{o}C, if the bulk powder was heated in the spinneret at a higher temperature or for a longer time during the spinning process. In addition, this change in T_g was partially reversed over time by storing NF samples in ambient air (NF Air) or in a dry desiccator (NF Dry) for 30 days.

The reversible change in T_g is likely due to the hygroscopic nature of phosphate glasses.[10, 35] First, water molecules that are physically absorbed in the glass network may act as plasticizers, enhancing the mobility of the phosphate backbone and hence reducing the T_g. Second, the P-O-P linkages in TFP glass are easily hydrolyzed by water,[28, 36-37] forming two chain ends terminated by hydroxyl groups (P-OH). This mechanism reduces the chain length and degree of crosslinks in the glass network, resulting in a lower T_g for the glass network. The first process is reversible depending on the thermodynamic equilibrium of water partitioning between the glass and ambient air,[35, 38] while the second process is reversible provided an appropriate chemical environment and thermal energy is present.[36]

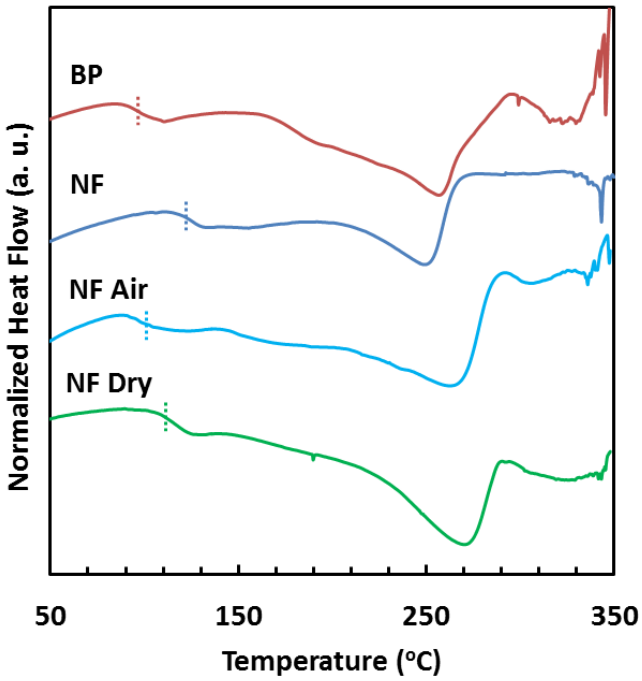

Figure 6.4: From top to bottom: DSC thermograms of bulk powder, neat fiber, neat fiber aged for 30 days in air or in a desiccator. Vertical dashed lines indicate the T_g. All DSC data have been normalized by sample weight and arbitrarily shifted vertically for clarity. Reprinted with permission from Ref. [30]. Copyright © 2014 Springer Science+Business Media New York.

During the spinning process, the glass powder was heated to a temperature much higher than its T_g; the chain mobility allows for the release of physically absorbed water while the thermal energy favors the dehydration of the hydroxyl group, forming bridging oxygen (BO) or P=O. Conversely, during the 30 day aging period, the fiber samples absorb moisture, reversing the previous process. The fiber sample stored in the desiccator absorbs less moisture than the fiber sample exposed to ambient air, and therefore has less reduction in T_g.

In addition, a series of control studies were conducted to explore other possible factors that may contribute to this reversible change in T_g. First, WXRD was used to investigate the structure of the TFP glass samples. The as-made TFP fibers were ground to a fine powder in order to receive sufficient signal from the measurement. The results are displayed in **Figure 6.5**. Both the bulk powder and the fibers exhibit only a broad amorphous halo from $2\Theta = 17^o$ to 35^o, indicating samples are completely amorphous. The WXRD results confirmed that the increase in glass transition temperature (T_g) of the fibers is not a result of development or change in crystal structure.

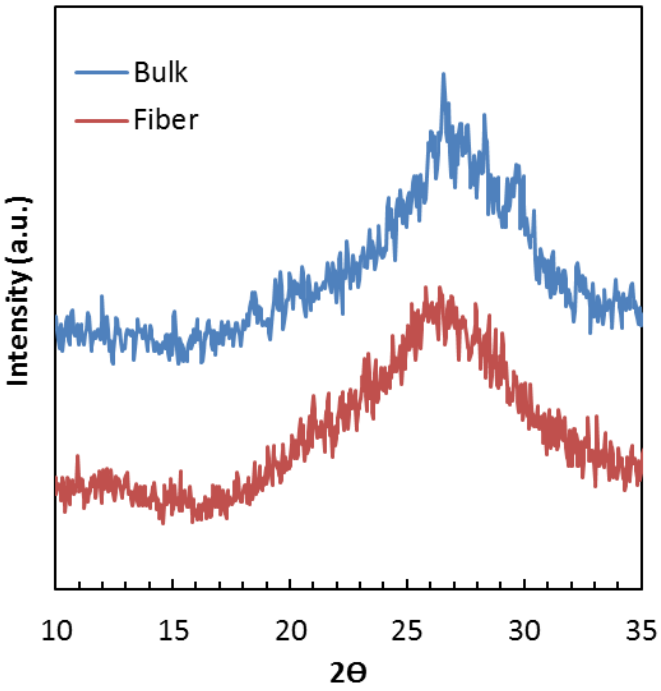

Figure 6.5: WXRD spectra of the bulk powder and the as-made fibers. Reprinted with permission from Ref. [30]. Copyright © 2014 Springer Science+Business Media New York.

A series of differential scanning calorimetry (DSC) control experiments were also conducted and the results are presented in **Figure 6.6** through **6.8**. One possible factor that may increase the T_g of TFP glass is the oxidation of tin (Sn) from Sn^{2+} to Sn^{4+}. To test this hypothesis, two batches of fibers were made under identical thermal conditions (heater temperature = 320 ^oC, melt temperature = 270 ^oC), and either ambient air or inert Argon (Ar) atmosphere was used. If tin oxidation plays an important role in changing T_g, then the increase in T_g will only be observed in the fibers made in air. However, as shown in **Figure 6.6**, the T_g of the fibers made in Ar increases by the same amount as that of the fibers made in air. This suggests that the oxidation of tin is not the cause of the change in T_g of as-made fibers.

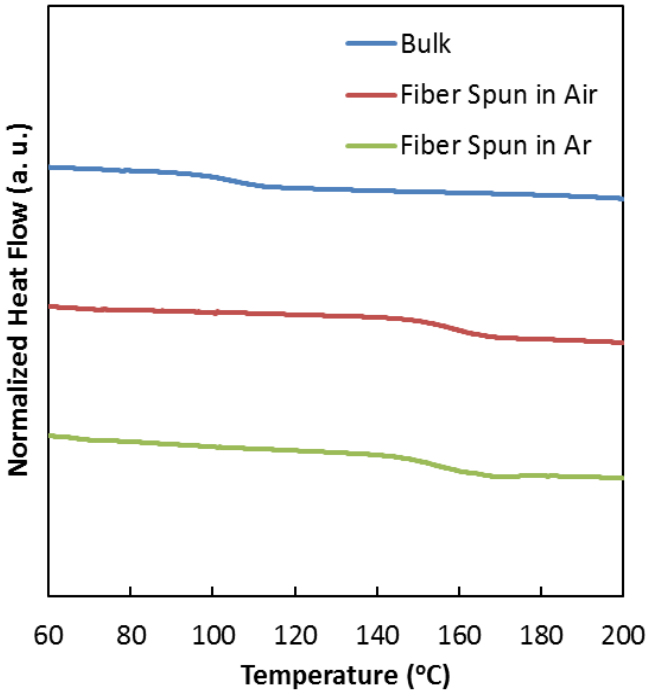

Figure 6.6: DSC thermograms of bulk powder, neat fibers made in air, and neat fibers made in Argon. All DSC data have been normalized by sample weight and arbitrarily shifted vertically for clarity. Reprinted with permission from Ref. [30]. Copyright © 2014 Springer Science+Business Media New York.

When subjected to rapid temperature quenching, an amorphous glass can vitrify in a non-equilibrium state, resulting in residual stress trapped in the network and a higher T_g compared to a glass cooled slowly to below its T_g. This phenomenon is relevant in our study because during fiber spinning, the temperature of the material drops rapidly from 270 ^oC to room temperature in less than a second. To investigate the effect of rapid quenching during the fiber spinning process, the bulk powder samples were quenched in DSC pans from 320 ^oC to room temperature at cooling rates of 5, 20, and 100 ^oC/min. The Tg's of the samples were measured using a second heating scan at 20 ^oC/min. As shown in **Figure 6.7**, the T_g of bulk powder is independent of the quench rate in the DSC, indicating that the

increase in as-made fiber T_g is not due to a rapid temperature decline during the fiber spinning process.

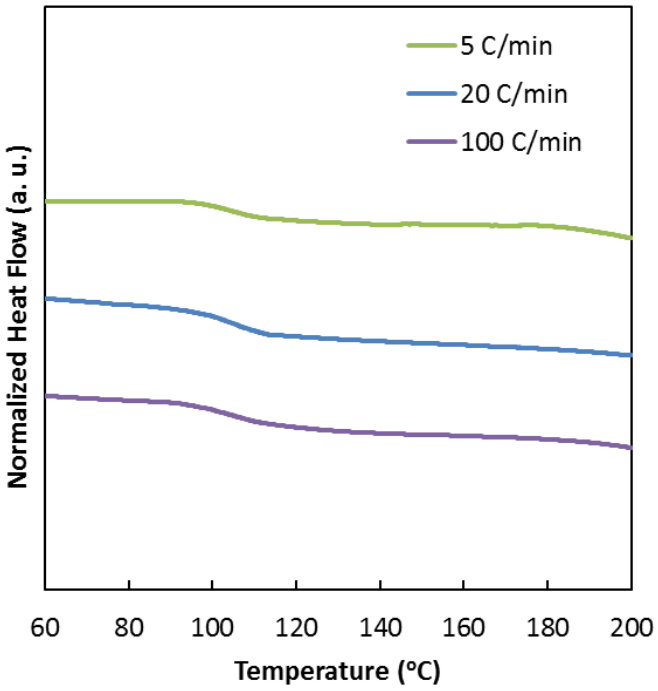

Figure 6.7: DSC thermograms of bulk powder with cooling rates of 5, 20, or 100 °C/min followed by a second heating scan at 20 °C/min for all three samples. All DSC data have been normalized by sample weight and arbitrarily shifted vertically for clarity. Reprinted with permission from Ref. [30]. Copyright © 2014 Springer Science+Business Media New York.

In addition to quenching, rapid deformation of melt into glass fiber by centrifugal force and air drag may also induce stress and lead to an increase in T_g. Here, the bulk powder was heated in the DSC pan at 320 °C for 3 minutes in air atmosphere and the T_g was subsequently measured by a second heating scan. This experiment was designed to mimic the fiber spinning heating procedure but without the deformation and the result is shown in **Figure 6.8**. The T_g of bulk powder annealed for 3 minutes in the DSC increases by 50 °C compared to the T_g of bulk powder without annealing, confirming that rapid

deformation is not the cause of the increase in T_g of the fibers. The results of these control studies suggest that the reversible change in T_g is most likely caused by thermodynamics driven water absorption / desorption of TFP glass fibers.

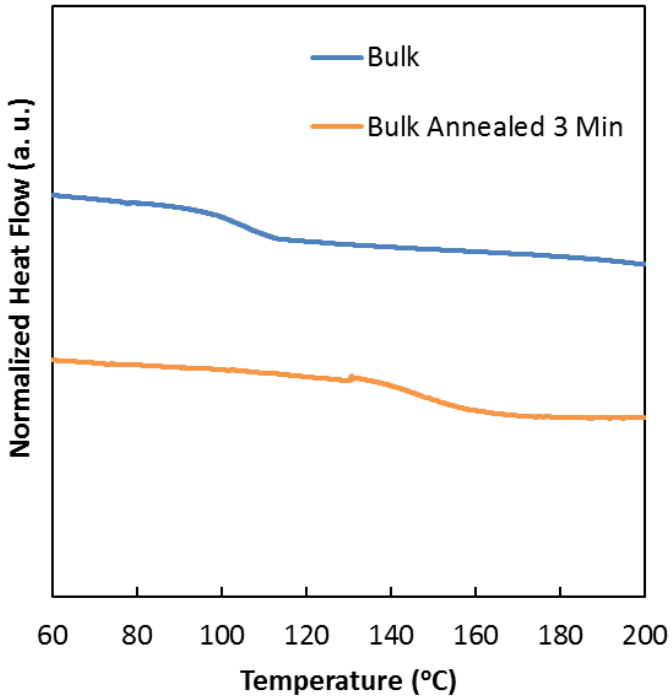

Figure 6.8: DSC thermograms of bulk powder with or without annealing in ambient, extra dry air. All DSC data have been normalized by sample weight and arbitrarily shifted vertically for clarity. Reprinted with permission from Ref. [30]. Copyright © 2014 Springer Science+Business Media New York.

Apart from the reversible T_g change, fibers that were made and then thermally annealed as previously described (AF1H and AF2H) also exhibited enhanced thermal stability compared to the original TFP glass powder (BP) and neat fiber. In **Figure 6.9 a**, the T_g of the bulk and fiber samples is labeled by vertical dashed lines, while the onset of the primary endothermic peak is indicated by an asterisk. This endothermic peak is not due to a melting transition because both the bulk powder and the fiber samples were confirmed to be completely amorphous by WAXD (**Figure 6.5**). The onset of the primary

endothermic peak is superimposed onto the TGA thermograms shown in **Figure 6.9 b** and corresponds well with the onset of weight loss, suggesting that the endothermic event in DSC is due to the evaporation of volatile components. An interesting feature is the plateau between 260 ºC and 345 ºC of the NF sample, which is present in both the DSC and TGA trace, again reflecting that the DSC endothermic peak and the TGA weight loss are closely related.

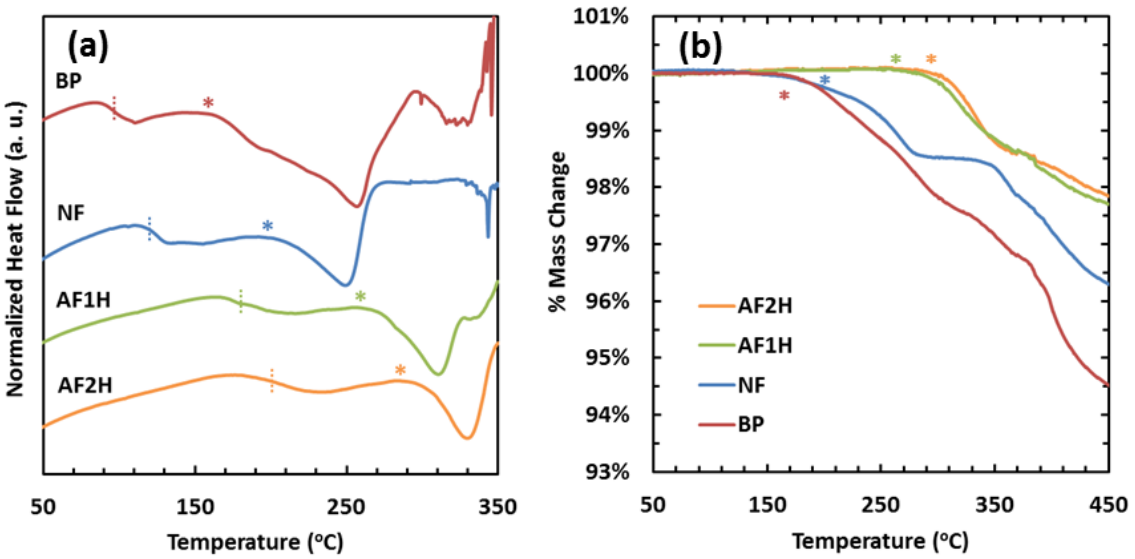

Figure 6.9: (a) DSC and (b) TGA thermograms of bulk powder (red), neat fibers (blue), annealed fibers at 300 ºC for 1 hour (green), and annealed fibers at 300 ºC for 2 hours (orange). All DSC data have been normalized by sample weight and arbitrarily shifted vertically for clarity. Reprinted with permission from Ref. [30]. Copyright © 2014 Springer Science+Business Media New York.

Comparing BP and AF2H, the T_g is increased from 100 ºC to 205 ºC and the onset of the evaporation and weight loss increased from 160 ºC to 290 ºC. Although drastic, this trend is expected, because both the fiber spinning and thermal annealing can be considered a dehydration process as previously explained, forming a more rigid glass network. Ehrt et al. also showed that TFP glass with a higher glass transition and lower OH content

exhibits better optical properties and chemical durability after seven years than one with a lower glass transition and higher OH content.[37] Along with the thermal stability, the thermally treated TFP fibers could be excellent candidates for catalysis and chemical filtration applications.

The thermally annealed TFP glass fibers were able to retain their shape up to 350 ^{o}C, which is much higher than the T_g of the starting BP as well as NF. This is atypical for a completely amorphous material, and suggests that other structural and compositional changes may have occurred in addition to dehydration.

6.3.4 Compositional and structural investigations

To investigate the compositional change of TFP bulk and fiber samples, semi-quantitative SEM-EDS analyses were conducted and the results are presented in **Figure 6.10**. There is no statistically significant compositional change between the bulk powder and the neat fiber sample. However, the thermally annealed fiber samples showed significant loss in F and gain in O, which agreed with previous observations of volatilization of F by Ehrt and others.[36-37] Further, the Sn and P content remains constant in all samples, suggesting that Sn is a network forming cation instead of network doping modifier for TFP glass.[25] This also indicates that the backbone structure (Sn-O-P-O) for TFP glass fibers is retained during thermal annealing.

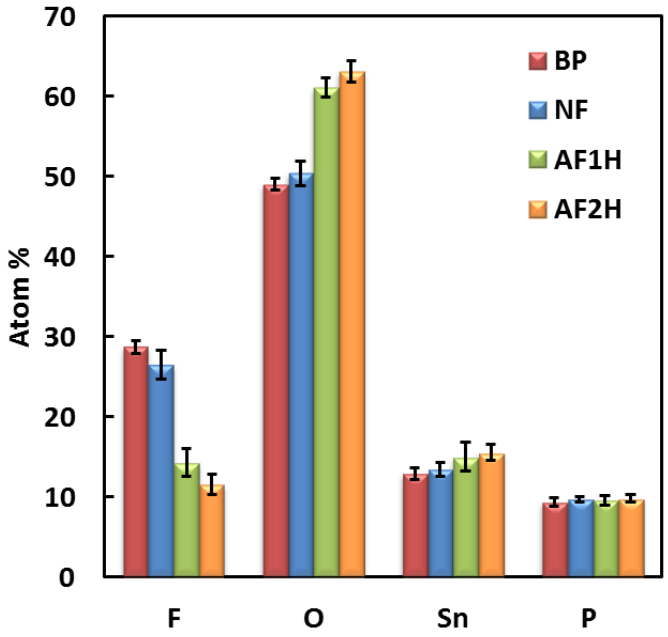

Figure 6.10: Atomic composition of TFP bulk and fiber samples from SEM-EDS. The scale bars represent statistical errors of 8 measurements from each sample. Systematic errors are reported in the experimental procedure. Reprinted with permission from Ref. [30]. Copyright © 2014 Springer Science+Business Media New York.

The atomic ratio between oxygen and phosphorus is an indicator of the degree of polymerization and crosslinking in phosphate glasses.[16, 39-40] As shown in **Figure 6.11**, AF1H and AF2H have higher O/P ratio than BP and NF, suggesting the presence of longer chains and a more crosslinked structure, both of which could hinder chain mobility and result in higher T_g. Such dependence of T_g on O/P has also been observed in aluminum phosphate glass.[41]

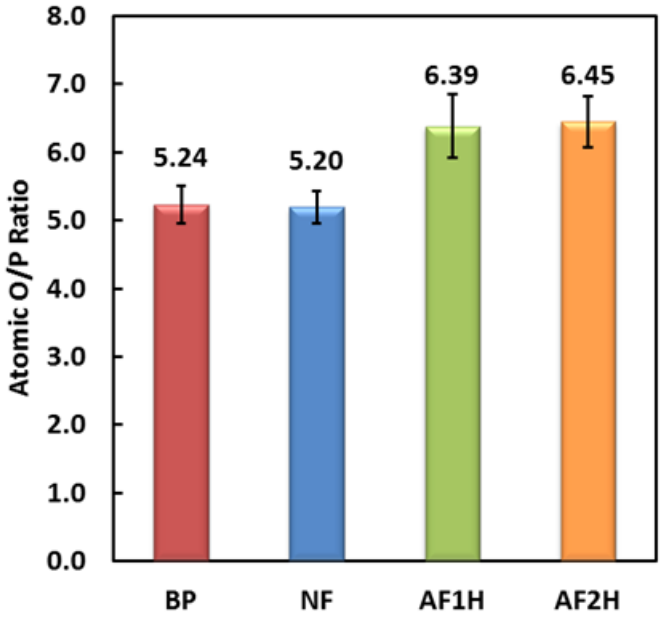

Figure 6.11: Atomic O/P ratio of TFP bulk and fiber samples. Reprinted with permission from Ref. [30]. Copyright © 2014 Springer Science+Business Media New York.

The atomic ratio between F and O is also significant as it not only affects the mass density and chemical durability,[25, 27-28] but also the thermal properties of TFP glass.[25] **Figure 6.12** shows that the T_g of TFP glass samples increases linearly as the F/O ratio decreases from 0.6 to 0.2 as a result of prolonged thermal treatment either during centrifugal spinning or post spinning thermal annealing. A similar correlation between T_g and the F/O ratio has been observed by Xu et al. for TFP containing the same initial P_2O_5 content but varied F/O ratio.[25] Sn-F-Sn, P-F-Sn and P-F-P linkages are believed to be weaker than Sn-O-Sn, P-O-Sn and P-O-P linkages. As F/O ratio decreases, the fluorine bonds are gradually replaced by the stronger oxygen bonds. The loss of F in conjunction with dehydration during thermal annealing again increases the network rigidity and consequently the T_g.

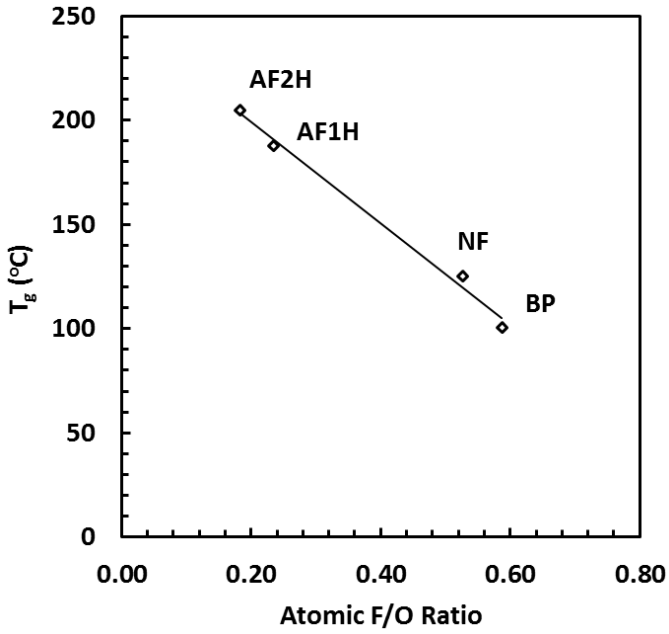

Figure 6.12: The effect of compositional change on T_g of the TFP fibers. Reprinted with permission from Ref. [30]. Copyright © 2014 Springer Science+Business Media New York.

FTIR spectroscopy was employed to investigate the structural evolution of the TFP glass after spinning and various stages of thermal annealing. The transmission FTIR spectra are shown in **Figure 6.13**. The transmittance at 1400 cm^{-1}, indicated by open circles, corresponds to the H-OH bending vibration.[25] The transmittance valley gradually diminishes as BP was made into NF, and even more markedly for the subsequently thermally annealed fibers, again confirming the release of structural water by prolonged heating. The complete disappearance of the valley for the AF2H sample indicates that the fiber sample was almost completely anhydrous after two hours of annealing at 300 °C.

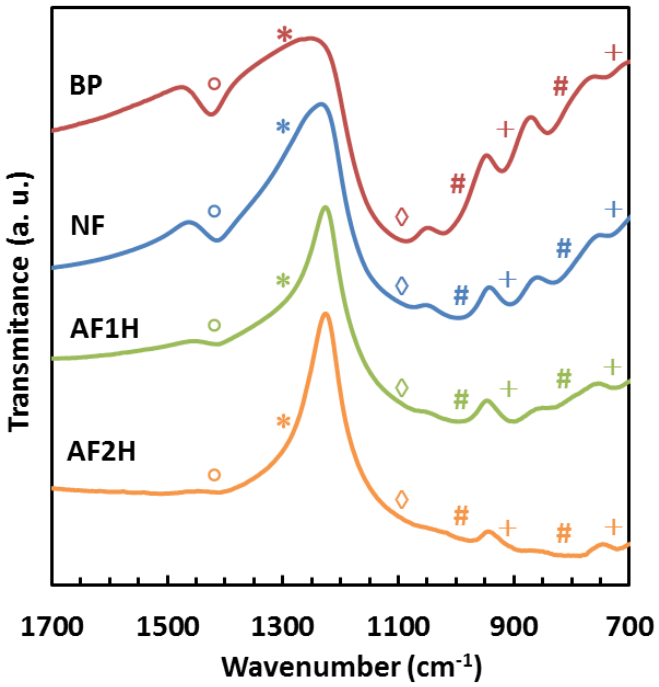

Figure 6.13: From top to bottom: FTIR spectra of BP, NF, AF1H and AF2H. All data have been shifted vertically for clarity. Reprinted with permission from Ref. [30]. Copyright © 2014 Springer Science+Business Media New York.

The asterisks at 1250-1300 cm^{-1} indicate the P=O stretching vibrations,[25, 42-44] while the open diamonds at 1100 cm^{-1} indicate the $P\text{-}O^-$ stretching vibrations[25, 42-45] of either the Sn-O-P linkage[25] or the phosphate group bonded to a non-bridging oxygen (NBO) in a Q^0, Q^1, or Q^2 state. As TFP glass samples undergo a series of thermal treatments, the transmission due to the P=O stretching vibration increases (decreasing P=O content) while the transmission due to $P\text{-}O^-$ stretching vibrations increases (decreasing $P\text{-}O^-$ content). Since Sn acts as a network former and the -Sn-O-P- linkage is strong, it is likely that the reduced $P\text{-}O^-$ groups is due to the annihilation of terminating hydroxyl groups, forming BO through polycondensation at elevated temperature. This again complements the EDS compositional analysis and suggests that the thermally annealed fibers contain more

crosslinks, which explains the enhanced thermal stability of the fiber samples with longer annealing time.

The transmittance valleys indicated by the '#' symbols at 1000 cm^{-1} and 820 cm^{-1} can be assigned to P-F vibrations; they are detectable because the fluorine content is high with F/O ratios greater than 0.3[25] for all samples investigated in this study. The transmittance valleys at 900 cm^{-1} and 720 cm^{-1} indicated by the '+' symbols are attributed to P-O-P stretching and bending vibrations, respectively. These absorption bands become less resolved as thermal treatment proceeds, perhaps due to the large loss of fluorine, and the less ideal glass structure that results.

6.4 CONCLUSION

Taking advantage of the low Tg and polymeric nature of TFP glass and the large fiber drawing force of Forcespinning, inorganic TFP nonwoven fibers with single micron average diameters were produced directly from the melt state. As-made fibers have a T_g that is 20 ^oC higher than the bulk powder, which can be reversed back to the T_g of the bulk powder by exposing the fibers to ambient air. This change is caused by removal of hydroxyl end groups and/or removal of physically absorbed water from the glass network during the brief heating of the spinning process.

After thermal treatment, the fibers exhibit close to a 100 ^oC increase in T_g and enhanced thermal stability as determined by DSC, TGA, and microscopy. SEM-EDS analysis of bulk and fiber samples reveals increasing loss of fluorine during thermal annealing, while FTIR data suggests the occurrence of dehydration with prolonged heating. Both changes lead to formation of a more rigid and crosslinked glass network and contribute to the enhanced thermal stability and increase in T_g of the thermally annealed fiber samples.

6.5 REFERENCES

1. Fletcher, L. B.; Witcher, J. J.; Troy, N.; Brow, R. K.; Krol, D. M., *Optics Letters* **2012,** *37* (7), 1148-1150.
2. Fletcher, L. B.; Witcher, J. J.; Troy, N.; Reis, S. T.; Brow, R. K.; Krol, D. M., *Optics Express* **2011,** *19* (9), 7929-7936.
3. Day, D.; Wu, Z.; Ray, C.; Hrma, P., *Journal of Non-Crystalline Solids* **1998,** *241* (1), 1-12.
4. Yu, X.; Day, D. E.; Long, G. J.; Brow, R. K., *Journal of Non-Crystalline Solids* **1997,** *215* (1), 21-31.
5. Reis, S.; Karabulut, M.; Day, D., *Journal of Non-Crystalline Solids* **2001,** *292* (1), 150-157.
6. He, Y.; Day, D., *Glass Technology* **1992,** *33* (6), 214-219.
7. MINAMF, T.; Mackenzie, J. D., *Journal of the American Ceramic Society* **1977,** *60* (5-6), 232-235.
8. Wei, T.; Hu, Y.; Hwa, L., *Journal of Non-Crystalline Solids* **2001,** *288* (1), 140-147.
9. Gupta, M.; Lin, Y.; Deans, T.; Baer, E.; Hiltner, A.; Schiraldi, D. A., *Macromolecules* **2010,** *43* (9), 4230-4239.
10. Gupta, M.; Lin, Y.; Deans, T.; Crosby, A.; Baer, E.; Hiltner, A.; Schiraldi, D. A., *Polymer* **2009,** *50* (2), 598-604.
11. Cha, J.; Asida, Y.; Takebe, H. In *Analysis of Viscoelastic Flow in Tin Phosphate Glass*, IOP Conference Series: Materials Science and Engineering, IOP Publishing: **2011**; p 112014.
12. Chang, K.; Lee, T.; Hwa, L., *Chinese Journal of Physics* **2003,** *41* (4), 414-21.
13. Hudgens, J. J.; Martin, S. W., *Journal of the American Ceramic Society* **1993,** *76* (7), 1691-1696.
14. Ray, N. H., *British Polymer Journal* **1979,** *11* (4), 163-177.
15. Otaigbe, J. U.; Beall, G. H., *Trends in Polymer science* **1997,** *5* (11), 369-379.
16. Brow, R. K., *Journal of Non-Crystalline Solids* **2000,** *263*, 1-28.
17. Ahmed, I.; Lewis, M.; Olsen, I.; Knowles, J., *Biomaterials* **2004,** *25* (3), 501-507.
18. Abou Neel, E.; Ahmed, I.; Pratten, J.; Nazhat, S.; Knowles, J., *Biomaterials* **2005,** *26* (15), 2247-2254.
19. Nazhat, S. N.; Abou Neel, E. A.; Kidane, A.; Ahmed, I.; Hope, C.; Kershaw, M.; Lee, P. D.; Stride, E.; Saffari, N.; Knowles, J. C., *Biomacromolecules* **2007,** *8* (2), 543-551.

20. Ahmed, I.; Jones, I.; Parsons, A.; Bernard, J.; Farmer, J.; Scotchford, C.; Walker, G.; Rudd, C., *Journal of Materials Science: Materials in Medicine* **2011,** *22* (8), 1825-1834.

21. Cai, M.; Painter, O.; Vahala, K.; Sercel, P., *Optics Letters* **2000,** *25* (19), 1430-1432.

22. Li, L.; Schülzgen, A.; Temyanko, V.; Qiu, T.; Morrell, M.; Wang, Q.; Mafi, A.; Moloney, J.; Peyghambarian, N., *Optics Letters* **2005,** *30* (10), 1141-1143.

23. Tick, P. A., *Physics and Chemistry of Glasses* **1984,** *25* (6), 149-154.

24. Tanner, T.; Oelgoetz, J.; Golovchak, R.; Brennan, C.; Kovalskyy, A., *Bulletin of the American Physical Society* **2013,** *58*.

25. Xu, X.; Day, D., *Physics and Chemistry of Glasses* **1990,** *31* (5), 183-187.

26. Urman, K.; Otaigbe, J. U., *Progress in Polymer Science* **2007,** *32* (12), 1462-1498.

27. Shaw, C. M.; Shelby, J. E., *Physics and Chemistry of Glasses* **1988,** *29* (2), 49-53.

28. Shaw, C.; Shelby, J. E., *Physics and Chemistry of Glasses* **1988,** *29* (3), 87-90.

29. Tischendorf, B. C.; Harris, D. J.; Otaigbe, J. U.; Alam, T. M., *Chemistry of Materials* **2002,** *14* (1), 341-347.

30. Fang, Y.; Herbert, M.; Schiraldi, D. A.; Ellison, C. J., *Journal of Materials Science* **2014,** *49* (24), 8252-8260.

31. Bell, N. S.; Missert, N. A.; Garcia, R. M.; Nagasubramanian, G.; Leung, K.; Rempe, S. L.; Rogers, D. M. *Surface Engineering of Electrospun Fibers to Optimize Ion and Electron Transport in Li% 2b Battery Cathodes*; Sandia National Laboratories: **2012**.

32. LOZANO, K.; ALTECOR, A.; MAO, Y., *Functional Materials Letters* **2012,** *05* (03), 1250020.

33. Ellison, C. J.; Phatak, A.; Giles, D. W.; Macosko, C. W.; Bates, F. S., *Polymer* **2007,** *48* (11), 3306-3316.

34. Shanmuganathan, K.; Fang, Y.; Chou, D. Y.; Sparks, S.; Hibbert, J.; Ellison, C. J., *ACS Macro Letters* **2012,** *1* (8), 960-964.

35. Nogami, M.; Nagao, R.; Wong, C., *The Journal of Physical Chemistry B* **1998,** *102* (30), 5772-5775.

36. Ebendorff-Heidepriem, H.; Seeber, W.; Ehrt, D., *Journal of Non-Crystalline Solids* **1993,** *163* (1), 74-80.

37. Ehrt, D., *Journal of Non-Crystalline Solids* **2008,** *354* (2), 546-552.

38. Nogami, M.; Nagao, R.; Wong, C.; Kasuga, T.; Hayakawa, T., *The Journal of Physical Chemistry B* **1999,** *103* (44), 9468-9472.

39. Montagne, L.; Daviero, S.; Palavit, G.; Shaim, A.; Et-Tabirou, M., *Chemistry of Materials* **2003,** *15* (25), 4709-4716.

40. Kirkpatrick, R. J.; Brow, R. K., *Solid State Nuclear Magnetic Resonance* **1995,** *5* (1), 9-21.

41. Brow, R. K.; Kirkpatrick, R. J.; Turner, G. L., *Journal of the American Ceramic Society* **1993,** *76* (4), 919-928.

42. Bunker, B.; Arnold, G.; Wilder, J. A., *Journal of Non-Crystalline Solids* **1984,** *64* (3), 291-316.

43. Morinaga, K.; Fujino, S., *Journal of Non-Crystalline Solids* **2001,** *282* (1), 118-124.

44. Moustafa, Y.; El-Egili, K., *Journal of Non-Crystalline Solids* **1998,** *240* (1), 144-153.

45. Shyu, J.-J.; Yeh, C.-H., *Journal of Materials Science* **2007,** *42* (13), 4772-4777.

Chapter 7: Melt State Centrifugal Spinning and Mechanical Properties of Nonwoven Liquid Crystalline Polymer Fibers

7.1 INTRODUCTION

Liquid crystalline polymers (LCPs) are well known for their excellent mechanical, thermal, optical, and transport properties, and have been used in a broad spectrum of applications such as bulletproof vests, cut-resistant gloves, reinforcement materials, and optical displays.[1-4] Different from conventional thermoplastic polymers, LCPs form a liquid crystal phase that can be considered an intermediate phase between an isotropic liquid and a crystalline solid. In the liquid crystal phase, LCPs are capable of forming regions of ordered structures while still flowing like a liquid. Processing LCPs in the liquid crystal state can often result in products with superior properties compared to conventional thermoplastics due to the potential for processing induced molecular orientation.

Vectra is a commercial aromatic main chain LCP, with its liquid crystal units connected in the polymer backbone. Its rigid rod like backbone structure and capability to form long range positional and orientational order makes it an ideal material for developing high strength and modulus fibers. In fact, melt spun Vectra yarn, has been commercialized by Kuraray under the tradename Vectran. By weight, Vectran is five times stronger than steel and ten times stronger than aluminum.[5] Tang et al. reinforced Vectra with 1 wt% carbon nanotubes to further increase the modulus of melt spun Vectra fibers.[6] While these melt spun Vectra fibers possess high orientation and good mechanical properties, they are generally 20 – 30 μm in diameter.[5-6]

In addition, processing Vectra into nonwoven fibers has been a long standing challenge due to its low solubility in common organic solvents and high thermal transition temperature. Inspection of the research literature shows that there is only one report on Vectra nonwoven fibers to date. Araujo et al. attempted to electrospin Vectra in

chloroform/pentafluorophenol solutions and obtained only droplets due to the limited viscoelasticity afforded by the rigid backbone structure.[7] Adding polyethylene oxide (PEO) to the Vectra solution improved the solution spinability and resulted in nanofibers. However, their mechanical properties were greatly compromised compared to bulk Vectra,[7] potentially because of the incompatibility of Vectra and PEO, or the lack of long range orientation of Vectra chains along the fiber axis due to the presence of PEO.

We believe melt state centrifugal spinning can be a useful manufacturing method to produce Vectra nonwoven fibers with high performance. Melt state processing is particularly attractive for Vectra compared to solution state processing, because the solvents for Vectra, such as pentafluophenol used in the previous study, are not only highly toxic but also possess low volatility and low Vectra solubility (1-2 wt%). Further, the large extensional deformation afforded by the intrinsically large centrifugal force may lead to production of LCP fibers with reduced fiber diameter, enhanced chain orientation and attractive mechanical properties. If successful, such Vectra-based nonwovens could have great potential in practical applications as reinforcement, lamination, and ballistic materials. Therefore, the primary aim of the present study is to demonstrate and optimize the centrifugal spinning of Vectra to produce high quality nonwoven fibers from polymer melts. The mechanical properties and orientational order of the resulting fibers are also described in detail.

7.2 EXPERIMENTAL

7.2.1 Materials

Vectra A950 (Ticona, USA) was kindly donated by Ticona and used as received. Vectra A950 is a commercial grade random copolyester of 27% 2,6-hydroxynaphthoic acid

(HNA) and 73% hydroxybenzoic acid (HBA) (see **Figure 7.1**) with a melting point of 280 ^{o}C. Vectra A950 was dried at 80 ^{o}C for at least 24 hours prior to centrifugal spinning.

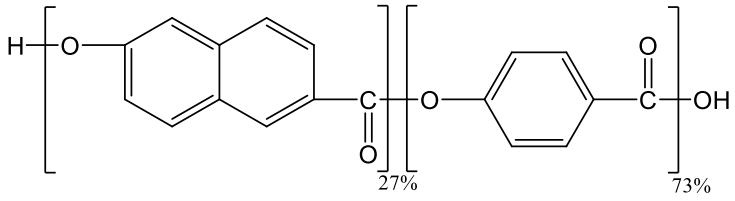

Figure 7.1: Chemical structure of Vectra A950.

7.2.2 Centrifugal spinning

Vectra A950 was melt-processed into fibers by centrifugal spinning using a Fiberio Cyclone L-1000M. Commercially available spinnerets (FibeRio) with 24 orifices of 20 gauge diameter (inner diameter of 603 μm) were used in this study. The heater temperature was set to 450 ^{o}C, which led to a spinneret orifice temperature of 350 ^{o}C as measured by an infrared temperature gun.

Centrifugal spinning Vectra A950 at a spinneret temperature of 350 ^{o}C and spin speeds ranging from 6000 rpm to 12000 rpm led to formation of short fiber strands of 3 to 5 cm in length. We believe this is due to the high melting point of Vectra A950 and the rapid cooling of the spinneret and extruded fiber during spinning. During centrifugal spinning, the fast rotating spinneret entrains cool ambient air causing the temperature of the spinneret orifices to rapidly drop below the desired processing temperature of the polymer (i.e., typically 50 ^{o}C above the melting temperature to facilitate polymer melt delivery and fiber drawing). One strategy to alleviate this problem is to increase the ambient air temperature surrounding the spinneret orifices. To facilitate this goal, an additional IR heating assembly (FibeRio) was implemented. The assembly include a 1400 W circularly-shaped IR lamp that could generate heat nearly instantaneously (potentially

up to 1000 ^{o}C) and a sliding bar which allowed the lamp to move laterally and vertically near the spinneret. A labeled photograph of the heating assembly is shown in **Figure 7.2**.

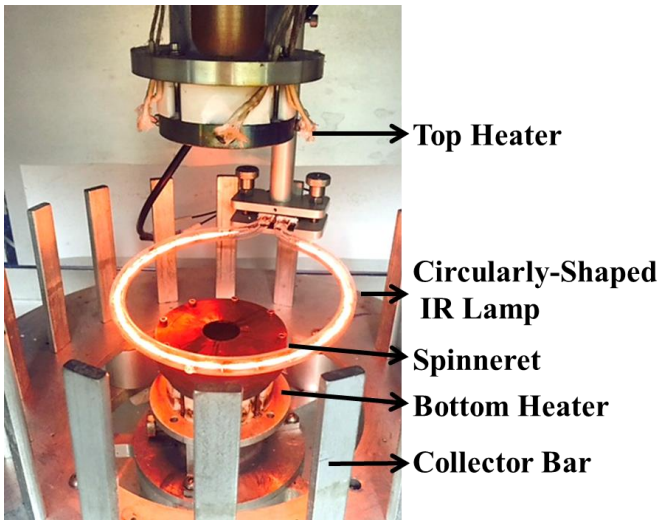

Figure 7.2: Centrifugal spinning equipped with circularly-shaped IR lamp.

The following centrifugal spinning protocol was used to reproducibly generate Vectra fibers in this study. After the spinneret was heated to 350 ^{o}C, the top heater was raised and approx. 0.25g of Vectra pellets were added through the spinneret opening in the top. The IR lamp was placed 3 cm above the top of the spinneret. (Caution: moving the IR lamp any closer to the spinneret impeded airflow during spinning and fibers attached to and re-melted on the IR lamp instead of migrating towards the collector.) The IR lamp stayed on for 60 seconds as the polymer was melting inside the spinneret prior to spinning. Fibers were then made at 8000 rpm with the IR lamp on and in place. It was observed that fibers were produced only in the first few seconds of a spinning cycle due to rapid cooling of the spinneret.

7.2.3 Dynamic mechanical analysis (DMA)

The mechanical properties of the resulting fiber mats were measured by DMA (TA instruments Q800). To prepare samples for single fiber tensile testing, single fibers were first carefully pulled out from as-processed fiber mats. A mounting window was prepared by cutting a 10 mm x 10 mm square in the center of a cardboard template. Two part epoxy glue was used to secure the single fiber sample across the window which was allowed to cure and dry overnight. The diameters of the mounted fiber samples were measured by optical microscope. The mounting window with fiber of known diameter was placed in the tensile film grips of the DMA. The two sides of the mounting window were cut, leaving only the single fiber between the grips. Stress-strain tests of Vectra single fibers were conducted at ambient conditions with a displacement of 10 mm/minute and a 0.01 N preload force.

7.2.4 Polarized infrared spectroscopy (ATR-FTIR)

Fourier Transform Infrared spectra were measured in attenuated total reflection mode (ATR-FTIR) on a FTIR (Thermo Scientific Nicolet 6700) equipped with a diamond ATR crystal accessory (PIKE MIRacle™). An IR wire grid Zn-Se polarizer (Thor Lab) was used to generate polarized IR light. Samples were characterized by FTIR for 64 scans with a 4 cm^{-1} resolution to obtain sufficient signal-to-noise ratio.

Due to sensitivity limitations of the instrument, a bundle of aligned fibers was prepared for FTIR studies by gently pulling a nonwoven mat. The two ends of the fiber bundle were taped to a cardboard mounting window prepared as described in Section 7.2.3. The comparative bulk film sample was prepared by melt pressing a Vectra pellet into an 800 μm thick film at 300 ^{o}C using a rheometer equipped with parallel plates.

The absorption intensities were obtained by integrating the area under the absorption bands. The dichroic ratio (DR) was calculated using the following equation:

$$\mathrm{DR} = \frac{A_{\parallel}}{A_{\perp}} \qquad \text{(Eq. 1)}$$

where $A_{\parallel}$ and $A_{\perp}$ are the absorption intensities measured with the IR beam polarized parallel and perpendicular to the direction of extensional deformation, respectively. The molecular orientational order for a uniaxially drawn material can be described by the Herman's orientation factor, f, calculated as follows:[8]

$$\mathrm{f} = \frac{DR-1}{DR+2} \qquad \text{(Eq. 2)}$$

7.2.5 Polarized optical microscopy

Molecular orientation in Vectra fibers and films was qualitatively imaged using an optical microscope (Olympus BX 60) with a Nikon camera and crossed polarizers. A single fiber was secured across a cardboard mounting window. A bulk film was made by melt pressing a Vectra pellet between a microscope slide and a cover slip at 300 ºC.

7.2.6 Scanning electron microscopy (SEM)

A thin layer of fibers was attached to the SEM sample holder with double sided carbon tape and sputter coated with Au/Pd to minimize charging. The coated samples were imaged by a Hitachi S-4500 SEM at an accelerating voltage of 15 kV.

7.3 Results and Discussion

7.3.1 Fiber processing

Nonwoven Vectra fibers were made by centrifugal spinning (spinneret temperature = 350 ºC, spin speed = 8000 rpm), and an SEM image of the fiber sample is shown in **Figure 7.3**. The fiber diameters ranged from 3 to 20 μm. The fiber diameter variation is fairly large, mainly because of the high melting point of the material and the very narrow temperature processing window in which the polymer melt elongates into fibers.

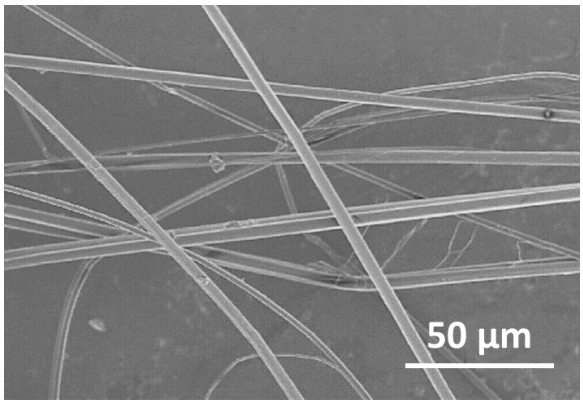

Figure 7.3: A representative SEM image of Vectra fiber made at 350 ºC, 8000 rpm.

Other fiber spinning conditions were also considered. It was found that decreasing spinneret temperature led to formation of large polymer globules (much larger than 50 µm in size, some attached to fibers and some isolated droplet like structures) and shorter fibers. In addition, below 320 ºC the orifices were clogged by the polymer and no fiber was formed. It is expected that further increasing the spinneret temperature to 380 ºC (Vectra A950 has an onset degradation temperature of 430 ºC[9] and has been processed at as high as 390 ºC previously)[10] would likely produce fibers with smaller average fiber diameter and narrower fiber distribution. Unfortunately, 350 ºC is the maximum spinneret temperature that could be achieved in our current spinning setup.

On the other hand, varying spin speed from 6000 to 10000 rpm had no observable impact on fiber diameter or fiber morphology. However, increasing the spin speed to 12000 rpm produced more fiber fragments and small polymer globules. It is hypothesized that higher spin speeds entrained more cool ambient air, which causes the polymer melt to solidify near the spinneret orifices before being drawn into fibers.

7.3.2 Mechanical properties

Due to their importance in end-use applications, the mechanical properties of Vectra fibers made by centrifugal spinning were characterized. **Figure 7.4** shows representative stress-strain curves of uniaxial tensile testing for three single fibers with different diameters. Like the ones shown in the figure, most fiber samples exhibit a maximum in stress followed by sudden rupture without yielding. This behavior is expected due to the rigid rod like backbone structure of Vectra. In addition, Young's modulus, defined as the initial slope of the stress-strain curve, increases significantly with decreasing fiber diameter. **Figure 7.5** presents the Young's modulus as a function of the fiber diameter, obtained from the stress-strain tests of over 50 single fibers. The fibers were divided into groups by diameter with bin size of 2 µm and the average of the modulus and fiber diameter were calculated. The vertical and horizontal error bars correspond to one standard deviation of the Young's modulus and fiber diameter data in each bin.

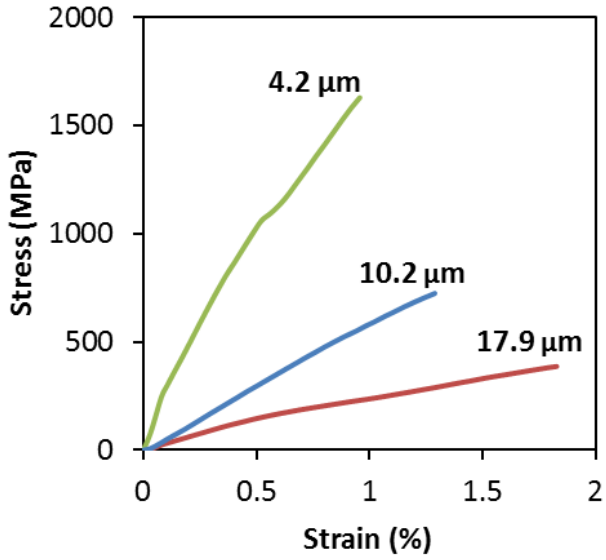

Figure 7.4: Representative stress strain curves of three individual fibers with different fiber diameter.

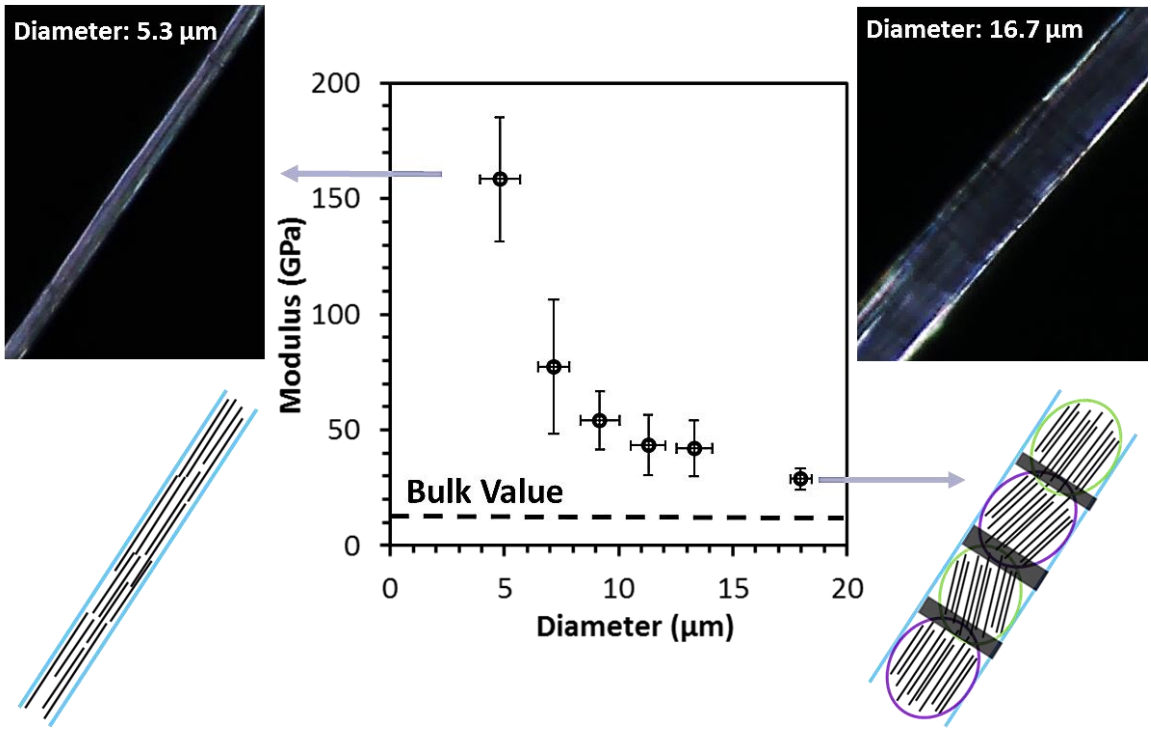

Figure 7.5: Dependence of fiber modulus on fiber diameter for over 50 single fiber samples. The fibers were grouped by their diameter into bins of 2 µm. The vertical and horizontal error bars corresponds to one standard deviation of the measurements. The horizontal dashed line represents the modulus of bulk Vectra.[11-12] The left and right cross-polarized microscope images and structural schematics represent typical molecular orientation in fibers with small and large diameters.

Figure 7.5 clearly shows that Young's modulus increases with reducing diameter. It is worth noting that the modulus of the smallest fibers (with average diameter centers at 5 µm) in the fiber mat is 158 ± 27 GPa, over an order of magnitude higher than the modulus of the bulk Vectra.[11-12] Such dramatic increase in Young's modulus can also be attributed to the thermotropic liquid crystal nature of Vectra and its ability to assist in orienting chains along the extensional flow or drawing direction.[13-14] For example, a number of studies reported increased modulus ranging from 15 to 56 GPa for uniaxially oriented films or tapes made by extrusion.[8, 12] In addition, commercial melt spun Vectran fibers with average

diameters = 25.5 ± 2.1 μm[15] possess moduli ranging from 52 to 103 GPa.[5] Compared to commercially available Vectran fibers, the smallest diameter fibers from the present study have a 1.5 to 3 times higher modulus, while large diameter Vectra fibers similar in size to Vectran fibers possess lower modulus values approaching that of the bulk materials. It is possible that the effect of transient elongational deformation in centrifugal spinning is less effective at chain orientation compared to melt spinning where there is a more continuous shear flow during extrusion of the material coupled with uniaxial stretching following extrusion.

Another possible explanation for this is the increased number of grain boundaries with increasing fiber diameter, which act as mechanical defect points during tensile testing.[6, 16] As revealed by the two cross-polarized microscope images in **Figure 7.5**, fibers with both small (diameter = 5.3 μm) and large (diameter = 16.7 μm) diameters exhibit uniform brightness, indicating that the polymer chains are on average highly oriented for both fibers. However, several dark lines perpendicular to the fiber axis were observed in the large fiber. These dark regions in cross-polarized microscopy indicate a lack of local order, and may arise as the different crystal domains intersect as shown by the schematic diagram in the figure. This observation suggests fibers with smaller diameter have molecular orientation with greater continuity down the fiber axis and less defects.

7.3.3 Molecular orientation

Polarized optical microscopy was used to qualitatively examine the molecular orientation of the Vectra fiber made by centrifugal spinning and bulk film made by melt pressing a polymer pellet between a microscope . **Figure 7.6** shows the regular and cross-polarized microscope images of the two samples. The bulk film exhibits a thread-like pattern which is consistent with the previously observed nematic phase for neat Vectra.[9, 17]

In addition, the film exhibits nematic liquid crystal texture when the sample is placed both parallel and 45° to the cross polarization axis, indicating the lack of long range molecular orientation in the bulk film. On the contrary, Vectra fiber appears completely dark when placed parallel to the cross polarization axis and appears bright when placed 45° to the cross polarization axes, qualitatively indicating that there is a significant amount of orientational order along the fiber axis.

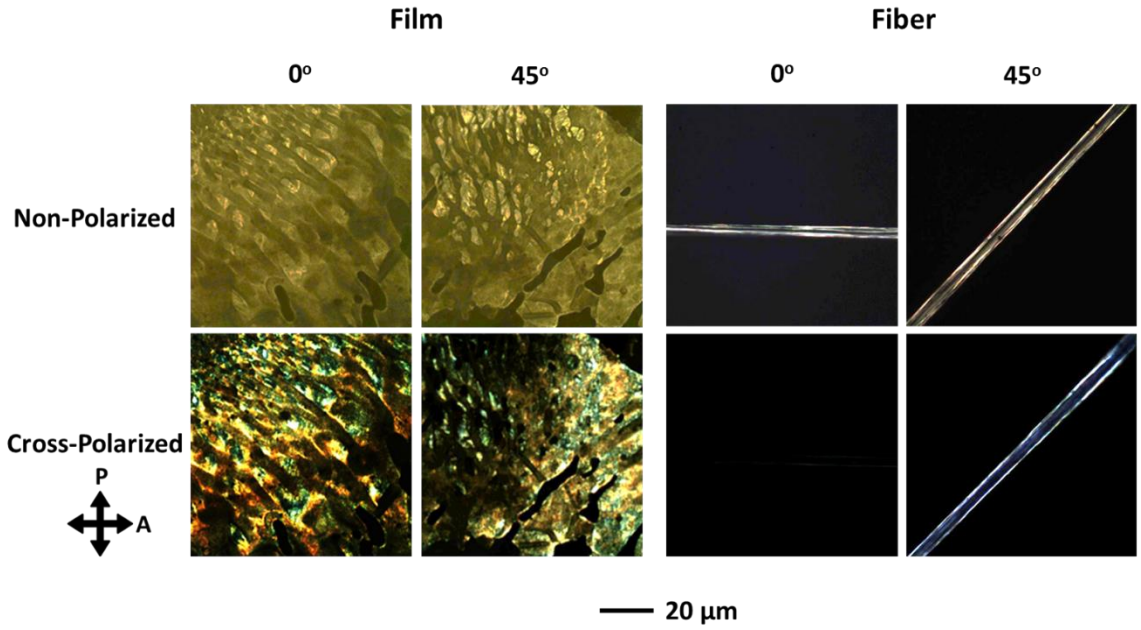

Figure 7.6: Regular and crossed polarized microscopy of Vectra bulk film and fibers. The 20 µm scale bar applies to all images in this figure.

The molecular orientation of Vectra bulk film and fiber can be further quantified by polarized infrared spectroscopy. **Figure 7.7** shows the polarized FTIR spectra of film and fiber measured when the IR beam is polarized either parallel or perpendicular to a reference direction, which is the direction of elongation in this study. The spectra of the melt-pressed film are nearly identical, while the fiber exhibits strong dichroism in IR absorption with different polarization directions.

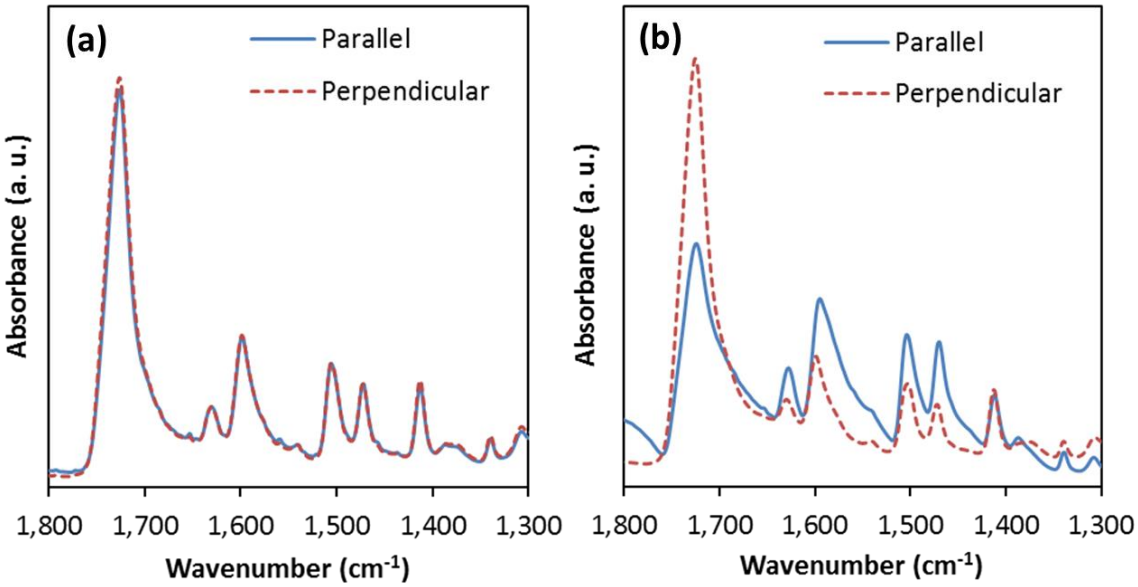

Figure 7.7: Polarized ATR-FTIR of Vectra (a) bulk film and (b) fiber. The solid line and the dash line represent spectra collected under parallel and perpendicular polarization of the IR beam to the direction of elongation, respectively.

In this study, the spectra were normalized by the absorption band at 1410 cm^{-1}, which is assigned to the benzene ring vibration that is insensitive to orientation.[8, 18] The absorption bands at 1470 cm^{-1}, which are assigned to the stretching vibration of naphthalene, is used to characterize the polymer chain orientation.[8, 19] Hermann's orientation factor, f, describes the extent of polymer chain orientation relative to either the extrusion direction or the elongation direction of the fiber. f has values ranging from -0.5 to 1. The material is isotropic, parallel oriented, and perpendicularly oriented to a reference direction, when f equals to 0, 1, and -0.5, respectively.

The orientation factor f is calculated by Eq. 2 to be 0.03 and 0.63 for bulk film and fiber, respectively. This suggests that the molecular orientation in the bulk film is mostly isotropic on average, while the Vectra backbone preferentially orients parallel to the fiber axis. These more quantitative results corroborate with the previous evaluation by cross-

polarized microscopy images. This is expected as it is commonly accepted that main chain LCPs prefer to align along the extrusion or elongation direction.[13-14] For instance, Branciforti et al. reported parallel orientation of Vectra chains to the extrusion direction with f as high as 0.75.[8]

The lower orientational order of Vectra fiber may be contributed to imperfect alignment of the FTIR sample. In addition, the fiber bundles included fibers with a range of diameters possibly reflecting a range of orientational orders that are averaged during the IR measurement. Pai et al. investigated the mechanical properties and orientational order of electrospun nylon 6 fibers with varying diameters. They observed a two fold increase in modulus and increased f from -0.1 to 0.4 as fiber diameter decreased from 3600 nm to 170 nm.[20] Considering the strong dependence of modulus on fiber diameter as described in section 7.3.2, it is very likely that there is a distribution of f values dependent on the diameter of Vectra fibers.

7.4 CONCLUSION

In this chapter, the centrifugal spinning of Vectra LCP fibers is described. Mechanical testing showed that the Young's modulus is highly dependent on fiber diameter. The Young's modulus of the smallest fibers with diameters around 5 μm was almost an order of magnitude higher than that of the bulk material. This can be attributed to the high molecular orientational order with the Vectra backbone preferentially aligning along the fiber axis, as revealed by cross-polarized optical microscopy and polarized ATR-FTIR studies. The nonwoven Vectra fibers made by centrifugal spinning not only possess enhanced mechanical properties and molecular orientation, but they were also made into nonwovens in a single step negating the need for post processing steps such as cutting the fibers into short fragments and dispersing the fragments into nonwovens.

7.5 REFERENCES

1. Afshari, M.; Chen, P.; Kotek, R., *Journal of Applied Polymer Science* **2012,** *125* (3), 2271-2280.
2. Flambard, X.; Ferreira, M.; Vermeulen, B.; Bourbigot, S.; POUTCH, F., *Journal of Textile and Apparel, Technology and Management* **2003,** *3* (2), 1-13.
3. Narh, K. A., Liquid Crystalline Polymer Blends as Fillers for Self-Reinforcing Polymer Composites. In *Liquid Crystalline Polymers*, Springer: **2015**, pp 241-264.
4. Gibbons, W. M.; Shannon, P. J.; Sun, S.-T.; Swetlin, B. J., *Nature* **1991,** (351), 49-50.
5. Product Information: Vectran. www.vectranfiber.com: **2006**.
6. Tang, Y.; Fang, L.; Gao, P., *Journal of Materials Science* **2012,** *47* (23), 8094-8102.
7. Araujo, T. M.; Sinha-Ray, S.; Pegoretti, A.; Yarin, A. L., *Journal of Materials Chemistry C* **2013,** *1* (2), 351-358.
8. Branciforti, M. C.; Silva, L. B.; Bretas, R. E., *Journal of Applied Polymer Science* **2006,** *102* (3), 2241-2248.
9. Li, Z.; Garza, P. A. G.; Baer, E.; Ellison, C. J., *Polymer* **2012,** *53* (15), 3245-3252.
10. Sun, T.; Baird, D.; Huang, H.; Done, D.; Wilkes, G., *Journal of Composite Materials* **1991,** *25* (7), 788-808.
11. Product Information: Vectra. www.ticona.com: **2006**.
12. Lefèvre, J.; Feldman, K.; Giesbrecht, J.; Smith, P.; Tervoort, T. A.; Meijer, H. E., *Journal of Polymer Science Part B: Polymer Physics* **2012,** *50* (24), 1713-1727.
13. Jin, J.-I.; Kang, C.-S., *Progress in Polymer Science* **1997,** *22* (5), 937-973.
14. Sawyer, L. C.; Jaffe, M., *Journal of Materials Science* **1986,** *21* (6), 1897-1913.
15. Pegoretti, A.; Zanolli, A.; Migliaresi, C., *Composites Science and Technology* **2006,** *66* (13), 1970-1979.
16. De'Neve, T.; Kléman, M.; Navar, P., *Liquid Crystals* **1995,** *18* (1), 67-71.
17. Taguchi, Y.; Yen, C.-C.; Kang, S.; Tokita, M.; Watanabe, J., *Macromolecules* **2009,** *42* (8), 3179-3185.
18. Guevremont, J.; Ajji, A.; Cole, K.; Dumoulin, M., *Polymer* **1995,** *36* (17), 3385-3392.
19. Li, Z.; Zhou, Z.; Armstrong, S. R.; Baer, E.; Paul, D. R.; Ellison, C. J., *Polymer* **2014,** *55* (19), 4966-4975.
20. Pai, C.-L.; Boyce, M. C.; Rutledge, G. C., *Polymer* **2011,** *52* (10), 2295-2301.

Chapter 8: Future Work

The previous chapters detailed research that developed process capabilities and fundamental understanding for a new reactive fiber spinning platform that couples thiol-ene photopolymerization and centrifugal spinning. A portion of the research in this dissertation was also committed to the melt state centrifugal spinning of polymeric and inorganic materials which have been notoriously challenging to process into fibers. In this final chapter, I will suggest several future research directions that could be pursued.

8.1 Incorporating Crystallinity in a Highly Crosslinked Network

The first proposed direction evolves around introducing crystallinity, as physical crosslinks, into the highly chemically crosslinked fiber network to further enhance fiber properties. It is well accepted that many high performance polymers, such as Kevlar, Nylon and various polyesters, possess excellent mechanical strength, chemical resistance, and high service temperature stability owing to their high crystallinity.

On the other hand, the effects of crystallinity on a lightly crosslinked network and its various properties have also been reported for a number of gel materials. For example, Winey and coworkers attributed the mechanical properties of crosslinked samples to their network structural changes in an analogue of polymers containing varying lengths of alkyl spacer between the acrylic acid groups serving as transient crosslinks.[1] Peppas and others investigated many properties such as network mesh size, controlled release behavior, swelling behavior, etc. of acrylate modified polyvinyl alcohol as a function of degree of crystallinity.[2-4] Medel and coworkers correlated the fatigue strength of crosslinked polyethylene to the lamellae crystal thickness controlled by post thermal treatments.[5]

However, all of these aforementioned studies focus on bulk materials, and were prepared in processes where crosslinking kinetics is important but not a critical parameter

that dictates sample formation. In contrast, in the process of simultaneous centrifugal spinning and thiol-ene photopolymerization, the formation of fibers depends greatly on the polymerization kinetics as well as the relationship of the kinetics to the viscoelastic and processing timescales (as previously discussed in Chapter 2). Therefore, it is essential to design the monomer architecture in order to enable the formation of crystals in a highly crosslinked network, while still retaining sufficiently fast polymerization kinetics compatible with fiber processes, and suitable viscoelastic properties for monomer mixture delivery.

8.1.1 Crystallizable macro-monomer

The first aspect of this proposed research is to understand structure-property relationships by fine tuning the monomer architecture. While the processing conditions, viscoelasticity and reaction kinetics constraints of monomers can be optimized based on previous results presented in Chapter 2 to 4, the capability to synthesize reactive monomers with desired architecture (backbone structure of monomer, reactivity, functional group density, and placement of functional groups, etc.) will be necessary.

Here, we propose to incorporate into the monomer mixture a macro-monomer containing both a polyethylene backbone and pendant acrylate functional groups. Ideally, this macro-monomer will have a molecular weight (MW) of several thousand Dalton and multiple reactive functional groups distributed along the long alkyl backbone. One candidate of the starting macro-monomer as shown in **Figure 8.1**, poly(ethylene-co-acrylic acid) (PEAA), is commercially available from DuPont and Dow under the tradenames of Nucrel and Primacore with a range of acrylic acid content values and viscosities. Some solvent or reactive diluent will be needed to solubilize the macro-monomer and tailor the viscoelastic properties demanded by the fiber spinning process as discussed in Chapter 2

and 3. However, commercial polymers typically have large molecular weights (ca. 100 kDa), and may be difficult to solubilize or too viscous for this spinning process. If this is the case, PEAA can also be synthesized by high pressure, free radical polymerization[6] or acrylic diene metathesis[1, 7-8] as previously reported. As shown in **Figure 8.1**, the pendant acrylic acid can be readily modified into photocurable acrylate, via either ring opening of epoxide[9-11] or esterification with alcohol.[12-13] This general reaction scheme is also applicable to modify PEAA with other photocurable moieties such as vinyl ether, allyl ether, methacrylate, etc. Many variations of such small functional molecules are readily available from the radiation-cure coating industry.

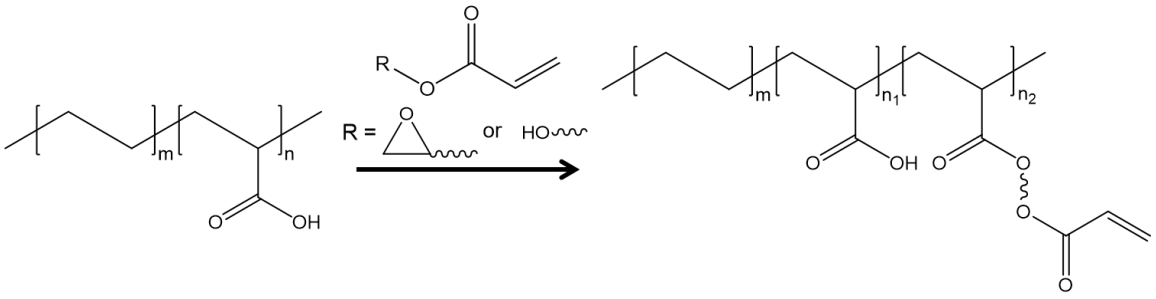

Figure 8.1: Potential synthesis route for acrylate modification of PEAA.

In this system, there are several material parameters, such as the MW of the macro-monomer, the fraction of polyethylene segments, and the conversion of acrylic acid to acrylate or other photocurable moieties, etc., that can be used to adjust network mesh size, the ratio of crystalline to amorphous regions, curing kinetics, and ultimately fiber morphology and properties.[1-2, 14-15] It is anticipated that there will be a tradeoff between curing kinetics and crystal formation. For example, as the fraction of polyethylene segments increases, the crystallizable fraction will increase, leading to formation of more physical crosslinks. However, this also dilutes the concentration of reactive functional groups in the monomer mixture which will hinder the formation of chemical crosslinks. It

is therefore essential to identify the optimal fraction of polyethylene segments and optimal number of reactive groups for both crosslinked network formation and crystal formation. In addition, it will be interesting to observe how the coexistence of physical and chemical crosslinks in an altered network impacts the properties (e.g. thermal, mechanical, swelling) of the crosslinked fibers.

8.1.2 Process and conditions of crystallization

The second aspect of this proposed research entails investigating the process of introducing crystallinity to the crosslinked network and how the process impacts crystal morphology, network structure, and fiber properties. **Figure 8.2** represents two distinct methods of incorporating crystals. In the first approach, as shown in **Figure 8.2 a**, the monomers prior to spinning do not contain crystallinity, because the polyethylene chains of macro-monomers are solubilized by solvents or reactive diluents. During fiber spinning, crystallization of polyethylene chains occurs throughout the network upon removal of solvents and curing of the small molecules. Due to the large shear and extensional deformation of the fiber spinning process, we speculate that crystals may have preferential orientation along the fiber axis, leading to enhanced mechanical properties.[16-18]

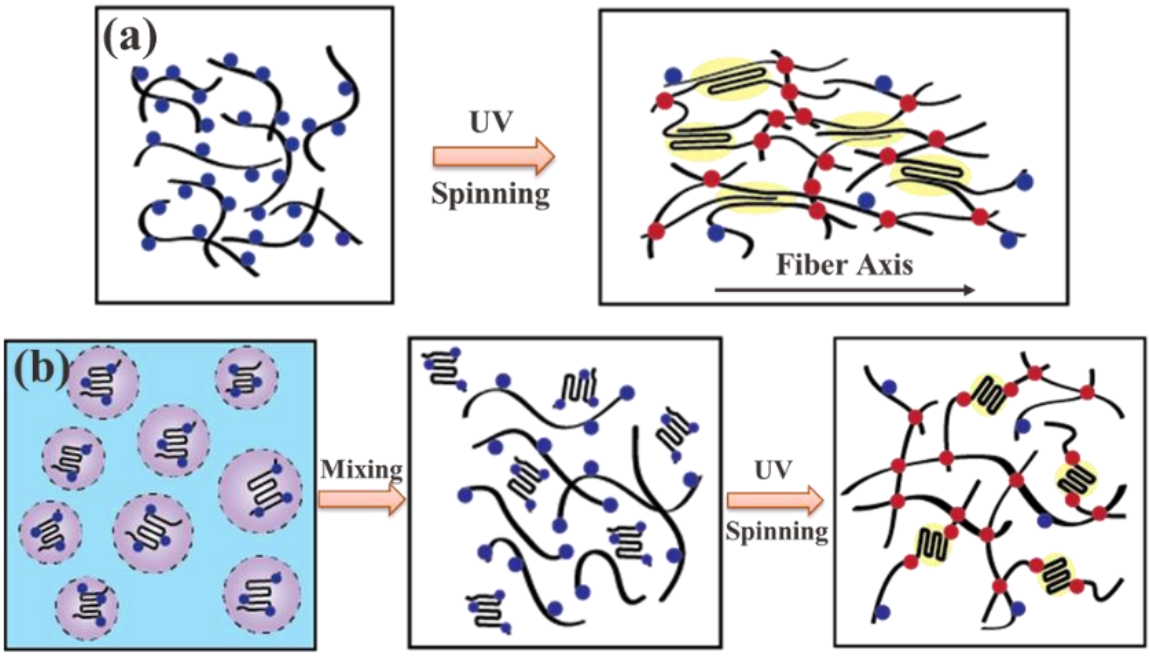

Figure 8.2: Introducing crystallinity in a crosslinked network (a) in-situ or (b) by pre-crystallization via miniemulsion. The blue circles, red circles, and yellow patches indicate reactive functional groups, chemical crosslinks, and crystals, respectively.

In the second approach, as shown in **Figure 8.2 b**, the same macro-monomer is first pre-crystallized in an oil in water miniemulsion, forming crystals within droplets with 0.1 to 0.5 μm in size. The methods and conditions for pre-crystallization have been optimized and reported by numerous research groups on a variety of semi-crystalline polymers.[19-21] The pre-crystallized monomers with reactive moieties can then be dispersed in the monomer mixture and photopolymerized, forming pockets of crystals within the chemically crosslinked network. Further, it is possible for these preformed crystals to act as heterogeneous nucleation sites that promote crystallization during the fiber formation and polymerization process.[20]

These two approaches provide unique and versatile platforms to study methods of incorporating crystallinity into a crosslinked fiber network. The results will shed light on

how fiber mechanical properties change with morphology, size distribution and orientation of crystals.

8.2 DUAL CURE SYSTEM

Despite the numerous applications (coatings, dental, biomaterials, lithography, etc.) for thiol-ene click chemistry,[22-25] diversification of our fibers "on-demand" approach to multiple polymer chemistries will greatly expand the accessible properties and end-use applications. One strategy to accomplish this goal is to adopt a dual cure approach, where the fiber shape is rapidly set by photopolymerization, while the remainder of the network is polymerized by an alternative stimulus some time later.[26-27]

8.2.1 Urethane chemistry

Polyurethane based chemistry is of interest for the dual cure system because it offers the ability to tailor the ratio of hard to soft segments which is advantageous for broadly tuning mechanical properties. The versatility of polyurethane chemistry has enabled polyurethane materials to be used in applications ranging from engineering materials to commercial products such as polyurethane foams to soft materials used in biomedical applications, and even specialty applications such as shape memory polymers. Additionally, temperature, time, and moisture can all be used to further control the final properties of polyurethanes, which are stimuli that could be applied without extended exposure to light.

A schematic diagram of this concept for incorporating polyurethane chemistry into in-situ thiol-ene photopolymerization and fiber spinning is presented in **Figure 8.3**. Here, a monomer mixture is prepared of di- or mono-acrylated polyols, penta-acrylates, tetra-thiols, and di-isocynates (**Figure 8.3 a**). The use of acrylated polyols allows the rapid formation of a cross-linked network via thiol-ene photopolymerization (**Figure 8.3 b**) and

the subsequent polymerization of isocyanates with these acrylated polyols is accomplished in a second phase (**Figure 8.3 c**). We envision that a nearly continuous spectrum of thiol-ene and polyurethane component arrangements could be possible. At one extreme lies polyurethane oligomers/polymers dispersed in a thiol-ene network while the other extreme is a system that is predominately polyurethane crosslinked by a thiol-ene reaction with the intermediate case being two fully interpenetrating components (one thiol-ene, the other polyurethane).

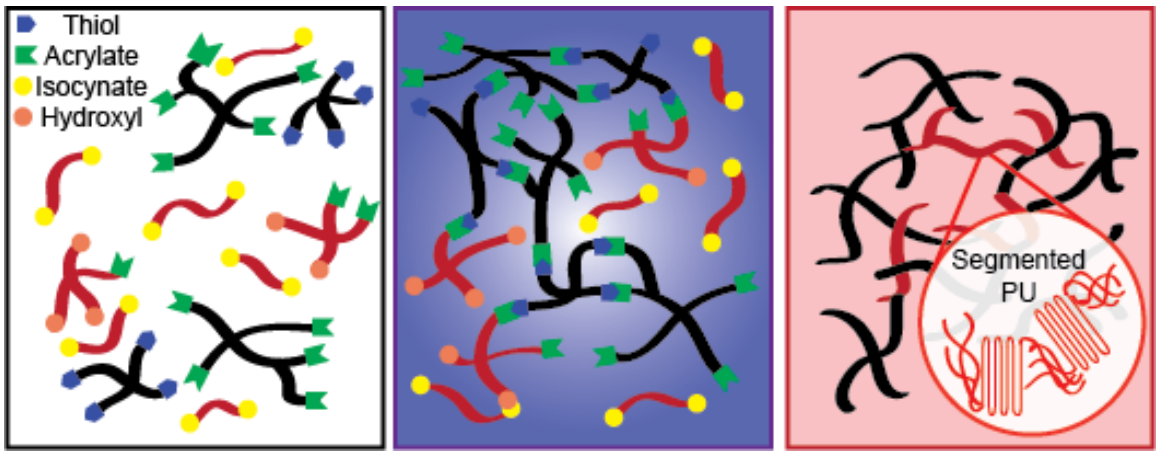

Figure 8.3: A schematic representation of thiol-ene and polyurethane dual cure system where (a) a monomer mixture consisting of thiol, acrylate, acrylated-polyol, and isocyanate oligomers is mixed and (b) exposed to UV radiation during fiber spinning. (c) A second post cure step is used to complete the polymerization of polyurethane. Image courtesy of Amanda Jones.

The required monomers are commercially available from Sartomer/Arkema, Allnex, and Dymax (to name a few), but the ability to control the functionality of the monomers may be required for the rapid formation of fibers. One possible synthesis route for a mono-acrylated polyol is shown in **Figure 8.4**.[28-29] This synthesis route can also be extended to other acrylated polyols with various backbone structures and numbers of reactive moieties.

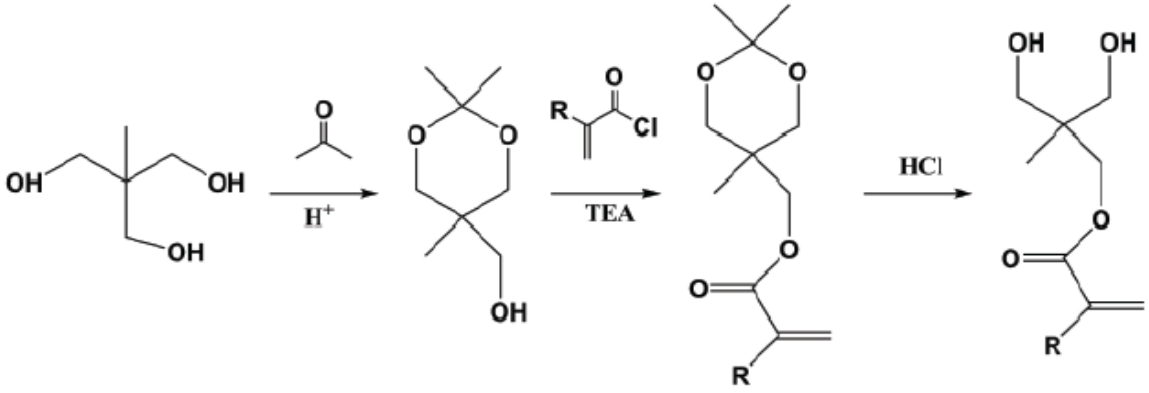

Figure 8.4: Potential synthesis route for production of an acrylated polyol.

Varying acrylate functionality and concentration in the monomer mixture will allow fine tuning of the polymerization kinetics to ensure defect free fiber formation, while varying acrylated-polyurethane formulations (the ratio of hard to soft segments) will lead to tunable final fiber properties. The simultaneous study of chemical structure and mechanical properties for acrylated-polyurethane fibers will provide key insight for solventless production of cross-linked fibers "on demand" that we envision could be further extended to polyamide or polyester chemistries, thus greatly expanding the "monomer-toolbox" for direct tailoring of fiber properties.

8.2.2 Cationic polymerization

Another chemistry of interest is UV initiated cationic polymerization, a subset of so-called living polymerizations. This means that once initiated, the polymerization is able to continue in the dark, which is not the case for free radical based thiol-ene polymerization due to the highly reactive and short-lived radical species. This feature is particularly advantageous for processes with transient light exposure, such as the fiber spinning process developed as part of this thesis research. The ability to polymerize in the dark could result

in post curing capabilities of the nonwoven products and enhanced mechanical robustness over time.

For example, **Figure 8.5** is a photograph of a series of monomer mixtures containing various amounts of di-functional vinyl ether and tetra-functional thiol monomers with both free radical and cationic photoinitiators. From left to right of the photograph, the molar ratio of ene to thiol decreases from 10:8 to 10:0. This corresponds to an increasing fraction of the monomer mixture system that polymerizes via cationic polymerization instead of free radical polymerization. The photograph was taken after the monomer mixtures were briefly exposed to UV light and then stored in the dark for six months. The colors of the monomer mixtures indicate that the cationic species are still active and polymer chains are still growing, while the intensity of the color indicates the concentration of the cationic species. It is expected the structural and mechanical properties of the monomer mixtures have undergone significant changes over time in the dark, although additional control studies and thorough characterization are needed to confirm this. Fibers made with such a dual cure system may have useful industrial applications. For instance, manufacturing of thiol-ene nonwoven products with an extended lifetime, where their properties are maintained or even enhanced by the secondary network facilitated by cationic polymerization.

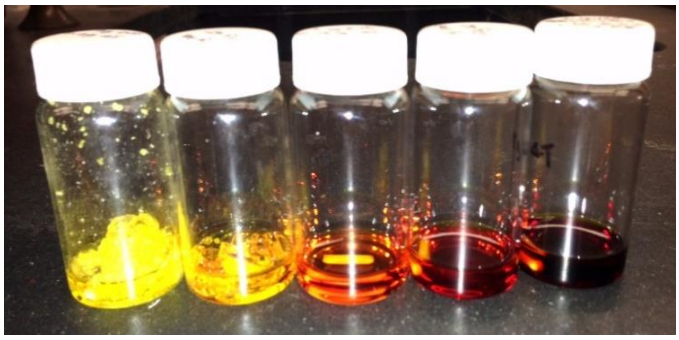

Figure 8.5: A photograph of monomer mixtures containing vinyl ether, thiol, 3 wt% Irgacure 2100 (photoinitiator) and 3 wt% Irgacure 290 (photoacid generator). The photograph was taken after a brief UV exposure and storage in the dark for six months. From left to right, the ene to thiol molar ratio of the monomer mixture is 10:8, 10:6, 10:4, 10:2, and 10:0, respectively.

One major challenge associated with cationic photopolymerization is that it can exhibit an unproductive induction period[30-31] followed by rapid polymerization. The induction period is problematic and may not be tolerated by the short processing time in this reactive fiber spinning process. This issue could be addressed with the dual cure strategy above, where some fraction of the monomers first undergo radical polymerization to form fibers and a loosely crosslinked network, while the residual functional groups continue to react in the dark over time via cationic polymerization to further fortify the network. Under optimized centrifugal spinning conditions, it has been observed that our model monomer mixture system of 5A-4T containing an adequate amount of PEO (as described in Chapter 2 and 3) can form defect free fibers with significant amount of diluent, as long as the reaction kinetics is robust and viscosity of the monomer mix is appropriate. A sample monomer mixture formulation is as follows: 40 wt% 5A, 12 wt% 4T, 40 wt% Heloxy 67, 5 wt% Irgacure 2100 and 3 wt% Irgacure 290. This formulation yields an ene to thiol functional group molar ratio of 4, which generates good fibers as demonstrated in Chapters 2 to 4. Heloxy 67 is a commercially available di-epoxy monomer from

Momentive (now Hexion), which acts an inert diluent for thiol-ene polymerization, but a reactive monomer for cationic polymerization. It should be mentioned that many other commercial multifunctional epoxy monomers, such as Heloxy 48, Heloxy 68, and Heloxy 107, are also promising alternatives. Irgacure 290 is a photoacid generator for cationic photopolymerization from BASF. This will be a promising starting point for this proposed research. Another option is to use photosensitizers, which can help generate more active centers by capturing a broader portion of the curing light spectrum (i.e., those that would not otherwise be effective for photolysis of photoinitiator), thereby shortening the induction time.[32-35]

Additionally, cationic photopolymerization is a good complement to thiol-ene photopolymerization, since monomers which are inactive towards radicals, such as epoxides and lactones, can undergo cationic polymerization.[36-37] Meanwhile, other monomers such as vinyl ethers[33] can undergo either cationic or free radical photopolymerization, but may result in very different structural, thermal, and mechanical properties. Also, a large fraction of commercial bio-based (such as soybean oil and linseed oil) radiation curing monomers come with epoxide functional groups. The ability to incorporate these monomers into crosslinked fiber production without further chemical modifications will be increasingly attractive as our community becomes more environmentally conscious and major chemical companies look for renewable raw materials instead of petroleum based ones.

8.3 REFERENCES

1. Middleton, L. R.; Szewczyk, S.; Azoulay, J.; Murtagh, D.; Rojas, G.; Wagener, K. B.; Cordaro, J.; Winey, K. I., *Macromolecules* **2015**.
2. Peppas, N. A.; Merrill, E. W., *Journal of Polymer Science: Polymer Chemistry Edition* **1976,** *14* (2), 441-457.
3. Martens, P.; Anseth, K., *Polymer* **2000,** *41* (21), 7715-7722.

4. Hassan, C. M.; Peppas, N. A., *Macromolecules* **2000,** *33* (7), 2472-2479.

5. Medel, F. J.; Pena, P.; Cegoñino, J.; Gómez-Barrena, E.; Puertolas, J., *Journal of Biomedical Materials Research Part B: Applied Biomaterials* **2007,** *83* (2), 380-390.

6. Wakabayashi, K.; Register, R. A., *Polymer* **2005,** *46* (20), 8838-8845.

7. Baughman, T. W.; Chan, C. D.; Winey, K. I.; Wagener, K. B., *Macromolecules* **2007,** *40* (18), 6564-6571.

8. Wagener, K.; Boncella, J.; Nel, J., *Macromolecules* **1991,** *24* (10), 2649-2657.

9. Shechter, L.; Wynstra, J., *Industrial & Engineering Chemistry* **1956,** *48* (1), 86-93.

10. Alvey, F. B., *Journal of Polymer Science Part A-1: Polymer Chemistry* **1969,** *7* (8), 2117-2124.

11. Bukowska, A.; Bukowski, W., *Organic Process Research & Development* **2002,** *6* (3), 234-237.

12. Onuki, Y.; Hoshi, M.; Okabe, H.; Fujikawa, M.; Morishita, M.; Takayama, K., *Journal of Controlled Release* **2005,** *108* (2), 331-340.

13. Onuki, Y.; Nishikawa, M.; Morishita, M.; Takayama, K., *International Journal of Pharmaceutics* **2008,** *349* (1), 47-52.

14. Peppas, N. A.; Wright, S. L., *Macromolecules* **1996,** *29* (27), 8798-8804.

15. Stauffer, S. R.; Peppast, N. A., *Polymer* **1992,** *33* (18), 3932-3936.

16. Liu, Y.; Cui, L.; Guan, F.; Gao, Y.; Hedin, N. E.; Zhu, L.; Fong, H., *Macromolecules* **2007,** *40* (17), 6283-6290.

17. Zhang, Y.; Rutledge, G. C., *Macromolecules* **2012,** *45* (10), 4238-4246.

18. Kongkhlang, T.; Tashiro, K.; Kotaki, M.; Chirachanchai, S., *Journal of the American Chemical Society* **2008,** *130* (46), 15460-15466.

19. Taden, A.; Landfester, K., *Macromolecules* **2003,** *36* (11), 4037-4041.

20. Montenegro, R.; Antonietti, M.; Mastai, Y.; Landfester, K., *The Journal of Physical Chemistry B* **2003,** *107* (21), 5088-5094.

21. Montenegro, R.; Landfester, K., *Langmuir* **2003,** *19* (15), 5996-6003.

22. Decker, C., *Macromolecular Rapid Communications* **2002,** *23* (18), 1067-1093.

23. Hoyle, C. E.; Bowman, C. N., *Angewandte Chemie International Edition* **2010,** *49* (9), 1540-1573.

24. Carioscia, J. A.; Lu, H.; Stanbury, J. W.; Bowman, C. N., *Dental Materials* **2005,** *21* (12), 1137-1143.

25. Kade, M. J.; Burke, D. J.; Hawker, C. J., *Journal of Polymer Science Part A: Polymer Chemistry* **2010,** *48* (4), 743-750.

26. Tumbleston, J. R.; Shirvanyants, D.; Ermoshkin, N.; Janusziewicz, R.; Johnson, A. R.; Kelly, D.; Chen, K.; Pinschmidt, R.; Rolland, J. P.; Ermoshkin, A., *Science* **2015,** *347* (6228), 1349-1352.

27. Campos, L. M.; Meinel, I.; Guino, R. G.; Schierhorn, M.; Gupta, N.; Stucky, G. D.; Hawker, C. J., *Advanced Materials* **2008,** *20* (19), 3728-3733.

28. Tallón, C.; Moreno, R.; Nieto, M. I.; Jach, D.; Rokicki, G.; Szafran, M., *Journal of the American Ceramic Society* **2007,** *90* (5), 1386-1393.

29. Chen, W.; Yang, H.; Wang, R.; Cheng, R.; Meng, F.; Wei, W.; Zhong, Z., *Macromolecules* **2009,** *43* (1), 201-207.

30. Bulut, U.; Crivello, J. V., *Macromolecules* **2005,** *38* (9), 3584-3595.

31. Cho, J. D.; Hong, J. W., *Journal of Applied Polymer Science* **2004,** *93* (3), 1473-1483.

32. Aydogan, B.; Gundogan, A. S.; Ozturk, T.; Yagci, Y., *Macromolecules* **2008,** *41* (10), 3468-3471.

33. Cho, J. D.; Hong, J. W., *Journal of Applied Polymer Science* **2005,** *97* (3), 1345-1351.

34. Crivello, J.; Lam, J., *Journal of Polymer Science: Polymer Chemistry Edition* **1978,** *16* (10), 2441-2451.

35. Hua, Y.; Crivello, J. V., *Macromolecules* **2001,** *34* (8), 2488-2494.

36. Cho, J.-D.; Hong, J.-W., *European Polymer Journal* **2005,** *41* (2), 367-374.

37. Decker, C.; Moussa, K., *Journal of Polymer Science Part A: Polymer Chemistry* **1990,** *28* (12), 3429-3443.

References

1. Product Information: Vectran. www.vectranfiber.com: **2006**.
2. Product Information: Vectra. www.ticona.com: **2006**.
3. Abou Neel, E.; Ahmed, I.; Pratten, J.; Nazhat, S.; Knowles, J., *Biomaterials* **2005,** *26* (15), 2247-2254.
4. Adkins, S. S.; Chen, X.; Nguyen, Q. P.; Sanders, A. W.; Johnston, K. P., *Journal of colloid and interface science* **2010,** *346* (2), 455-463.
5. Afshari, M.; Chen, P.; Kotek, R., *Journal of Applied Polymer Science* **2012,** *125* (3), 2271-2280.
6. Ahmed, I.; Jones, I.; Parsons, A.; Bernard, J.; Farmer, J.; Scotchford, C.; Walker, G.; Rudd, C., *Journal of Materials Science: Materials in Medicine* **2011,** *22* (8), 1825-1834.
7. Ahmed, I.; Lewis, M.; Olsen, I.; Knowles, J., *Biomaterials* **2004,** *25* (3), 501-507.
8. Ahn, Y.; Hu, D.-H.; Hong, J. H.; Lee, S. H.; Kim, H. J.; Kim, H., *Carbohydrate polymers* **2012,** *89* (2), 340-345.
9. Alemán, B.; Reguero, V.; Mas, B.; Vilatela, J. J., *ACS Nano* **2015,** *9* (7), 7392-7398.
10. Altecor, A.; Mao, Y.; Lozano, K., *Functional Materials Letters* **2012,** *5* (03), 1250020.
11. Alvey, F. B., *Journal of Polymer Science Part A-1: Polymer Chemistry* **1969,** *7* (8), 2117-2124.
12. Anseth, K. S.; Bowman, C. N.; Peppas, N. A., *Polymer Bulletin* **1993,** *31* (2), 229-233.
13. Anseth, K. S.; Bowman, C. N.; Peppas, N. A., *Journal of Polymer Science Part A: Polymer Chemistry* **1994,** *32* (1), 139-147.
14. Anton, F., Process and Apparatus for Preparing Artificial Threads. Google Patents: **1934**.
15. Araujo, T. M.; Sinha-Ray, S.; Pegoretti, A.; Yarin, A. L., *Journal of Materials Chemistry C* **2013,** *1* (2), 351-358.
16. Aydogan, B.; Gundogan, A. S.; Ozturk, T.; Yagci, Y., *Macromolecules* **2008,** *41* (10), 3468-3471.
17. Badami, A. S.; Kreke, M. R.; Thompson, M. S.; Riffle, J. S.; Goldstein, A. S., *Biomaterials* **2006,** *27* (4), 596-606.
18. Banik, K.; Mennig, G., *Polymer Engineering & Science* **2008,** *48* (5), 957-965.

19. Bao, N.; Wei, Z.; Ma, Z.; Liu, F.; Yin, G., *Journal of Hazardous Materials* **2010,** *174* (1), 129-136.

20. Baughman, T. W.; Chan, C. D.; Winey, K. I.; Wagener, K. B., *Macromolecules* **2007,** *40* (18), 6564-6571.

21. Behabtu, N.; Young, C. C.; Tsentalovich, D. E.; Kleinerman, O.; Wang, X.; Ma, A. W.; Bengio, E. A.; ter Waarbeek, R. F.; de Jong, J. J.; Hoogerwerf, R. E., *Science* **2013,** *339* (6116), 182-186.

22. Beigi, S.; Yeganeh, H.; Atai, M., *Dental Materials* **2013,** *29* (7), 777-787.

23. Bell, N. S.; Missert, N. A.; Garcia, R. M.; Nagasubramanian, G.; Leung, K.; Rempe, S. L.; Rogers, D. M. *Surface Engineering of Electrospun Fibers to Optimize Ion and Electron Transport in Li% 2b Battery Cathodes*; Sandia National Laboratories: **2012**.

24. Bhattarai, N.; Edmondson, D.; Veiseh, O.; Matsen, F. A.; Zhang, M., *Biomaterials* **2005,** *26* (31), 6176-6184.

25. Boyd, D. A.; Shields, A. R.; Naciri, J.; Ligler, F. S., *ACS Applied Materials & Interfaces* **2012,** *5* (1), 114-119.

26. Branciforti, M. C.; Silva, L. B.; Bretas, R. E., *Journal of Applied Polymer Science* **2006,** *102* (3), 2241-2248.

27. Bresee, R. R.; Ko, W.-c., *International Nonwovens Journal* **2003,** *12* (2), 21-28.

28. Brow, R. K., *Journal of Non-Crystalline Solids* **2000,** *263*, 1-28.

29. Brow, R. K.; Kirkpatrick, R. J.; Turner, G. L., *Journal of the American Ceramic Society* **1993,** *76* (4), 919-928.

30. Bukowska, A.; Bukowski, W., *Organic Process Research & Development* **2002,** *6* (3), 234-237.

31. Bulut, U.; Crivello, J. V., *Macromolecules* **2005,** *38* (9), 3584-3595.

32. Bunker, B.; Arnold, G.; Wilder, J. A., *Journal of Non-Crystalline Solids* **1984,** *64* (3), 291-316.

33. Burger, C.; Hsiao, B. S.; Chu, B., *Annual Review Materials Research* **2006,** *36*, 333-368.

34. Cai, M.; Painter, O.; Vahala, K.; Sercel, P., *Optics Letters* **2000,** *25* (19), 1430-1432.

35. Campo-Deano, L.; Clasen, C., *Journal of Non-Newtonian Fluid Mechanics* **2010,** *165* (23), 1688-1699.

36. Campos, L. M.; Meinel, I.; Guino, R. G.; Schierhorn, M.; Gupta, N.; Stucky, G. D.; Hawker, C. J., *Advanced Materials* **2008,** *20* (19), 3728-3733.

37. Campostrini, R.; D'Andrea, G.; Carturan, G.; Ceccato, R.; Sorarù, G. D., *Journal of Materials Chemistry* **1996,** *6* (4), 585-594.

38. Carioscia, J. A.; Lu, H.; Stanbury, J. W.; Bowman, C. N., *Dental Materials* **2005,** *21* (12), 1137-1143.

39. Carr, P. L.; Jakeways, R.; Klein, J. L.; Ward, I. M., *Journal of Polymer Science Part B: Polymer Physics* **1997,** *35* (15), 2465-2481.

40. Catalani, L. H.; Collins, G.; Jaffe, M., *Macromolecules* **2007,** *40* (5), 1693-1697.

41. Černý, M.; Chlup, Z.; Strachota, A.; Halasová, M.; Rýglová, Š.; Schweigstillová, J.; Svítilová, J.; Havelcová, M., *Ceramics International* **2015,** *41* (5), 6237-6247.

42. Cha, J.; Asida, Y.; Takebe, H. In *Analysis of Viscoelastic Flow in Tin Phosphate Glass*, IOP Conference Series: Materials Science and Engineering, IOP Publishing: **2011**; p 112014.

43. Chang, K.; Lee, T.; Hwa, L., *Chin. J. Phys* **2003,** *41* (4), 414-21.

44. Chen, J.-P.; Su, C.-H., *Acta Biomaterialia* **2011,** *7* (1), 234-243.

45. Chen, T.; Li, L.; Huang, X., *Journal of Applied Polymer Science* **2005,** *97* (4), 1750-1752.

46. Chen, T.; Wang, X.; Huang, X., *Textile Research Journal* **2005,** *75* (1), 76-80.

47. Chen, W.; Yang, H.; Wang, R.; Cheng, R.; Meng, F.; Wei, W.; Zhong, Z., *Macromolecules* **2009,** *43* (1), 201-207.

48. Cho, J. D.; Hong, J. W., *Journal of Applied Polymer Science* **2004,** *93* (3), 1473-1483.

49. Cho, J. D.; Hong, J. W., *Journal of Applied Polymer Science* **2005,** *97* (3), 1345-1351.

50. Cho, J.-D.; Hong, J.-W., *European Polymer Journal* **2005,** *41* (2), 367-374.

51. Chrissafis, K.; Paraskevopoulos, K.; Bikiaris, D., *Thermochimica Acta* **2005,** *435* (2), 142-150.

52. Christopherson, G. T.; Song, H.; Mao, H.-Q., *Biomaterials* **2009,** *30* (4), 556-564.

53. Chuah, H. H., *Polymer Engineering & Science* **2001,** *41* (2), 308-313.

54. Cole, M. A.; Bowman, C. N., *Journal of Polymer Science Part A: Polymer Chemistry* **2013,** *51* (8), 1749-1757.

55. Colombo, P.; Mera, G.; Riedel, R.; Sorarù, G. D., *Journal of the American Ceramic Society* **2010,** *93* (7), 1805-1837.

56. Cong, H.-P.; Ren, X.-C.; Wang, P.; Yu, S.-H., *Scientific reports* **2012,** *2*.

57. Cozza, E. S.; Bruzzo, V.; Carniato, F.; Marsano, E.; Monticelli, O., *ACS Applied Materials & Interfaces* **2012,** *4* (2), 604-607.

58. Cramer, N. B.; Bowman, C. N., *Journal of Polymer Science Part A: Polymer Chemistry* **2001,** *39* (19), 3311-3319.

59. Cramer, N. B.; Davies, T.; O'Brien, A. K.; Bowman, C. N., *Macromolecules* **2003,** *36* (12), 4631-4636.

60. Cramer, N. B.; Reddy, S. K.; Lu, H.; Cross, T.; Raj, R.; Bowman, C. N., *Journal of Polymer Science Part A: Polymer Chemistry* **2004,** *42* (7), 1752-1757.

61. Crivello, J.; Lam, J., *Journal of Polymer Science: Polymer Chemistry Edition* **1978,** *16* (10), 2441-2451.

62. Crowley, M. M.; Zhang, F.; Koleng, J. J.; McGinity, J. W., *Biomaterials* **2002,** *23* (21), 4241-4248.

63. Day, D.; Wu, Z.; Ray, C.; Hrma, P., *Journal of Non-Crystalline Solids* **1998,** *241* (1), 1-12.

64. Decker, C., *Macromolecular Rapid Communications* **2002,** *23* (18), 1067-1093.

65. Decker, C.; Moussa, K., *Journal of Polymer Science Part A: Polymer Chemistry* **1990,** *28* (12), 3429-3443.

66. Deitzel, J.; Kleinmeyer, J.; Harris, D.; Tan, N. B., *Polymer* **2001,** *42* (1), 261-272.

67. De'Neve, T.; Kléman, M.; Navar, P., *Liquid Crystals* **1995,** *18* (1), 67-71.

68. Deshmukh, G. S.; Peshwe, D. R.; Pathak, S. U.; Ekhe, J. D., *Journal of Polymer Research* **2011,** *18* (5), 1081-1090.

69. Ebendorff-Heidepriem, H.; Seeber, W.; Ehrt, D., *Journal of Non-Crystalline Solids* **1993,** *163* (1), 74-80.

70. Eckel, Z. C.; Zhou, C.; Martin, J. H.; Jacobsen, A. J.; Carter, W. B.; Schaedler, T. A., *Science* **2016,** *351* (6268), 58-62.

71. Ehrt, D., *Journal of Non-Crystalline Solids* **2008,** *354* (2), 546-552.

72. Ellison, C. J.; Phatak, A.; Giles, D. W.; Macosko, C. W.; Bates, F. S., *Polymer* **2007,** *48* (11), 3306-3316.

73. Fairbanks, B. D.; Schwartz, M. P.; Halevi, A. E.; Nuttelman, C. R.; Bowman, C. N.; Anseth, K. S., *Advanced Materials* **2009,** *21* (48), 5005-5010.

74. Fang, Y.; Dulaney, A. D.; Gadley, J.; Maia, J. M.; Ellison, C. J., *Polymer* **2015,** *73*, 42-51.

75. Fang, Y.; Dulaney, A. R.; Gadley, J.; Maia, J. M.; Ellison, C. J., *Polymer doi:10.1016/j.polymer.2016.02.029.*

76. Fang, Y.; Herbert, M.; Schiraldi, D. A.; Ellison, C. J., *Journal of Materials Science* **2014,** *49* (24), 8252-8260.

77. Fina, A.; Tabuani, D.; Frache, A.; Camino, G., *Polymer* **2005,** *46* (19), 7855-7866.

78. Flambard, X.; Ferreira, M.; Vermeulen, B.; Bourbigot, S.; POUTCH, F., *Journal of Textile and Apparel, Technology and Management* **2003,** *3* (2), 1-13.

79. Fletcher, L. B.; Witcher, J. J.; Troy, N.; Brow, R. K.; Krol, D. M., *Optics Letters* **2012,** *37* (7), 1148-1150.

80. Fletcher, L. B.; Witcher, J. J.; Troy, N.; Reis, S. T.; Brow, R. K.; Krol, D. M., *Optics Express* **2011,** *19* (9), 7929-7936.

81. Forouharshad, M.; Saligheh, O.; Arasteh, R.; Farsani, R. E., *Journal of Macromolecular Science Part B-Physics* **2010,** *49* (4), 833-842.

82. Forward, K. M.; Rutledge, G. C., *Chemical Engineering Journal* **2012,** *183*, 492-503.

83. Fridrikh, S. V.; Jian, H. Y.; Brenner, M. P.; Rutledge, G. C., *Physical Review Letters* **2003,** *90* (14), 144502.

84. Gardella, L.; Basso, A.; Prato, M.; Monticelli, O., *ACS Applied Materials & Interfaces* **2013,** *5* (16), 7688-7692.

85. Gibbons, W. M.; Shannon, P. J.; Sun, S.-T.; Swetlin, B. J., *Nature* **1991,** (351), 49-50.

86. Grafe, T.; Graham, K., *Nonwoven Technology Review* **2003,** *12*, 51-55.

87. Guenthner, A. J.; Lamison, K. R.; Lubin, L. M.; Haddad, T. S.; Mabry, J. M., *Industrial & Engineering Chemistry Research* **2012,** *51* (38), 12282-12293.

88. Guevremont, J.; Ajji, A.; Cole, K.; Dumoulin, M., *Polymer* **1995,** *36* (17), 3385-3392.

89. Guo, W.; Leu, W.-T.; Hsiao, S.-H.; Liou, G.-S., *Polymer Degradation and Stability* **2006,** *91* (1), 21-30.

90. Gupta, M.; Lin, Y.; Deans, T.; Baer, E.; Hiltner, A.; Schiraldi, D. A., *Macromolecules* **2010,** *43* (9), 4230-4239.

91. Gupta, M.; Lin, Y.; Deans, T.; Crosby, A.; Baer, E.; Hiltner, A.; Schiraldi, D. A., *Polymer* **2009,** *50* (2), 598-604.

92. Gupta, P.; Elkins, C.; Long, T. E.; Wilkes, G. L., *Polymer* **2005,** *46* (13), 4799-4810.

93. Gustafsson, Y.; Haag, J.; Jungebluth, P.; Lundin, V.; Lim, M. L.; Baiguera, S.; Ajalloueian, F.; Del Gaudio, C.; Bianco, A.; Moll, G., *Biomaterials* **2012,** *33* (32), 8094-8103.

94. Hammami, M. A.; Krifa, M.; Harzallah, O., *The Journal of The Textile Institute* **2014,** *105* (6), 637-647.

95. Hanrahan, B.; Angeli, S.; Runt, J., *Polymer Bulletin* **1985,** *14* (5), 399-406.

96. Hassan, C. M.; Peppas, N. A., *Macromolecules* **2000,** *33* (7), 2472-2479.

97. Hassan, M. A.; Yeom, B. Y.; Wilkie, A.; Pourdeyhimi, B.; Khan, S. A., *Journal of Membrane Science* **2013,** *427*, 336-344.

98. He, Y.; Day, D., *Glass Technology* **1992,** *33* (6), 214-219.

99. Heidebrecht, A.; Eisoldt, L.; Diehl, J.; Schmidt, A.; Geffers, M.; Lang, G.; Scheibel, T., *Advanced Materials* **2015,** *27* (13), 2189-2194.

100. Hoyle, C. E.; Bowman, C. N., *Angewandte Chemie International Edition* **2010,** *49* (9), 1540-1573.

101. Hoyle, C. E.; Lee, T. Y.; Roper, T., *Journal of Polymer Science Part A: Polymer Chemistry* **2004,** *42* (21), 5301-5338.

102. Hua, Y.; Crivello, J. V., *Macromolecules* **2001,** *34* (8), 2488-2494.

103. Huang, J.; You, T., *by R. Maguire,(InTech, 2013)* **2013**, 35-83.

104. Hudgens, J. J.; Martin, S. W., *Journal of the American Ceramic Society* **1993,** *76* (7), 1691-1696.

105. Huo, P. P.; Cebe, P., *Macromolecules* **1993,** *26* (12), 3127-3130.

106. Hur, J. S.; Shaqfeh, E. S.; Babcock, H. P.; Smith, D. E.; Chu, S., *Journal of Rheology (1978-present)* **2001,** *45* (2), 421-450.

107. Iyer, S.; Schiraldi, D. A., *Macromolecules* **2007,** *40* (14), 4942-4952.

108. James, D. F., *Annual Review of Fluid Mechanics* **2009,** *41*, 129-142.

109. Janes, D. W.; Shanmuganathan, K.; Chou, D. Y.; Ellison, C. J., *ACS Macro Letters* **2012,** *1* (9), 1138-1142.

110. Jassal, M.; Sengupta, S.; Bhowmick, S., *Journal of Biomaterials Science, Polymer Edition* **2015**, 1-14.

111. Jefferson, L. U.; Netchaev, A. D.; Jefcoat, J. A.; Windham, A. D.; McFarland, F. M.; Guo, S.; Buchanan, R. K.; Buchanan, J. P., *ACS Applied Materials & Interfaces* **2015**.

112. Ji, Y.; Ghosh, K.; Li, B.; Sokolov, J. C.; Clark, R. A.; Rafailovich, M. H., *Macromolecular Bioscience* **2006,** *6* (10), 811-817.

113. Jiang, J.; Xie, J.; Ma, B.; Bartlett, D. E.; Xu, A.; Wang, C.-H., *Acta Biomaterialia* **2014,** *10* (3), 1324-1332.

114. Jin, C.; Jiang, Y.; Niu, T.; Huang, J., *Journal of Materials Chemistry* **2012,** *22* (25), 12562-12567.

115. Jin, H.-J.; Kaplan, D. L., *Nature* **2003,** *424* (6952), 1057-1061.

116. Jin, J.-I.; Kang, C.-S., *Progress in Polymer Science* **1997,** *22* (5), 937-973.

117. Joshi, M.; Butola, B.; Simon, G.; Kukaleva, N., *Macromolecules* **2006,** *39* (5), 1839-1849.

118. Kade, M. J.; Burke, D. J.; Hawker, C. J., *Journal of Polymer Science Part A: Polymer Chemistry* **2010,** *48* (4), 743-750.

119. Kim, G.; Cho, Y.-S.; Kim, W. D., *European Polymer Journal* **2006,** *42* (9), 2031-2038.

120. Kim, S. H.; Kim, S.-H.; Nair, S.; Moore, E., *Macromolecules* **2005,** *38* (9), 3719-3723.

121. Kirkpatrick, R. J.; Brow, R. K., *Solid State Nuclear Magnetic Resonance* **1995,** *5* (1), 9-21.

122. Kongkhlang, T.; Tashiro, K.; Kotaki, M.; Chirachanchai, S., *Journal of the American Chemical Society* **2008,** *130* (46), 15460-15466.

123. Koo, S. H.; Lee, S. G.; Bong, H.; Kwark, Y.-J.; Cho, K.; Lim, H. S.; Cho, J. H., *Polymer* **2014,** *55* (11), 2661-2666.

124. Kwisnek, L.; Nazarenko, S.; Hoyle, C. E., *Macromolecules* **2009,** *42* (18), 7031-7041.

125. Lazaris, A.; Arcidiacono, S.; Huang, Y.; Zhou, J.-F.; Duguay, F.; Chretien, N.; Welsh, E. A.; Soares, J. W.; Karatzas, C. N., *Science* **2002,** *295* (5554), 472-476.

126. Lee, Y.; Wadsworth, L. C., *Polymer* **1992,** *33* (6), 1200-1209.

127. Lee, Y. E.; Wadsworth, L. C., *Journal of Applied Polymer Science* **2007,** *105* (6), 3724-3727.

128. Lefèvre, J.; Feldman, K.; Giesbrecht, J.; Smith, P.; Tervoort, T. A.; Meijer, H. E., *Journal of Polymer Science Part B: Polymer Physics* **2012,** *50* (24), 1713-1727.

129. Létant, S. E.; Herberg, J.; Dinh, L. N.; Maxwell, R. S.; Simpson, R. L.; Saab, A. P., *Catalysis Communications* **2007,** *8* (12), 2137-2142.

130. Li, L.; Schülzgen, A.; Temyanko, V.; Qiu, T.; Morrell, M.; Wang, Q.; Mafi, A.; Moloney, J.; Peyghambarian, N., *Optics Letters* **2005,** *30* (10), 1141-1143.

131. Li, X.; Chen, H.; Yang, B., *Carbohydrate Polymers* **2016,** *137*, 459-465.

132. Li, Z.; Garza, P. A. G.; Baer, E.; Ellison, C. J., *Polymer* **2012,** *53* (15), 3245-3252.

133. Li, Z.; Zhou, Z.; Armstrong, S. R.; Baer, E.; Paul, D. R.; Ellison, C. J., *Polymer* **2014,** *55* (19), 4966-4975.

134. Liivak, O.; Blye, A.; Shah, N.; Jelinski, L. W., *Macromolecules* **1998,** *31* (9), 2947-2951.

135. Liu, H.-Y.; Chen, Y.; Liu, G.-S.; Pei, S.-G.; Liu, J.-Q.; Ji, H.; Wang, R.-D., *Materials and Manufacturing Processes* **2013,** *28* (2), 133-138.

136. Liu, Y.; Cui, L.; Guan, F.; Gao, Y.; Hedin, N. E.; Zhu, L.; Fong, H., *Macromolecules* **2007,** *40* (17), 6283-6290.

137. Liu, Y.; Huang, Y.; Liu, L., *Polymer Degradation and Stability* **2006,** *91* (11), 2731-2738.

138. Liu, Y.; Jun, Y.; Steinberg, V., *Journal of Rheology (1978-present)* **2009,** *53* (5), 1069-1085.

139. Liu, Y.; Shao, Z.; Vollrath, F., *Nature Materials* **2005,** *4* (12), 901-905.

140. LLC, C. A. Textile Glossary. http://textileengineerr.blogspot.com/p/textile-glossary_06.html.

141. LOZANO, K.; ALTECOR, A.; MAO, Y., *Functional Materials Letters* **2012,** *05* (03), 1250020.

142. Lozano, K.; Sarkar, K., Superfine Fiber Creating Spinneret and Uses Thereof. Google Patents: **2012**.

143. Lu, B.; Wang, Y.; Liu, Y.; Duan, H.; Zhou, J.; Zhang, Z.; Wang, Y.; Li, X.; Wang, W.; Lan, W., *Small* **2010,** *6* (15), 1612-1616.

144. Lu, H.; Carioscia, J. A.; Stansbury, J. W.; Bowman, C. N., *Dental Materials* **2005,** *21* (12), 1129-1136.

145. Lu, P.; Xia, Y., *ACS Applied Materials & Interfaces* **2013,** *5* (13), 6391-6399.

146. Lu, Y.; Li, Y.; Zhang, S.; Xu, G.; Fu, K.; Lee, H.; Zhang, X., *European Polymer Journal* **2013,** *49* (12), 3834-3845.

147. Luitel, K.; Hudson, D.; Ethridge, D. In *Evaluating Potential for Cotton Utilization in Alternative Nonwoven Textile Technologies*, 2013 Annual Meeting, February 2-5, 2013, Orlando, Florida, Southern Agricultural Economics Association: **2013**.

148. Lukas, D.; Sarkar, A.; Pokorny, P., *Journal of Applied Physics* **2008,** *103* (8), 084309.

149. Lundberg, P.; Bruin, A.; Klijnstra, J. W.; Nyström, A. M.; Johansson, M.; Malkoch, M.; Hult, A., *ACS Applied Materials & Interfaces* **2010,** *2* (3), 903-912.

150. Ma, M.; Gupta, M.; Li, Z.; Zhai, L.; Gleason, K. K.; Cohen, R. E.; Rubner, M. F.; Rutledge, G. C., *Advanced Materials* **2007,** *19* (2), 255-259.

151. Ma, M.; Mao, Y.; Gupta, M.; Gleason, K. K.; Rutledge, G. C., *Macromolecules* **2005,** *38* (23), 9742-9748.

152. Ma, Z.; Kotaki, M.; Yong, T.; He, W.; Ramakrishna, S., *Biomaterials* **2005,** *26* (15), 2527-2536.

153. Macossay, J.; Marruffo, A.; Rincon, R.; Eubanks, T.; Kuang, A., *Polymers for Advanced Technologies* **2007,** *18* (3), 180-183.

154. Mahalingam, S.; Raimi-Abraham, B. T.; Craig, D. Q.; Edirisinghe, M., *Chemical Engineering Journal* **2015,** *280*, 344-353.

155. Mantz, R.; Jones, P.; Chaffee, K.; Lichtenhan, J.; Gilman, J.; Ismail, I.; Burmeister, M., *Chemistry of Materials* **1996,** *8* (6), 1250-1259.

156. Martens, P.; Anseth, K., *Polymer* **2000,** *41* (21), 7715-7722.

157. Marvel, C.; Caesar, P., *Journal of the American Chemical Society* **1951,** *73* (3), 1097-1099.

158. Marvel, C.; Chambers, R., *Journal of the American Chemical Society* **1948,** *70* (3), 993-998.

159. McEachin, Z.; Lozano, K., *Journal of Applied Polymer Science* **2012,** *126* (2), 473-479.

160. McKee, M. G.; Wilkes, G. L.; Colby, R. H.; Long, T. E., *Macromolecules* **2004,** *37* (5), 1760-1767.

161. McKinley, G. H.; Tripathi, A., *Journal of Rheology (1978-present)* **2000,** *44* (3), 653-670.

162. McNair, O. D.; Brent, D. P.; Sparks, B. J.; Patton, D. L.; Savin, D. A., *ACS Applied Materials & Interfaces* **2014,** *6* (9), 6088-6097.

163. Medeiros, E. S.; Glenn, G. M.; Klamczynski, A. P.; Orts, W. J.; Mattoso, L. H., *Journal of Applied Polymer Science* **2009,** *113* (4), 2322-2330.

164. Medel, F. J.; Pena, P.; Cegoñino, J.; Gómez-Barrena, E.; Puertolas, J., *Journal of Biomedical Materials Research Part B: Applied Biomaterials* **2007,** *83* (2), 380-390.

165. Meerman, J. J.; Jelijs, R., Centrifugal Spinning Process for Spinnable Solutions. Google Patents: **2000**.

166. Mellado, P.; McIlwee, H. A.; Badrossamay, M. R.; Goss, J. A.; Mahadevan, L.; Parker, K. K., *Applied Physics Letters* **2011,** *99* (20), 203107.

167. Middleton, L. R.; Szewczyk, S.; Azoulay, J.; Murtagh, D.; Rojas, G.; Wagener, K. B.; Cordaro, J.; Winey, K. I., *Macromolecules* **2015**.

168. Milligan, M.; Haynes, B., *Journal of Applied Polymer Science* **1995,** *58* (1), 159-163.

169. Milliman, H. W.; Boris, D.; Schiraldi, D. A., *Macromolecules* **2012,** *45* (4), 1931-1936.

170. Milliman, H. W.; Ishida, H.; Schiraldi, D. A., *Macromolecules* **2012,** *45* (11), 4650-4657.

171. MINAMF, T.; Mackenzie, J. D., *Journal of the American Ceramic Society* **1977,** *60* (5-6), 232-235.

172. Montagne, L.; Daviero, S.; Palavit, G.; Shaim, A.; Et-Tabirou, M., *Chemistry of Materials* **2003,** *15* (25), 4709-4716.

173. Montenegro, R.; Antonietti, M.; Mastai, Y.; Landfester, K., *The Journal of Physical Chemistry B* **2003,** *107* (21), 5088-5094.

174. Montenegro, R.; Landfester, K., *Langmuir* **2003,** *19* (15), 5996-6003.

175. Morinaga, K.; Fujino, S., *Journal of Non-Crystalline Solids* **2001,** *282* (1), 118-124.

176. Moroni, L.; Licht, R.; de Boer, J.; de Wijn, J. R.; van Blitterswijk, C. A., *Biomaterials* **2006,** *27* (28), 4911-4922.

177. Moustafa, Y.; El-Egili, K., *Journal of Non-Crystalline Solids* **1998,** *240* (1), 144-153.

178. Mutin, P. H., *Journal of the American Ceramic Society* **2002,** *85* (5), 1185-1189.

179. Naka, K.; Itoh, H.; Chujo, Y., *Nano Letters* **2002,** *2* (11), 1183-1186.

180. Narh, K. A., Liquid Crystalline Polymer Blends as Fillers for Self-Reinforcing Polymer Composites. In *Liquid Crystalline Polymers*, Springer: **2015**, pp 241-264.

181. Nason, C.; Roper, T.; Hoyle, C.; Pojman, J. A., *Macromolecules* **2005,** *38* (13), 5506-5512.

182. Naumov, S.; Schöneich, C., *The Journal of Physical Chemistry A* **2009,** *113* (15), 3560-3565.

183. Nazhat, S. N.; Abou Neel, E. A.; Kidane, A.; Ahmed, I.; Hope, C.; Kershaw, M.; Lee, P. D.; Stride, E.; Saffari, N.; Knowles, J. C., *Biomacromolecules* **2007,** *8* (2), 543-551.

184. Nichols, M. E.; Robertson, R. E., *Journal of Polymer Science Part B: Polymer Physics* **1992,** *30* (7), 755-768.

185. Nogami, M.; Nagao, R.; Wong, C., *The Journal of Physical Chemistry B* **1998,** *102* (30), 5772-5775.

186. Nogami, M.; Nagao, R.; Wong, C.; Kasuga, T.; Hayakawa, T., *The Journal of Physical Chemistry B* **1999,** *103* (44), 9468-9472.

187. O'Brien, A. K.; Cramer, N. B.; Bowman, C. N., *Journal of Polymer Science Part A: Polymer Chemistry* **2006,** *44* (6), 2007-2014.

188. Oliveira, M. S.; Yeh, R.; McKinley, G. H., *Journal of Non-Newtonian Fluid Mechanics* **2006,** *137* (1), 137-148.

189. Onuki, Y.; Hoshi, M.; Okabe, H.; Fujikawa, M.; Morishita, M.; Takayama, K., *Journal of Controlled Release* **2005,** *108* (2), 331-340.

190. Onuki, Y.; Nishikawa, M.; Morishita, M.; Takayama, K., *International Journal of Pharmaceutics* **2008,** *349* (1), 47-52.

191. Otaigbe, J. U.; Beall, G. H., *Trends in Polymer Science* **1997,** *5* (11), 369-379.

192. Padron, S.; Fuentes, A.; Caruntu, D.; Lozano, K., *Journal of Applied Physics* **2013,** *113* (2), 024318.

193. Padron, S.; Patlan, R.; Gutierrez, J.; Santos, N.; Eubanks, T.; Lozano, K., *Journal of Applied Polymer Science* **2012,** *125* (5), 3610-3616.

194. Pai, C.-L.; Boyce, M. C.; Rutledge, G. C., *Polymer* **2011,** *52* (10), 2295-2301.

195. Pai, C.-L.; Boyce, M. C.; Rutledge, G. C., *Polymer* **2011,** *52* (26), 6126-6133.

196. Palangetic, L.; Reddy, N. K.; Srinivasan, S.; Cohen, R. E.; McKinley, G. H.; Clasen, C., *Polymer* **2014,** *55* (19), 4920-4931.

197. Patel, S. S.; Takahashi, K. M., *Macromolecules* **1992,** *25* (17), 4382-4391.

198. Paul, D., *Journal of Applied Polymer Science* **1968,** *12* (10), 2273-2298.

199. Pegoretti, A.; Zanolli, A.; Migliaresi, C., *Composites Science and Technology* **2006,** *66* (13), 1970-1979.

200. Peppas, N. A.; Merrill, E. W., *Journal of Polymer Science: Polymer Chemistry Edition* **1976,** *14* (2), 441-457.

201. Peppas, N. A.; Wright, S. L., *Macromolecules* **1996,** *29* (27), 8798-8804.

202. Raghavan, B.; Soto, H.; Lozano, K., *Journal of Engineered Fabrics & Fibers (JEFF)* **2013,** *8* (1).

203. Ray, N. H., *British Polymer Journal* **1979,** *11* (4), 163-177.

204. Reddy, S. K.; Cramer, N. B.; Bowman, C. N., *Macromolecules* **2006,** *39* (10), 3681-3687.

205. Reddy, S. K.; Cramer, N. B.; Cross, T.; Raj, R.; Bowman, C. N., *Chemistry of Materials* **2003,** *15* (22), 4257-4261.

206. Reddy, S. K.; Okay, O.; Bowman, C. N., *Macromolecules* **2006,** *39* (25), 8832-8843.

207. Regev, O.; Vandebril, S.; Zussman, E.; Clasen, C., *Polymer* **2010,** *51* (12), 2611-2620.

208. Reis, S.; Karabulut, M.; Day, D., *Journal of Non-Crystalline Solids* **2001,** *292* (1), 150-157.

209. Ren, L.; Kotha, S. P., *Materials Letters* **2014,** *117*, 153-157.

210. Ren, L.; Ozisik, R.; Kotha, S. P.; Underhill, P. T., *Macromolecules* **2015**.

211. Rodriguez, F.; Cohen, C.; Ober, C.; Archer, L. A., *Principles of Polymer Systems*. Taylor & Francis Washington, DC: **1996**; Vol. 4.

212. Rubinstein, M.; Colby, R., *Polymers Physics*. Oxford: **2003**.

213. Sarkar, K.; Gomez, C.; Zambrano, S.; Ramirez, M.; de Hoyos, E.; Vasquez, H.; Lozano, K., *Materials Today* **2010,** *13* (11), 12-14.

214. Sawyer, L. C.; Jaffe, M., *Journal of Materials Science* **1986,** *21* (6), 1897-1913.

215. Senyurt, A. F.; Hoyle, C. E.; Wei, H.; Piland, S. G.; Gould, T. E., *Macromolecules* **2007,** *40* (9), 3174-3182.

216. Senyurt, A. F.; Wei, H.; Hoyle, C. E.; Piland, S. G.; Gould, T. E., *Macromolecules* **2007,** *40* (14), 4901-4909.

217. Shambaugh, R. L., *Industrial & Engineering Chemistry Research* **1988,** *27* (12), 2363-2372.

218. Shanmuganathan, K.; Elliot, S. M.; Lane, A. P.; Ellison, C. J., *ACS Applied Materials & Interfaces* **2014,** *6* (16), 14259-14265.

219. Shanmuganathan, K.; Fang, Y.; Chou, D. Y.; Sparks, S.; Hibbert, J.; Ellison, C. J., *ACS Macro Letters* **2012,** *1* (8), 960-964.

220. Shanmuganathan, K.; Sankhagowit, R. K.; Iyer, P.; Ellison, C. J., *Chemistry of Materials* **2011,** *23* (21), 4726-4732.

221. Shaw, C.; Shelby, J. E., *Physics and Chemistry of Glasses* **1988,** *29* (3), 87-90.

222. Shaw, C. M.; Shelby, J. E., *Physics and Chemistry of Glasses* **1988,** *29* (2), 49-53.

223. Shechter, L.; Wynstra, J., *Industrial & Engineering Chemistry* **1956,** *48* (1), 86-93.

224. Shenoy, S. L.; Bates, W. D.; Frisch, H. L.; Wnek, G. E., *Polymer* **2005,** *46* (10), 3372-3384.

225. Shyu, J.-J.; Yeh, C.-H., *Journal of Materials Science* **2007,** *42* (13), 4772-4777.

226. Silberstein, M. N.; Pai, C.-L.; Rutledge, G. C.; Boyce, M. C., *Journal of the Mechanics and Physics of Solids* **2012,** *60* (2), 295-318.

227. Sparks, B. J.; Hoff, E. F.; Hayes, L. P.; Patton, D. L., *Chemistry of Materials* **2012,** *24* (18), 3633-3642.

228. Sparks, B. J.; Hoff, E. F.; Xiong, L.; Goetz, J. T.; Patton, D. L., *ACS Applied Materials & Interfaces* **2013,** *5* (5), 1811-1817.

229. Stauffer, S. R.; Peppast, N. A., *Polymer* **1992,** *33* (18), 3932-3936.

230. Sun, T.; Baird, D.; Huang, H.; Done, D.; Wilkes, G., *Journal of Composite Materials* **1991,** *25* (7), 788-808.

231. Taden, A.; Landfester, K., *Macromolecules* **2003,** *36* (11), 4037-4041.

232. Taghavi, S.; Larson, R., *Physical Review E* **2014,** *89* (2), 023011.

233. Taguchi, Y.; Yen, C.-C.; Kang, S.; Tokita, M.; Watanabe, J., *Macromolecules* **2009,** *42* (8), 3179-3185.

234. Tallón, C.; Moreno, R.; Nieto, M. I.; Jach, D.; Rokicki, G.; Szafran, M., *Journal of the American Ceramic Society* **2007,** *90* (5), 1386-1393.

235. Tan, A. R.; Ifkovits, J. L.; Baker, B. M.; Brey, D. M.; Mauck, R. L.; Burdick, J. A., *Journal of Biomedical Materials Research Part A* **2008,** *87* (4), 1034-1043.

236. Tan, D. H.; Herman, P. K.; Janakiraman, A.; Bates, F. S.; Kumar, S.; Macosko, C. W., *Chemical Engineering Science* **2012,** *80*, 342-348.

237. Tan, D. H.; Zhou, C.; Ellison, C. J.; Kumar, S.; Macosko, C. W.; Bates, F. S., *Journal of Non-Newtonian Fluid Mechanics* **2010,** *165* (15), 892-900.

238. Tan, S.; Inai, R.; Kotaki, M.; Ramakrishna, S., *Polymer* **2005,** *46* (16), 6128-6134.

239. Tang, Y.; Fang, L.; Gao, P., *Journal of Materials Science* **2012,** *47* (23), 8094-8102.

240. Tanner, T.; Oelgoetz, J.; Golovchak, R.; Brennan, C.; Kovalskyy, A., *Bulletin of the American Physical Society* **2013,** *58*.

241. Tarbell, D. S.; Harnish, D. P., *Chemical Reviews* **1951,** *49* (1), 1-90.

242. Tate, B. D.; Shambaugh, R. L., *Industrial & Engineering Chemistry Research* **2004,** *43* (17), 5405-5410.

243. Termonia, Y., *Macromolecules* **1994,** *27* (25), 7378-7381.

244. Theron, S.; Yarin, A.; Zussman, E.; Kroll, E., *Polymer* **2005,** *46* (9), 2889-2899.

245. Tibiletti, L.; Ferry, L.; Longuet, C.; Mas, A.; Robin, J.-J.; Lopez-Cuesta, J.-M., *Polymer Degradation and Stability* **2012,** *97* (12), 2602-2610.

246. Tick, P. A., *Physics and Chemistry of Glasses* **1984,** *25* (6), 149-154.

247. Tirtaatmadja, V.; McKinley, G. H.; Cooper-White, J. J., *Physics of Fluids (1994-present)* **2006,** *18* (4), 043101.

248. Tischendorf, B. C.; Harris, D. J.; Otaigbe, J. U.; Alam, T. M., *Chemistry of Materials* **2002,** *14* (1), 341-347.

249. Tumbleston, J. R.; Shirvanyants, D.; Ermoshkin, N.; Janusziewicz, R.; Johnson, A. R.; Kelly, D.; Chen, K.; Pinschmidt, R.; Rolland, J. P.; Ermoshkin, A., *Science* **2015,** *347* (6228), 1349-1352.

250. Urman, K.; Otaigbe, J. U., *Progress in Polymer Science* **2007,** *32* (12), 1462-1498.

251. Uyar, T.; Besenbacher, F., *Polymer* **2008,** *49* (24), 5336-5343.

252. Vazquez, B.; Vasquez, H.; Lozano, K., *Polymer Engineering & Science* **2012,** *52* (10), 2260-2265.

253. Voelker, H.; Zettler, H. D.; Fath, W.; Berbner, H., Production of Fibers by Centrifugal Spinning. Google Patents: **1996**.

254. Vollrath, F.; Knight, D. P., *Nature* **2001,** *410* (6828), 541-548.

255. Wagener, K.; Boncella, J.; Nel, J., *Macromolecules* **1991,** *24* (10), 2649-2657.

256. Wakabayashi, K.; Register, R. A., *Polymer* **2005,** *46* (20), 8838-8845.

257. Wang, B.; Wang, Y.; Lei, Y.; Wu, N.; Gou, Y.; Han, C.; Fang, D., *Journal of Materials Chemistry A* **2014,** *2* (48), 20873-20881.

258. Wang, C.; Fang, C.-Y.; Wang, C.-Y., *Polymer* **2015**.

259. Wang, D.; Sun, G.; Chiou, B.-S.; Hinestroza, J. P., *Polymer Engineering & Science* **2007,** *47* (11), 1865-1872.

260. Wang, M.; Jin, H.-J.; Kaplan, D. L.; Rutledge, G. C., *Macromolecules* **2004,** *37* (18), 6856-6864.

261. Wang, N.; Wang, X.; Ding, B.; Yu, J.; Sun, G., *Journal of Materials Chemistry* **2012,** *22* (4), 1445-1452.

262. Wang, X.; Ke, Q., *Polymer Engineering and Science* **2006,** *46* (1), 1.

263. Ward, G., *Filtration & Separation* **2001,** *38* (9), 42-43.

264. Watton, W. A.; Snyder, J. G., Fiber Manufacturing Spinner and Fiberizer. Google Patents: **1996**.

265. Wei, T.; Hu, Y.; Hwa, L., *Journal of Non-Crystalline Solids* **2001,** *288* (1), 140-147.

266. Weng, B.; Xu, F.; Salinas, A.; Lozano, K., *Carbon* **2014,** *75*, 217-226.

267. Xie, S.; Zheng, Y.; Zeng, Y., *Industrial & Engineering Chemistry Research* **2014,** *53* (32), 12866-12871.

268. Xu, H.; Chen, H.; Li, X.; Liu, C.; Yang, B., *Journal of Polymer Science Part B: Polymer Physics* **2014,** *52* (23), 1547-1559.

269. Xu, X.; Day, D., *Physics and Chemistry of Glasses* **1990,** *31* (5), 183-187.

270. Yang, G.; Kristufek, S. L.; Link, L. A.; Wooley, K. L.; Robertson, M. L., *Macromolecules* **2015**.

271. Yang, H.; Zhang, Q.; Lin, B.; Fu, G.; Zhang, X.; Guo, L., *Journal of Polymer Science Part A: Polymer Chemistry* **2012,** *50* (20), 4182-4190.

272. Yu, J. H.; Fridrikh, S. V.; Rutledge, G. C., *Polymer* **2006,** *47* (13), 4789-4797.

273. Yu, X.; Day, D. E.; Long, G. J.; Brow, R. K., *Journal of Non-Crystalline Solids* **1997,** *215* (1), 21-31.

274. Zeleny, J., *Physical Review* **1917,** *10* (1), 1.

275. Zeng, J.; Kumar, S.; Iyer, S.; Schiraldi, D. A.; Gonzalez, R., *High Performance Polymers* **2005,** *17* (3), 403-424.

276. Zhang, J.; Liu, Z.; Kong, Q.; Zhang, C.; Pang, S.; Yue, L.; Wang, X.; Yao, J.; Cui, G., *ACS Applied Materials & Interfaces* **2012,** *5* (1), 128-134.

277. Zhang, S.; Shim, W. S.; Kim, J., *Materials & Design* **2009,** *30* (9), 3659-3666.

278. Zhang, Y.; Rutledge, G. C., *Macromolecules* **2012,** *45* (10), 4238-4246.

279. Zhao, R.; Wadsworth, L. C., *Polymer Engineering and Science* **2003,** *43* (2), 463.

280. Zhao, Y.; Schiraldi, D. A., *Polymer* **2005,** *46* (25), 11640-11647.

281. Zhou, C.; Tan, D. H.; Janakiraman, A. P.; Kumar, S., *Chemical Engineering Science* **2011,** *66* (18), 4172-4183.

282. Zhou, H. J.; Green, T. B.; Joo, Y. L., *Polymer* **2006,** *47* (21), 7497-7505.

283. Zong, X.; Kim, K.; Fang, D.; Ran, S.; Hsiao, B. S.; Chu, B., *Polymer* **2002,** *43* (16), 4403-4412.